NASA/CR–2020-220425

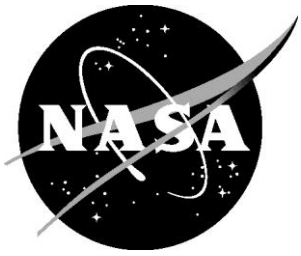

Passive Aeroelastic Tailoring

Final Report

Benjamin Smith and Timothy Brooks
Aurora Flight Sciences, Inc., Manassas, Virginia

Mark Leader, Ting Wei Chin and Graeme Kennedy
Georgia Institute of Technology, Atlanta, Georgia

Joaquim Martins and Carlos Cesnik
University of Michigan, Ann Arbor, Michigan

February 2020

NASA STI Program . . . in Profile

Since its founding, NASA has been dedicated to the advancement of aeronautics and space science. The NASA scientific and technical information (STI) program plays a key part in helping NASA maintain this important role.

The NASA STI program operates under the auspices of the Agency Chief Information Officer. It collects, organizes, provides for archiving, and disseminates NASA's STI. The NASA STI program provides access to the NTRS Registered and its public interface, the NASA Technical Reports Server, thus providing one of the largest collections of aeronautical and space science STI in the world. Results are published in both non-NASA channels and by NASA in the NASA STI Report Series, which includes the following report types:

- TECHNICAL PUBLICATION. Reports of completed research or a major significant phase of research that present the results of NASA Programs and include extensive data or theoretical analysis. Includes compilations of significant scientific and technical data and information deemed to be of continuing reference value. NASA counter-part of peer-reviewed formal professional papers but has less stringent limitations on manuscript length and extent of graphic presentations.

- TECHNICAL MEMORANDUM. Scientific and technical findings that are preliminary or of specialized interest, e.g., quick release reports, working papers, and bibliographies that contain minimal annotation. Does not contain extensive analysis.

- CONTRACTOR REPORT. Scientific and technical findings by NASA-sponsored contractors and grantees.

- CONFERENCE PUBLICATION. Collected papers from scientific and technical conferences, symposia, seminars, or other meetings sponsored or co-sponsored by NASA.

- SPECIAL PUBLICATION. Scientific, technical, or historical information from NASA programs, projects, and missions, often concerned with subjects having substantial public interest.

- TECHNICAL TRANSLATION. English-language translations of foreign scientific and technical material pertinent to NASA's mission.

Specialized services also include organizing and publishing research results, distributing specialized research announcements and feeds, providing information desk and personal search support, and enabling data exchange services.

For more information about the NASA STI program, see the following:

- Access the NASA STI program home page at http://www.sti.nasa.gov

- E-mail your question to help@sti.nasa.gov

- Phone the NASA STI Information Desk at 757-864-9658

- Write to:
  NASA STI Information Desk
  Mail Stop 148
  NASA Langley Research Center
  Hampton, VA 23681-2199

NASA/CR–2020-220425

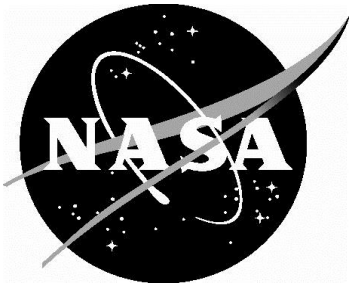

Passive Aeroelastic Tailoring

Final Report

Benjamin Smith and Timothy Brooks
Aurora Flight Sciences, Inc., Manassas, Virginia

Mark Leader, Ting Wei Chin and Graeme Kennedy
Georgia Institute of Technology, Atlanta, Georgia

Joaquim Martins and Carlos Cesnik
University of Michigan, Ann Arbor, Michigan

National Aeronautics and
Space Administration

Langley Research Center
Hampton, Virginia 23681-2199

Prepared for Langley Research Center
under Contract NNL15AA01C

February 2020

Available from:

NASA STI Program/Mail Stop 148
NASA Langley Research Center
Hampton, Virginia 23681-2199
Fax: 757-864-6500

Table of Contents

List of Figures

List of Tables

1 Introduction

The Passive Aeroelastic Tailoring (PAT) project was tasked with investigating novel methods to achieve passive aeroelastic tailoring on high aspect ratio wings. The goal of the project was to identify structural designs or topologies that can improve performance and/or reduce structural weight for high-aspect ratio wings. This project considered two unique approaches, which were pursued in parallel: through-thickness topology optimization and composite tow-steering.

The through-thickness topology optimization, performed by Georgia Tech, sought to explore through-thickness, free-form wing box topologies that deviate substantially from traditional spar-rib-stringer designs. This approach was premised on continued improvement in additive manufacturing technologies over the next decades that may enable the efficient fabrication of large, arbitrarily shaped structures with material properties approaching those of conventional aluminum. The focus of the effort for the PAT project was to develop and advance low technology readiness level (TRL) design techniques to apply volumetric topology optimization to high-aspect ratio structures within an aircraft wing analysis framework. For this effort, emphasis was placed on developing efficient algorithms to handle the very large meshes required to sufficiently discretize a high-aspect ratio volume (driven largely by the wing thickness aspect ratio, nearly an order of magnitude larger than the planform aspect ratio) and methods for efficiently calculating and incorporating stability (buckling) constraints. This effort is detailed in Appendix E.

The composite tow-steering approach, performed by Aurora Flights Sciences (Aurora) and the University of Michigan, leveraged high-TRL Automated Fiber Placement (AFP) technology to enable the fabrication of wing skins with curvilinear fiber paths. By opening the design space to include spatially varying material directions, the wing box design was improved by exploiting both structural efficiency (e.g., aligning fibers to the principal strain axis) as well as aeroelastically, through maneuver load alleviation.

The approach for the composite tow-steering effort is depicted in Figure 1.1. In the first phase, representative test panels were manufactured to demonstrate the feasibility of fabricating steered tow paths with conventional AFP equipment and materials. These panels were utilized for mechanical coupon testing to characterize the strength differences between steered and traditional (unsteered) laminates for subsequent design purposes. A six-foot semispan proof-of-concept ‘Hershey Bar’ wing was fabricated featuring tow-steered wing skins with material orientation varying from 15° from the spanwise axis at the root to 75° at the tip to validate the tow-steering fabrication approach.

The second phase of the tow-steering effort focused on optimizing the tow-steered wing and was performed by the University of Michigan Multidisciplinary Design Optimization Laboratory (MDO Lab). The uCRM-13.5 ‘Common Research Model’ was utilized as the basis for this effort. Optimization was performed at full scale with the objective of minimizing fuel burn. The optimization included scaled constraints where appropriate (e.g., minimum gauge thicknesses, tow-steering curvature) to facilitate the subsequent design of a scaled test article. The optimization resulted in the final outer mold line (OML) of the wing, along with sized structural members (including thickness gradients for the skins and spars) and the spatially varying orientation field for the tow-steered wing skins.

In addition to generating the optimized design to serve as a basis for the design of a scaled test article, comparisons were drawn to traditional (nonsteered) optimized configurations to quantify the performance benefit afforded by tow-steering. It is noted that the latter parts of this research effort were independently funded by the University of Michigan and that material more extensively covered in references [1] and [2] are included here with permission.

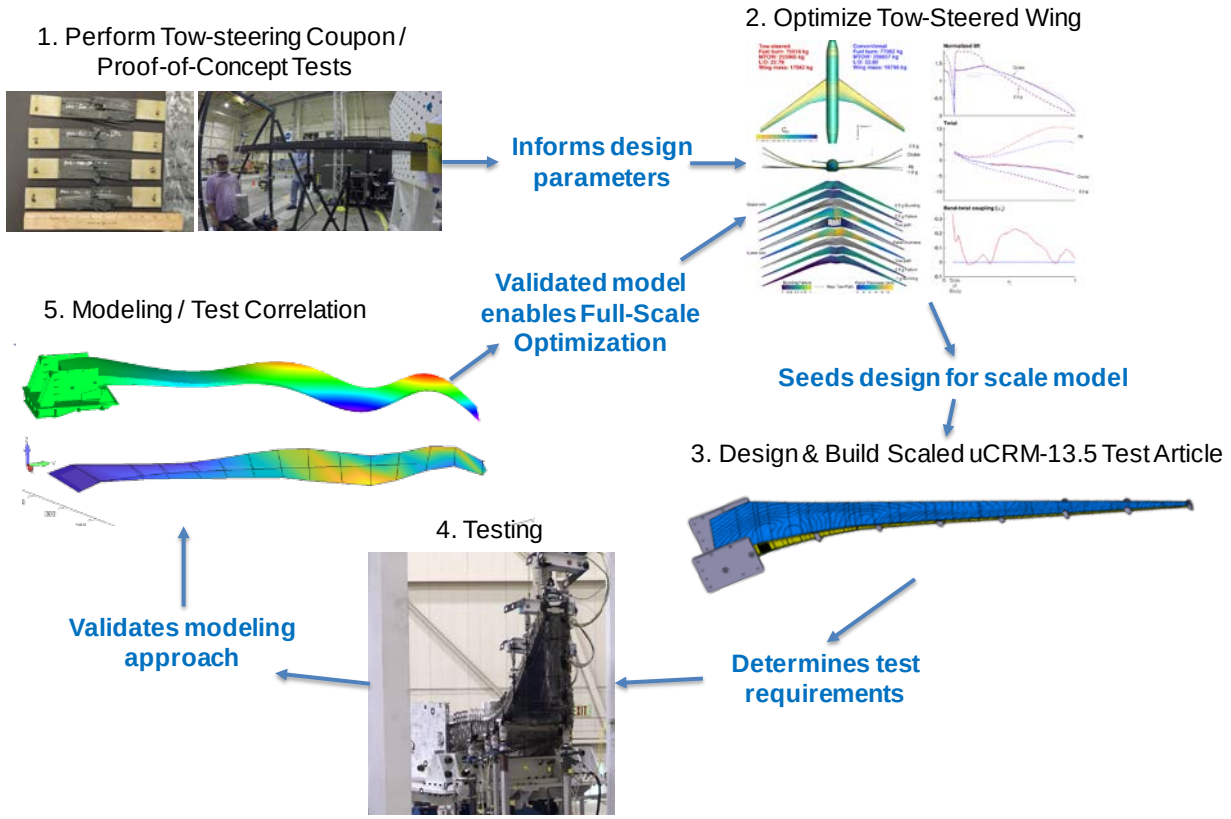

Figure 1.1. Passive Aeroelastic Tailoring approach to tow-steering development.

The third phase of the tow-steering project was to design and build the uCRM-13.5 test article based on the optimized design. The test article was geometrically scaled 27% and utilized the tow-steering patterns identified by the optimization. Local thicknesses were also scaled geometrically, with local pad-ups added to accommodate discrete load application points, or fastener bearing loads as identified by the detailed stress analysis. The test article was fully modeled with computer aided design (CAD), including composite part design (CPD) data to aid in manufacturing. Aurora fabricated all composite parts, including the tow-steered skins, and subsequently assembled the test article at its Columbus, MS manufacturing facility.

The test article was delivered to the National Aeronautics and Space Administration (NASA) Armstrong Flight Research Center (AFRC) Flight Loads Laboratory (FLL) for structural testing, consisting of ground vibration testing (GVT), flexural axis testing, and -1G and +2.5G limit load tests. NASA AFRC personnel led the test planning process, with input from NASA Langley Research Center (LaRC) and Aurora engineers, including test requirements, instrumentation, test equipment/fixtures, test procedures, and test execution.

Finally, the structural test data were correlated to the test article predictions to validate the overall modeling approach, identify possible sources of discrepancy, and suggest improvements to the overall modeling and design process. Ultimately, the test data provided confidence in the modeling approach, and by extension, the optimization results.

2 Manufacturing & Materials Development

Maturing and validating the tow-steering manufacturing process to identify and characterize the limitations of the tow-steering and the effects of tow-steering on the mechanical properties of the material were prerequisites to conducting the tow-steering design and optimization. The tow-steering maturation effort proceeded in three stages. First, practical limitations for the tow-steering were identified, including with unique features such as puckers and gaps/overlaps, which develop during the steering process, along with mathematical relations (e.g., tow curvature, divergence) to characterize the occurrence of these features for design purposes. Second, test panels were designed and fabricated representing the manufacturing limits identified in the first stage. These panels were used for coupon testing to characterize the effects tow-steering has on local mechanical properties. Finally, a proof-of-concept wing box was fabricated to validate the findings of the previous steps through an assembled structure.

2.1 Tow-Steering Development & Considerations

In general, there are two sources of strength reduction of concern for tow-steered laminates: inherent geometric complexities due to tow convergence zones (e.g., gaps and overlaps) and manufacturing defects related to the in-plane curvature of the tows. The potential impact of gaps on strength and stiffness is due to the creation of resin-rich areas, which are void of fiber within a given region. On the other hand, overlaps contribute to additional local thickness, which may provide additional strength or stiffness. In either case, the existence of gaps or overlaps creates a complex three-dimensional geometry, which may have secondary impacts on strength or stiffness as subsequent plies are placed. Each gap or overlap acts as a local tow-drop with corresponding resin-rich areas and the potential to cause fiber crimping in the through-thickness direction, adversely impacting strength.

As tow-paths converge or diverge, triangular gaps or overlaps develop, called “convergence zones.” The geometry of the gaps and overlaps and to a lesser degree, their locations, can be influenced by the AFP programming, by setting tow-drop criteria and seed locations for the fiber paths. The tow-drop criteria are typically specified as a percentage of the tow width: a 50% lap/gap criteria criterion results in a tow drop once that tow overlaps its neighboring tow by 50% of its tow width, resulting in a gap at the location of the drop. A convergence zone is depicted in Figure 2.1 where the cyan tow overlaps the blue tow. In the figure, once the overlap (shown in purple) reaches half a tow width, the tow is dropped, resulting in the gap region (shown in red). Gaps could be eliminated by dropping tows once the overlap reaches 100% of the tow width, while overlaps could be eliminated by dropping the tow as soon as it first contacts an adjacent course of tows.

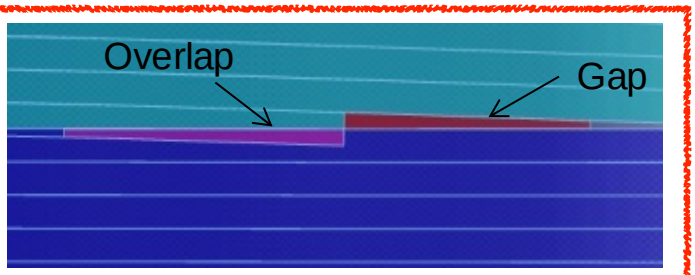

Figure 2.1. Typical geometry of a convergence zone.

While gaps and overlaps arise due to the convergence or divergence of tows, 'puckers' arise due to tow curvature, and are characterized by material from the inside edge of the tow lifting from the tool surface. Puckers were seen in prefabrication tow-steering development trials as shown in Figure 2.2. As a pucker flattens out during the debulk process or application of subsequent plies, a local fiber crimp may occur, which adversely affects strength. The minimum radius at which tows tend to pucker depends on a wide range of factors, including: tow width, resin tack, prepreg stiffness, curvature of the tool surface, and specific features and processing parameters of the AFP itself.

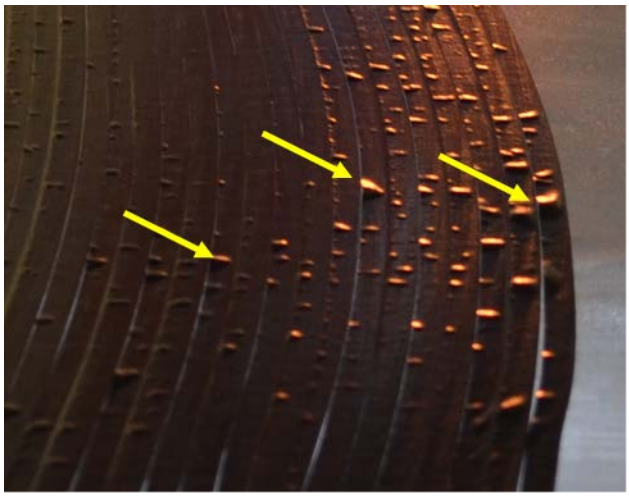

Figure 2.2. Picture of high-curvature region exhibiting tow puckering on the first ply.

The degree of curvature and divergence may be assessed by calculating the curl and divergence of the unit vector field, which describes the local material orientation of a given ply. The curl provides an exact, quantitative description of curvature. The calculation of divergence is to describe the density of convergence zones, and in special cases, can be used to predict the actual locations of convergence zones. For a two-dimensional unit vector field, curl and divergence are calculated in the traditional vector calculus sense as provided in Equations 1 and 2, respectively:

$$\nabla \times \boldsymbol{u} = \left[\frac{\partial v}{\partial x} - \frac{\partial u}{\partial y}\right] \hat{\boldsymbol{z}} \tag{1}$$

$$\nabla \cdot \boldsymbol{u} = \frac{\partial u}{\partial x} + \frac{\partial v}{\partial y} \quad (2)$$

where $\boldsymbol{u} = u\hat{\boldsymbol{x}} + v\hat{\boldsymbol{y}}$ is the unit vector field describing the local fiber orientation.

There is a reciprocal relationship between the curvature (as calculated by curl of the orientation field) and the divergence of the orientation field when off-angle plies, most notably the orthogonal (90 degree) plies, are considered. It can be shown through vector calculus identities that the magnitude of the curl of an orientation field is equal to the magnitude of the divergence of its orthogonal orientation field, and vice versa. Therefore, for a laminate that includes plies steered 90 degrees relative to the primary steering direction, the more restrictive constraint on curvature or divergence must be satisfied for both. This requirement may be observed visually in Figure 2.3 by comparing the curvature or divergence contour plots with the divergence and contour plots, respectively, of an orthogonal ply.

One potential method briefly considered for avoiding this limitation and potentially increasing the robustness of the tow-steered laminate would be to consider a laminate wherein some of the tows are not steered, but instead remain fixed relative to a global rosette. One such laminate considered for the current project would keep half the plies unsteered, representing the quasi-isotropic component of the laminate. An equal number of steered plies, all oriented in the primary steering direction, would be interspersed with the unsteered plies to provide the desired directionality to the laminate. A sample 16-ply laminate would be: $[0°+\theta,90°,0°+\theta,0°,+45,0°+\theta,-45°,0°+\theta]_s$, where θ is the local primary steering direction. Because there are no off-angle steered plies, the constraints on orthogonal plies need not be considered. Furthermore, and perhaps more advantageously, half of the plies are unsteered and therefore would not generate tow-steering ‘’features” such as convergence zones or tow-puckering, which may result in a more robust laminate. The drawback, however, is that the layup sequence continuously varies with the local steering angle, potentially requiring a very large test matrix to characterize the various laminate sequences.

Because the tow-steered laminate stack sequence was predetermined, no opportunity existed to tailor the flexural stiffness properties of the laminate. Approaches that would enable the simultaneous tailoring of both in-plane and flexural properties by defining tow-steering on a ply-by-ply basis were not considered for the present work due to the complexity in analyzing and testing the resulting laminates.

Park Electrochemical’s 130gsm HTS45/E-752-LT material system slit to a tow width of 0.25 in. was selected for its performance and positive prior experience with the system for AFP. Based on prior experience with the material system, a minimum radius of curvature of 70 in. was utilized. A ply fraction of [62.5%, 12.5%, 12.5%, 12.5%], corresponding to lamina angles of [0°, +45°, -45°, 90°] was selected, with the plies distributed to maintain a laminate as balanced and symmetric as possible.

2.2 Materials Testing

One challenge of conducting mechanical testing of tow-steered laminates is that the tow-steering introduces several additional parameters to the laminate design, which vary spatially. To perform a cursory assessment of the performance of tow-steered laminates, panels were fabricated with alternating regions of high curvature/low divergence and low curvature/high divergence. This pattern was accomplished by defining a sinusoidally varying orientation field that varied up to ± 6.1° from the nominal fiber direction, resulting in radius of curvatures approaching 70 in. The tow-steering orientation field utilized for these panels is described in degrees (with the 0° direction aligned to the *x*-axis) by Equation 3, with the spatial coordinates *x* and *y* described in inches:

$$\theta = 90 - 6.1\sin(7.5x)\cos(7.5y) \tag{3}$$

The resulting tow paths are shown in Figure 2.3. Contours of curl (curvature) and divergence are also shown, indicating the alternating regions of high curvature/low divergence and low curvature/high divergence. Coupons cut from the high curvature regions are referred to as “Steered-Curvature,” coupons from the high divergence region as “Steered-Divergence,” and coupons cut from intermediate areas with moderate curvature and moderate divergence were referred to as “Steered-Neutral.” Coupons from panels with unsteered (traditional) tows are referred to as “Unsteered.”

Four master panels were fabricated for mechanical testing: Panels 1 & 2 were tow-steered panels approximately 38 in. x 64 in. with fiber paths as described in the previous section. Panel 1 was designated for shear and compressive tests and was comprised of 24 plies with a laminate sequence: $[0°,90°,0°_2,+45°,0°,-45°,0°_3,90°,-45°,+45°,0°_4,$ $-45°,0°,+45°,0°_2,90°,0°]+\theta$, where θ denotes the local steering angle. Panel 2 was a 16-ply panel with laminate sequence: $[0°,90°,0°_2,+45°,0°,-45°,0°]_s+\theta$ and designated for tensile tests. Both panels were cut into subpanels and categorized according to the local tow-steering characteristics (curvature, divergence, or neutral). Panels 3 and 4 were both unsteered control panels and were comprised of the same layup sequence as Panels 1 and 2, respectively. The thickness of the test panels was chosen to conform to ASTM test standards.

The test matrix performed is shown in Table 1. Both unnotched and notched tensile and compressive tests were performed, as well as a V-notch shear test, in both T12 and T21 orientations.

Test data, normalized to the corresponding unsteered data, are provided in Appendix B. Panel and coupon cutting diagrams, coupon test results, and non-normalized aggregated data are provided in Attachment 7. The coefficient of variation associated with the tow-steered coupons is much higher than the unsteered population – this difference may be due to the distribution of tow-steering ‘features’ amongst coupons. Due to the discrete nature of the location of convergence zones (or even puckers, for that matter), variation between even adjacent coupons is expected.

The unnotched tow-steered specimens reflected a larger reduction in strength compared to unsteered laminates than did the notched specimens, which generally retained about 93% of the unsteered strength. For design purposes, all steered coupons for a given test

(i.e., longitudinal open hole tension (OHT), transverse open hole compression (OHC), etc.) were aggregated into a single population for which an equivalent b-basis design value was calculated using the National Institute for Aviation Research (NIAR)'s AGATE Statistical Analysis Program (ASAP) calculator.

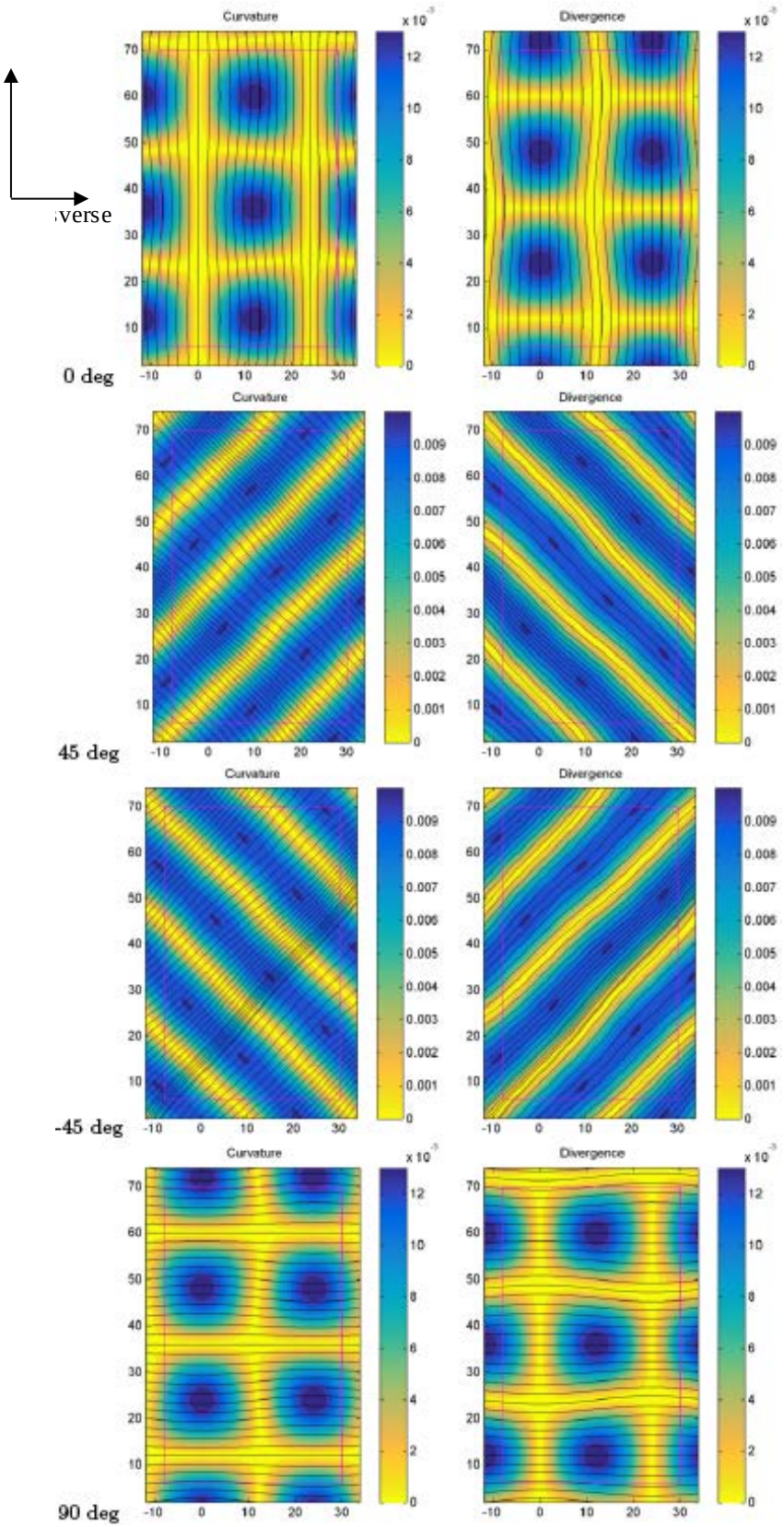

Figure 2.3. Tow-steering fiber guide curves (black) with curl (curvature) contours (left) and divergence contours (right) for various ply angles.

Table 1. Mechanical coupon test matrix.

		Unnotched			Notched (1/4" Hole)		
		Unsteered	Steered/ Neutral	Steered/ Divergence	Unsteered	Steered/ Curvature	Steered/ Divergence
	Method	ASTM D3039	ASTM D3039	ASTM D3039	ASTM D5766	ASTM D5766	ASTM D5766
	Size	1.0"x10"	1.0"x10"	1.0"x10"	1.5"x10"	1.5"x10"	1.5"x10"
σ^t_0	# Plies	16	16	16	16	16	16
	Method	ASTM D3039	ASTM D3039	ASTM D3039	ASTM D5766	ASTM D5766	ASTM D5766
	Size	1.0"x10"	1.0"x10"	1.0"x10"	1.5"x10"	1.5"x10"	1.5"x10"
σ^t_{90}	# Plies	16	16	16	16	16	16
	Method	ASTM D6641	ASTM D6641		ASTM D6484	ASTM D6484	ASTM D6484
	Size	0.5"x5.5"	0.5"x5.5"	-	0.5"x5.5"	0.5"x5.5"	0.5"x5.5"
σ^c_0	# Plies	24	24		24	24	24
	Method	ASTM D6641	ASTM D6641	ASTM D6641	ASTM D6484	ASTM D6484	ASTM D6484
	Size	1.5"x12"	1.5"x12"	1.5"x12"	1.5"x12"	1.5"x12"	1.5"x12"
σ^c_{90}	# Plies	24	24	24	24	24	24
		Unsteered	Steered/ Curvature	Steered/ Divergence			
	Method	ASTM D5379	ASTM D5379	ASTM D5379			
	Size	0.75"x3"	0.75"x3"	0.75"x3"	-	-	-
τ_{12}	# Plies	24	24	24			
	Method	ASTM D5379	ASTM D5379	ASTM D5379			
	Size	0.75"x3"	0.75"x3"	0.75"x3"			
τ_{21}	# Plies	24	24	24	-	-	-

A trend found by comparing the data between the longitudinal and transverse test for the divergence and curvature populations was observed. As discussed above, for a given steering pattern, the curvature and divergence properties are orthogonal, and this difference appears to be reflected in the summary data. For example, for both longitudinal OHC and OHT cases, the divergence-dominated coupons appear to have nearly double the coefficient of variation and slightly higher mean strength compared to the curvature-dominated coupons. However, this relationship reverses for the transverse coupons, where the curvature-dominated coupons show higher variation and slightly higher mean strength (noting that the transverse plies for these coupons would be divergence dominated).

2.3 Hershey-Bar Proof of Concept

A 6' semispan, 10" chord, and 2.6" deep 'Hershey-bar' wing was produced as a tow-steering fabrication and assembly risk reduction exercise. The Hershey-bar wing was also used to validate the full design process, including transitioning a conceptual tow-steering pattern to a Finite Element Model (FEM) and CAD representation and onward to AFP programming and manufacturing. As an opportunity, static load testing was utilized to evaluate the flexural and minimum strength properties of the assembled wing.

Both wing skins consist of a 12-ply laminate with a $[0°, 90°, 0°, 45°, 0°, -45°]_s$ stacking sequence. The laminate steering angle corresponding to the 0° ply direction continuously varied from 15° from the spanwise axis at the root to 75° (predominantly chordwise) at the tip, as shown in Figure 2.4. The test article is shown in Figure 2.5.

Because of the simple loading condition (a single point tip load), the rib-spacing was biased toward the root for optimal spacing for skin buckling. Ribs were not necessary in the outboard regions of the wing due to low bending moment (noting that the chord, height, and skin thickness remained constant in span).

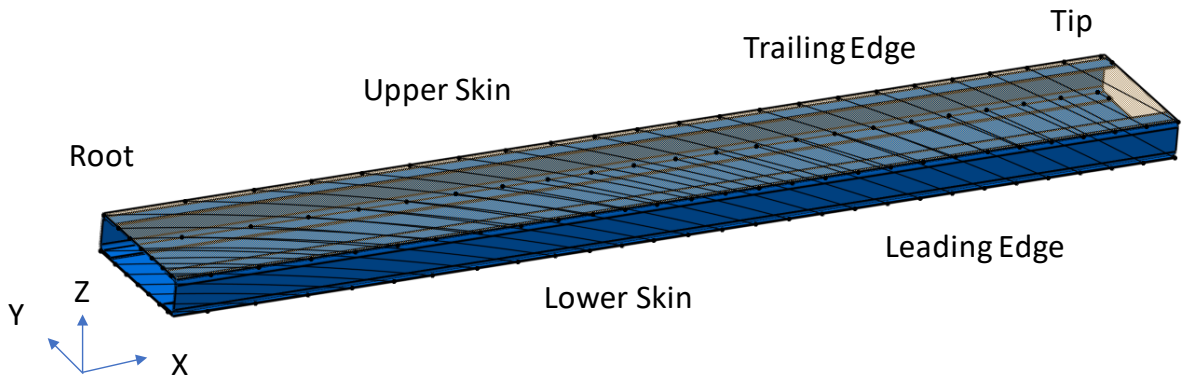

Figure 2.4. Hershey wing box CAD representations, showing tow steering guide splines (ribs omitted from figure).

Figure 2.5. Partial assembly of Hershey wing box (left) and final assembly (right).

Aurora performed static loads testing of the Hershey-bar test article prior to shipping to AFRC, as described in Appendix F. Because the primary objective of this test was as a proof-load test, the test itself was rudimentary with minimal instrumentation (deflection data were obtained with a hand-held laser tracker probe) and crude boundary conditions. As a result, significant rigid body motion was observed and while post-processing was utilized to correct for the compliant boundary conditions, the lack of instrumentation limited the accuracy of the correction. Testing performed at AFRC made use of robust constraints and instrumentation and is expected to be of higher quality, however, correlation of AFRC test data to predictions was not performed as part of this effort. Details of the testing performed at Aurora, along with the FEM analysis are available in Appendix F.

Because the Hershey bar wing was modeled and tested prior to the availability of coupon test results, the material modulus was based on previously established lamina values for unsteered properties and was therefore identified as a possible source of discrepancy between the estimated wing stiffness and the apparent wing stiffness observed during the Aurora test. While the Hershey bar wing skins were comprised of a different ply fraction (50%, 16.6%, 16.6%, 16.6%) than the coupon laminates (62.5%, 12.5%, 12.5%, 12.5%), the Classical Lamination Theory (CLT) can be utilized to predict the equivalent coupon modulus based on the Hershey-bar material assumptions for the purpose of comparison. Table 2 compares the predicted coupon stiffness using Hershey-bar material assumptions with the coupon test results. As can be seen from the results, the assumed value lies between the tensile and compressive modulus observed during coupon testing, and is approximately 3% higher than the combined modulus, which suggests that the material modulus was well estimated and is not a likely source of error.

Table 2. Comparison of estimated Hershey-bar modulus to coupon test results

	Predicted Modulus (Hershey-bar material assumptions)	Average Coupon Tensile Modulus	Average Coupon Compressive Modulus	Combined Modulus (Average of Tensile and Compressive)
Modulus (msi)	11.96	12.446	10.764	11.605

3 Conceptual Design & Tow-Steering Optimization

The conceptual design and optimization work described in this section was performed by the University of Michigan MDOLab.

3.1 Baseline uCRM-9/uCRM-13.5

The design optimization problems considered in this study were performed on the undeflected Common Research Models (uCRM). These models were based on the aerodynamic benchmark NASA Common Research Model (CRM) developed by Vassberg et al. [3] and extended for use in aeroelastic design analysis and optimization by Brooks et al. [4]. A brief summary of the models will be given here, for a more detailed description readers should consult Brooks et al. [4].

The uCRM models come in two variants. The first variant (uCRM-9) maintains the original wing planform of the CRM, with wing dimensions and structural topology similar to that of the Boeing 777 aircraft. The second variant (uCRM-13.5) features a modified wing design with a higher aspect ratio of 13.5, which is higher than any commercial transonic aircraft designs flying to date. The planforms of each uCRM model are shown in Figure 3.1, and the wing specifications are listed in Table 3. The geometry of both models include the aircraft wing, fuselage, and horizontal stabilizer. In these models, only the wing structure is modeled and considered to be flexible, while the remaining aircraft components are rigid. To understand the effect of tow steering on both medium and high-aspect-ratio wing design, optimizations are performed on both models in this work.

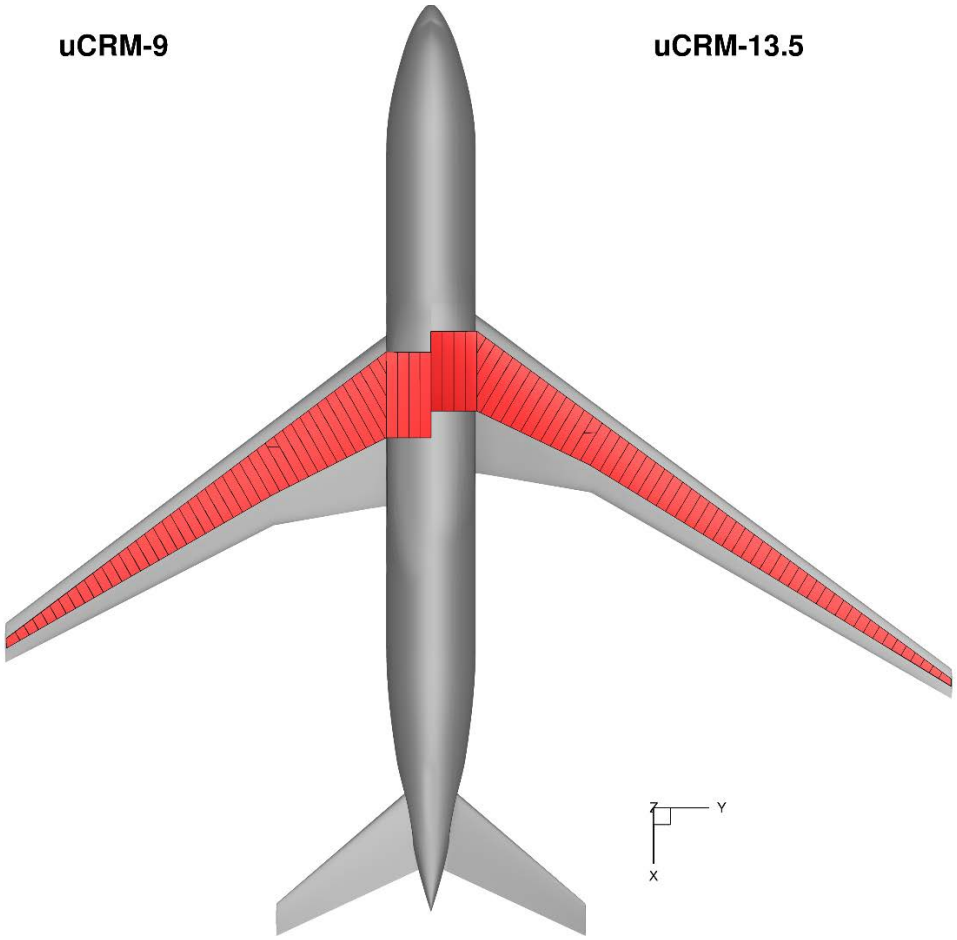

Figure 3.1 Wing and structural wing box planform for the uCRM-9 (left) and uCRM-13.5 (right).

Table 3. uCRM wing specifications.

Parameter	uCRM-9	uCRM-13.5
Aspect ratio	9.0	13.5
Span (m)	58.76	72.00
Reference area (m^2)	383.74	383.78
Quarter-chord sweep (deg)	35	35
MAC (m)	7.01	5.77

For each uCRM model, the aerodynamic performance is analyzed using a Reynolds-averaged Navier–Stokes (RANS) computational fluid dynamics (CFD) solver on an overset mesh of each model with roughly 1.2 million volume cells. The engine nacelle, pylon, and vertical stabilizer are not considered. To account for the drag of these missing components, a fixed offset of 30 drag counts is added to the drag predicted by the CFD solver.

The CRM wing box is composed of an upper and lower skin, two spars, ribs (49 on the uCRM-9 and 58 on the uCRM-13.5), and an engine mount panel. The leading-edge spar is straight, except for a kink at the wing-body junction, whereas the trailing-edge spar features an additional kink at the Yehudi break. The center wing box section includes four

ribs oriented parallel to the fuselage, with the remaining ribs distributed along the span of the wing perpendicular to the leading edge, with the exception of the closeout rib at the tip. An additional panel is included between the two ribs at the Yehudi break. This panel is used to mount the engine to the wing, along with the leading-edge spar at this location. The structural model also includes external nonstructural masses. The masses include discrete leading- and trailing-edge lumped masses, which are used to model the effect of the mounted actuators and control surfaces. These masses are attached at spanwise locations along either spar. Finally, the inertial effects of the engine and the fuel weight present in the fuel bays of the wing box are modeled by adding the appropriate masses. The wing box structure is modeled using a half-wing model with enforced symmetry conditions. Figure 3.2 illustrates the boundary conditions used to link the wing box structural FEM to the fuselage geometry.

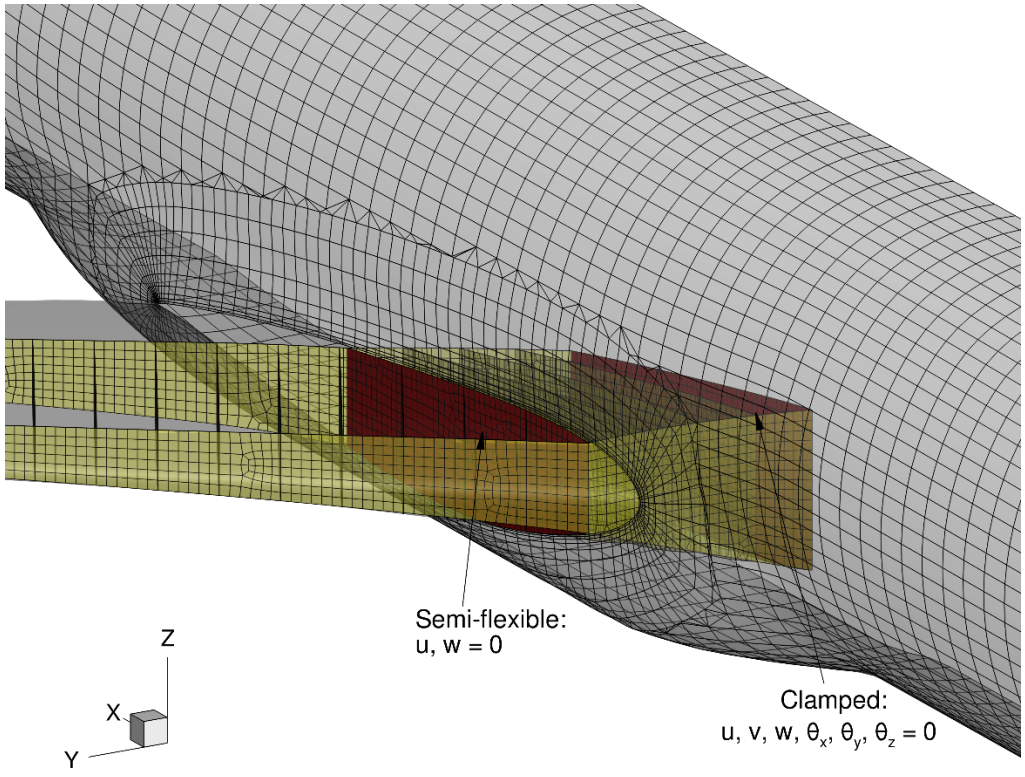

Figure 3.2 The wing box structure is clamped at the symmetry plane, and partially constrained at the wing-fuselage junction.

The inner most wing box rib is clamped at the symmetry plane, so all the displacements and rotations for the elements in that rib are fixed to zero. In addition, the rib at the wing-fuselage junction is constrained such that the vertical and longitudinal displacements are fixed. Thus, small displacements in the spanwise direction and rotation are permitted, allowing for some bending deformation in this region. However, these displacements are very small in practice. The choice in boundary conditions for the model were made to be consistent with previous iterations of the uCRM design. The FEM mesh for each wing

model has roughly 24,000 mixed interpolation tensorial component finite elements [5] with a total of about 136,000 degrees of freedom. The stiffeners of the design are included implicitly through a smeared stiffness approach, where their stiffness is added ("smeared") into that of the ribs, skins, and spars [6]. This allows for the stiffeners' design variables—height, width, and spacing—to be treated as continuous design variables by the optimizer.

3.2 Tow-Steering Optimization

In this section, the aeroelastic benefits of tow-steering specific to wing design will be explored. To this end, a series of fuel burn minimization problems were performed on the uCRM-9. To quantify the benefits, the optimizations were run with both a tow-steered and fixed ply orientation conventional composite wing box design. The benefits of tow-steering were then reassessed with a conventional design where the plies of the wing skins were free to be rotated by the optimizer. Then, the performance penalty associated with the AFP manufacturing constraints were quantified by reoptimizing the tow-steered design without them. The tow-steered and fixed ply orientation conventional composite design optimizations were then performed on the uCRM-13.5. Including this design provided insight into the benefits of tow steering with respect to high-aspect-ratio wing design. Finally, the effect of aspect ratio on the wing design performance was refined. This was accomplished by reoptimizing the tow-steered and fixed ply orientation conventional composite designs on the uCRM model for a wing aspect ratio of 7.5, 9, 10.5, 12, and 13.5 and analyzing the resulting trends in performance.

3.2.1 Computational Framework

To quantify the benefits of passive load alleviation, it is necessary to consider the coupling between aerodynamics and structural deformation that is particularly strong in high aspect ratio wings. To this end, a static aeroelastic analysis is performed, where the internal structural forces are in equilibrium with the aerodynamic loads. The analysis features a RANS-based Computational Fluid Dynamics (CFD) solver to compute aerodynamic loads, coupled to a Computational Structural Mechanics (CSM) solver, to compute structural deformations. The optimization and analysis scheme used to solve this problem is implemented in the University of Michigan's MACH (MDO for Aircraft Configurations with High fidelity) framework [7], described throughout the rest of this subsection. The MACH workflow is depicted in Figure 3.3.

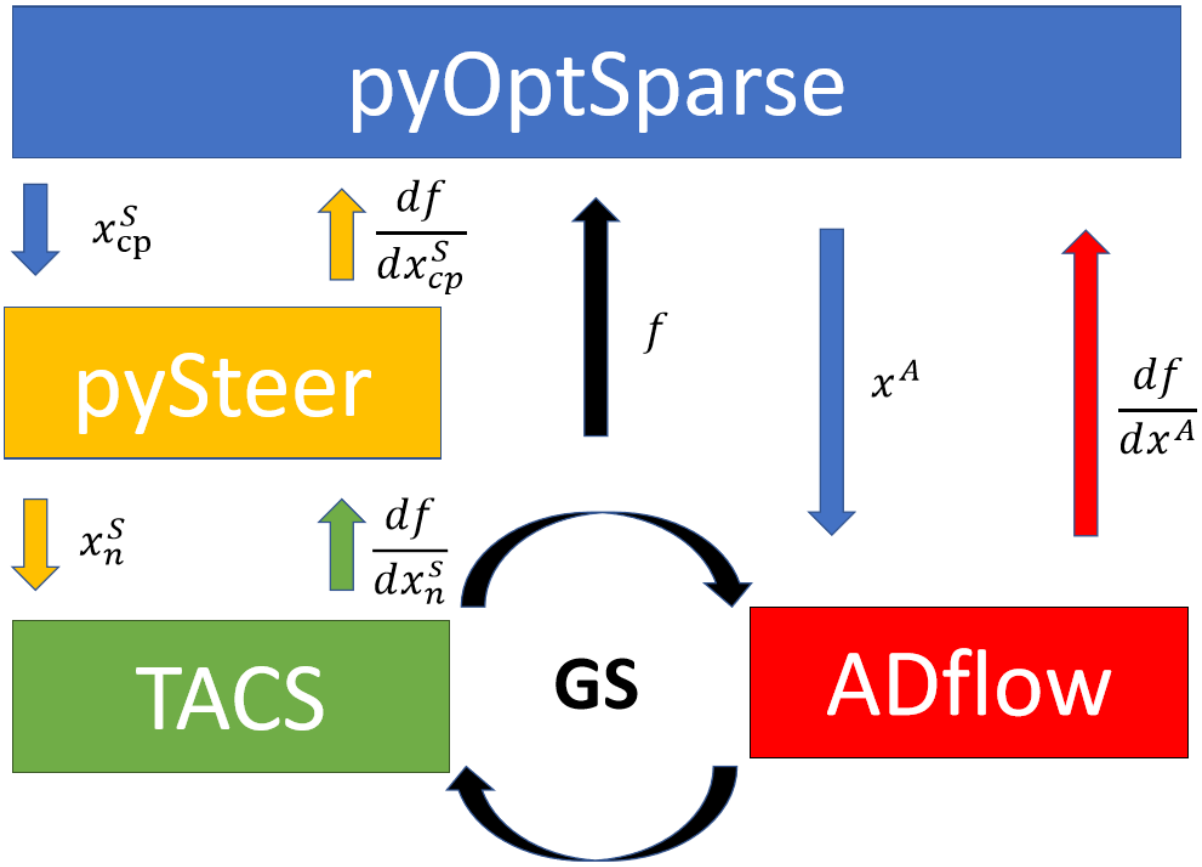

Figure 3.3 Tow-steering optimization flowchart

3.2.1.1 Aerodynamic Solver

A high-fidelity CFD solver is necessary for capturing the full physics of the aerodynamics. In the MACH framework ADflow [8], a second order finite-volume CFD solver, is used. ADflow can solve both the steady Euler and Reynolds-Averaged Navier-Stokes (RANS) equations on structured multiblock and overset meshes, with some capability of unsteady and time spectral analysis. ADflow is used to compute the aerodynamic forces, such as lift, drag, and pitching moment. Through the use of a discrete adjoint implementation, developed by Mader et al. [9] and Lyu et al. [8] using Automatic Differentiation (AD), derivatives of aerodynamic functions of interest with respect to large numbers of design variables are computed efficiently. The aerodynamic analyses considered in this work will be exclusively steady RANS, utilizing both overset and multiblock meshes. To model turbulence, a single equation Spalart-Allmaras model is used.

3.2.1.2 Structural Solver

To accurately compute the aeroelastic deflection of the wing, a high-fidelity structural solver is also required. The structural solver used in the MACH framework is the Toolkit for Analysis of Composite Structures (TACS) [10]. TACS is a CSM solver that is specifically designed for solving structures consisting of thin shell components, which are typical in aerospace structures. The solver employs a parallel direct factorization method, which allows it to efficiently and accurately solve the poorly conditioned structural problems that are inherent in thin shell structures. In addition to computing the structural

displacements, TACS computes other structural functions of interest, such as material failure and buckling loads. Like its aerodynamic counterpart, TACS features an efficient adjoint method for computing structural sensitivities.

3.2.1.3 Mesh Movement

A mesh movement algorithm was required to perform aerostructural analysis and to apply changes in geometric shape during optimization. The purpose of the mesh movement was to regenerate a new CFD mesh given changes in the surface geometry. It takes the changes to the wing surface geometry and corresponding surface mesh and propagates them through the volume of the CFD mesh. The main mesh movement algorithm used in MACH is an inverse distance weighting method, like that described by Uyttersprot [11]. This method has the benefit of preserving the mesh quality near surfaces, which is necessary for capturing boundary layer effects.

3.2.1.4 Aerostructural Solver

To solve aerostructural problems, there must be a coupling scheme between the structural and aerodynamic solvers. In MACH, this coupling is accomplished through a block Gauss-Seidel scheme. First, the tractions due to the aerodynamic loads were solved using ADflow. These loads were then applied to the TACS finite-element model from which the displacements of the wing can be calculated along with structural functions of interest, such as buckling and material failure. The structural displacements were then transferred to the nodes on the surface of the wing in the CFD mesh using a system of rigid links, as proposed by Brown [12]. The displacements at the surface nodes were then extrapolated to the rest of the nodes throughout the CFD volume mesh using the mesh movement algorithm mentioned above. The aerodynamics were solved again for the new mesh, and the process was repeated until convergence. As with the previous solvers, the aerostructural solver can assemble the coupled adjoint from the adjoint of each discipline, structures and aerodynamics, to evaluate the coupled aerostructural derivatives required to solve the design optimization problem [7]. This approach computes the cross-disciplinary sensitivities inherent to flexible wing design in an accurate and efficient manner, enabling gradient-based optimization with $O(10^3)$ design variables.

3.2.1.5 Optimizer

Due to the large number of design variables considered in the design optimizations in this work and the relative computational expense of the high-fidelity solvers used, a gradient-based approach was required. Aerostructural design problems typically feature a large sparse constraint Jacobian. Therefore, it was desirable to use an optimizer that takes advantage of the sparse nature of the problem. For this reason, all optimization problems in this study were solved using SNOPT [13], a quasi-Newton gradient-based optimizer that works well for optimization problems featuring large numbers of sparse nonlinear constraints. The optimization tool was wrapped using the Python interface pyOPT [14]. SNOPT sits on top of the aerostructural solver in the MACH framework, providing the current design variables to the solvers as inputs and requesting the objective, constraints, and corresponding sensitivities as outputs at each major iteration of the optimization.

3.2.1.6 pySteer

In the scheme of the MACH framework, pySteer can be thought of as a "middle-man" between the optimizer, pyOptSparse, and the structural solver, TACS. In this setup, the optimizer provides two inputs to the aerostructural problem: the aerodynamic, $\boldsymbol{x}^A$, and structural, $\boldsymbol{x}_{cp}^S$, design variable vectors. The aerodynamic design variables, $\boldsymbol{x}^A$—which may contain variables that control the aircraft angle-of-attack, wing shape, twist, etc.—are passed directly to the CFD solver, ADFlow. On the structural side, the structural design variables, $\boldsymbol{x}_{cp}^S$, are set at the B-spline control points for each parametric component. pySteer then interpolates the design variable values to the nodes to create a nodal design variable vector, $\boldsymbol{x}_{cp}^n$. By the nature of the B-spline interpolation, this takes the form of a linear transformation:

$$\boldsymbol{x}_n^S = \boldsymbol{C}(\boldsymbol{\xi}_n, \boldsymbol{\eta}_n)\, \boldsymbol{x}_{cp}^S.$$

Where $\boldsymbol{C}$ is the B-spline transformation matrix that interpolates the values from the control points to each node. $\boldsymbol{C}$ is a function only of the parametric coordinates of each node, $\boldsymbol{\xi}_n$ and $\boldsymbol{\eta}_n$, and remains constant during the optimization. These nodal design variables are then passed to TACS and are then used to set and assemble the element stiffness matrices. Once this is done, the structural problem, or aerostructural problem in conjunction with ADFlow, can then be solved. The relevant design functions of interest, f, are then passed back to the optimizer. In the case of a structural optimization, these functions may include values such as weight, stress, and buckling and in the case of aerostructural optimization, these can also include lift, drag, and moment. In addition to translating structural design variables between the optimizer and TACS, pySteer is also responsible for computing relevant tow-steering manufacturing constraints, as were discussed in Section 2.1.

3.2.2 Structural Parametrization

In this section, the technique used by pySteer to parametrize the structural design for the conventional and tow-steered composite wing boxes will be discussed in more detail. All wing structural components are modeled as composite laminates with the ply properties listed in Table 4. For the tow-steered design, only the skins of the wing structure are steered, while the ribs and spars are modeled using conventional composite laminates. To avoid dependence on discrete design variables related to the laminate stacking sequence, for which a gradient-based optimizer is not well suited, a smeared stiffness procedure is employed to model the stiffener and laminate properties of the wing box panels.

Table 4. Mechanical properties for the composites used on skin, ribs, and spars.

Material	E_1 [GPa]	E_2 [GPa]	G_{12} [GPa]	G_{13} [GPa]	G_{23} [GPa]	ν_{12}	X_t [MPa]	X_c [MPa]	Y_t [MPa]	Y_c [MPa]	S [MPa]	ρ [kg/m^3]
Unidirectional tape E752LT/AS4 (Skin)	117.9	9.7	4.8	4.8	4.8	0.34	1648	1034	64	228	71	1550
PW Fabric AS4/8552 (Ribs and Spars)	62.1	62.1	5	4.8	4.8	0.045	279	266	279	266	70	1550

The first step in the structural parametrization procedure is to define the tow paths for each layer of the laminate. In theory, each layer of the laminate can take on a unique tow pattern. For relatively thick laminates with many plies, like those used in wing structures,

this requires a prohibitive number of design variables to parametrize. Therefore, each layer of the laminate is instead restricted to take on one of four unique tow patterns. This is done by first defining a reference tow orientation field, θ_0, using B-spline control points distributed over the laminate. This reference orientation field gives the local tow direction for the first tow pattern, referred to as the main tow pattern. The remaining three tow patterns are then defined by offsetting the main tow orientation by 45°, -45° and 90°, such that the resulting laminate remains locally orthotropic with respect to the main tow path. If all tow orientation control point variables are set to zero, a conventional orthotropic laminate design (i.e., 0°, ±45°, 90°) can also be reproduced. The reference axis for all ply angles in the skins (i.e., the 0° direction) is defined to be parallel to the leading edge of the wing. An example of the tow pattern parametrization is shown in Figure 3.4.

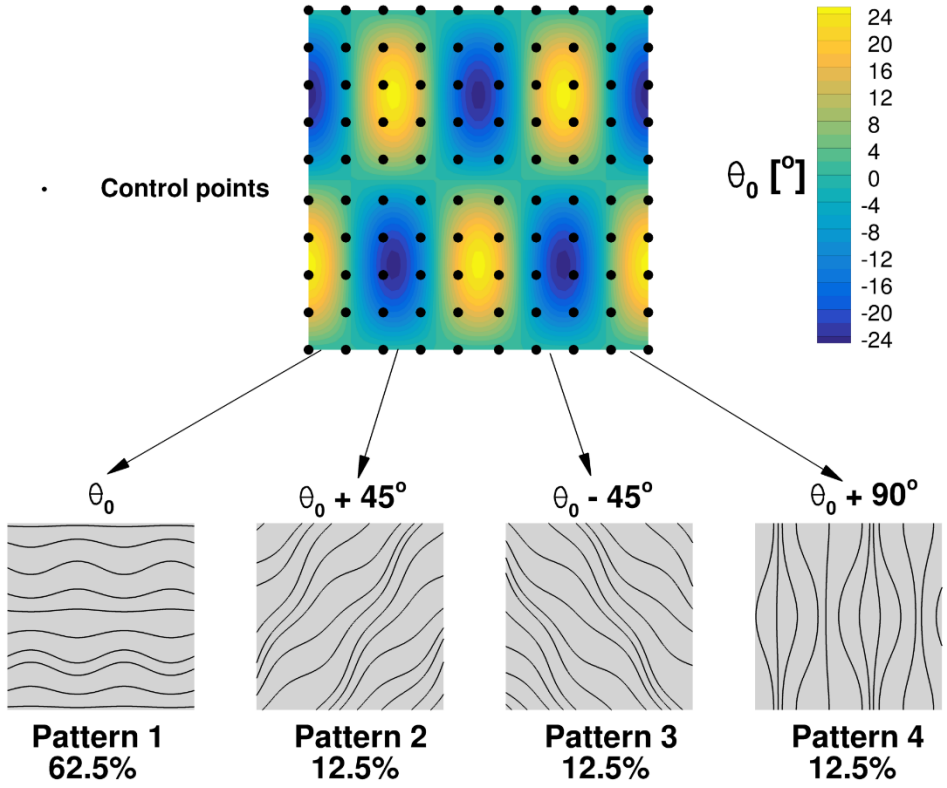

Figure 3.4. Example of the procedure used to define the main tow path and subsequent patterns.

The percentage of the plies, or ply fractions, corresponding to each pattern is defined to remain constant throughout the laminate, and the main pattern makes up the majority of the plies and therefore contributes the most to the stiffness properties as well. This allows us to reduce the number of design variables necessary to parametrize the tow patterns of each ply down to one pattern. The ply fractions for each unique ply of each wing box component are listed in Table 5. This approach results in a homogenized laminate definition. For the test article, these optimized homogenized laminates were refined into discrete ply stacking sequences in a separate detailed design phase (see Section 4).

Table 5. Ply fraction breakdown by wing box component.

Component	Patterns	Pattern ply fractions
Skins	$\{\theta_0 + 0°, \theta_0 + 45°, \theta_0 - 45°, \theta_0 + 90°\}$	$\{0.625, 0.125, 0.125, 0.125\}$
Spars	$\{0°, 45°, -45°, 90°\}$	$\{0.125, 0.375, 0.375, 0.125\}$
Ribs	$\{0°, 45°, -45°, 90°\}$	$\{0.25, 0.25, 0.25, 0.25\}$

In the second step of the procedure, the stiffness properties of each pattern are smeared through the thickness of the laminate based on their respective ply fractions. This approximation works well for laminates with large numbers of plies with a uniform stacking sequence. This allows the dependence of laminate stiffness on stacking sequence to be neglected and the local panel thickness to be approximated as an independent continuous design variable. Finally, the panel thickness is then assigned spatially using the same B-spline control points from the tow path definition step.

Typical conventional and tow-steered composite wing box designs resulting from this parametrization are shown in Figure 3.5. Note that the bunching up of the tow paths on the tow-steered layups are caused by the divergence effects introduced in Section 2.1. The procedure for taking this information and converting it into the necessary layup instructions for the AFP machine is straightforward. The tow patterns specify to the AFP machine the local direction of tows for the plies of the laminate as a function of spatial location. The number of plies of each pattern to be laid by the AFP machine can be computed by multiplying the local panel thickness and ply fractions and rounding the value up for each pattern to the nearest ply.

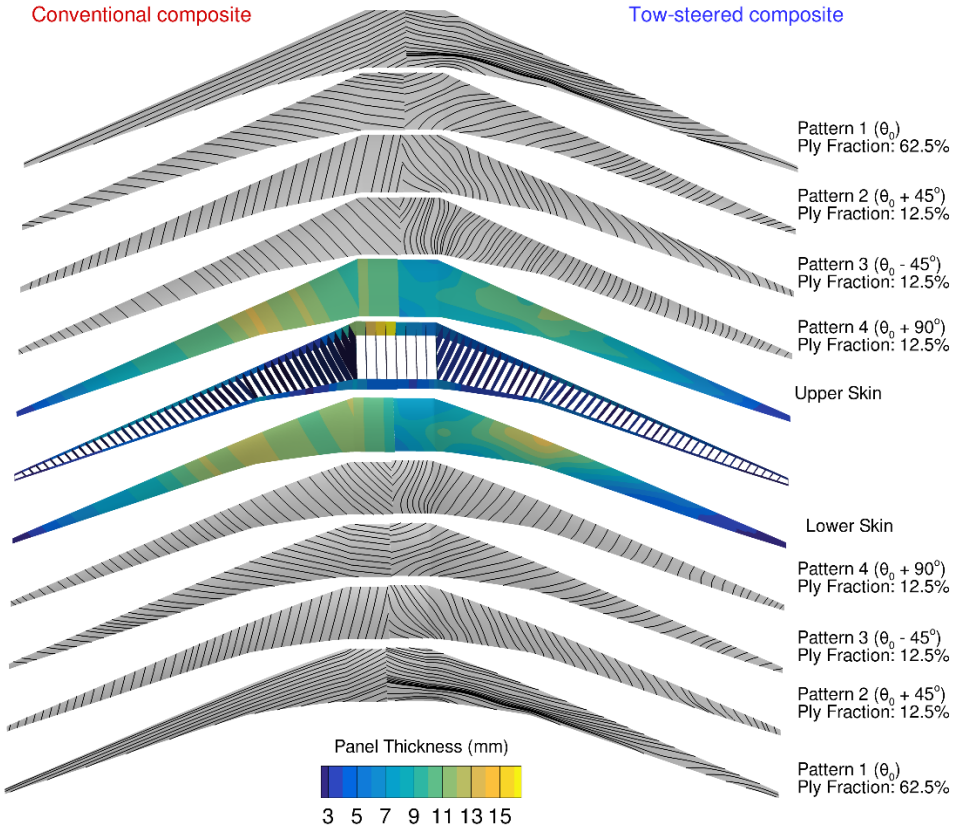

Figure 3.5. Exploded view of conventional composite (left) and tow-steered composite (right) wing designs using the developed parametrization.

3.2.2.1 Laminate Failure

To ensure that the wing box model is adequately sized for each structurally critical flight condition, laminate failure margins are computed using the maximum strain criterion:

$$\max\left\{\frac{\epsilon_1}{\epsilon_{1t}}, \frac{\epsilon_1}{\epsilon_{1c}}, \frac{\epsilon_2}{\epsilon_{2t}}, \frac{\epsilon_2}{\epsilon_{2c}}, \frac{\gamma_{12}}{\gamma_{12s}}, -\frac{\gamma_{12}}{\gamma_{12s}}\right\} \tag{4}$$

where ϵ_1, ϵ_2, and γ_{12} are the in-plane tangential, transverse, and shear strains, respectively, relative to the local fiber direction, and

$$\epsilon_{1t} = \frac{X_t}{E_1}, \quad \epsilon_{1c} = \frac{X_c}{E_1}, \quad \epsilon_{2t} = \frac{Y_t}{E_2}, \quad \epsilon_{2c} = \frac{Y_c}{E_2}, \quad \gamma_{12} = \frac{S}{G_{12}},$$

where the values are listed in Table 4.

Due to the difficulties introduced by the discontinuous nature of the maximum function in Equation 4, the function is instead approximated using a smooth Kreisselmeier—Steinhauser (KS) aggregation function [15, 16]. The failure constraint is applied using a first-ply failure criterion, where no ply in the laminate is permitted to fail. The failure criteria are applied conservatively by evaluating Equation 4 at the centroid of each CSM element for the outer most plies. Because the stacking sequence is never specified in the laminate parametrization scheme, the calculation is performed in the local fiber direction for each

of the four tow patterns. The failure value for each pattern at each location is then aggregated one final time, again using a KS function, into a single scalar value for each structural component (ribs, spars, and skins). The value for each component is then provided to the optimizer as a constraint.

3.2.2.2 Panel Buckling

Each wing box panel (rib, spar, and skin), shown in Figure 3.6, is also constrained against buckling in the optimization problem formulation. The buckling behavior is approximated through a simplified panel-level buckling analysis of the stiffened panels applied to every wing box component. This buckling analysis considers both longitudinal and shear buckling modes through several different buckling mechanisms, including: interstiffener panel buckling, stiffener buckling, and overall panel buckling (including skin and stiffeners). Each panel is treated as simply supported at each rib/spar/skin intersection. For the skins, the panel length is set by the rib pitch and the principal axis is aligned with the wing sweep. For the ribs and spars, the panel length is defined by the wing box depth and the principal axis is aligned with the vertical direction. Due to the high aspect ratio of the panels, the second panel dimension is approximated as being infinite. This allows the critical buckling loads in the transverse direction, $N_{2,cr}$, to be neglected. Lastly, panel curvature effects are neglected.

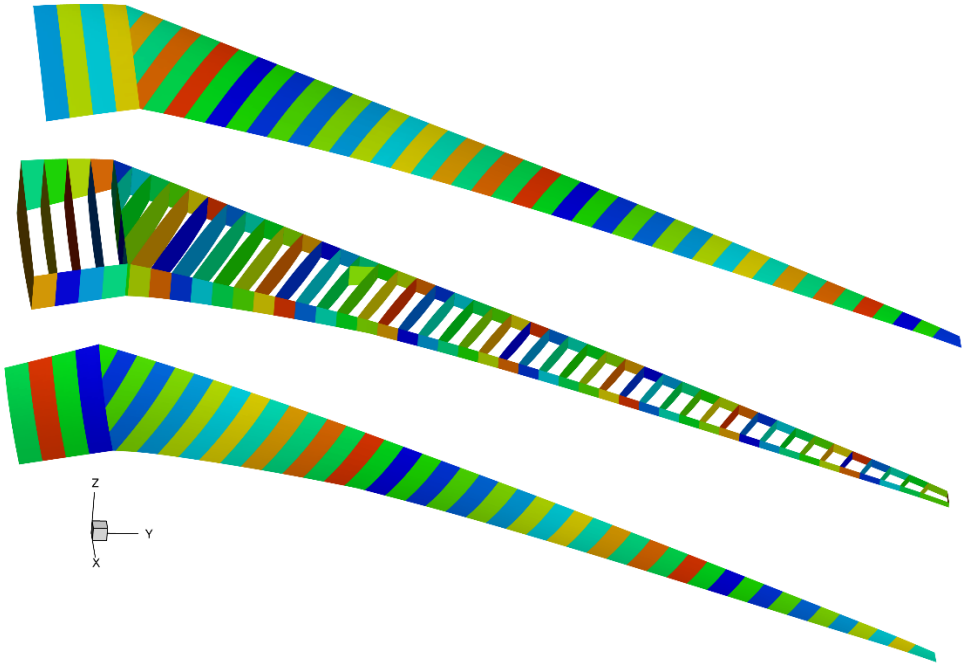

Figure 3.6 Panel definitions used for buckling and manufacturing constraints.

The first step of the procedure is to compute the critical buckling loads for each mechanism—compression ($N_{1,cr}$) and shear ($N_{12,cr}$)—for each panel. These critical loads are dependent on the local stiffness and geometric properties and are calculated using the approach of Stroud and Agranoff [17], later applied by Kennedy et al. [18, 19]. In this approach, each mode is treated separately and computed based on the formula

summarized in Table 6. Here, EI_s is the effective bending stiffness of the panel, while D_1, D_2, and D_3 are the overall longitudinal, transverse, and twist bending stiffness of the smeared panel. The panel length, L_x, dimension is defined as the spanwise dimension for the skin panels and the wing depth dimension for the ribs and spars. D_{11}, D_{22}, D_{12}, and D_{66} are components of the bending stiffness matrix, $\boldsymbol{D}$, for the skin laminate and relate the midplane bending curvatures of the laminate, κ, to the moment resultants, M, as follows:

$$\begin{bmatrix} M_{xx} \\ M_{yy} \\ M_{xy} \end{bmatrix} = \begin{bmatrix} D_{11} & D_{12} & D_{16} \\ D_{12} & D_{22} & D_{26} \\ D_{16} & D_{26} & D_{66} \end{bmatrix} \begin{bmatrix} \kappa_{xx} \\ \kappa_{yy} \\ \kappa_{xy} \end{bmatrix}.$$

Since the stacking sequence for the laminate is not specified in the optimization, the $\boldsymbol{D}$ matrix is approximated by assuming a uniformly stacked layup using the equation below:

$$\boldsymbol{D} = \frac{t_p^3}{12} \cdot \overline{\boldsymbol{Q^p}} + \boldsymbol{D}^s$$

where $\overline{\boldsymbol{Q_p}}$ is the ply fraction weighted average in-plane ply stiffness matrix of the panel. The nonzero stiffener contributions to the component of the stiffness matrix are given by:

$$D_{11}^s = \frac{E_s(h_s^2 A_s + 4I_s)}{4p_s}$$

where h_s, p_s, A_s, and I_s are the stiffener height, pitch, cross-sectional area, and second moment of area, respectively. E_s is the stiffener extensional modulus and is given by:

$$E_s = \overline{Q_{11}^s} - \frac{\overline{Q_{21}^s Q_{12}^s}}{\overline{Q_{66}^s}}.$$

Next, the local running load in each element, N_1 and N_{12}, are computed and used to evaluate the buckling constraint for each buckling mechanism based on an interaction criterion:

$$B(N_1, N_{12}) = \frac{N_{12}^2}{N_{12,cr}^2} + \frac{N_1}{N_{1,cr}} \leq 1.$$

This results in a conservative envelope that is applied to every element in the panel. This method has the advantage of being computationally inexpensive relative to performing a full buckling eigenvalue analysis for each panel. Like the failure constraints, the buckling envelope constraints are evaluated at the centroid of every element. Finally, these element constraints are aggregated over each component group using a KS function.

Table 6. Critical loads for overall and skin buckling [17][4].

	Overall buckling	Skin buckling
$N_{1,cr}$	$\frac{\pi^2 EI_s}{p_s L_x^2}$	$\frac{2\pi^2}{p_s^2}\left(\sqrt{D_{11}D_{22}} + D_{12} + 2D_{66}\right)$
$N_{12,cr}$	$\xi = \frac{\sqrt{D_1 D_2}}{D_3}$	$\xi = \frac{\sqrt{D_{11}D_{22}}}{D_{12} + 2D_{66}}$
If $\xi > 1$	$\frac{4}{L_x^2}(D_1^3 D_2)^{0.25}\left(8.125 + \frac{5.045}{\xi}\right)$	$\frac{4}{p_s^2}(D_{11}D_{22}^3)^{0.25}\left(8.125 + \frac{5.045}{\xi}\right)$
If $\xi \leq 1$	$\frac{4}{L_x^2}\sqrt{D_1 D_3}\left(11.7 + 0.532\xi + 0.938\xi^2\right)$	$\frac{4}{p_s^2}\sqrt{D_{22}(D_{12} + 2D_{66})}\left(11.7 + 0.532\xi + 0.938\xi^2\right)$

3.2.3 Manufacturing Constraints

To ensure that the resulting optimized tow-steered layups are physically realizable with modern-day AFP machines, several manufacturing restrictions are considered in this study. The first is a bound on the minimum turning radius, $R_{\min}$, of the tow paths for each tow pattern in the skins. This value is typically specified by the manufacturer to prevent the tow from puckering or twisting out of plane as it is being laid down by the machine, particularly in highly curved regions of the tow path. Smaller values of $R_{\min}$ can often be achieved by using narrower tows; however, this may lead to longer manufacturing time for the same layup area.

The second restriction is on the minimum cut and add lengths for the AFP machine tows. When the tows are laid down for a ply by the AFP machine, gaps or overlaps may occur between adjacent tow paths. To keep the layup smooth, the machine is often preprogrammed to add or cut tows in regions where the gaps or overlaps sizes, respectively, exceed a specified value expressed as a percentage of tow width. The machine has a minimum cut length for the tow (L_{cut}), which is limited by the distance between the AFP tow placing head and cutting mechanism. The minimum add length (L_{add}) defines the minimum length of tow for two adjacent tow paths that must be laid before the machine may add a tow between the gap of the previous two. Unlike the minimum cut length value, the add length is not limited by the dimensions of the AFP machine and, as such, is at the designer's discretion. The definition of each of these lengths is illustrated in Figure 3.7. Tow patterns featuring smaller cut and add lengths require more frequent cutting and repositioning of the tows in the layup process, leading to higher manufacturing cost and time. To ensure the manufacturability of the optimized design, each of these values is constrained in the optimization.

[4] In the original work by Stroud and Agranoff an additional factor appears in the critical overall compression buckling equation. In this work, the factor is assumed to be unity due to the panels' dimensions.

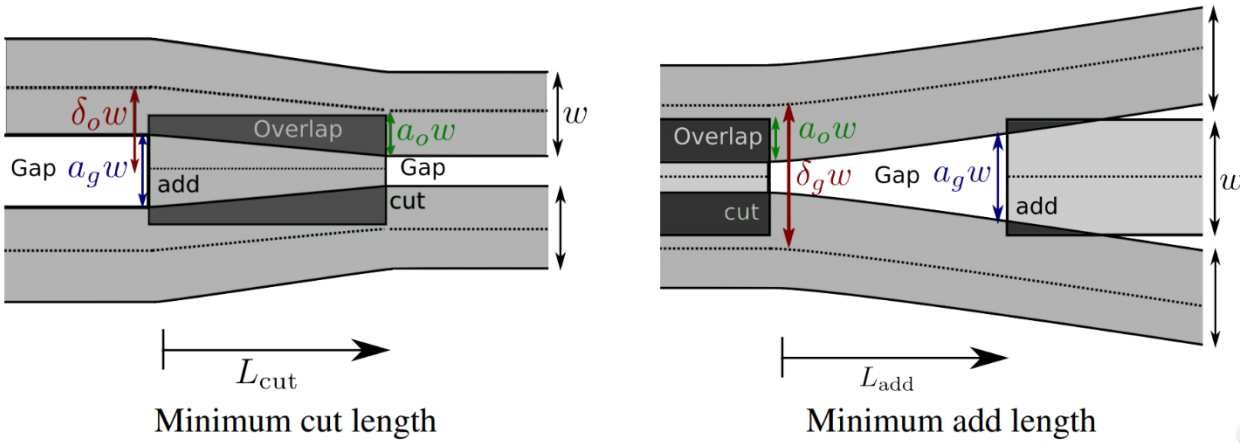

Figure 3.7. Definition of tow cut and add length (reproduced from Brooks and Martins [35]).

The final restriction is on how quickly the number of plies can vary spatially through the laminate. This is typically constrained in the design process to prevent stress concentrations from occurring in regions featuring a large decrease in the number of plies.

For the minimum tow-path turning radius and cut/add length constraints, the relationships derived by Brooks and Martins [20] are used. In that work, it was shown that the tow paths of each ply of a tow-steered layup can be defined as the streamlines of a 2D unit vector field as,

$$\vec{v}(\theta) = \cos\big(\theta(x,y)\big)\,\hat{\boldsymbol{\imath}} + \sin\big(\theta(x,y)\big)\,\hat{\boldsymbol{\jmath}}$$

Through this relationship and further derivation, the minimum tow-path turning radius and tow-path cut/add lengths can be bounded by constraining the magnitude of the vector field curl, $\kappa = (\nabla \times \vec{v}) \cdot \hat{\boldsymbol{k}}$, and divergence, $\psi = \nabla \cdot \vec{v}$, respectively as shown below:

$$-\frac{1}{R_{\min}} \le \kappa \le \frac{1}{R_{\min}}, \quad -\frac{\ln\left(\frac{1+a_g}{2(1-a_o)}\right)}{L_{\text{cut}}} \le \psi \le \frac{\ln\left(\frac{1+a_g}{2(1-a_o)}\right)}{L_{\text{add}}} \tag{5}$$

where a_g and a_o are the gap and overlap cut sizes for the AFP machine in percent tape width, respectively.

The ply drop rate can be bound by constraining the thickness gradient of the smeared laminate:

$$\left\|\nabla t_p(x,y)\right\| \le \|\nabla t_0\|.$$

To constrain the tow-path turning radius, cut/add length, and ply drop rate, a KS aggregation function is used once again. This is accomplished by computing the tow-path curl and divergence for each pattern as well as the panel thickness gradient at each node on the skins of the CSM model, and then aggregating these into three scalar values (one for each constraint) over each wing box skin panel shown in Figure 3.6.

3.2.4 Problem Definition

As was mentioned previously, the goal of this study is to provide insights into the aeroelastic benefits of tow steering when applied to wing design. To this end, a series of fuel burn minimization problems were first performed on the uCRM-9. This model is optimized with a tow-steered, fixed-ply, and rotated-ply conventional composite wing box design. The manufacturing constraints are then removed from the optimization problem and the tow-steered design is then optimized once more. Next, the tow-steered and fixed-ply-orientation conventional composite design optimizations are performed on the uCRM-13.5. Including this design provides insight into the benefits of tow steering for high-aspect-ratio wing designs that are more flexible. Finally, an aspect ratio study is performed for the uCRM-9 design, where the wing aspect ratio is fixed at several values (7.5, 9, 10.5, 12, and 13.5) and reoptimized using the tow-steered and fixed-ply-orientation conventional composite designs. This provides insight into how the design trends change as aspect ratio is increased.

Each optimization requires three aerostructural analyses: one cruise condition for evaluating the fuel burn performance, and two conditions for which the structural constraints are enforced—a -1G push-over and 2.5G pull-up maneuver condition. The lift of the cruise condition is set to be that of the nominal CRM ($C_L = 0.5$), while the lift of the maneuver conditions are based on the maximum takeoff weight (MTOW) of the aircraft. The choice to fix the cruise condition lift in C_L rather than utilizing a weight constraint like the maneuver condition was made for simplicity, though in practice this value does correspond to roughly the required lift of the aircraft given that the total weight of the aircraft does not vary substantially during the optimization. The parameters for these three flight conditions are listed in Table 7. In the remainder of this section, the optimization problems are described by detailing the objective function, design variables, and design constraints.

Table 7. Optimization flight condition parameters

Parameter	Cruise	2.5G	−1.0G
Mach number	0.85	0.64	0.64
Altitude (ft)	37 000	0	0
C_L or lift	0.5	$2.5 \cdot$ MTOW	$-1.0 \cdot$ MTOW

3.2.4.1 Objective

The objective of the optimization problem is to minimize the fuel burn (FB) of the aircraft at cruise, which is calculated using the Breguet range equation,

$$\mathrm{FB} = \mathrm{ZFW}\left[\exp\left(\frac{R\,c_T}{V_\infty\left(\frac{L}{D}\right)}\right) - 1\right], \tag{6}$$

where ZFW, R, and c_T are the aircraft zero-fuel weight, design range, and thrust-specific fuel consumption, respectively, and V_∞ and $\frac{L}{D}$ are the cruise speed and lift-to-drag ratio, respectively. The zero-fuel weight is defined as the total weight of the aircraft including payload and crew without the fuel required for the mission and is given by:

$$ZFW = 1.25 \times W_{\text{wing}} + W_{\text{secondary}} + W_{\text{fixed}} + W_{\text{payload}} + W_{\text{reserve}},$$

where W_{wing} is the weight of the wing box structure, $W_{\text{secondary}}$ is the weight of non-structural masses associated with the wing (e.g., control surfaces, actuators), W_{fixed} is the weight of the aircraft structure without the wing (e.g., fuselage, tail), W_{payload} is the weight of the payload (e.g., passengers, luggage), and W_{reserve} is the weight of the reserve fuel. The only portion of this weight that the optimizer can affect is the wing structural weight, W_{wing}. A factor of 1.25 is added onto the wing structural weight predicted by the CSM model to account for the weight of missing overlaps and fasteners. The values of the constants used to compute the objective are given in Table 8.

Table 8. Problem specifications.

Parameter	Symbol	Value	Units
Design range	R	7 725	nm
Design payload	W_{payload}	34 000	kg
Reserve fuel	W_{reserve}	15 000	kg
Fixed weight	W_{fixed}	107 814	kg
Thrust specific fuel consumption	c_T	0.53	lb/(lbf · h)

The fuel burn makes for a good multidisciplinary objective function due to its dependence on both structural performance, through the zero-fuel weight, as well as aerodynamic performance, through $\frac{L}{D}$. In addition, its relationship to the direct operating cost of the aircraft makes fuel burn an appropriate metric for the aircraft performance.

3.2.4.2 Design Variables

The design variables can be broken down into structural, aerodynamic, and geometric variables. As was already mentioned, in this study, several different design parametrizations are considered. These design parametrizations include: tow-steered composite (TS), conventional (C) and conventional rotated (CR) composite, tow-steered composite without manufacturing constraints (TS-NM), and tow-steered and conventional composite with varying wing aspect ratio (TS-AR and C-AR, respectively). Each one of these parameterizations contain their own set of design variables and are summarized in Table 9. The definition of all possible design variables is shown in Figure 3.8.

Table 9. Fuel burn optimization design variables.

Variable/function	Description	TS	C	CR	TS-NM	TS-AR	C-AR
$x_{\text{stiff thick}}$	Stiffener thickness (skin/spar/ribs)	238					
$x_{\text{stiff height}}$	Stiffener height (skin/spar/ribs)	238					
$x_{\text{stiff pitch}}$	Stiffener pitch (skin/spar/ribs)	4					
$x_{\text{panel length}}$	Panel length (skin/spar/ribs)	238					
$x_{t^{\text{cp}}}$	Panel thickness control points (skin/spar)	280					
x_{ribs}	Panel thickness (ribs)	49					
$x_{\theta_0^{\text{cp}}}$	Tow offset control points (skin)	240	0	2	240	240	0
x_{α_i}	Angle of attack for each case	3					
x_{tail}	Tail trim angle for each case	3					
x_{shape}	FFD control points	240					
x_{twist}	Wing twist	8					
x_{chord}	Chord scaling	0	0	0	0	1	1
x_{span}	Span	0	0	0	0	1	1
x_{sweep}	Sweep	0	0	0	0	1	1
	Total design variables	**1541**	**1301**	**1303**	**1541**	**1544**	**1304**

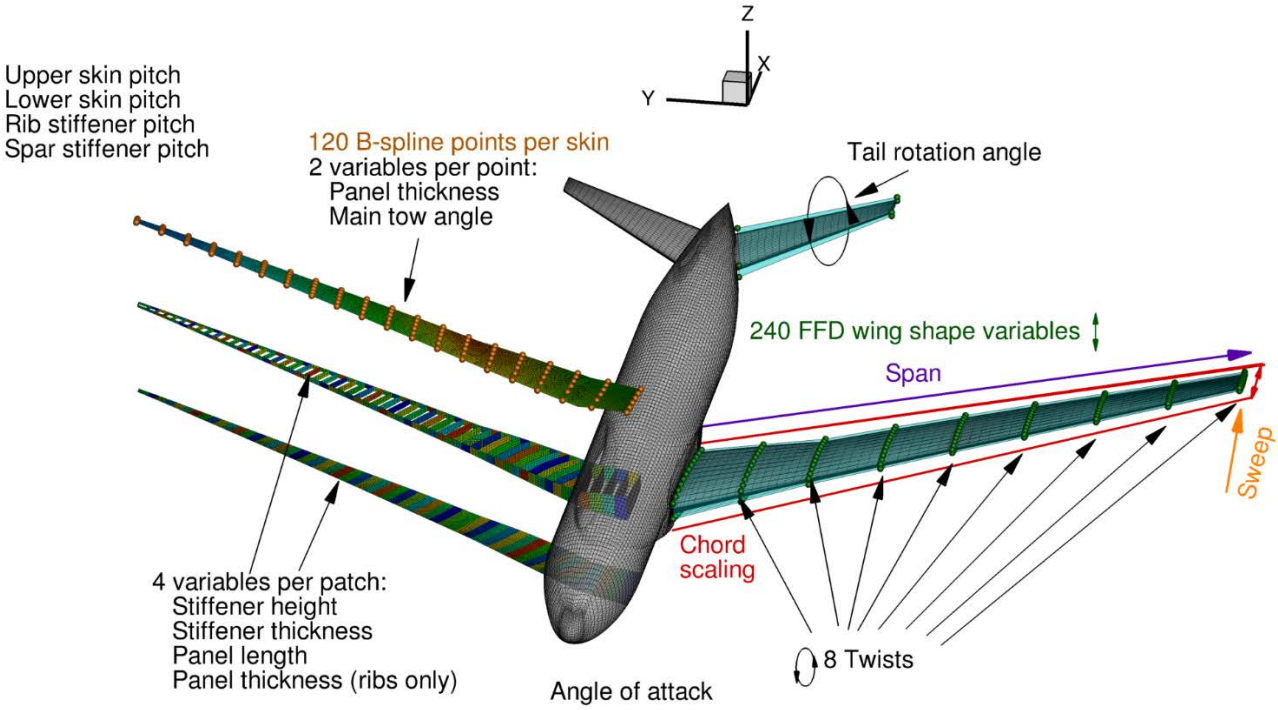

Figure 3.8. Optimization problem design variables.

The first of the structural variables is the panel thickness. This is set using 120 B-spline control points distributed over each skin, 20 control points distributed over each spar, and one variable for each rib. The structural variables also include the stiffener height, stiffener thickness, and panel length for each panel shown in Figure 3.6, for a total of 287 of each of these types of variables. The panel length variable is only used in the prediction of the analytical panel buckling formulas. In the case of the fixed planform designs (TS, C, CR, and TS-NM) the panel length variables are fixed throughout the optimization, while they are free to vary for the variable planform designs (TS-AR and C-AR). All panels in each component (upper skin, lower skin, ribs, and spars) share a stiffener pitch variable, for a total of 4. In addition, the tow-steered design parametrizations (TS, TS-NM, and TS-AR)

also include the tow-offset control point variable, θ_0^{cp}, on each skin, for a total of 240 additional variables. The main ply orientations in the skins for the conventional composite designs (C and C-AR) are forced to remain parallel to the leading edge of the wing. This restriction is relaxed for the conventional rotated design (CR) by setting one tow-offset design variable for each skin. This gives the optimizer the freedom to rigidly rotate the plies of each skin with respect to the wing.

The two aerodynamic design variables are the angle of attack and the horizontal tail incidence for each flight condition. These variables ensure the optimizer can satisfy the lift and moment constraints to trim the aircraft at each flight condition. The tail rotation is controlled by a small free form deformation (FFD) volume surrounding the tail geometry.

The geometric variables are parametrized using an FFD volume approach [21, 22]. In this approach, the wing and its internal structure are enclosed by a volume whose surface includes a number of control points. As each control point is moved in space, the geometries inside the volume are deformed in a similar fashion. The FFD volume used for this study is shown on the right in Figure 3.8. The optimizer is given freedom to control the wing cross-sectional shape by moving each of the 240 control points in the vertical (z) direction. The optimizer can control the wing twist at eight spanwise locations by rotating each chordwise segment of control points. The last set of geometric design variables control the planform of the wing. These design variables are only active for the variable aspect ratio designs, TS-AR and C-AR. These design variables include one chord variable, used to uniformly scale the chord of all of the wing spanwise cross-sections. A single design variable is used to control the span of the wing. Finally, the sweep can be controlled by translating the tip of the wing in the streamwise direction.

3.2.4.3 Constraints

The design constraints can also be broken down into structural, geometric, and aerodynamic constraints. As was the case for the design variables, only a select set of constraints are applied to each design parametrization. The constraints for each case are summarized in Table 10.

Table 10. Optimization problem constraints.

Variable/function	Description	TS	C	CR	TS-NM	TS-AR	C-AR
$\text{KS}_{\text{stress}} < 1.0$	2.5G Material Failure	———			4	———	
$\text{KS}_{\text{buckling}} < 1.0$	2.5G and −1.0G Buckling	———			6	———	
$\left\|x_{\text{stiff height}_i} - x_{\text{stiff height}_{i+1}}\right\| \leq 0.0005$	Stiffener height adjacency	———			183	———	
$\left\|x_{\text{stiff thick}_i} - x_{\text{stiff thick}_{i+1}}\right\| \leq 0.0005$	Stiffener thickness adjacency	———			183	———	
$\left\|x_{\text{stiff thick}} - x_{\text{panel thick}}\right\| < 0.0025$	Maximum stiffener-panel difference	———			238	———	
$\text{KS}_{\|\|\nabla t_p\|\|} < \|\|\nabla t_0\|\|$	Panel thickness gradient	———			183	———	
$-\frac{1}{R_{\min}} < \text{KS}_\kappa < \frac{1}{R_{\min}}$	Minimum tow-path turning radius	96	0	0	0	96	0
$-\frac{\ln\left(\frac{1+a_g}{2(1-a_o)}\right)}{L_{\text{cut}}} < \text{KS}_\psi < \frac{\ln\left(\frac{1+a_g}{2(1-a_o)}\right)}{L_{\text{add}}}$	Minimum tow cut/add length	96	0	0	0	96	0
$C_L = 0.5$	Cruise lift conditions	———			1	———	
$L_i = n_i\,\text{TOGW}$	Maneuver lift conditions	———			2	———	
$c^i_{m_y} = 0$	Trimmed flight	———			3	———	
$t_{LE}/t_{LE_{init}} \geq 1.0$	Leading-edge radius	———			20	———	
$t_{TE}/t_{TE_{init}} \geq 1.0$	Trailing-edge thickness	———			20	———	
$(t/c)_{\text{TE Spar}} \geq 0.80(t/c)_{\text{TE spar}_{init}}$	Minimum trailing-edge spar height	———			20	———	
$\Delta z_{\text{TE,upper}} = -\Delta z_{\text{TE,lower}}$	Fixed trailing edge	———			8	———	
$\Delta z_{\text{LE,upper}} = -\Delta z_{\text{LE,lower}}$	Fixed leading edge	———			8	———	
$V - V_{\text{fuel}} \geq 0.0$	Minimum fuel volume	———			1	———	
$L_{\text{panel}} - x_{\text{panel length}} = 0$	Target panel length	———			238	———	
$\text{AR} = [7.5, 9, 10.5, 12, 13.5]$	Aspect ratio	0	0	0	0	1	1
$\Lambda_{c/4} = 34.8°$	Quarter-chord sweep	0	0	0	0	1	1
$S_{\text{ref}} = 191.8\,\text{m}^2$	Reference area	0	0	0	0	1	1
	Total constraints	**1316**	**1124**	**1124**	**1124**	**1319**	**1127**

Structural constraints are added to ensure that the resulting optimized wing box design is adequately sized and manufacturable. The first set of constraints consist of the aggregated material failure and buckling constraints, discussed in 3.2.2. The failure constraint is applied only on the 2.5G maneuver, since this condition is the most restrictive in terms of stress. The buckling constraint is applied to both the -1G and 2.5G conditions to ensure that the skins, ribs and spars are sized for buckling. A safety factor of 1.5 is placed on both the failure and buckling constraints to provide the necessary margin of safety as required by the Federal Aviation Regulations Part 25 [23]. Linear adjacency constraints are enforced on the stiffener height and thickness variables to ensure that they do not vary too abruptly between adjacent panels. The last set of structural constraints pertain to the AFP manufacturing constraints described in 3.2.3. These include a constraint on the panel thickness gradient of the skins and spars used to limit the ply drop rate. The maximum thickness gradient value, $\|\nabla t_0\|$, is set to $1.3\frac{\text{mm}}{\text{m}}$, which corresponds to a ply drop rate of roughly 10 plies per meter. The tow-steering-specific manufacturing constraints are applied only to tow-steered cases TS and TS-AR. These cases include a constraint on the tow-path turning radius of each steering pattern, which is constrained to a minimum turning radius, $R_{\min}$, of 70 in. This value is recommended by AFP technicians at the Aurora Flight Sciences company for a 0.25 in wide prepreg tape. As mentioned previously, while more aggressive values of tow-path curvature could be pursued by using narrower prepreg tape, this results in an increase in layup time and manufacturing cost. The final manufacturing constraint, the minimum tow cut and add lengths, are constrained to a value of $L_{\text{cut}} = L_{\text{add}} = 1\,\text{m}$, assuming a 50% gap/ 50% overlap rule ($a_g = a_o = 0.5$). This value was determined to be reasonable based on the dimensions of the uCRM wing structures. The curvature and divergence constraints are removed for the manufacturing-constraint-free case (TS-NM).

Aerodynamic constraints are added to enforce steady level flight at each analyzed flight condition. A lift constraint is added for each flight condition that match the conditions specified in Table 7. Constraints are added to enforce that the pitching moment of the

aircraft about its center of gravity be zero for each flight condition. Together, the lift and moment constraints ensure steady flight at the given flight conditions.

Geometric constraints that relate to the physical restrictions of a realistic wing design are also enforced. The first of these constraints prevents the cross-sectional depth at the leading-edge radius from decreasing along the span as the optimizer proceeds. This is mainly to maintain the aircraft's high-lift performance, a flight case that is not considered directly in the optimization. Manufacturing and handling issues are prevented by constraining the trailing-edge and spar cross-sectional thicknesses. The FFD shape variables are also constrained from moving the camberline at the leading- and trailing-edge of the wing. These constraints prevent the shape variables from twisting the wing and guarantee that the twist and shape variables are independent. A volume constraint is enforced on the fuel bays inside the wing to ensure that there is enough space for the fuel required for the mission, computed by Equation 6, in addition to the reserve fuel. Consistency constraints ensure that the panel length variables used in the panel buckling calculations match the physical dimensions of each panel. Additional geometric equality constraints are placed on the variable planform cases, TS-AR and C-AR. This includes a constraint on the aspect ratio of the wing. For these cases, an optimization will be run with this constraint set to a value of 7.5, 9, 10.5, 12, and 13.5. A constraint is placed on both the wing quarter-chord sweep, $\Lambda_{\frac{c}{4}}$, and reference area, S_{ref}, to force the wing to retain the original value of the uCRM-9. Because the span FFD variable scales the wing dimension in the y-direction, the wing sweep angle changes as the span variable is scaled. This constraint is required to ensure that the sweep FFD variable shears the wing geometry in the x-direction to counteract the effect and maintain the sweep. These three constraints are enough to uniquely prescribe the planform for each aspect ratio optimization.

3.2.5 Results

In this section, the results of the design optimization studies are presented. First, the benefits of tow-steering for a typical wide-body transport aircraft are demonstrated by comparing the results of the tow-steered and conventional composite optimizations on the uCRM-9. Then, the effect of tow-steering on high-aspect-ratio wing design is explored by performing conventional and tow-steered composite design optimizations on the uCRM-13.5. The scaled structural model, which will be discussed in the following section, was based on a uCRM-13.5 tow-steered optimized design.

3.2.5.1 uCRM-9 Optimization

Next, the results of the first two optimization cases based on the uCRM-9 model are analyzed. The convergence history of the optimization objective and feasibility (i.e., the magnitude of total constraint violation) for each uCRM-9 optimized case is shown in Figure 3.9. Each optimization was run for 48 hours with a total of 300 processors (100 processors per flight condition). From these optimization histories, it can be seen that the designs converge gradually before reaching the time limit. While further benefits in each design might be found by continuing the optimization for more iterations, the subsequent improvements were deemed to be small by the exit of each optimization.

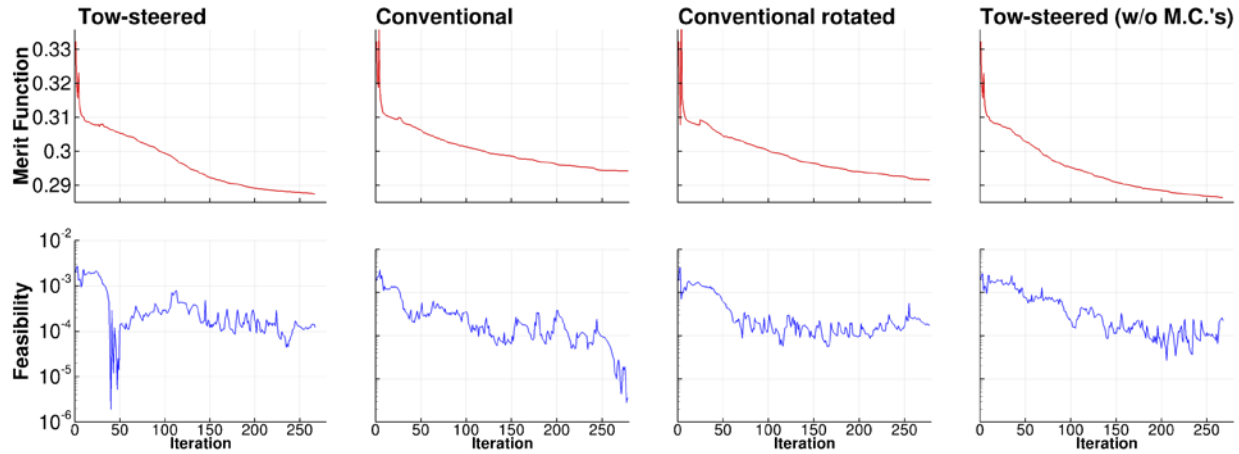

Figure 3.9. Optimization convergence histories for both uCRM-9 cases.

3.2.5.1.1 Conventional Versus Tow-steered Composite

The resulting designs from the conventional and tow-steered composite optimizations are summarized in Figure 3.10, which compares the aerodynamic and structural performance of the tow-steered (left) and conventional (right) composite wing designs. The conventional design maintains the same skin ply fraction breakdown as the tow-steered design (i.e., 62.5%, 12.5%, 12.5%, 12.5%), however, its ply orientations remain fixed to the quarter-chord sweep angle during the optimization. Shown in the upper left corner of this figure is the aerodynamic pressure distribution on the wing at cruise as well as several key performance metrics for both designs. Just below this is a front view of the aircraft, showing the relative deflection of the wing at each flight condition. Note that the wing jig shapes provided here are for reference only and that aerodynamic and structural state variables are calculated only for the aerostructurally converged cases (e.g., -1G, Cruise and +2.5G). Shown in the bottom left corner is the wing box structural information. This includes a plot showing the panel thickness distribution for each design and the tow paths for the main tow patterns for each skin. This structural information also includes contours for the failure and buckling constraints on the wing skins for the 2.5G and -1G maneuver conditions. On the right side of the figure are various spanwise metrics measuring the passive load alleviation and bend-twist coupling of each design. Starting from the top, is the normalized lift distribution for the cruise and 2.5G flight conditions, which represents the distributed lift per unit span over either aircraft. Below this is the aeroelastic spanwise twist distribution for both wing designs. Finally, in the bottom right is a plot of the spanwise nondimensional bend-twist coupling parameter, ψ_1. This parameter measures the amount of bend-twist coupling locally added to the wing through unbalanced steering in the skins. More information for how this parameter is derived and computed can be found in Appendix A.

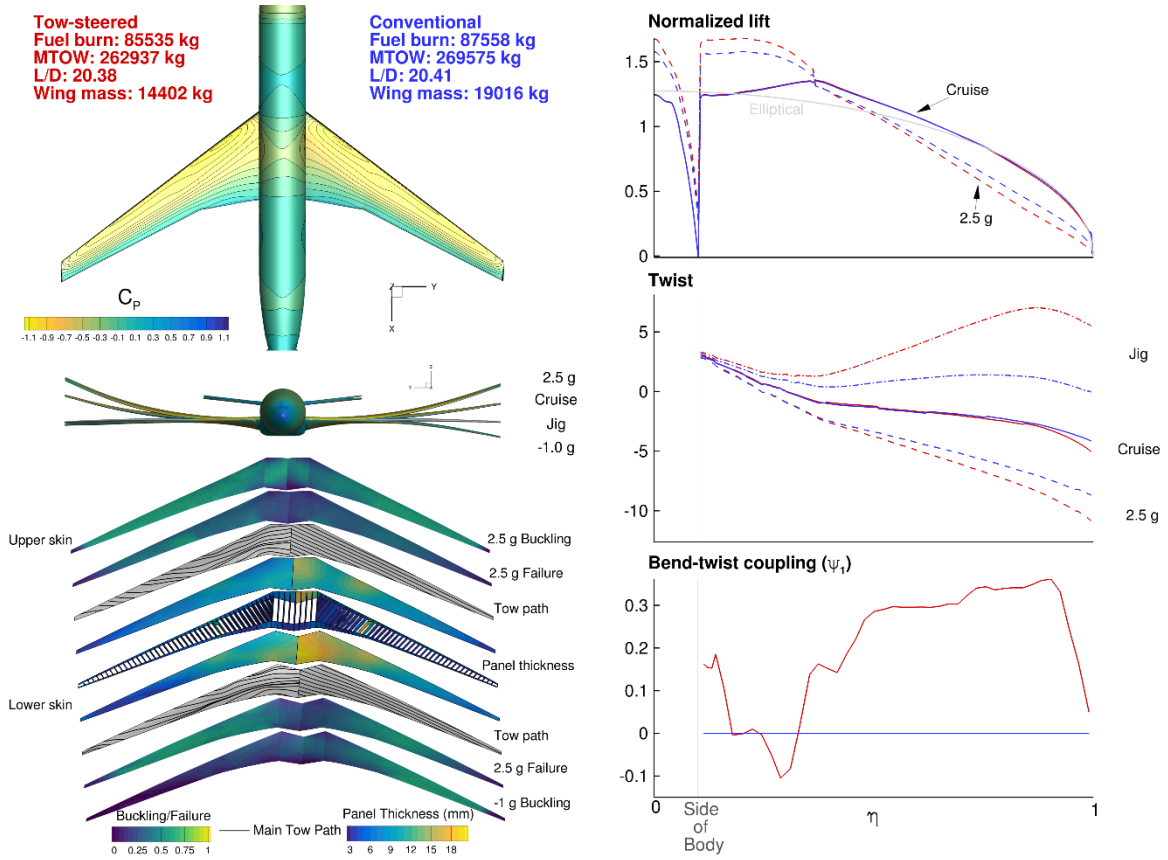

Figure 3.10. Comparison of the uCRM-9 aerostructural optimizations using tow-steered (left; red) versus conventional (right; blue) composites.

From Figure 3.10, it can be seen that there is a 2.3% and 2.5% improvement in the design fuel burn and MTOW, respectively, of the tow-steered design relative to the conventional composite one. The optimizer accomplishes this through a significant reduction in structural weight (24%) for almost no aerodynamic penalty, as seen in the $\frac{L}{D}$ performance of both designs (less than 0.15% difference). Examining the normalized lift distributions for each design reveals how this is achieved. What is found is that both designs achieve a more elliptical lift distribution at cruise, which minimizes the induced drag of the aircraft and improves the $\frac{L}{D}$. Where the two designs differ is in the passive load alleviation for the maneuver flight conditions. For these conditions, the tow-steered wing can shift more of the lift distribution inboard at the 2.5G maneuver condition. This means that the tow-steered design can more effectively reduce the bending moment in the wing for this condition, allowing the optimizer to reduce the wing box weight, most noticeably at the root and Yehudi break. This trend is similar to that observed by Stodieck et al. [24], when comparing a structural-weight-minimized tow-steered and conventional composite CRM wing design. The additional load alleviation contributes only in part to the lower structural weight seen on the tow-steered design. As will be seen in the following section, the second component is owed to the local tailoring of the load paths in the structure.

The cause for this additional load alleviation can be explained by examining the spanwise twist distribution of both wings. The twist distribution for both designs is nearly identical for the cruise condition. Again, this is due to the fact that both designs try to get close to

an elliptical lift distribution. Where the two designs differ is in the more pronounced difference between the wing twist of the jig, cruise, and maneuver flight shapes for the tow-steered design. This allows the tow-steered structure to aeroelastically twist the wing tips down even further at the maneuver condition, leading to the additional passive load alleviation benefit seen in the lift distribution. The tow-steered design has 2.1° more washout at the wing tip for the 2.5G maneuver than the conventional composite design. By examining the deflected wing shapes, it can be seen that the tow-steered design features much less deflection on the -1G maneuver condition (nearly coincident with the jig shape). This is likely due to the large amount of positive pretwist on the wingtips of the tow-steered jig design. This pretwist counteracts the negative angle of attack required to meet the lift requirements for the -1G condition and ensures that most of the negative lift occurs on inboard regions of the wing.

Examining the spanwise bend-twist coupling due to the wing skins, we see that, in general, the coupling increases along the span before reaching the maximum value and drops off rapidly toward the tip. The reason for this sudden decrease in use of coupling near the tips is that as the wingtip of the design is approached, while the aeroelastic deflections increase, there is also less remaining wing span left to tailor. These two factors counteract each other and lead to a peak in the effectiveness of the coupling occurring slightly before the tip of the wing.

Near the fuselage junction of the wing, the coupling initially drops and becomes negative. This is because the small degree of deformation leaves little ability to tailor the structure aeroelastically in this region. This suggests that the optimizer is focusing more on tailoring the strength of the structure in this region. From the twist distribution, we can also see that the optimizer twists the wing jig shape even further up on the tow-steered design. This is because as the bend-twist coupling of the tow-steered design is increased, the wing tips of the cruise and maneuver condition aeroelastically twist further down. In general, the change in aeroelastic twist on the 2.5G maneuver due to this increase in coupling is larger than that seen on the cruise shape. The optimizer, therefore, needs to increase the jig twist on the wing to keep the normalized lift distribution for the cruise case elliptical.

The source of this additional bend-twist coupling can be found by analyzing the main tow paths for the tow-steered wing. By comparing the two wing box designs, we find that the most noticeable difference is that the tow-steered optimized design sweeps the tow paths forward toward the tip of the wing. The use of swept-forward plies in this region leads to the increase in bend-twist coupling at the tip of the tow-steered design in Figure 3.10. This leads to the conclusion that the tow paths in this region of the tow-steered structure are driven by load manipulation through aeroelastic tailoring. In contrast, the tow paths of the tow-steered skins near the root seem to be driven by structural tailoring of the load paths and directional strength. Note that the wing box is structurally supported by the boundary conditions at the symmetry plane (clamped) and wing-fuselage intersection (no vertical displacement). For the portion of the skins inside the fuselage, the optimizer rotates the tow paths to be perpendicular to its supports, maximizing the compression strength of the skins. It is important to note that the portion of the skins in the carry-through structure are sensitive to the boundary conditions applied in this region. This means that a different choice of boundary conditions may result in slightly different tow paths in the region.

Looking at the structural performance of both wing boxes in Figure 3.10 provides additional information about the structural sizing for the maneuver cases. For the 2.5G maneuver, it can be seen that due to the compression in the upper skins, they are almost entirely sized by the buckling constraint for both designs. For this flight condition, the failure constraint also drives the sizing of most of the lower skins for both designs. Even though the region for both designs where these constraints are active is largely the same, the tow-steered structure is noticeably thinner near the root and Yehudi break on both the upper and lower skins. In the tow-steered design, the leading-edge spar is also noticeably thinner near the wing root, despite the fact this component is not tow-steered. These results show the ability of tow steering to redistribute loads in critical structural components through aeroelastic and structural tailoring, even if those components are not steered themselves. These differences account for the reduction in structural weight mentioned earlier.

Finally, the severity of the manufacturing constraints introduced in Section 3.2.3, minimum turning radius and cut/add length, on the tow-steered optimized design will be assessed. The minimum turning radius and cut/add length can be related to the tow-path curvature and divergence, respectively, through the inequalities provided in Equation 5. Substituting in the values specified in Section 3.2.3, gives the corresponding constraint bounds on the divergence and curvature used for the optimization, $|\psi| < 0.41\ \mathrm{m}^{-1}$, $|\kappa| < 0.56\ \mathrm{m}^{-1}$. By plotting the tow-path divergence and curvature for each pattern of tow-steered design in Figure 3.11, we can find where each constraint is active. For conciseness, we only include the tow patterns corresponding to the upper skin in Figure 3.11; however, the lower skins have a similar constraint activity. Regions featuring higher tow-path divergence magnitude will feature more rapid propagation of gaps and overlaps in the pattern, requiring more frequent tow cuts, while regions with higher curvature magnitude will require tighter turning radii. From this figure, we can see that due to the more restrictive constraint on tow path divergence, the tow path curvature constraint never approaches its bound. We also find that the most severe tow-path curvature and divergence occurs near the root of the wing box, with a small amount near the tip. We also see that the locations and magnitudes of these constraint values differ slightly from pattern to pattern. This highlights the importance of considering the manufacturing constraints for all patterns in the layup, not just the main tow pattern.

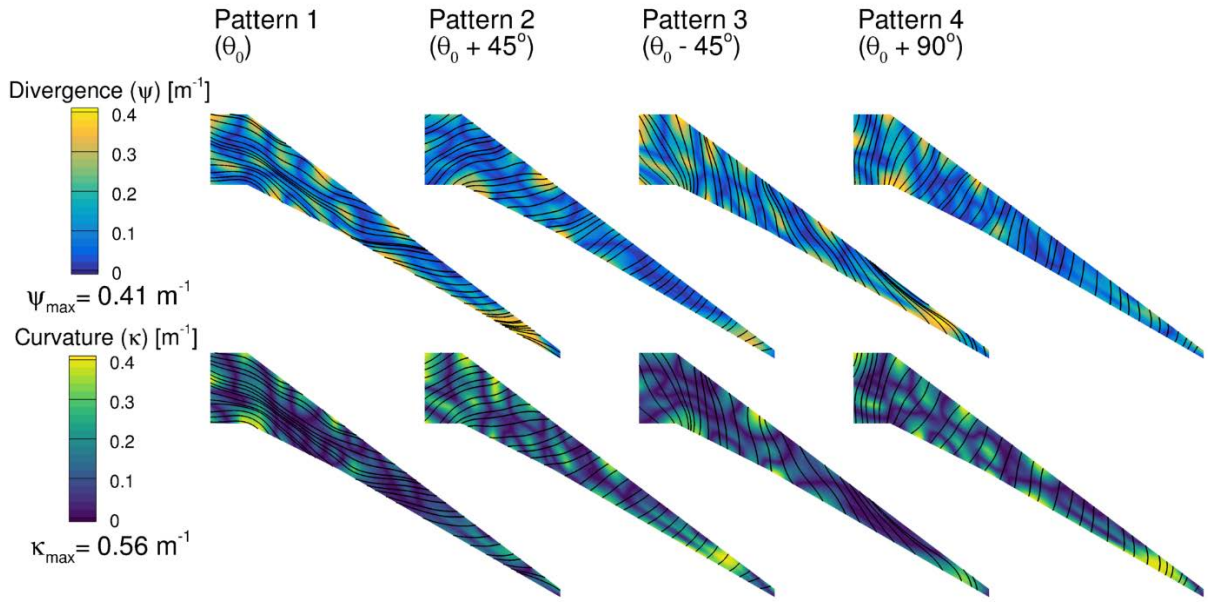

Figure 3.11. Tow-path curvature and divergence contours for upper skin of tow-steered optimized uCRM-9 design.

3.2.5.1.2 Conventional Rotated Versus Tow-steered Composite

Next, we relax the restriction on the conventional composite design by allowing the optimizer to rotate the wing skin plies. This is accomplished by giving the optimizer a single rotation design variable for each skin. These design variables control the orientation of the tow path for each skin by rigidly rotating all the plies in the layup. This gives the optimizer the freedom to control the bend-twist coupling of the conventional wing, and thus gives it the ability to aeroelastically tailor the design. Once these design variables were added, the conventional optimization was rerun and the results compared to the tow-steered design from the previous section (see Figure 3.12).

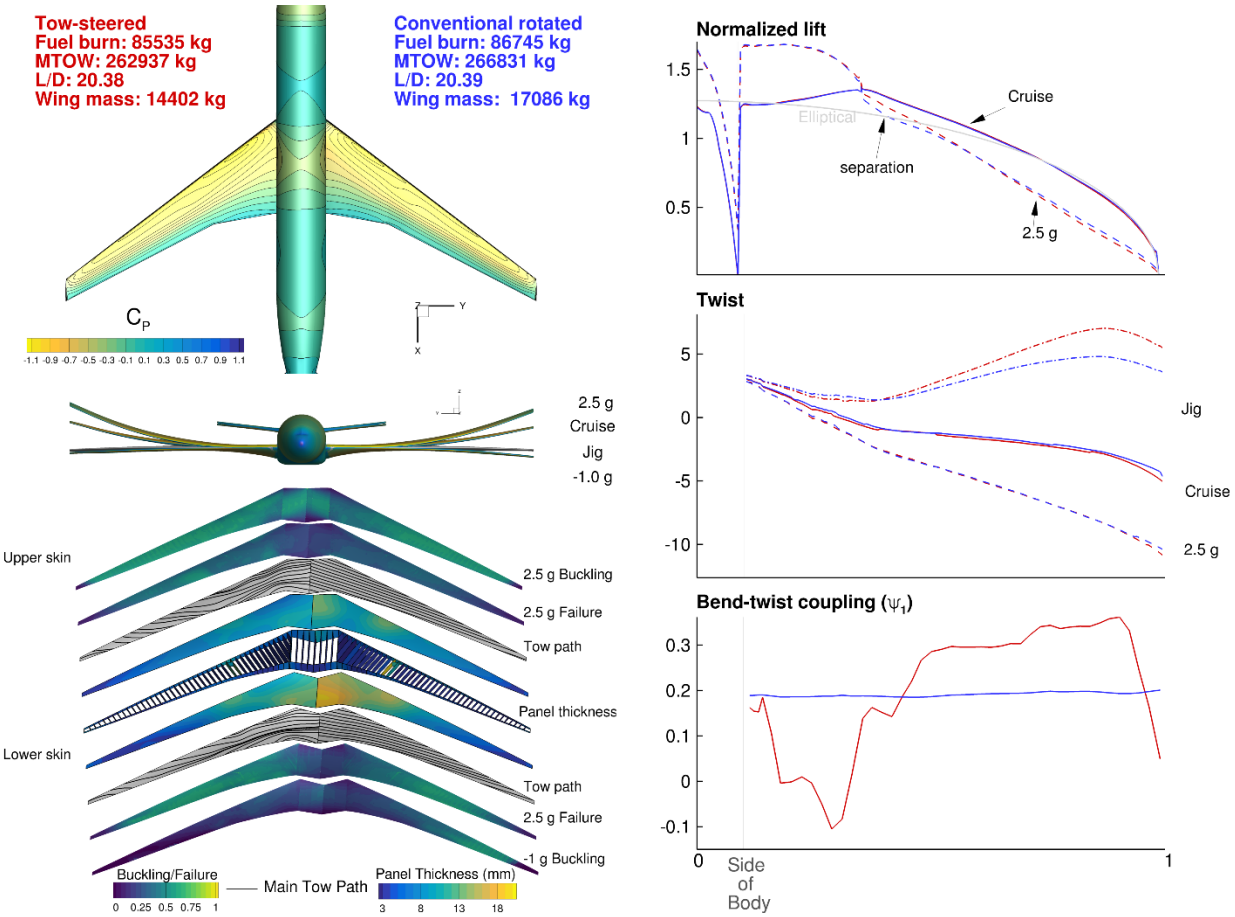

Figure 3.12. Comparison of optimal tow-steered (left; red) vs. conventional rotated (right; blue) composite aerostructural results for uCRM-9.

From Figure 3.12, it can be seen that by rotating the skin plies of the conventional composite design, the optimizer has cut the improvement margin in fuel burn and maximum takeoff weight to 1.4% and 1.5%, respectively, relative to the previous case. In addition, the structural weight improvement is now only 15.7%. By looking at the lift and twist distributions, it is clear that the optimizer was able to reduce this margin by increasing the load alleviation of the conventional design. In fact, the load alleviation performance for the 2.5G maneuver is nearly identical between the two designs. This means that any remaining benefit coming from the tow-steered design must be accounted for entirely by the local structural tailoring capability of the design. Using this information and the results from the previous case, it is possible to conclude that the benefit in fuel burn performance due to aeroelastic tailoring of the tow-steered design, when compared to the conventional design from the previous case, makes up roughly 0.9% of the previous 2.3% total. This means that the remaining 1.4% is due to local structural tailoring. Similarly, the additional load alleviation accounts for 8.3% of the 20% reduction in structural weight from the previous case. Looking back at the tow paths of the conventional rotated design in Figure 3.12, we see that the additional improvement in load alleviation is made possible by rotating the plies forward relative to the leading-edge spar of the wing, increasing the bend-twist coupling of the structure. The optimal angle of rotation of both skins of the rotated design is $8.3°$ forward relative to the quarter-chord line.

By examining the lift distribution during the 2.5G maneuver of the conventional rotated design in Figure 3.12, a small dip in the distribution can be seen at roughly the 40% span location (indicated on plot). To explore the cause of this phenomenon in more detail, we can plot aerodynamic streamlines of the flow on the upper surface of the wing in this region. Plotting these and a separation sensor contour (projection of local flow velocity in freestream direction), Figure 3.13, reveals that the dip in the lift distribution in this region is due to a small region of separated flow on the upper wing surface. Comparing the airflow in this region for the conventional and tow-steered composite designs, shows that this separated flow region is small for the conventional design, but grows larger for the tow-steered and conventional rotated designs. This is because as load alleviation is added into the design, the lift on the inboard section of the wing must increase to offset the loss of lift at the wingtips. This increase in lift causes the airflow over the inboard section of the wing to separate. This puts a potential upper limit on the maximum amount of load alleviation achievable by an aeroelastically tailored design. Because lower-fidelity aerodynamic models, such as panel methods and Euler-based CFD, do not possess the physics required to properly model separation, this highlights a benefit of using high-fidelity analysis in design optimization.

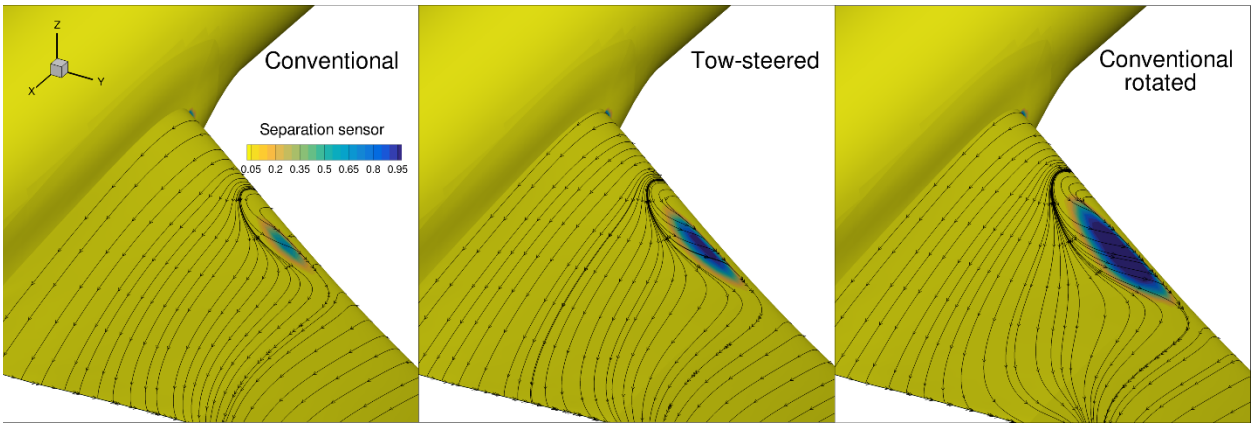

Figure 3.13. Separation sensor contour and airflow streamlines show region of separated flow on the 2.5G for the tow-steered and conventional rotated composite designs.

3.2.5.1.3 The effect of manufacturing constraints

Next, the effect of the manufacturing constraints on the tow-steered designs' performance will be investigated. To do this, the minimum curvature and tow cut/add length constraints are dropped from the tow-steered optimization problem. The optimization is then rerun and the results compared to the tow-steered optimized design with the original manufacturing constraint bounds ($|\psi| < 0.41\ \mathrm{m}^{-1}$, $|\kappa| < 0.56\ \mathrm{m}^{-1}$) used in the previous two cases. Figure 3.14 compares the designs for these two cases.

From Figure 3.14, it is seen that removing the AFP manufacturing constraints from the design problem leads to an additional improvement of 0.4% in fuel burn and 0.4% in MTOW. Similarly, the structural weight is reduced by an additional 4.5%. Looking at the lift, twist, and bend-twist coupling distributions show that both designs feature the same load alleviation performance. From this, it can be concluded that the manufacturing constraints do not hinder the ability of the tow-steered design to aeroelastically tailor the

structure. This means that the benefits in performance from removing the manufacturing constraints from the design must be purely due to local structural tailoring.

To show the severity of the AFP manufacturing constraints for the tow-steered wing boxes, the tow-path divergence contours are plotted for each pattern in Figure 3.15. For conciseness, only the tow-path divergence is shown. However, the tow-path curvature can be found by using the curvature-divergence relationship for offset patterns—see Figure 2.3. As expected, by removing the tow-path curvature and divergence constraints from the design optimization, the optimizer converged to tow paths with much higher values for these quantities. In particular, it can be seen that the most severe tow-path curvature and divergence occurs near the root of the wing box, with a small amount near the tip. This agrees well with the conclusion that the manufacturing constraints largely affect only regions of local structural tailoring. Examining the buckling and failure constraint contours in Figure 3.14, and noting that buckling is the predominant sizing constraint for the majority of the skins, leads to the conclusion that the trends in these regions are likely motivated by buckling performance. From this figure, it is seen that the locations and magnitudes of these constraint values differ slightly from pattern to pattern. This highlights the importance of considering the manufacturing constraints for all patterns in the layup, not just the main tow pattern.

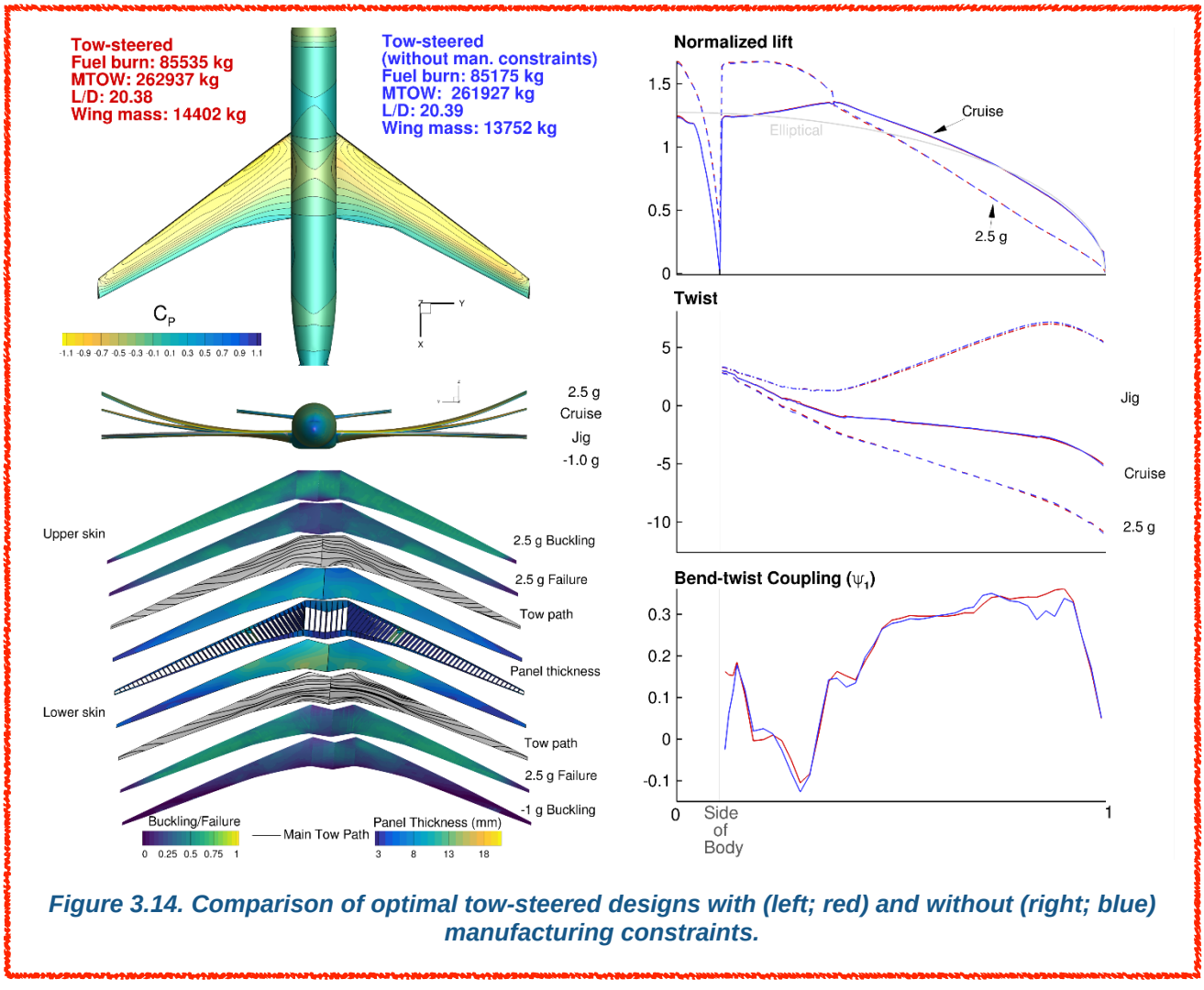

Figure 3.14. Comparison of optimal tow-steered designs with (left; red) and without (right; blue) manufacturing constraints.

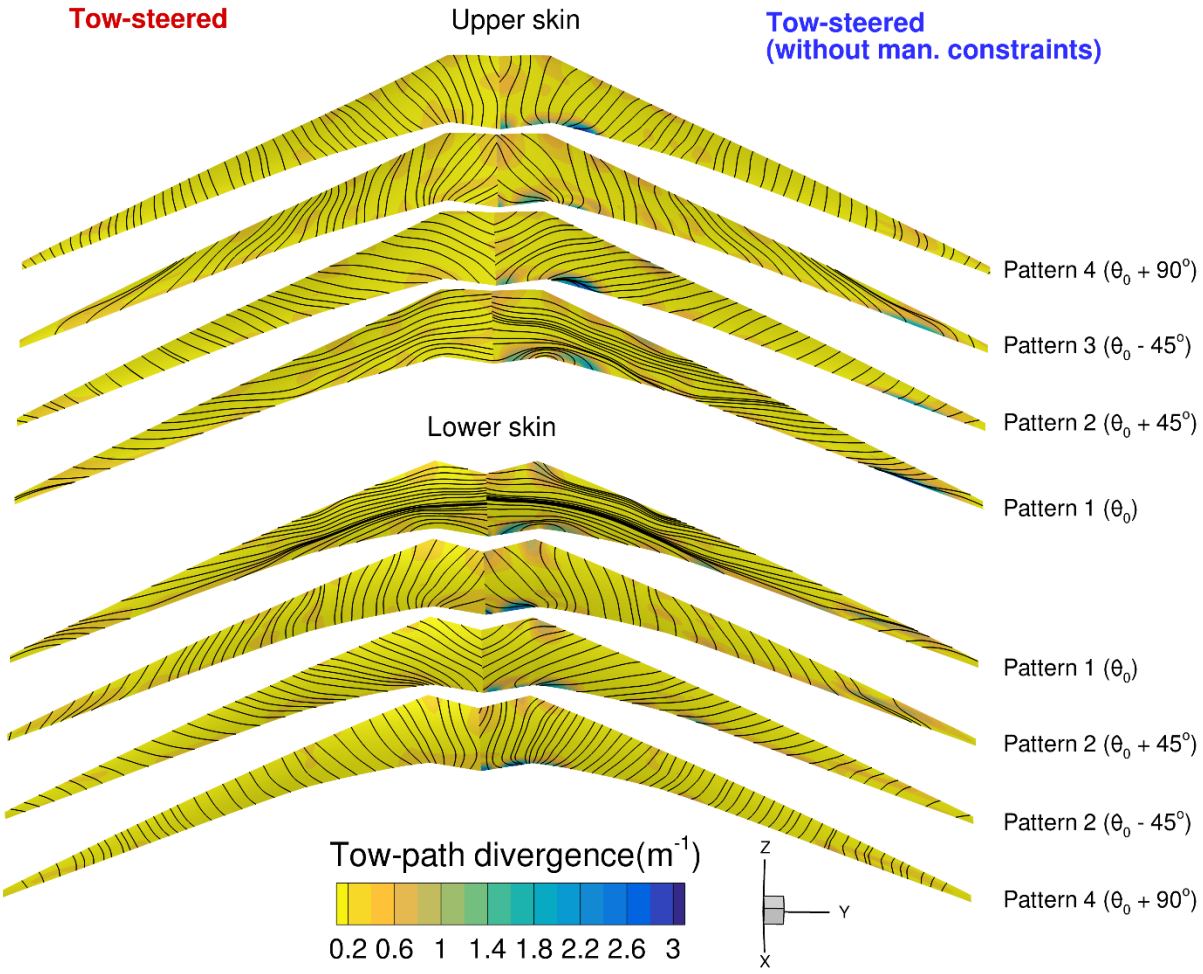

Figure 3.15. Comparison of tow-path divergence contours for aerostructurally optimized tow-steered design with (left) and without (right) manufacturing constraints.

3.2.5.2 uCRM-13.5 Optimization

Next, the optimization results for the higher aspect ratio uCRM-13.5 model are presented. For this case, two additional aerostructural optimizations are run: one with a tow-steered wing design, and one with a conventional composite design. These resulting designs are shown in Figure 3.16.

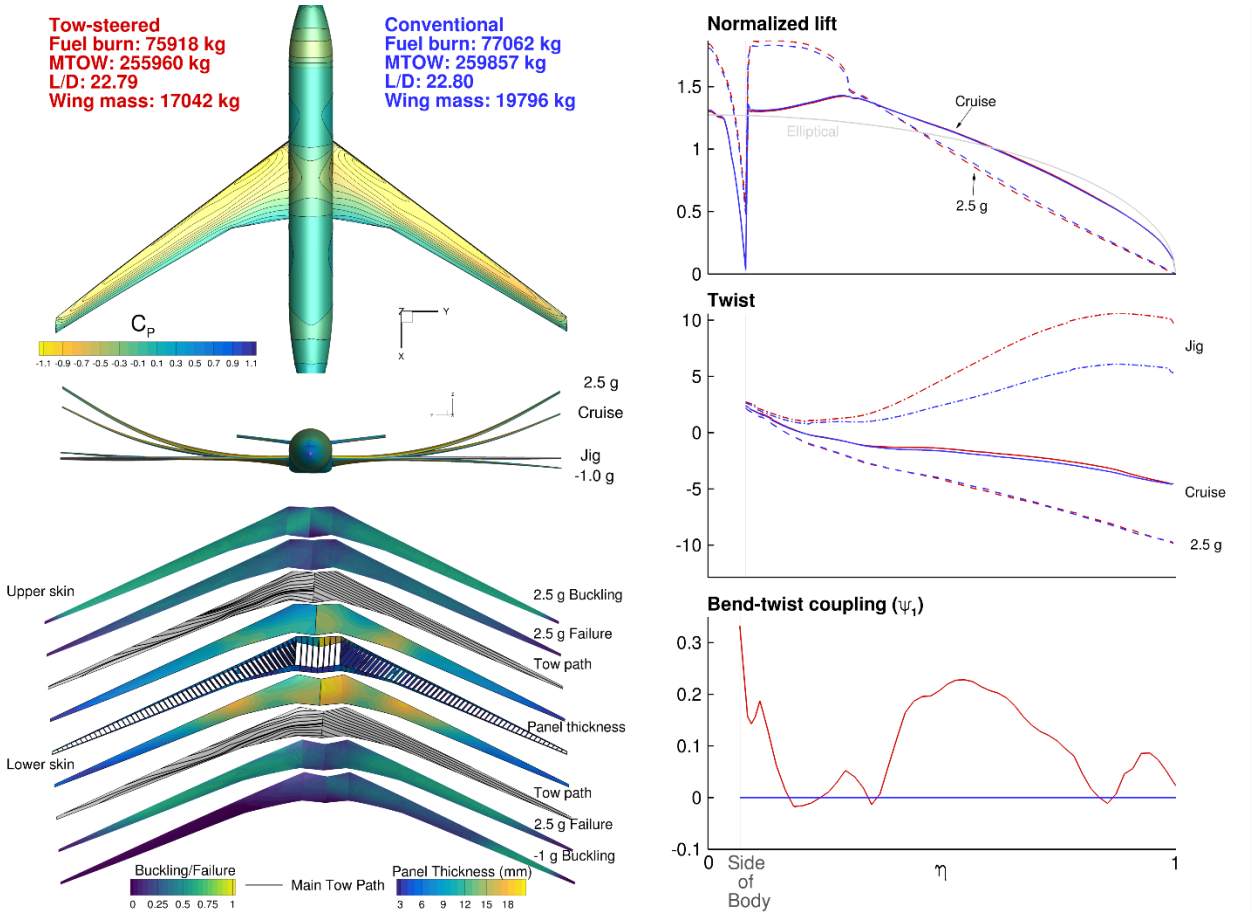

Figure 3.16. Comparison of the uCRM-13.5 aerostructural optimizations using tow-steered (left) and conventional (right) composites.

Comparing the performance of the uCRM-9 designs in Figure 3.10 with those of the uCRM-13.5 in Figure 3.13 reveals design trends expected of a higher aspect ratio wing design. Specifically, the fuel burn on both uCRM-13.5 designs have decreased relative to their uCRM-9 counterparts. This is due to the reduction in induced drag owed to the larger span, which increases $\frac{L}{D}$. In addition, due to the large moments on the wing structure, the structural weight increases for the uCRM-13.5 designs. From Figure 3.16, it can be seen that adding tow-steering to the uCRM-13.5 improves the fuel burn performance by 1.5% and MTOW by 1.5% relative to the conventional design. This benefit comes from the 14% reduction in weight achieved by the tow-steered design.

Examining the lift and twist distribution reveals that unlike the uCRM-9 case, the optimizer is not able to add any additional load alleviation to the tow-steered design. This means that the performance improvements seen on this design are entirely due to local structural tailoring. Upon closer examination of the two high-aspect-ratio designs in Figure 3.16, it can be seen that, while the spanwise twist distributions are nearly identical between each design under both cruise and maneuver loading, the initial jig twist of the tow-steered design is noticeably higher. This suggests that the bend-twist coupling of the tow-steered wing as measured from the jig (unloaded) to cruise wing shape is different than that measured from the cruise to 2.5G maneuver shape. This same trend can be seen in the uCRM-9 tow-steered and conventional rotated composite wing designs (see Figure 3.12).

This mean that the amount of bend-twist coupling seen on the 2.5G maneuver condition for these designs are being limited relative to what otherwise should be expected, which suggests a nonlinear behavior. Because the structural model used in this work is linear, the cause of this behavior must be either from the aerodynamics or aeroelastic coupling. In the case of the aerodynamics, this nonlinearity could be introduced through the RANS governing equations. In the case of the aeroelastic coupling, the nonlinearity may be introduced through the follower loads generated by the load/displacement transfer.

By plotting the airflow on the upper surface of the wing for the 2.5G maneuver, we find that, unlike for the uCRM-9 cases in Figure 3.13, the additional load alleviation is not being prevented by separated flow at the root of the wing, as shown in Figure 3.17. This suggests that the cause is not aerodynamic.

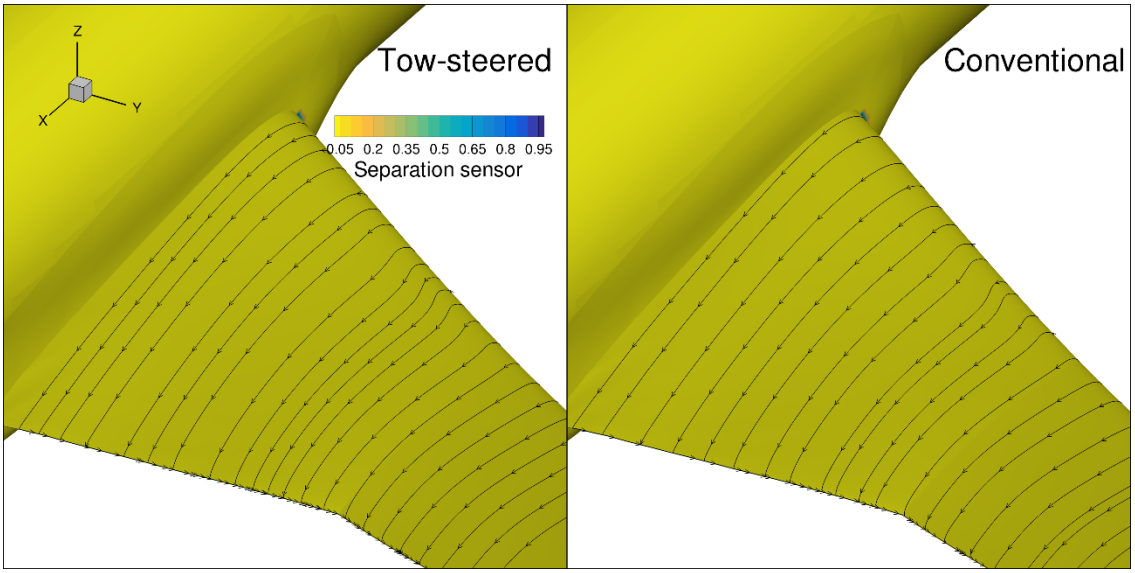

Figure 3.17. Comparison of optimal tow-steered (left) vs. conventional (right) composite aerostructural results for uCRM-13.5.

3.2.5.3 The Effect of Varying Aspect Ratio

In the previous sections, the aerostructural design benefits offered by adding tow-steering to a wing of aspect ratio 9 and 13.5 were analyzed. Now this trend will be extended by performing a sweep of optimizations of tow-steered and conventional fixed-ply composite designs with varying wing aspect ratios. This is accomplished by taking the uCRM-9 design optimization problem and adding planform variables—span, sweep, and chord—to the FFD variables. The optimization for each design is then run with a series of different aspect ratio constraints ($\mathrm{AR} = [7.5, 9, 10.5, 12, 13.5]$). The case for $\mathrm{AR} = 9$ did not need to be run, as it was equivalent to the uCRM-9 tow-steered and conventional optimized cases presented earlier. The $\mathrm{AR} = 13.5$ designs were not exactly equivalent to the uCRM-13.5 results presented earlier. The uCRM-9 and uCRM-13.5 designs feature a different number of ribs, wing taper ratio, and fuselage positioning, none of which is varied during this aspect ratio study on the uCRM-9. Because of this, the resulting 13.5 aspect ratio version of the uCRM-9 ends up being slightly different. It is important to note that since the optimizer is afforded only three planform variables (unknowns): chord (x-scaling), span (y-scaling), and sweep (x-shearing); and has to respect three planform constraints

(equations): prescribed area, prescribed aspect ratio, and prescribed sweep; the resulting wing planform for each aspect ratio optimization can be uniquely solved. The resulting wing planforms for each aspect ratio design are shown in Figure 3.18.

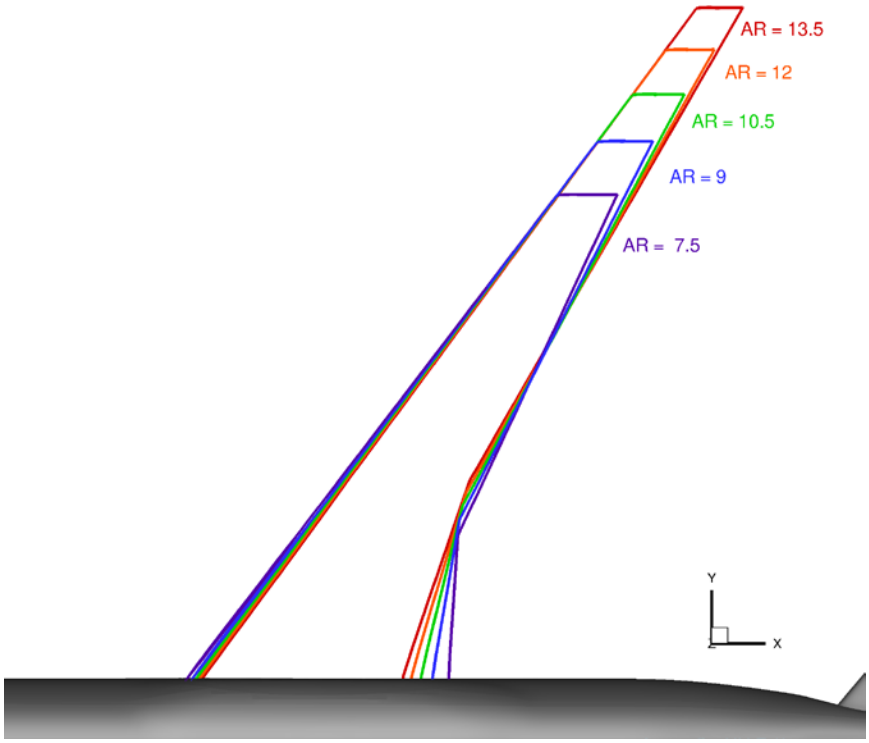

Figure 3.18. uCRM planforms for variable aspect ratio study.

The trend for fuel burn, MTOW, L/D, and wing structural mass for the optimal-fuel-burn designs as a function of aspect ratio is shown in Figure 3.19. From this, it can be seen that, in general, adding tow steering to the design provides benefits in fuel burn, MTOW, and wing mass for all aspect ratio designs. Like the previous cases, L/D is largely unaffected by the use of tow-steering. These trends show that as the aspect ratio is increased the fuel burn decreases. However, toward the higher aspect ratio end, the benefit in fuel burn decreases. By analyzing the trend in L/D, it can be concluded that this is because as the aspect ratio increases the amount of induced drag on the design left to be reduced becomes smaller, while the viscous and compressibility drag begin to dominate. Next, analyzing the trend in MTOW, we see that as the aspect ratio increases, the MTOW decreases, with exception of the last design ($\mathrm{AR} = 13.5$). By comparing the trends in fuel burn and wing mass, it is found that this increase in MTOW is due to the fact that as the aspect ratio increases the improvements in fuel burn begin to taper off, while the rate of increase in wing mass continues to increase. This causes the increase in wing structural mass to eventually outpace the decrease in fuel burn, which leads to an increase in MTOW.

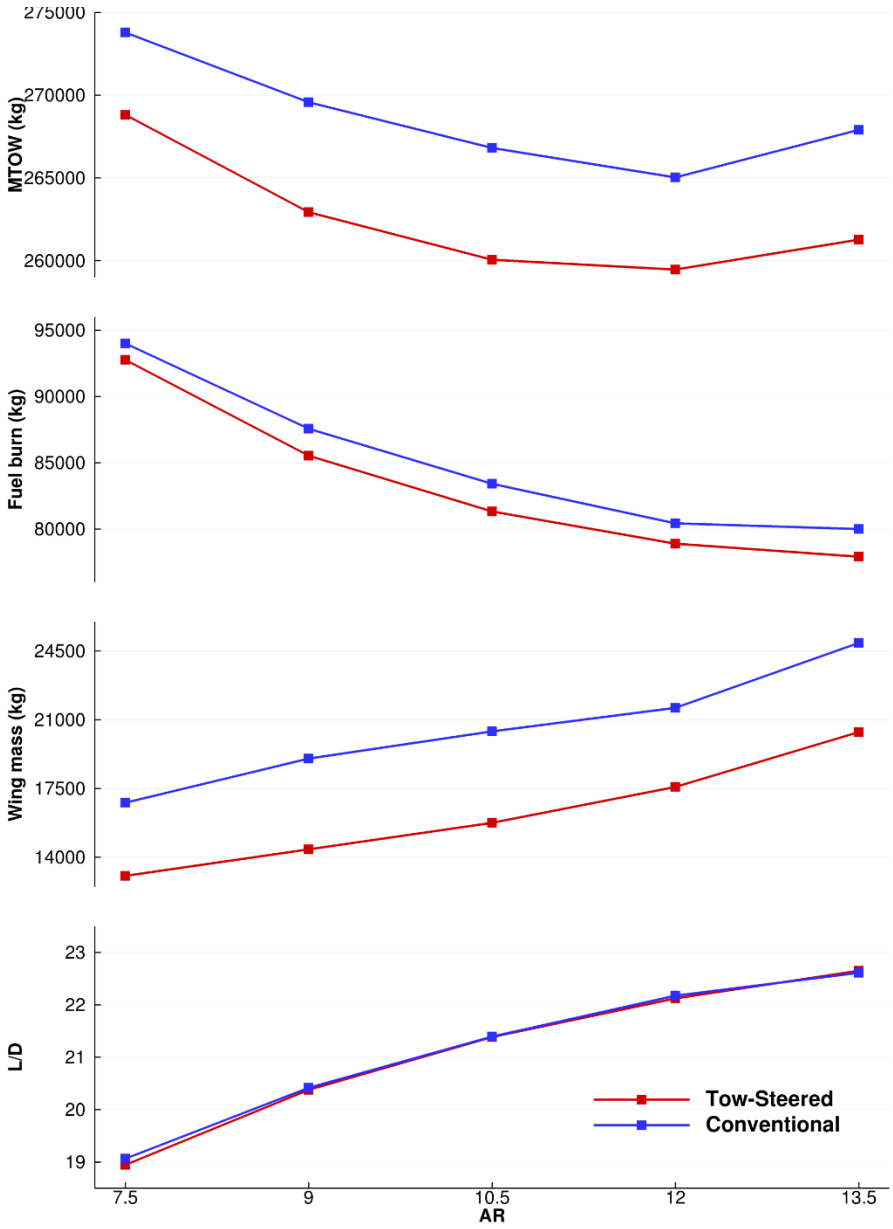

Figure 3.19. Fuel burn, MTOW, L/D, and wing mass trend for increasing aspect ratio.

The trend for passive load alleviation of each design can be seen in Figure 3.20. All designs feature a roughly elliptical lift distribution with some load alleviation on the maneuver. Another prominent dip in the 2.5G lift distribution of the tow-steered $\mathrm{AR} = 7.5$ case can be seen, indicating flow separation. This indicates that lower aspect ratio designs are more likely to be susceptible to this type of flow separation. The reason for this is likely because, according to Figure 3.19, these designs have higher maximum takeoff weights, meaning that the designs will have to meet higher lift requirements for their maneuver conditions. It can also be seen that as the aspect ratio increases, the amount of bend-twist coupling utilized on the tow-steered design by the optimizer, particularly near the tip, decreases. This confirms the trend seen earlier in Section 3.2.5.2, that is: as the aspect ratio of the wing is increased, the amount of additional load alleviation used by the tow-steered design decreases.

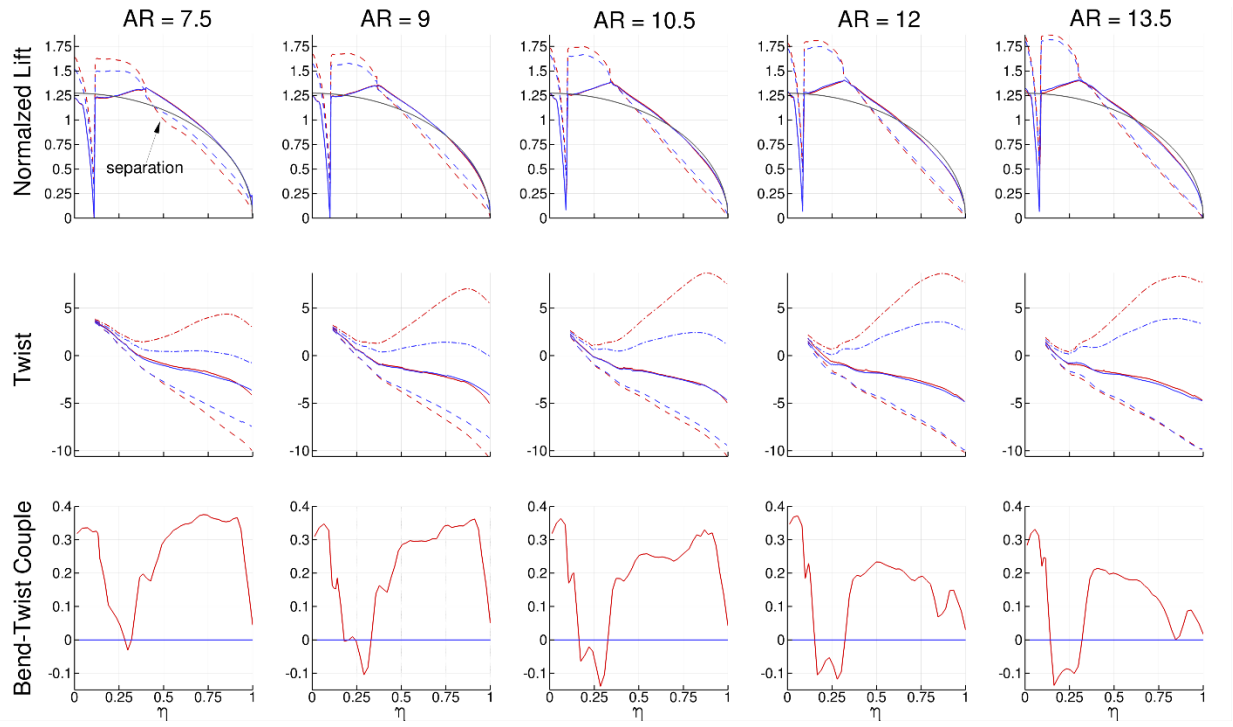

Figure 3.20. Passive load alleviation trend for increasing aspect ratio; tow-steered design (red), conventional design (blue).

3.2.6 Conclusions

In this series of design optimization studies, the aeroelastic benefits of tow-steering as applied to flexible-wing design have been investigated. To accomplish this, a series of high-fidelity gradient-based aerostructural fuel burn optimizations were performed on both tow-steered and conventional composite wing designs for both the uCRM-9 and uCRM-13.5 designs. The aerodynamics was modeled with a RANS-based CFD solver and structures were modeled with a 3D CSM solver using shell finite elements. The optimization problem included both geometric variables (airfoil shapes and twist) and structural sizing variables (component thicknesses and tow path). Comparing the results of each design optimization provided insights into the benefits that tow-steering manufacturing has to offer for flexible-wing design.

The first set of insights come from the results run on the uCRM-9 model, which is representative of a Boeing-777-type aircraft. These results are summarized in Table 11. From these results, it was found that the aircraft fuel burn and MTOW could be reduced by 2.3% and 2.5%, respectively, relative to a conventional composite design. This improvement was due to a 24% reduction in structural weight of the tow-steered design, owed to improvements in the design's structural and aeroelastic tailoring. When the conventional composite design is allowed to rotate the plies in the skins, the improvements in fuel burn and MTOW offered by tow steering is reduced to 1.4% and 1.5%, respectively, while the structural weight reduction is 15.7%. This is because the optimizer is largely able to match the load alleviation performance of the tow-steered design with the conventional design. From this, it was possible to gleam that 0.9% of the 2.3% decrease in fuel burn seen in the comparison between the tow-steered and conventional design's performance was due to the additional load alleviation, while the

remaining amount came from structural tailoring. Finally, the tow-steered design was re-optimized without a minimum tow-path curvature and cut/add length manufacturing constraint. Removing these constraints led to minor improvements in design performance. The constraints were found to only affect the structural tailoring performance of the design.

Table 11. Summary of results from uCRM-9 aerostructural optimization studies.

Quantity	TS	C	CR	TS-NM
Fuel Burn [kg]	85 535	87 558	86 745	85 175
MTOW [kg]	262 937	269 575	266 831	261 927
Wing mass [kg]	14 402	19 016	17 086	13 752

These uCRM-13.5 results are summarized in Table 12. For this design, it was found that the tow-steered wing could reduce the structural weight of the wing box by 14% and the fuel burn by 1.5%. This was made possible in large part by the increase in local structural tailoring of the wing design. When compared to the uCRM-9 design, the uCRM-13.5 tow-steered design featured nearly no passive load alleviation improvement relative to the conventional composite design. This suggests that aspect ratio plays a critical role in the amount of load alleviation that is possible for the tow-steered design.

Table 12. Summary of results from uCRM-13.5 aerostructural optimization results.

Quantity	TS	C
Fuel Burn [kg]	75 918	77 062
MTOW [kg]	255 960	259 857
Wing mass [kg]	17 042	19 796

The results presented here show that tow-steered wing designs have the potential to decrease aircraft fuel burn and structural weight relative to conventional composite designs. Further insight into the design process might be revealed by allowing the optimizer the freedom to vary the planform—sweep, span, and chord—of the wings. This allows the optimizer to find the optimal wing aspect ratio and planform to minimize fuel burn for both a tow-steered and conventional composite design. It would also be worth quantifying the effect that changing the optimization objective would have on both the tow-steered and conventional composite wing designs. This could be accomplished by producing a Pareto front between two objectives: one that focuses more on structural performance (e.g., structural weight) and another that focuses on aerodynamics (e.g., fuel burn or drag). Finally, in this section, only three flight conditions—a cruise, a 2.5G pull-up maneuver, and a -1G push-over maneuver—were considered. This was done to simplify the problem and to allow insights to be more easily drawn from the aerostructural performance of each design. Previous work on high-fidelity aerostructural design optimization has shown the need for considering multiple cruise flight conditions and constraints, such as gust loading, flutter [24, 25, 26], and buffet onset [27] to achieve more realistic designs. Flutter would likely be an active sizing constraint for the higher-aspect-ratio wing designs presented in this work. Another aspect that could be added to the model is geometric nonlinearity in the structural analysis, though as the results in

Section 7 will show this plays a relatively small role in the performance of the design and linear analysis is often sufficient. Nevertheless, the work presented herein provides valuable insights into the design of tow-steered composite wings. The methodology developed in this work opens the door to other multidisciplinary design optimization studies of tow-steered composite structures.

3.2.7 Optimized Finite Element Models

Five finite element models corresponding to the optimized structures discussed above are available. Each includes the full structural wing box mesh, including tow-steering orientations if applicable, as well as nonstructural masses such as engine weights, leading edge (LE) and trailing edge (TE) actuators, and fuel masses.

The following models are provided:

uCRM_9_US_BDF:
Full-scale "baseline" composite configuration of uCRM-9 without tow-steering (result of uCRM-9 conventional composite (C) optimization). Includes effects of smeared skin stiffeners.

uCRM_9_TS_BDF:
Full-scale tow-steered configuration of uCRM-9 with full-scale AFP constraints (result of uCRM-9 tow-steered composite (TS) optimization). Includes effects of smeared skin stiffeners.

uCRM_135_US_BDF:
Full-scale "baseline" composite configuration of uCRM-13.5 without tow-steering (result of uCRM-13.5 conventional composite (C) optimization). Includes effects of smeared skin stiffeners.

uCRM_135_TS_BDF:
Full-scale tow-steered configuration of uCRM-13.5 with full-scale AFP constraints (result of uCRM-13.5 tow-steered composite (TS) optimization). Includes effects of smeared skin stiffeners.

uCRM_135_test_article_optimization:
Full-scale tow-steered optimization with scaled AFP and minimum gauge constraints. Does not include skin stiffeners. This model served as the basis for the 27% test article design.

Additionally, both the uCRM-9 and uCRM-13.5 aluminum baseline models [4] are available from the University of Michigan MDOLAB website.

4 Test Article Design

The test article was based on the uCRM-13.5 tow-steering optimization described in Section 3.2, with scaling factors applied to tow-steering and minimum thickness parameters to account for manufacturing constraints at test scale. Because the test article was 27% scale, a factor of 3.7 was applied to the corresponding minimum thickness and tow-steering minimum radius for the full-scale optimization. Furthermore, it is noted that while the optimization is performed in metric units (newtons, meters), the test article detailed design and subsequent testing events were performed in English units (pounds, inches).

Geometric optimization results, including planform and thicknesses were scaled linearly based on the test article scale factor of 0.27. The tow-steering definition, which defines orientation via a unit vector field, did not need to be scaled (material orientation is independent of scale). Loads (forces) scaled quadratically, therefore, all loads were scaled by a factor of 0.0729. By scaling all geometric parameters linearly, and loads quadratically, the resulting designed test article is expected to have the same stress and strain values as the full-size design and resulting deflections will also be geometrically similar (scaled linearly). Critical Euler buckling loads also scale quadratically, therefore, the critical buckling stress also remained the same as the full-scale design. It is noted that while the test article does not include skin stiffeners, the scaled test article was based on a full-scale optimization that also omitted skin stiffeners, and therefore, lack of stiffeners was not a factor in scaling the test article.

To accommodate test requirements, the continuously distributed loads generated by the optimization were converted to a near-equivalent discrete load set. A total of 14 load points, positioned at the leading and trailing edge at 7 unique span locations, were selected for load application. The loads were determined such that total bending and twist moment diagrams were matched as closely as possible, as shown in Figure 4.1 and Figure 4.2. The short, discontinuous steps shown in the Vz and My curves, particularly in Figure 4.2 are due to slight differences in the exact spanwise location of the leading edge load and trailing edge load points. It is noted that the discrete loads shown in these curves, and subsequently applied to the linear FEM discussed in the following sections, the full resultant load is applied in the vertical direction (parallel to the Z-axis). The test loads described in Table 14 and Table 15 are also provided by a global axes component, which reflects the predicted follower load orientation under full load. Further details of the scaling process, generation of discrete loads, torque, moment and shear diagrams are available in Appendix G. The discrete load points required local pad-ups to be added to the spars to accomodate the local point loads; these are reflected in the FEM and CAD designs.

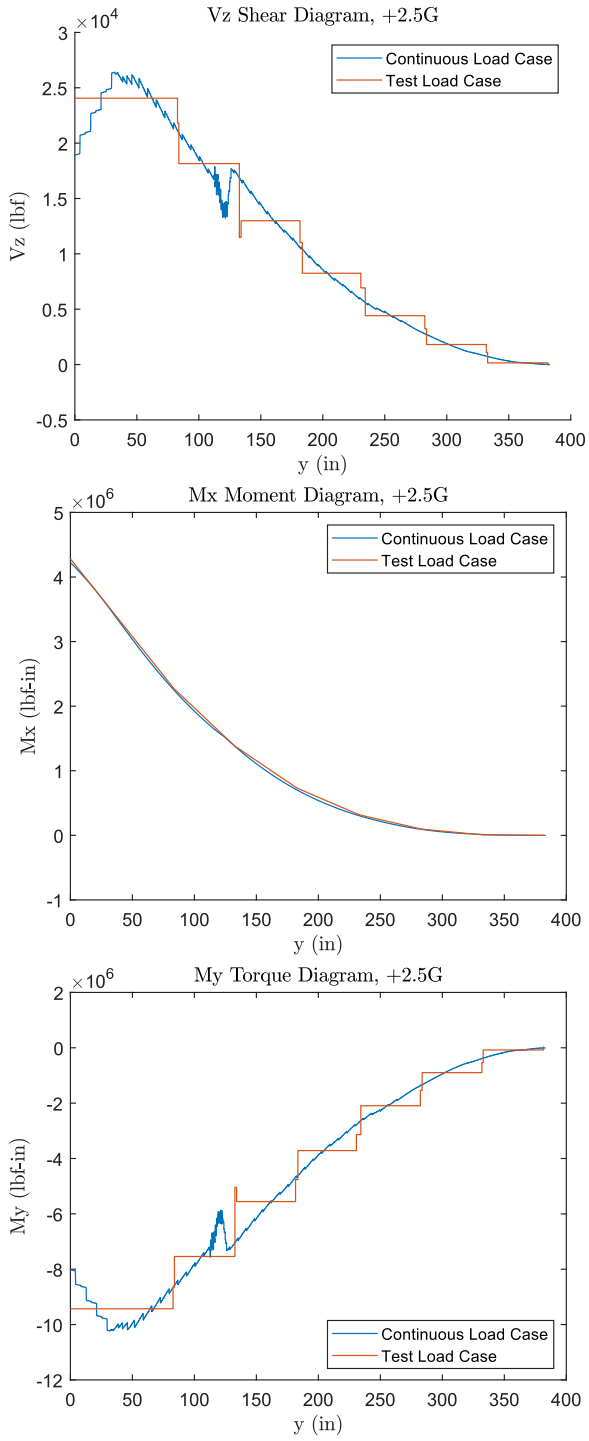

Figure 4.1. Shear and Moment Diagrams for +2.5G Load Case.

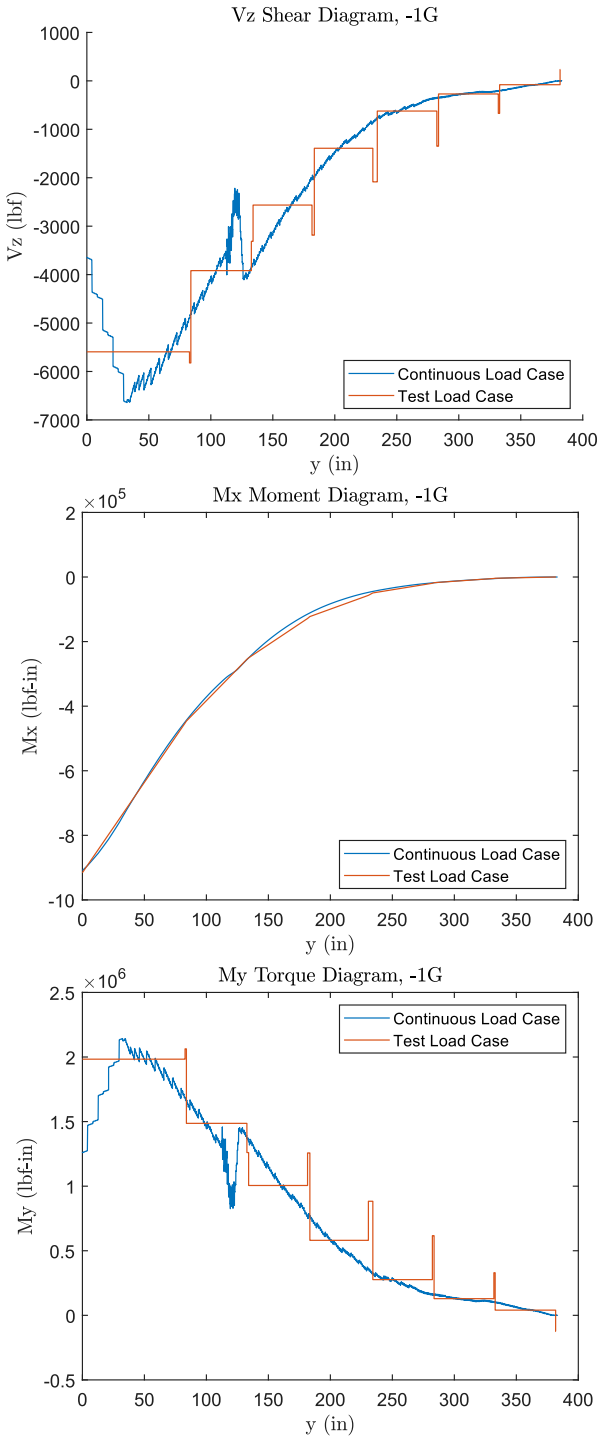

Figure 4.2. Shear and Moment Diagrams for -1G Load Case.

A further modification was added to simplify manufacturing and improve assembly fit-up: nonstructural sacrificial plies were added to the root spar webs, allowing for the web to be machined to a flat surface to ensure that the reaction plates mated in the correct alignment (thus adjusting for any twist that may have developed during the cure process). For the LE spar, 16 plies were secondarily bonded with FM300 film adhesive. For the trailing edge spar, 20 sacrificial plies were cocured (no film adhesive).

An additional modification of the optimized FEM to the test article was a change in boundary conditions. The optimization utilized a fixed constraint at all BL0 nodes (at the root closeout rib) and additional pin constraints at the fuselage intersection (at the kink, approximately Rib 4). The test article, however, was constrained by four pin locations mounted on the spar webs; two each on the leading and trailing edge spars. The outboard pins, located between Rib 3 and Rib 4, provided constraint in the vertical and spanwise direction, while the inboard pins, between Rib 0 and Rib 1, provided a constraint in the vertical direction only due to a spanwise slot for fit and assembly purposes. The fore/aft constraint was provided by sandwiching the spar webs between the steel reaction plates, which also accepted the pins. The reaction plates were subsequently bolted to the AFRC reaction table fixtures.

The upper skin steering and ply-drop contours are depicted in Figure 4.3. Steering contours were obtained by fitting streamlines to the optimized material direction vector field. Ply drops were obtained by rounding the optimized skin thickness up to the nearest whole ply after geometric scaling. No pad-ups were required for the upper skin. Skin laminates were designed with repeating units of $[0°,0°,90°,0°,0°,45°,0°\text{-}45°]_s$, with ply drops taken from the center of the laminate and selected such that the desired ply fraction was maintained. The laminate ply drop sequence for the upper skin is depicted in Figure 4.4. Because the minimum upper skin thickness consisted of 44 plies, the ply-fraction remained well homogenized, as shown in Figure 4.5. The upper skin actual ply fraction for 0° plies ranged from 61.7-64.0%; 90° plies from 12.0-13.8%; 45° plies from 11.4-13.3%; and -45° plies from 10.9-12.8%.

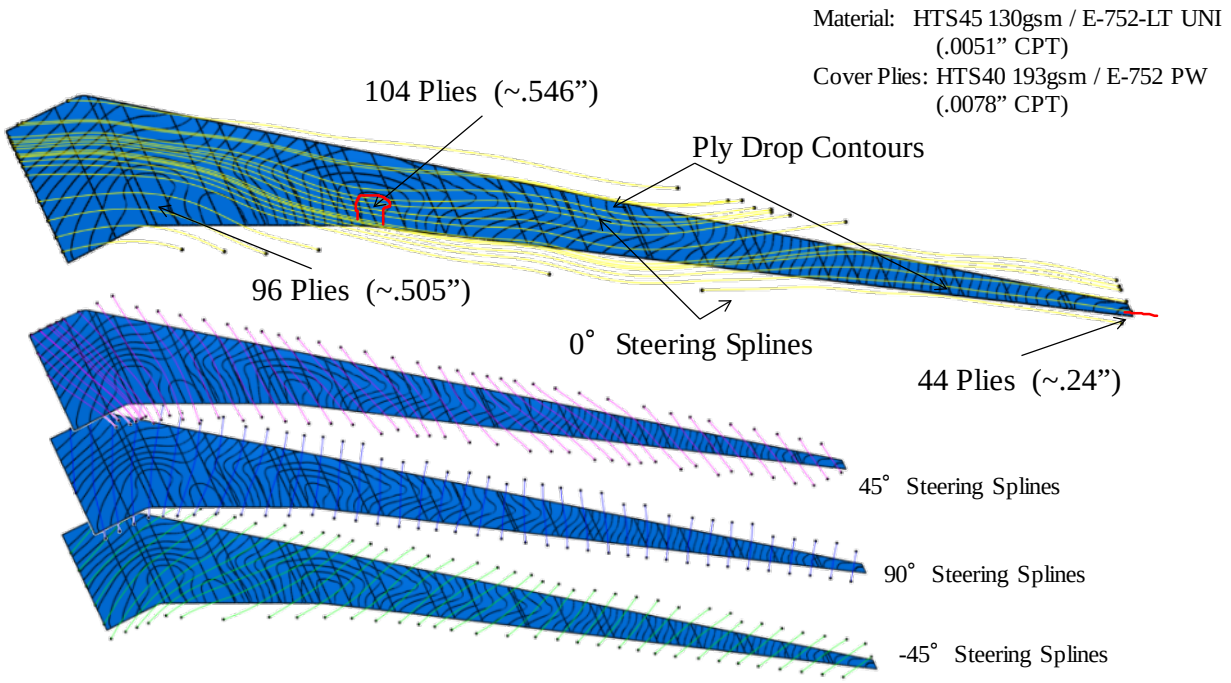

Figure 4.3. Upper skin steering splines and ply drop contours.

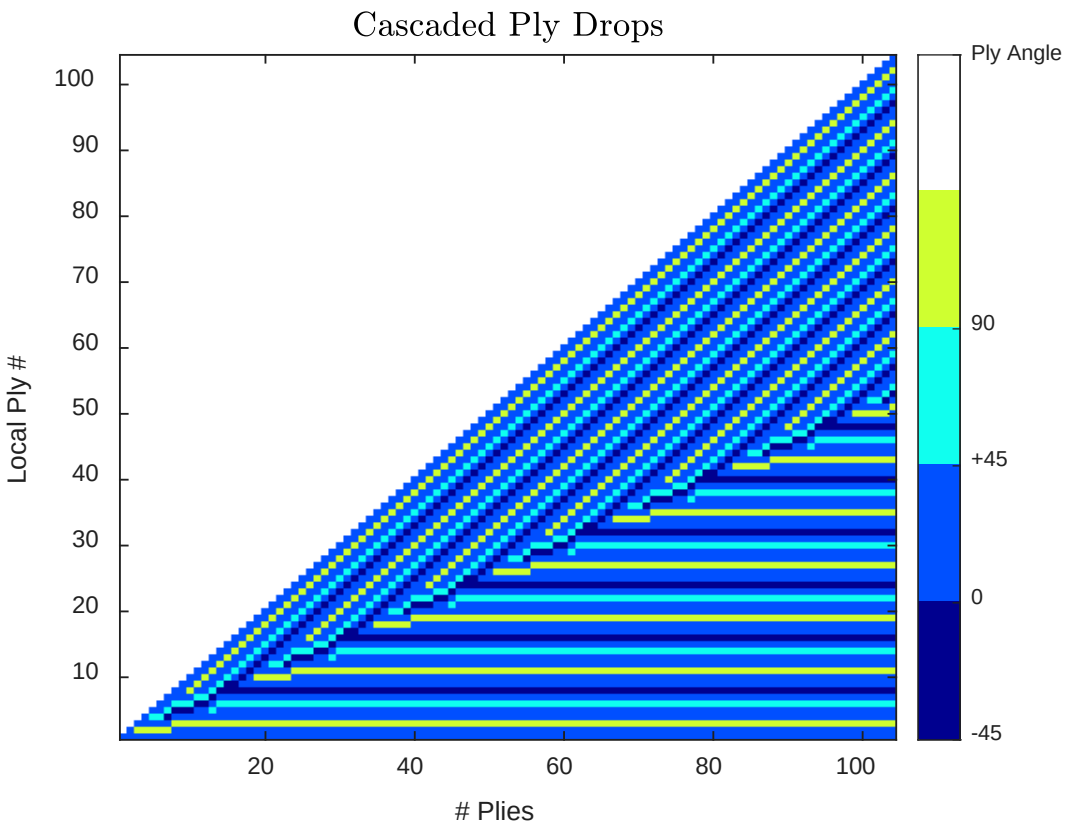

Figure 4.4. Upper skin laminate ply drop sequence.

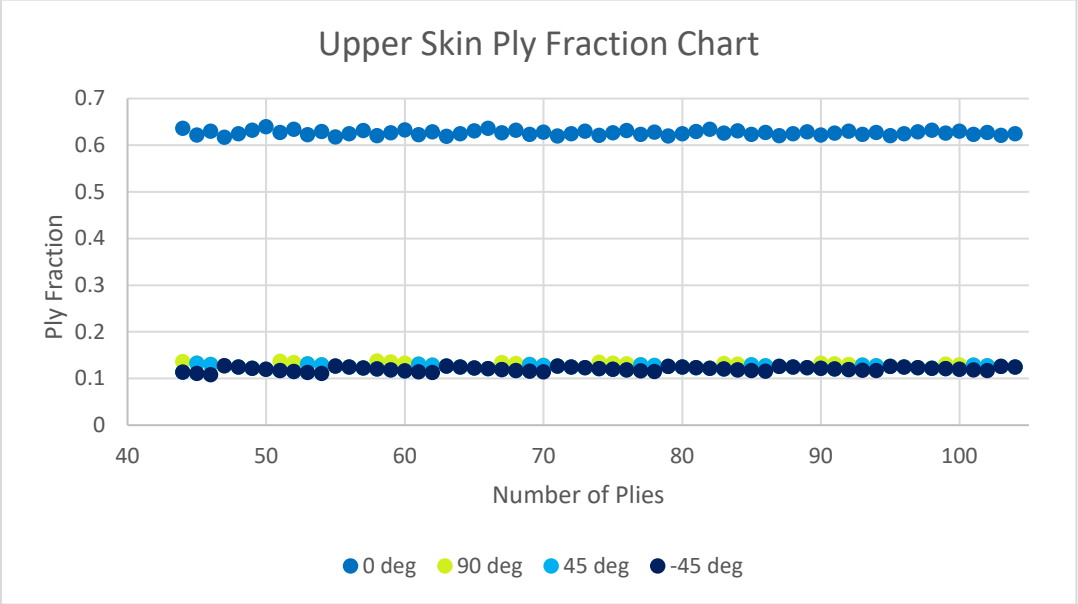

Figure 4.5. Upper skin ply fraction chart.

The change in boundary conditions did affect the load distribution in the root region, which required some local pad-ups on the lower skin, primarily where it interfaced with the spar caps and Rib 4. The resulting design of the lower skin is shown in Figure 4.6, with the lower skin pad-up details depicted in Figure 4.7. Many of these pad-ups were driven by fastener bearing strength requirements, which were not considered during the optimization. The pad-ups increased the maximum thickness of the lower skin from 61 plies to 114 plies in the thickest pad-up region, not counting fabric cover plies. In pad-up regions exceeding 64 plies, the additional pad-up plies consisted of 45°, -45°, and 90° plies to add additional strength in the transverse direction to improve transverse strength in areas of complex loading (e.g., the pad-up near Rib 4 experienced large chordwise loading due to the spar kink). The laminate ply sequence for the lower skin is depicted in Figure 4.8, where the change in laminate sequence above 64 plies for pad-up regions is evident.

The actual ply fraction for the lower skin outside of pad-up regions had slightly greater variation than the upper skin, due to the smaller minimal thickness of 14 plies. The lower skin actual ply fraction for 0° plies ranges from 60.0-66.7%; 90° plies from 11.1-15.8%; 45° plies from 10.0-14.3%; and -45° plies from 7.1-13.3%.

The ply fractions for the pad-up regions of the lower skin were intentionally designed to become more quasi-isotropic as thickness increased. For the 70-ply pad-up at the leading edge the ply fraction was [57.1%, 14.3%,14.3%, 14.3%]; the 76-ply pad-ups at the trailing edge had a ply fraction of [52.6%, 15.8%, 15.8%, 15.8%]; and the 114 ply trailing edge pad-up at Rib 4 was [35.1%, 21.9%, 21.1%, 21.9%]. Actual lower skin ply fractions are provided in Figure 4.9.

Upper and lower rib and spar caps were designed to be offset 0.030” from the skin inner mold line (IML). Because both the skin IML and spar and rib cap surfaces are bag-side surfaces, minor surface profile deviations were expected and accommodated by designing in the 0.030” gap and filling with a liquid shim to achieve flush mating surfaces.

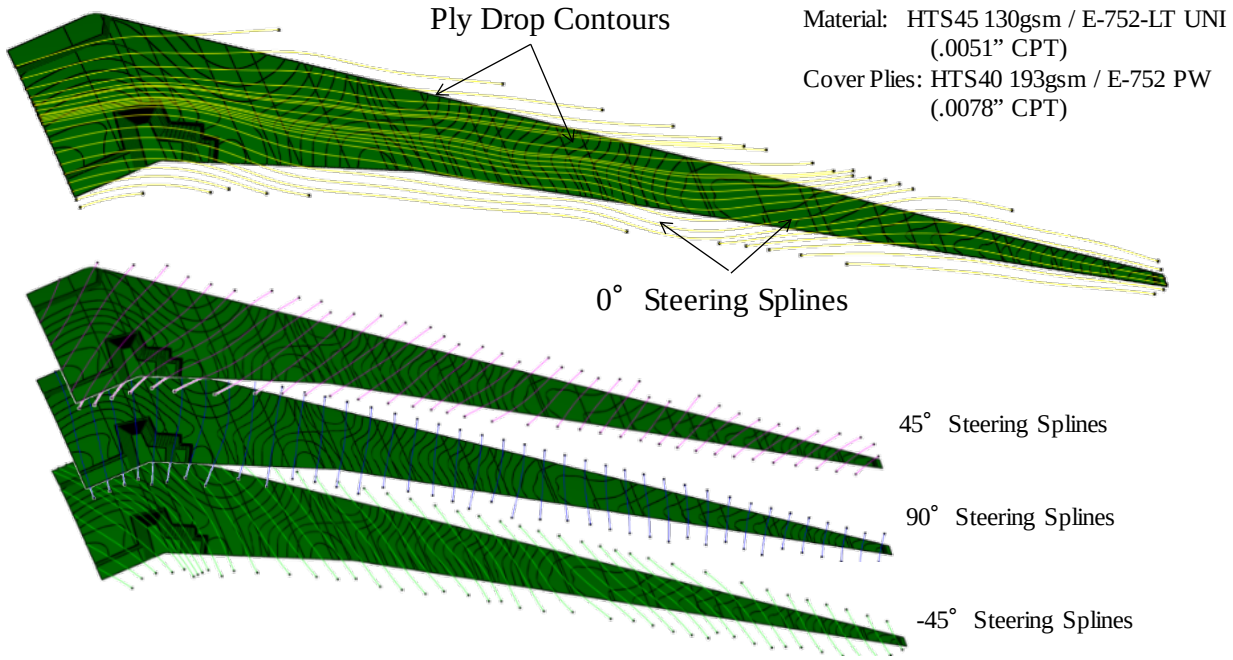

Figure 4.6. Lower skin steering splines and ply drop contours.

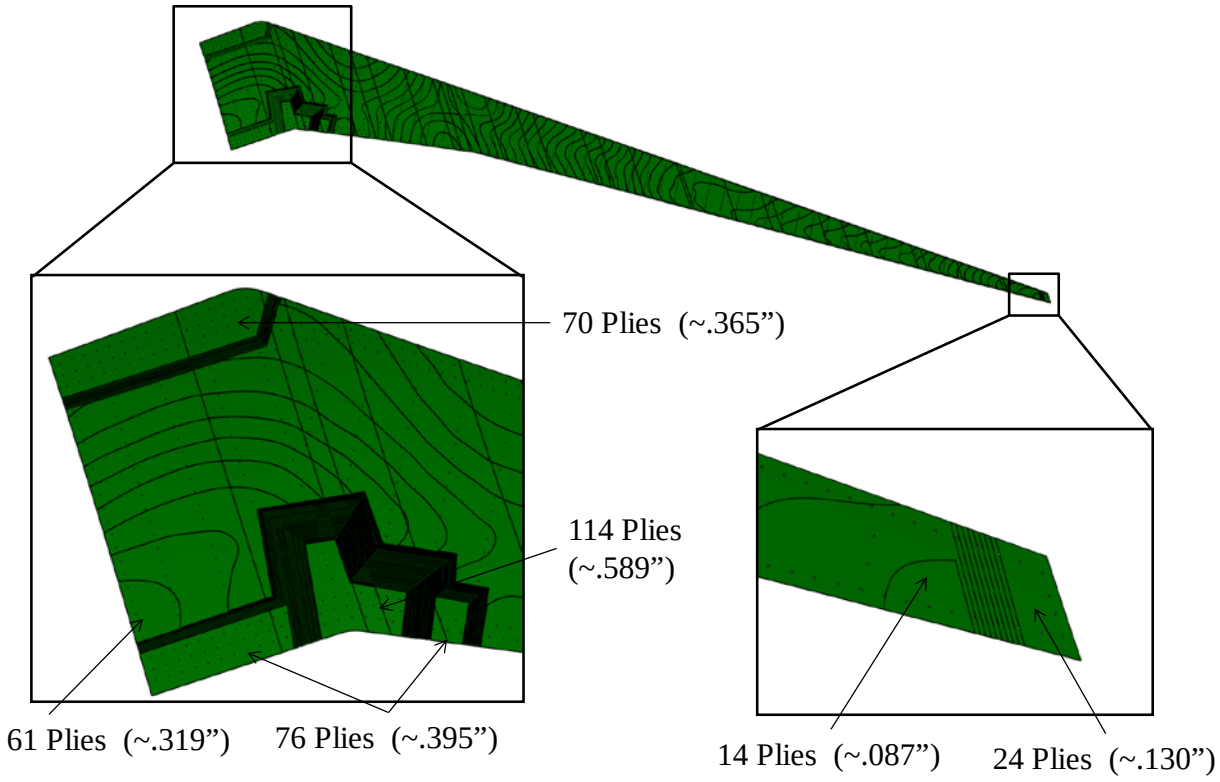

Figure 4.7. Lower skin pad-ups.

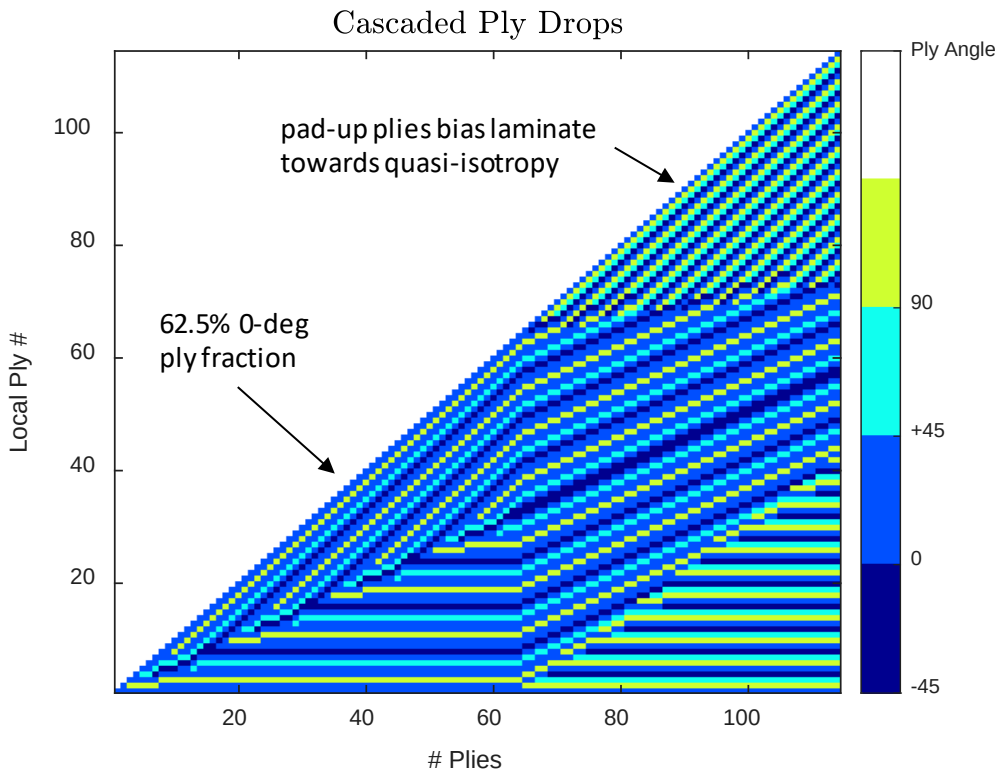

Figure 4.8. Lower skin ply drop and pad-up sequence.

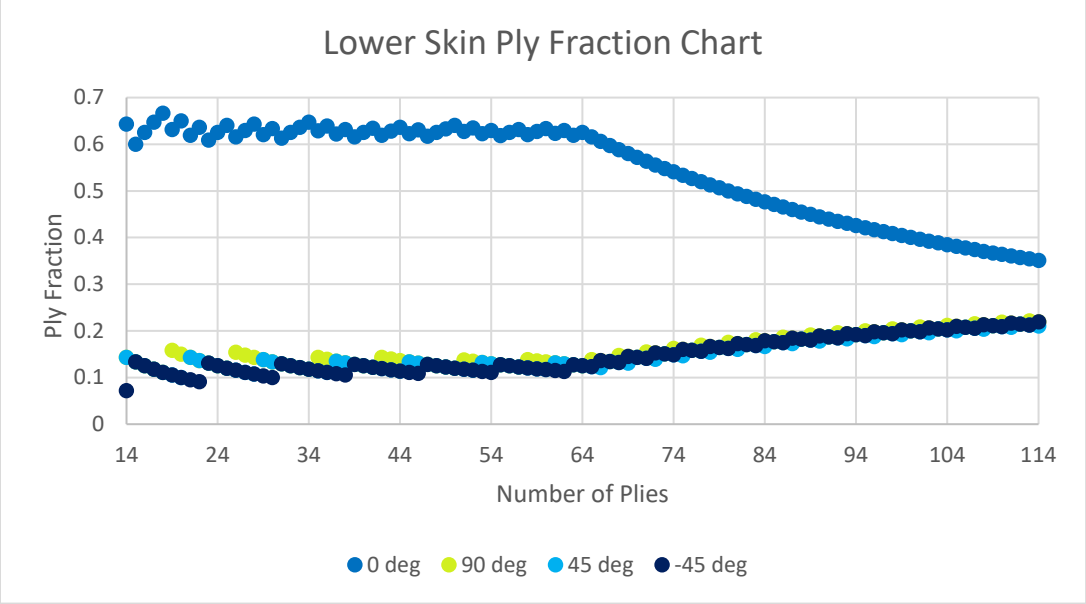

Figure 4.9. Lower skin ply fraction chart.

Ribs were designed with upper and lower flanges to fasten to skins and leading and trailing edge flanges to fasten to spar webs. The flanges ended before the rib corners to avoid the spar caps. Ribs in the root area included a pass-thru hole for internal instrumentation wiring. A typical rib geometry is depicted in Figure 4.10. Ribs were fabricated with IM7/8552 plain weave carbon fiber, with fibers oriented in the 0°/90° directions.

Ribs 55 and 56, near the tip, omitted the leading and trailing edge flanges due to spar height constraints, and Rib 57, the tip closeout rib was machined from aluminum. Additionally, Ribs 5-7 were located at the wing kink and terminated at Rib 4 rather than the trailing edge, as shown in Figure 4.11.

The trailing edge flanges of Ribs 3 and 4 were fabricated as an aluminum fixture to handle the high loads due to the kink and local reaction forces due to the adjacent pin. These fixtures are shown in Figure 4.12 and Figure 4.13. Additionally, a 7” long, 1” x 1” angle, 3/16” thick, was added to the lower, trailing edge corner of Rib 2 to improve local buckling margin.

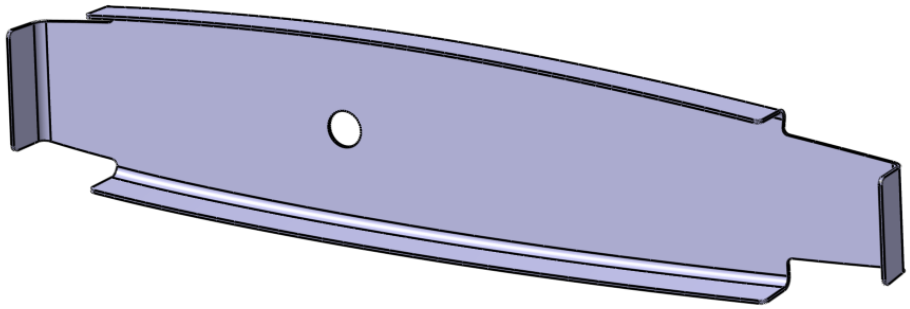

Figure 4.10. Typical rib with instrumentation pass-thru hole.

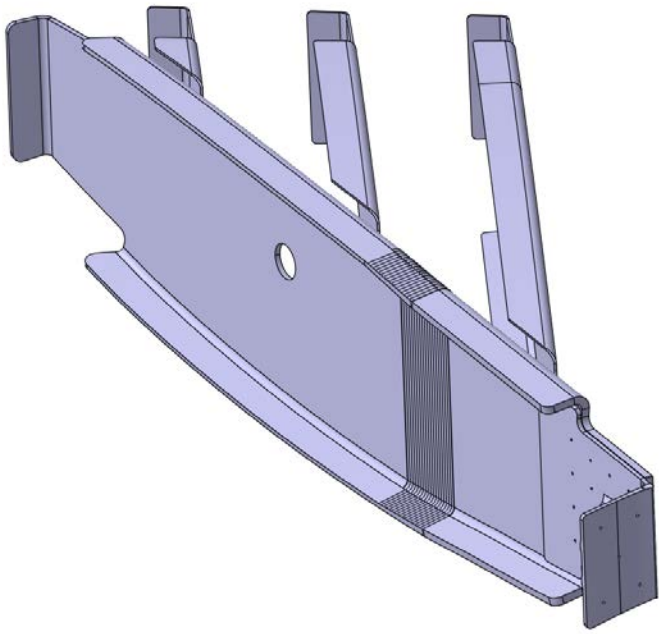

Figure 4.11. Ribs 4-7. Ribs 5-7 terminate at Rib 4 rather than the trailing edge spar due to the wing kink.

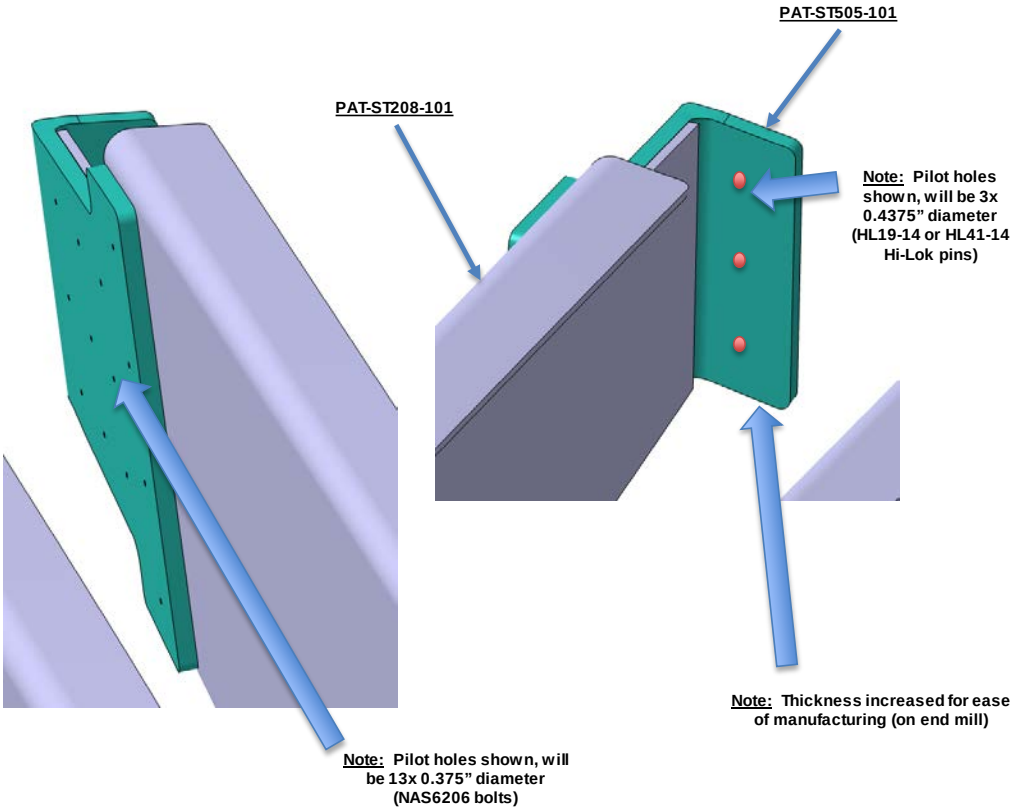

Figure 4.12. Rib 3 trailing edge fitting.

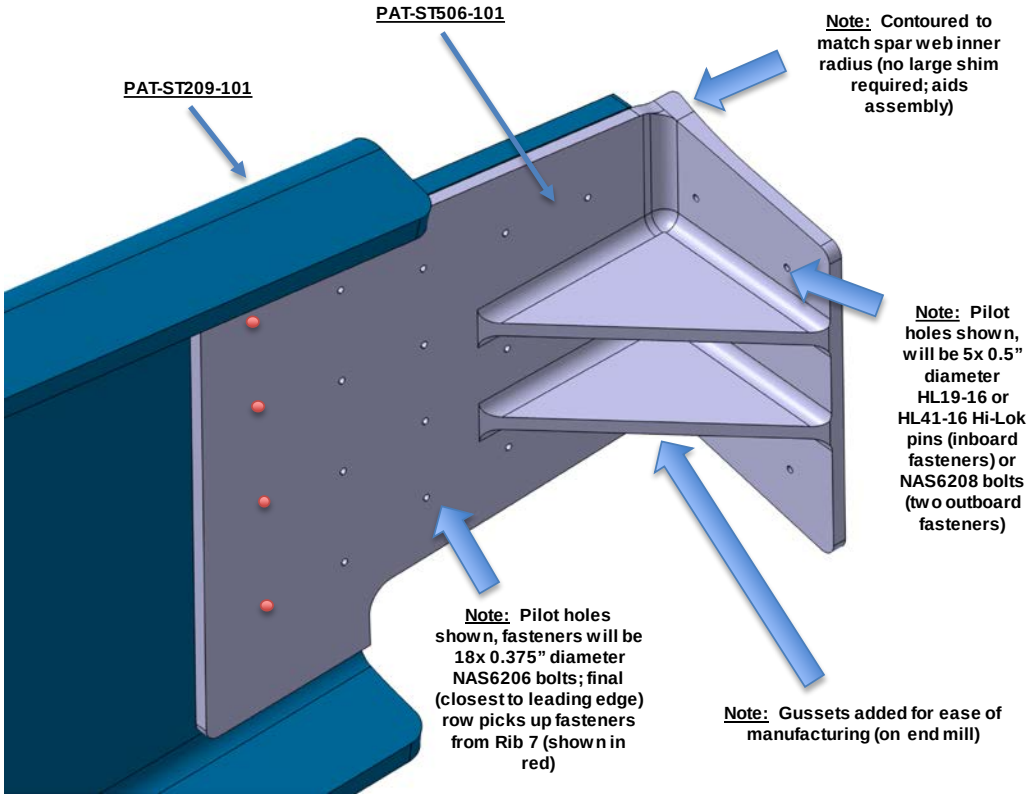

Figure 4.13. Rib 4 trailing edge fitting.

5 Test Article Fabrication

During fabrication and assembly, further modifications were required to address defects and discrepancies from design. Each of these modifications went through a thorough manufacturing review board (MRB) process to ensure that the proposed correction maintained the structural integrity of the test article and would not adversely affect test results. An overview is provided here, with additional MRB documentation available for each case.

Nondestructive Inspection (NDI) Results & Repairs

Each composite part underwent ultrasonic nondestructive inspection to check for defects such as porosity and delamination. Ribs and spars utilized a hand-held ‘A-scan’ pulse echo technique, while the skins utilized an automated ‘C-scan’ through-transmission technique.

Rib 0 exhibited small wrinkles on the lower rib cap, but no ultrasonic indications were found so the rib was dispositioned ‘use as is’. Ribs 13, 32, 37, 40, 41, 42, 43, 44, 50, 51, 52, 54, and 56 exhibited NDI indications showing delamination at the spar flange. A residual strength calculation was conducted as part of the MRB process, and rivets were installed interior to the defects to prevent propagation. Details of the defect and repair are available in Attachment 1. It is noted that Rib 49, although listed as ‘repaired’ in the defect and disposition report, was subsequently remade.

Three indications were reported on the trailing edge spar. The first indication was located just above the outboard pin hole near the start of the cap radius. The location corresponds to the edge of the cocured sacrificial plies and appeared to be porosity associated with the nonstructural plies. This indication was dispositioned as “use as is”. The second indication was located on the top cap edge, between Rib 36 and 37. The indication mapped an area approximately 2.25 in. x 0.55 in. and was determined to be a delamination. Residual strength calculations indicated sufficient strength in both the spar and skin. A resin draw was performed to infuse resin into the delamination, and four NAS1921-04 fasteners were installed through the spar cap to ensure the delamination remained closed. The third indication was found on the bottom cap edge near Rib 10, measured 0.25” x 0.24”, which was less than the open-hole allowable. The area was treated with an edge sealant and used as is. Additional details are available in Attachment 4.

The leading edge spar had several NDI indications, as documented in Attachment 2. The most concerning defects were located in the outboard 11 ft. of the spar. Rather than repairing these defects, the outboard 11.3 ft. of the LE spar was removed and an aluminum spar section was spliced in. The aluminum spar was sized to be substantially equivalent to the composite section it replaced, replicating both form and function to the extent possible. The total effect on tip deflection was estimated to be a 0.7 in. decrease. The aluminum section was spliced utilizing a double-shear configuration, which utilized steel cap straps on the inside of the wing and the skins as the outer splice member. Aluminum splice plates were utilized to splice the aluminum web to the carbon web. A view of the complete splice joint is shown in Figure 5.1. No changes were made to the design as provided to NASA in CAD format November 15, 2017. Many of the NDI

indications in the root section corresponded to visible wrinkles on the web-to-cap radii, as shown in Figure 5.2 (note that the machined sacrificial plies are also visible on the spar web). Radius wrinkles and remaining NDI indications were dispositioned “use as is”.

The nonstructural web shim (sacrificial plies) partially disbonded at the secondary bond line around both pin holes as shown in Figure 5.3. An attempt to repair the delamination by infusing resin was performed but subsequently disbonded during assembly, however, since the shim was considered nonstructural, no impact to flexural behavior was expected. This delamination may have further propagated during the +2.5G static loads test.

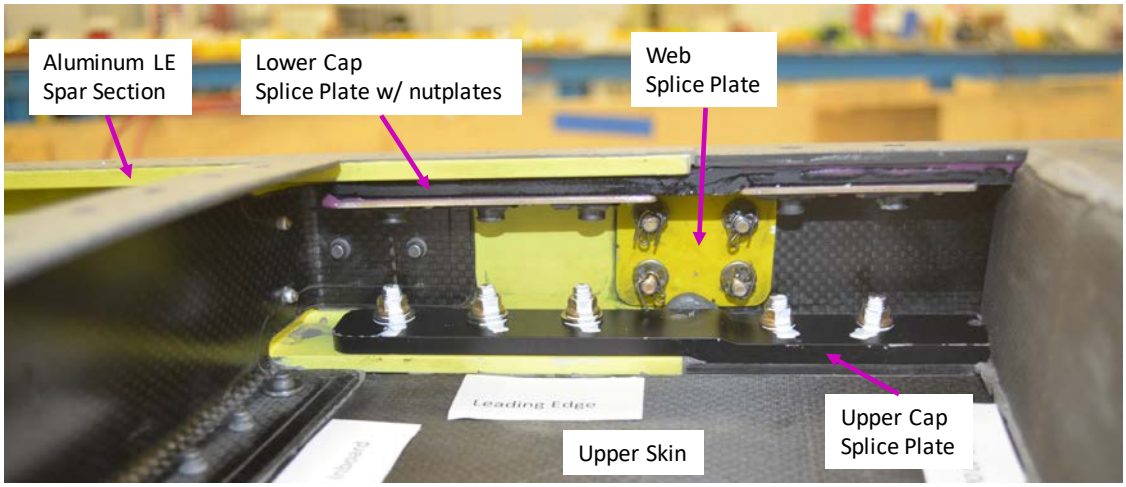

Figure 5.1. Leading edge spar splice joint.

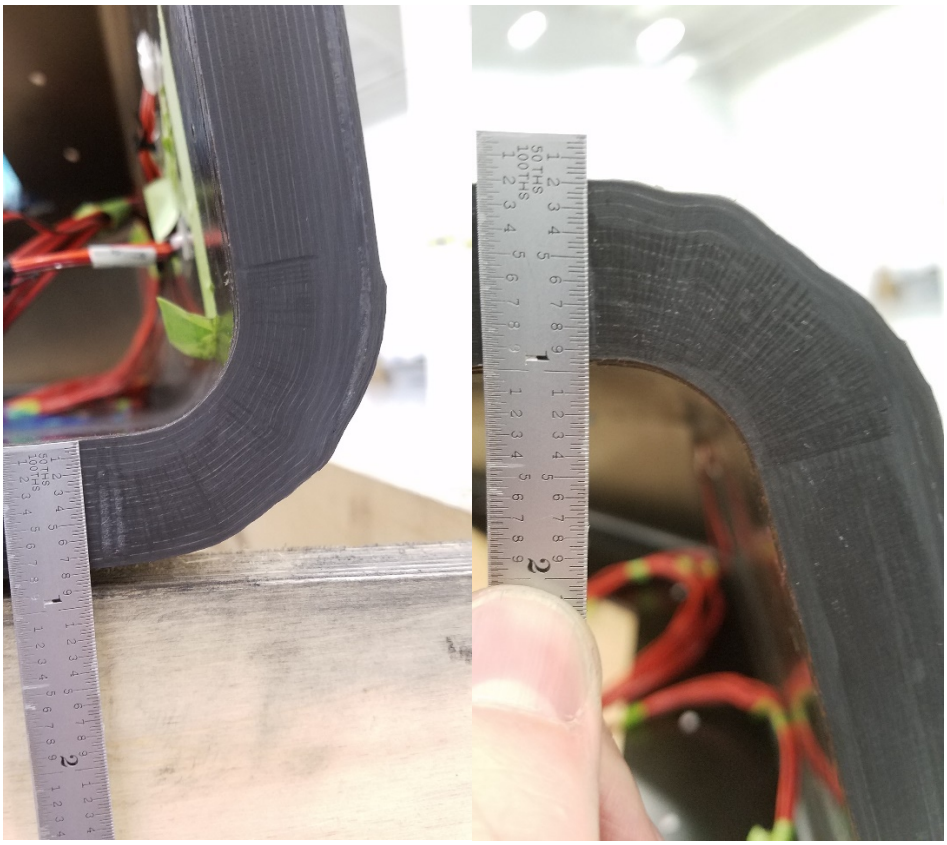

Figure 5.2. Leading edge spar view of root: upper radius (left) and lower radius (right).

Figure 5.3. Leading edge spar web sacrificial ply delamination (left) and attempted repair (right). The repair delaminated during assembly but shim was deemed to be nonstructural.

Assembly Nonconformances & Corrections

During assembly, skins were match-drilled to the spar caps and rib webs prior to final installation. During the match drilling process, excessive drill plunge resulted in damage to the webs of several ribs. Each of these locations was reviewed and dispositioned for repair or replacement. In most areas, repairs consisted of blending out the damage heightwise by adding a notch and radius, or by blending the defect out from the thickness of the part, as in a scarf repair, both of which are depicted in Figure 5.4. By blending out the defect, stress concentrations were significantly reduced. For ribs where a simple blend of the rib web would not result in sufficient residual strength, a reinforcement clip was installed on the outboard side of the rib web, as shown in Figure 5.5. The reinforcement clip was bonded to both the rib web and spar web and both the clip itself and the bond areas were sized to transfer the full flange loads.

Two additional repair techniques were utilized in the root section. An aluminum doubler plate was installed on the Rib 4 leading edge web to provide reinforcement after the defect was notch-blended height-wise. At the Rib 2 leading edge, upper edge of the web, a 1” x 1” x 3/8” aluminum angle was installed to preserve buckling stability, similar to the reinforcement added to the same rib on the lower, trailing edge corner.

Additional discrepancies addressed during assembly included a grind mark on the center of Rib 8, which was blended out thicknesswise, obsolete skin holes near Rib 35 due to a local repitching of fastener locations to improve bearing strength and at the LE carbon/aluminum splice joint, which were filled, and a minor modification to the fastener pattern utilized on the upper ‘bathtub’ fitting at Load Station 7B. All noncomformances are addressed in further detail, including analysis justification and repair disposition, in Attachment 3.

The leading edge flanges of ribs 42-47 were misdrilled as a result of the leading edge spar shifting during assembly. Each of these rib flanges was repaired with a bonded aluminum doubler and reinstalled per design specifications. Additional details are available in Attachment 5.

Geometric Nonconformances & Corrections

Both leading and trailing edge spars experienced springback during the postcure cycle, resulting in larger than desired distance between the spar caps, primarily toward the root, which would result in a significant misalignment of the skins. To correct this condition, a detailed analysis was performed to confirm that material could be safely removed from the spar caps without jeopardizing structural integrity or significantly affecting wing behavior. Ultimately, the spar caps were sanded to bring the profile back within acceptable tolerances. The reduction in cap thickness was accounted for test correlation FEMs as discussed in Section 6.

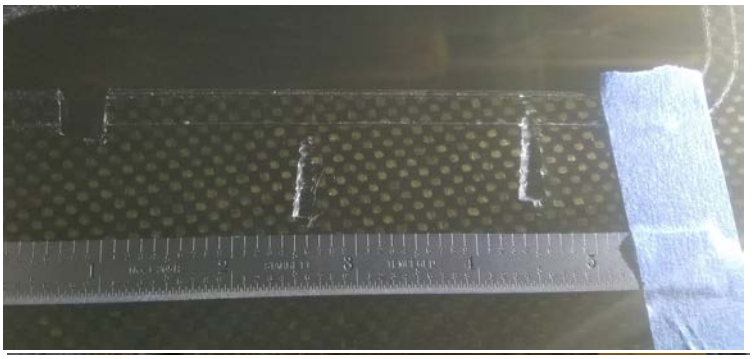

a) Defect.

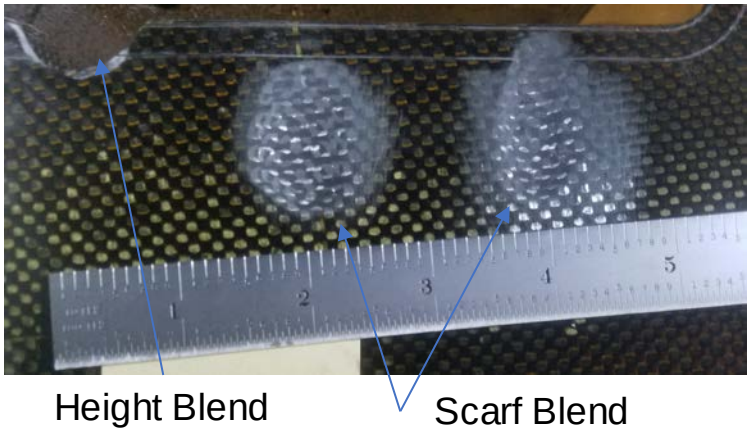

b) Repaired.

Figure 5.4. Typical rib defect and repair.

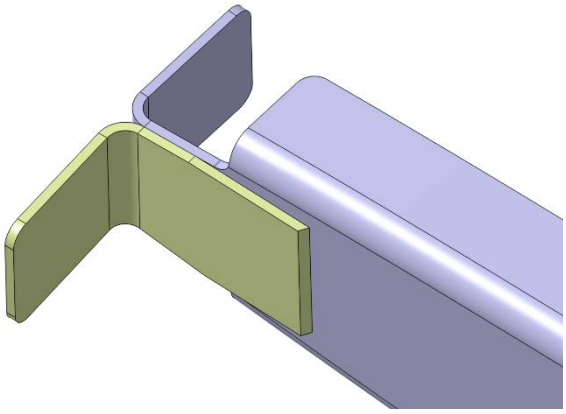

Figure 5.5. Rib reinforcement clip.

After assembly was complete, small ripples were observed on the lower skin in rib bays 36-40, with consistent periodicity and orientation, as well as the leading edge between Ribs 12 and 16, as shown in Figure 5.6. While the ripples were not a structural concern, they were of unknown origin. The skin ripples were only detected after assembly and were not noted during part inspection. The skin tool was reinspected to confirm that the surface was smooth. One speculation as to their origin was that they were a result of

residual stresses being relieved during part trim and/or fastener hole upsizing. The ripples were not a structural concern and were not expected to affect the structural response.

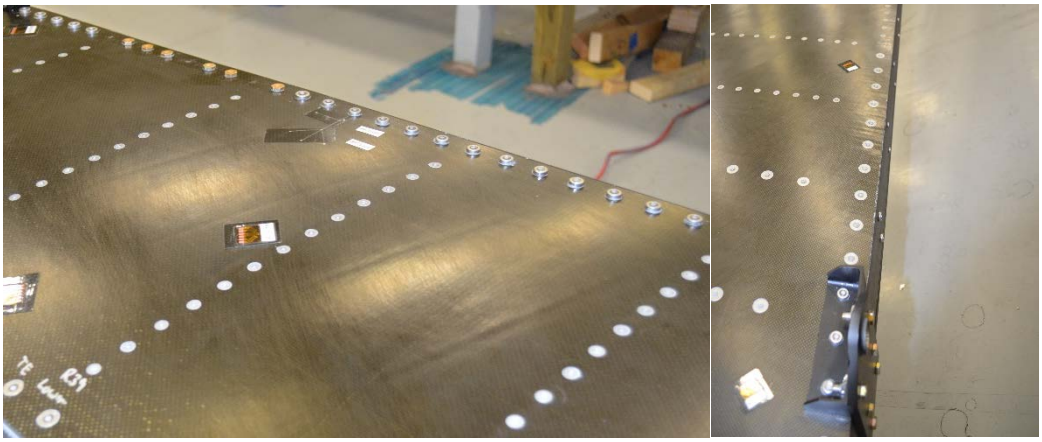

Figure 5.6. Lower skin ripples.

The primary geometric nonconformance that was expected to affect the structural response of the wing was a thicker than designed liquid shim between the skins and spar and rib caps. The increased shim thickness resulted in an overall increase in wing height, which was expected to result in increased wing stiffness. The skins were profiled by laser measurement in a two-step process: the wing was first placed in the upper skin assembly cradle and the lower skin was profiled. The wing was then flipped into the lower skin assembly cradle, the laser measurement system realigned to the wing, and the upper skin was profiled. The resulting profiles were used to update the FEM, as discussed in the next section.

Fasteners

A small variety of fasteners were utilized depending on the local strength and sizing requirements, access, and availability. In most outboard areas, flush head fasteners such as the NAS1921 or MS21140 were utilized, which allow for a blind installation. Protruding head fasteners such as MS21141 or NAS1919 were also utilized, primarily in spar to rib connections, root (nonaerodynamic) skin areas, load reinforcement fittings, or areas where installing a countersunk fastener would be problematic, due to limited skin thickness, which would result in a near knife-edge condition, for example. In some areas, including the root skin-to-spar interface, NAS6200-series bolts were utilized for strength. The bolts were secured using nutplates, which had been attached to an aluminum sheet and subsequently bonded to the interior of the spars, as shown in Figure 5.7. The full interface control model of all fastener types and locations is available in the “PAT-ST200-902” model.

Figure 5.7. Nutplate carrier assembled (left) and installed (right).

Weight

The total shipment weight of the test article, inclusive of the steel reaction plates as well as temporary braces installed to stabilize the plates for shipping and handling, was 2,760 lb. A detailed mass breakdown by part is available in Attachment 6.

6 Finite Element Model

The finite element model used for test prediction and correlation purposes was based on the NASA-provided mesh, which modeled the test article as well as the AFRC fixtures and reaction table as shown in Figure 6.1. As shown in Figure 6.2, constraints were applied to the bottom of the AFRC reaction table where it is pinned into the test fixture pedestal. Fasteners were modeled discretely, utilizing CFAST elements with a nominal stiffness of $1x10^6$. The FEM also included the leading edge spar aluminum spar section, including the cap and web splice plates, as shown in Figure 6.5. Skin tow-steering was modeled using PCOMP properties with homogenized material properties based on the skin ply fraction. Unique material orientations were assigned to each element to account for the spatially varying tow-steering paths.

Typical FEM meshing of the test article is shown in Figure 6.3. Rib flanges were modeled as shell elements and connected to spars and skins via CFAST elements. Instrumentation pass-through cutouts were included in rib webs. Loads were applied via RBE3 elements and the load plate mass was modeled via a point mass.

Figure 6.1. Test article finite element model.

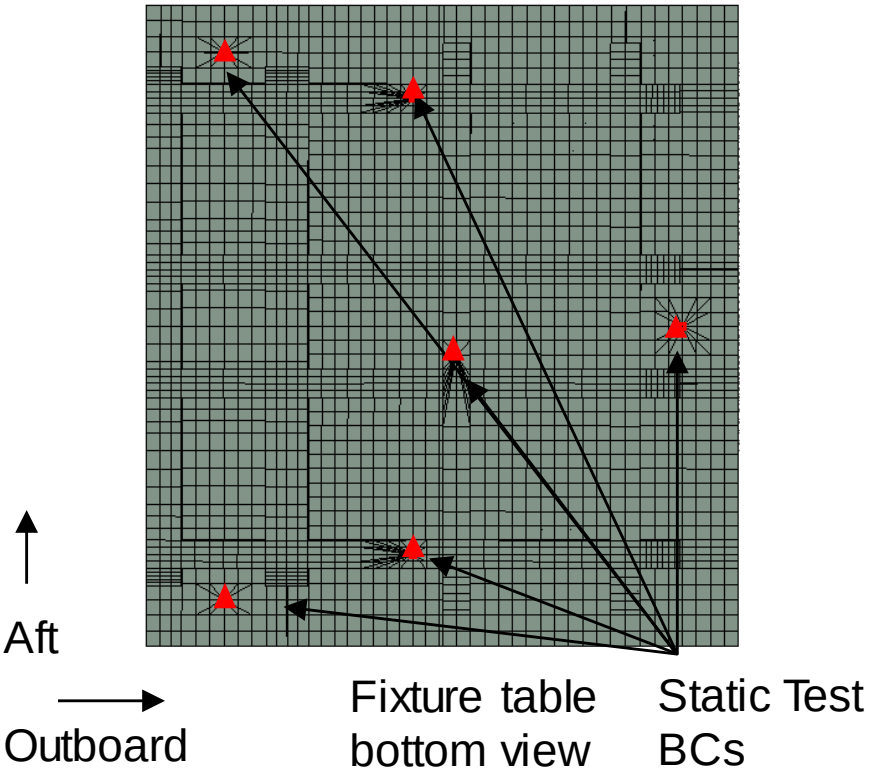

Figure 6.2. AFRC reaction table boundary conditions locations (bottom view).

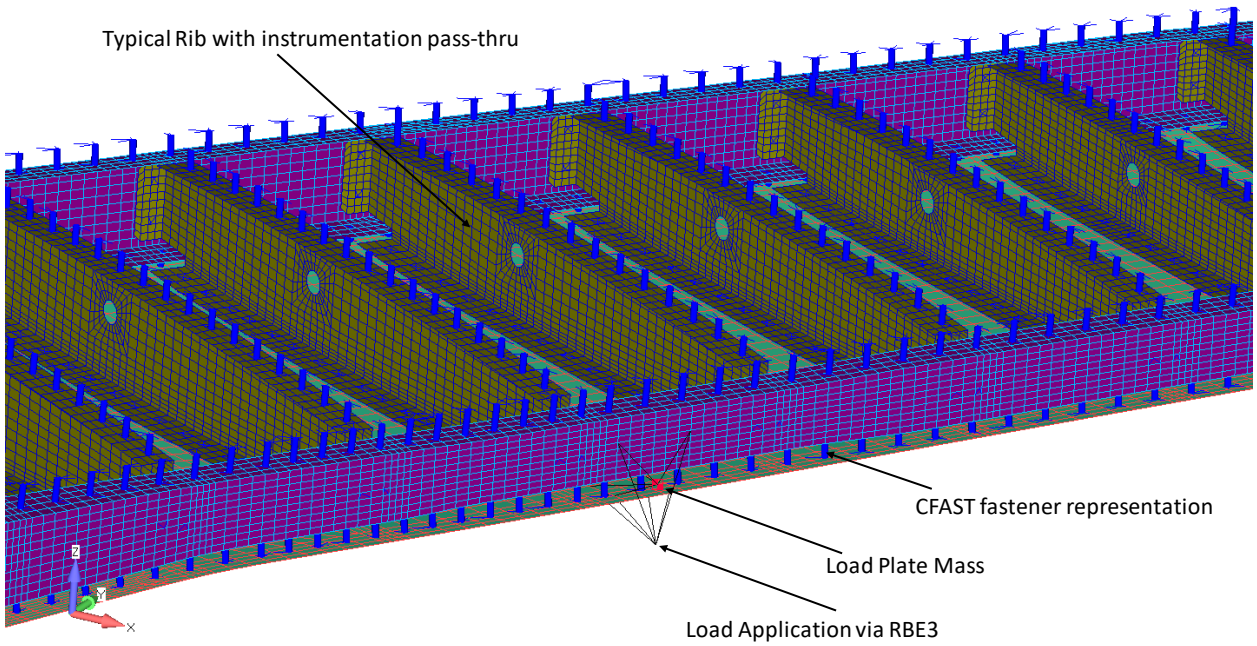

Figure 6.3. Typical FEM construction, showing lower skin, leading and trailing edge spars and ribs connected via CFAST elements.

Aurora subsequently modified the FEM to conform to the test article as fabricated. In particular, the following adjustments were implemented:

- Spar cap thicknesses were reduced to reflect the spar springback correction (see Figure 6.4)
- Offsets were applied to skin elements to reflect the skin height due to thicker liquid shims. Contour plots of the skin offsets are depicted in Figure 6.6.
- The Rib 4 leading edge doubler, and Rib 3 and Rib 4 trailing edge flange fixtures were added
- Reaction plate thicknesses were updated to match as-machined thicknesses
- Nonstructural masses (both point masses and regions) were added to account for masses not specifically modeled (e.g., pins, load plate masses) or to update part masses to as-measured values.
- Rotational stiffness was added to fasteners to account for joint stability in nonlinear and buckling analyses

Additional details are available in Appendix H. This configuration is referred to as the 'with skin offset' FEM and most accurately reflects the mass and geometric properties of the as-built test article. A second model is also utilized for test correlation, which is referred to as the 'no skin offset' model. The sole difference is that the 'no skin offset' model does not include the skin offsets to account for liquid shim thickness.

It is also noted that the FEMs used for correlation in this report were based on a linear analysis unless otherwise noted. The total resultant test loads were applied vertically (parallel to the Z-axis) to best replicate the resulting bending and twist moment distributions, consistent with those shown in Figure 4.1 and Figure 4.2.

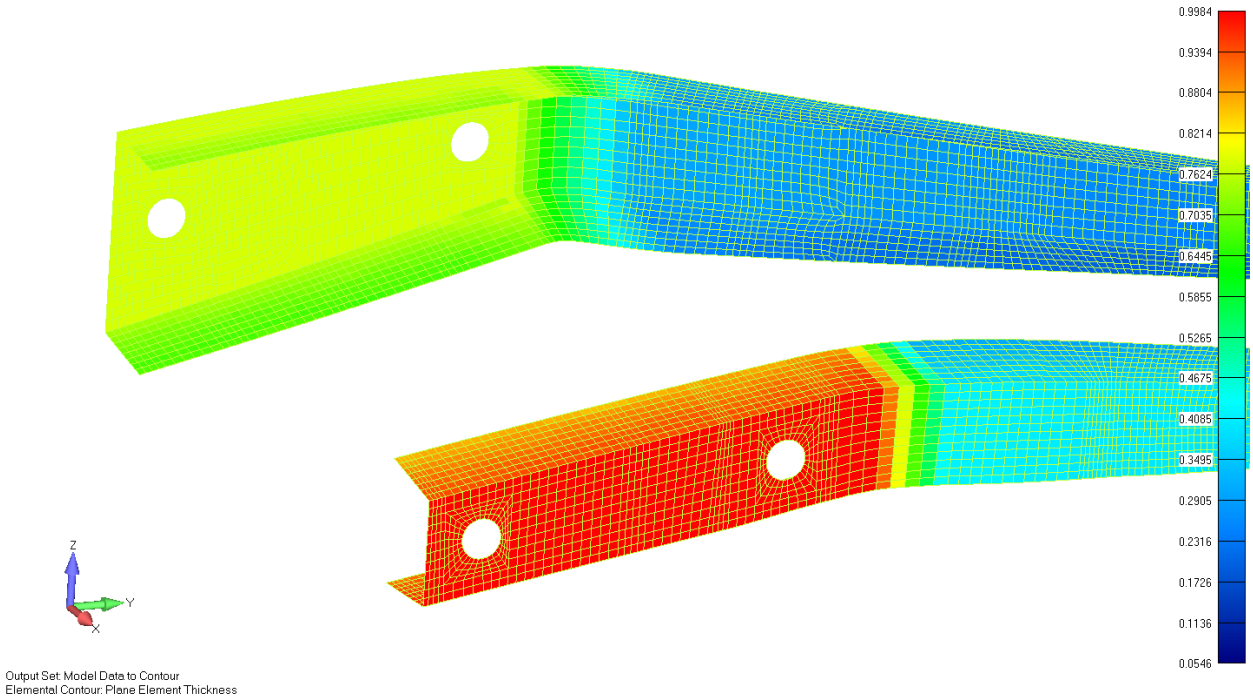

Figure 6.4. Root sections of spars, showing shell representation of caps with thickness grading due to removed material to correct for cap springback.

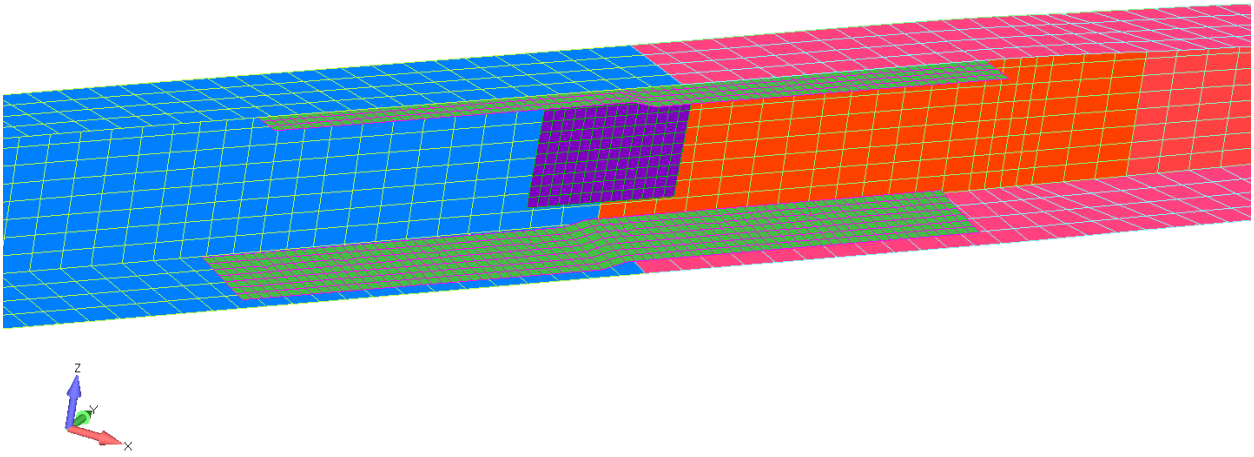

Figure 6.5. Leading Edge spar splice joint. Steel splice plates are utilized to splice the spar caps; aluminum splice plates are used on the interior (shown) and exterior (not visible) to splice the spar webs. (fasteners not shown).

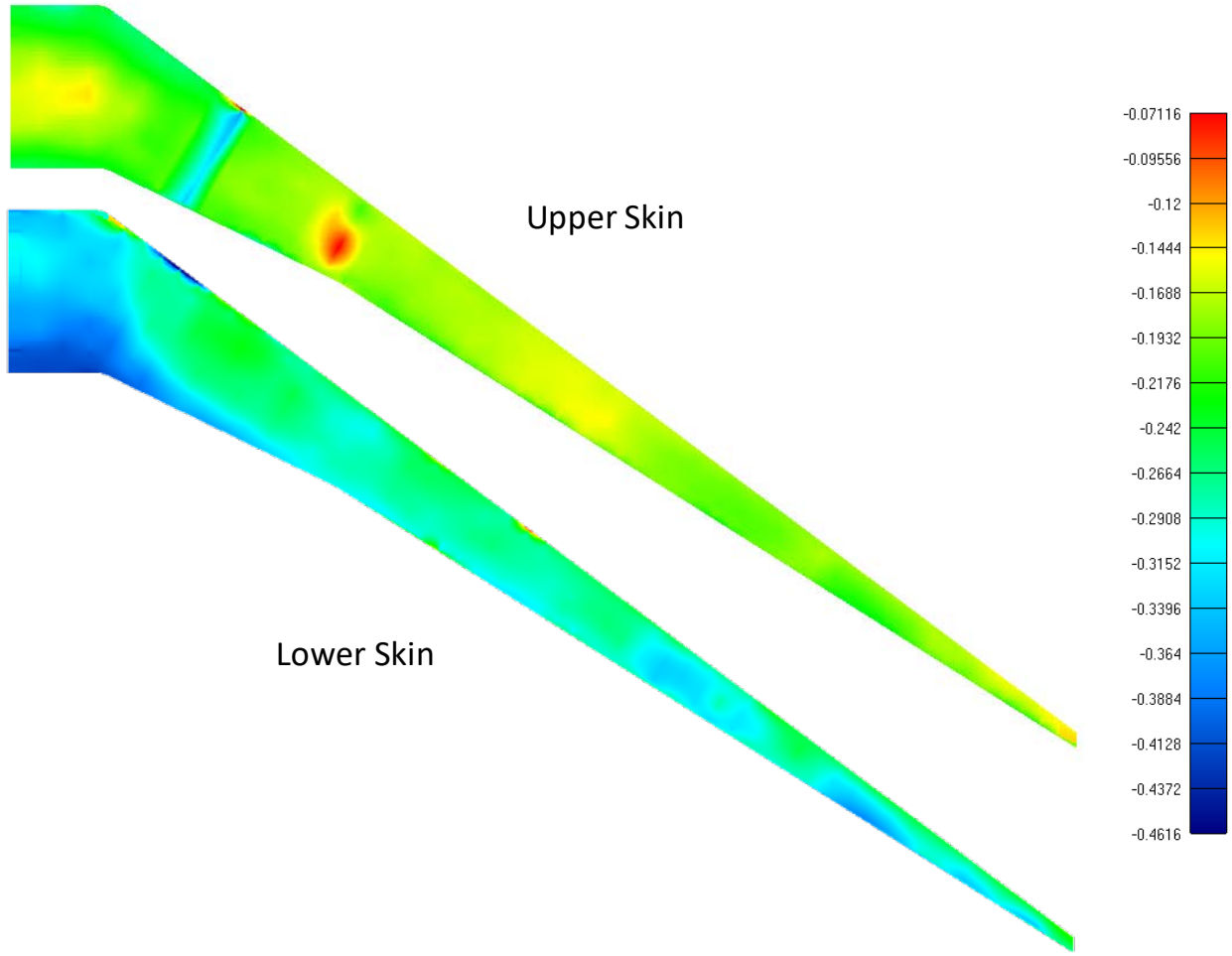

Figure 6.6. Skin offsets applied to 'with skin offset' FEM accounting for increased liquid shim thickness.

6.1 Note on Principal Axes vs. Fiber Direction Correlation

It is noted that fiber direction in general is not expected to have a strong correlation to the principal strain direction due to the optimizer primarily sizing the skins for buckling (a stress-based criteria) and a fundamental difference in the principal stress and strain angles for anisotropic materials. The degree to which the principal strain angle varies from the principal stress angle is dependent on both the degree of anisotropy of the material as well as the local loading profile. It is further observed from the laminate failure and buckling constraint variable contours provided in the lower left of Figure 3.16 that the buckling constraint is generally active rather than the laminate failure constraint. As a result, the optimizer will generally orient the fiber direction with the principal stress axis (rather than the principal strain axis) for structural optimization, with the caveat that the optimized fiber direction may also be influenced by manufacturing constraints or compromises due to multiple load cases or passive load alleviation.

For anisotropic materials, principal strain and principal stress axes generally differ. The discrepancy between principal stress angle and principal strain angle becomes apparent by expressing strains in terms of the applied stress, substituting those terms into the principal strain angle formula (Eq. 7) and comparing to the principal stress angle formula (Eq. 8).

$$\boldsymbol{tan\,2\theta_{\varepsilon 1}} = \frac{\boldsymbol{\gamma_{xy}}}{\boldsymbol{\varepsilon_x - \varepsilon_y}} \tag{7}$$

$$\boldsymbol{tan\,2\theta_{\sigma 1}} = \frac{\boldsymbol{2\tau_{xy}}}{\boldsymbol{\sigma_x - \sigma_y}} \tag{8}$$

To express strain in terms of the applied stress, the classical lamination theory $[ABD]$ matrix is inverted as: $[abd] = [ABD]^{-1}/t$, where the thickness, t, is used to express the applied load as a stress rather than as a traction. Considering the case of plane stress, strain can be expressed in terms of applied stress and the $[a]$ matrix as:

$$\begin{bmatrix} \epsilon_x \\ \epsilon_y \\ \gamma_{xy} \end{bmatrix} = \begin{bmatrix} a_{11} & a_{12} & a_{13} \\ a_{12} & a_{22} & a_{23} \\ a_{13} & a_{23} & a_{33} \end{bmatrix} \begin{bmatrix} \sigma_x \\ \sigma_y \\ \tau_{xy} \end{bmatrix}, \tag{9}$$

Combining Eqs. 8 and 9 yields:

$$\boldsymbol{tan\,2\theta_{\varepsilon 1}} = \frac{\boldsymbol{a_{13}\sigma_x + a_{23}\sigma_y + a_{33}\tau_{xy}}}{\boldsymbol{(a_{11}-a_{12})\sigma_x - (a_{22}-a_{12})\sigma_y + (a_{13}-a_{23})\tau_{xy}}}, \tag{10}$$

which in comparison to Eq. 7, shows that the principal strain angle is generally not equivalent to the principal stress angle. It is noted that for the special case of an isotropic material system, for which entries of the $[\boldsymbol{a}]$ matrix can be expressed as $\boldsymbol{a_{11} = a_{22} = \frac{1}{E}}$; $\boldsymbol{a_{33} = \frac{1+\nu}{E}}$; $\boldsymbol{a_{12} = \frac{-\nu}{E}}$; and $\boldsymbol{a_{13} = a_{23} = 0}$, the right hand side of Eq. 10 does become identical to that of Eq. 7, showing equivalency of principal strain angle and principal stress angle for isotropic materials.

To illustrate this point, Figure 6.7 compares the resulting principal strain angle of three different laminates as a result of applying a uniaxial principal tensile stress ($\sigma_2 = 0$) oriented at principal stress angles from 0° to 90°, using lamina properties representative of the PAT test article skins (E1 = 17.1 msi, E2 = 1.4 msi, G12 = 0.7 msi, and v12 = 0.04) Equation 10 is used to calculate the principal strain angle from the applied principal stress state and laminate $[a]$ matrix per the stress and strain axes conventions depicted in Figure *6.8*. As expected, the principal strain angle of the quasi-isotropic laminate correlates exactly to the applied stress angle; however, the principal strain angles of nonisotropic materials begin to deviate quickly from the applied stress angle. For the ply fraction utilized for the test article, a 5° principal stress angle would result in a 13.6° principal strain angle. In the limit case of a unidirectional laminate, the same 5° applied principal stress results in a 33° principal strain!

Figure 6.9 further illustrates the sensitivity of combined loading on principal strain angle for the PAT test article laminate, where the minor principal stress, σ_2, is allowed to vary from -100% to 100% of the major principal stress value (the case $\frac{\sigma_2}{\sigma_1} = 0$ is the uniaxial loading case for the PAT laminate depicted in Figure 6.7).

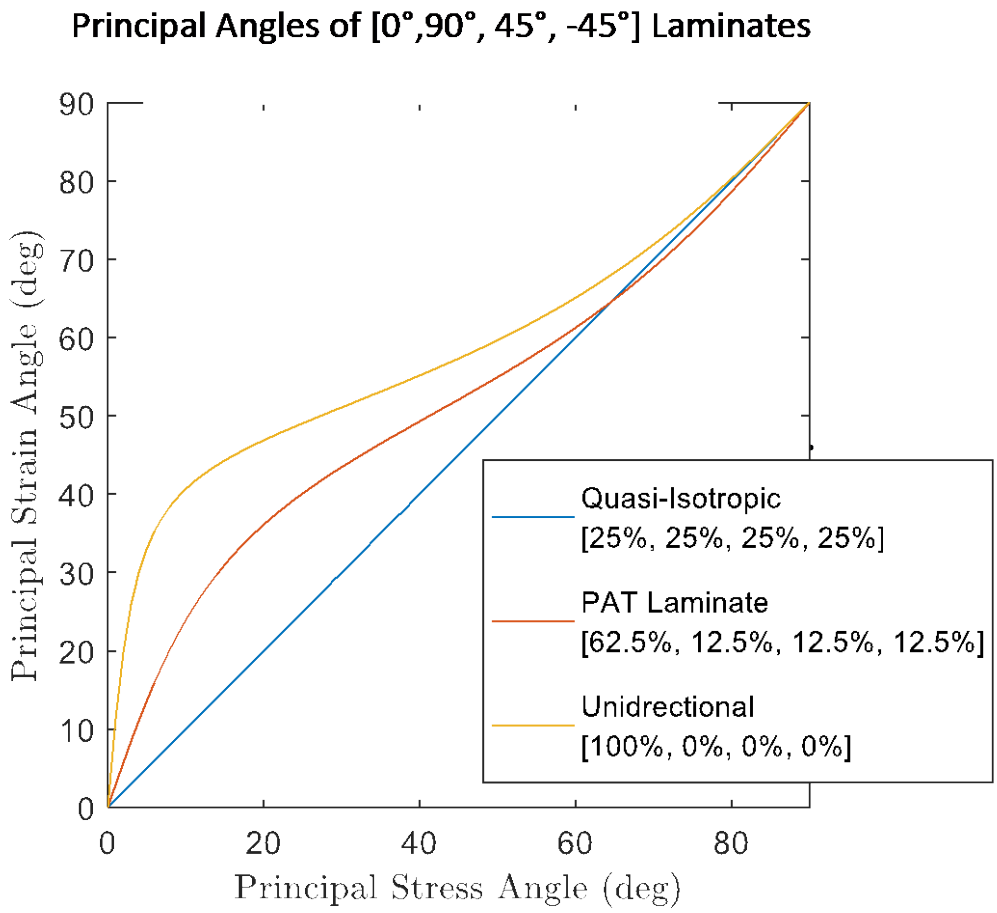

Figure 6.7. Principal strain angle vs principal stress angle to uniaxial loading.

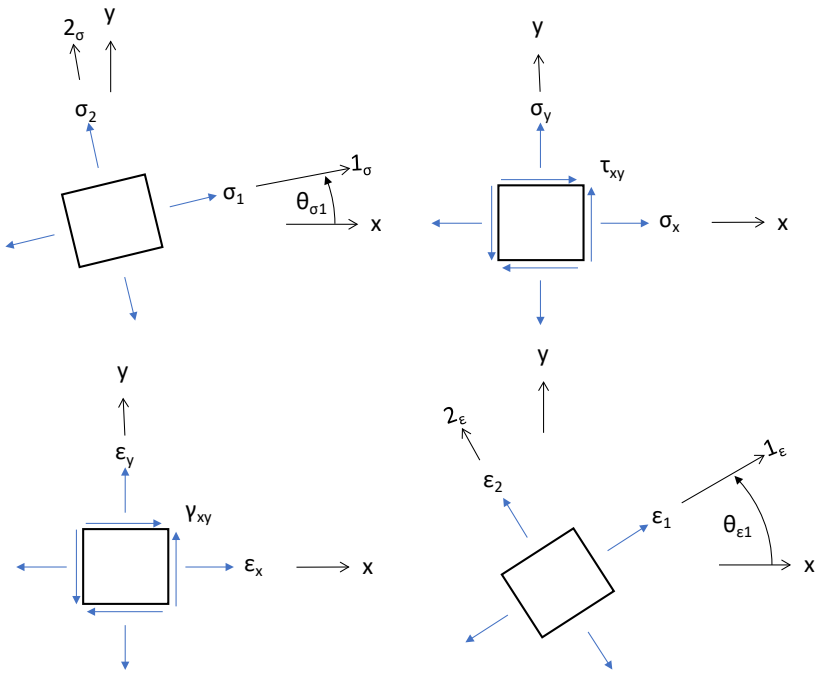

Figure** 6.8. **Stress and strain coordinate axes.

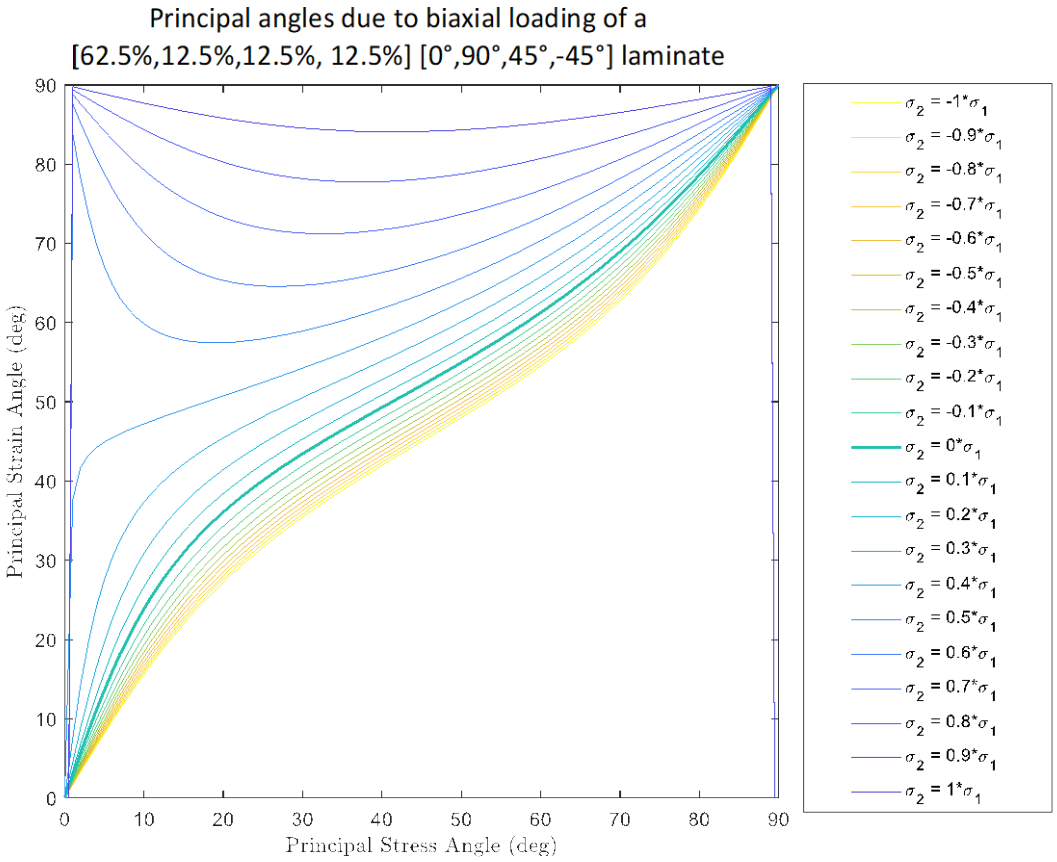

Figure 6.9. Principal strain angle vs principal stress angle due to combined loading.

Figure 6.10 and Figure 6.11 show a measure of correlation between the fiber steering angle and predicted principal stress and principal strain axes for the +2.5G and -1G load cases, respectively. The contour plots on the left are based on the test article full scale optimization ("uCRM_135_test_article_optimization" of Section 3.2.7) and the contour plots on the right are based on the "without shim offset" FEM described in the preceding section. The "without shim offset" FEM is utilized for these comparisons over the "with shim offset" FEM as it is expected to provide a closer correlation to the test article full scale optimization since it is geometrically closer to the optimized design. Contour plots are based on the vector dot-product of the unit steering vector with stress and strain principal vectors, normalized to unit length. A correlation value of 1.0 implies that the principal stress or strain axis is exactly aligned to the fiber axis; a correlation value of 0.71 correlates to a 45° difference in angle, and a value of 0 correlates to a 90° (orthogonal) angle. For each skin/load case, the dominating principal stress or strain was selected: for example, for the +2.5G load case, the minor principal strain (ε_2) and stress (σ_2) were selected, as the upper skin is primarily in compression and the principal axes are selected such that $\varepsilon_1 > \varepsilon_2$ and $\sigma_1 > \sigma_2$.

Areas of strong correlation between principal stress and fiber direction suggest that the optimizer is locally choosing to prioritize pure structural optimization by aligning the fiber direction with the principal loading direction. Areas of lower correlation (e.g., the outboard regions at approximately 2/3 span) suggest that the optimizer is prioritizing passive load alleviation, or, that the magnitude of the local stress is relatively low and not an active constraint. The low correlation of principal stress to fiber direction at the TE root is due to very low stress magnitudes locally. The local decrease in stress at the TE root is due to the boundary conditions utilized in the optimization FEM, combined with the root 'kink', which effectively 'shadows' this corner from bending-induced stress, as observed by the blue contours at the TE root for the optimization FEM.

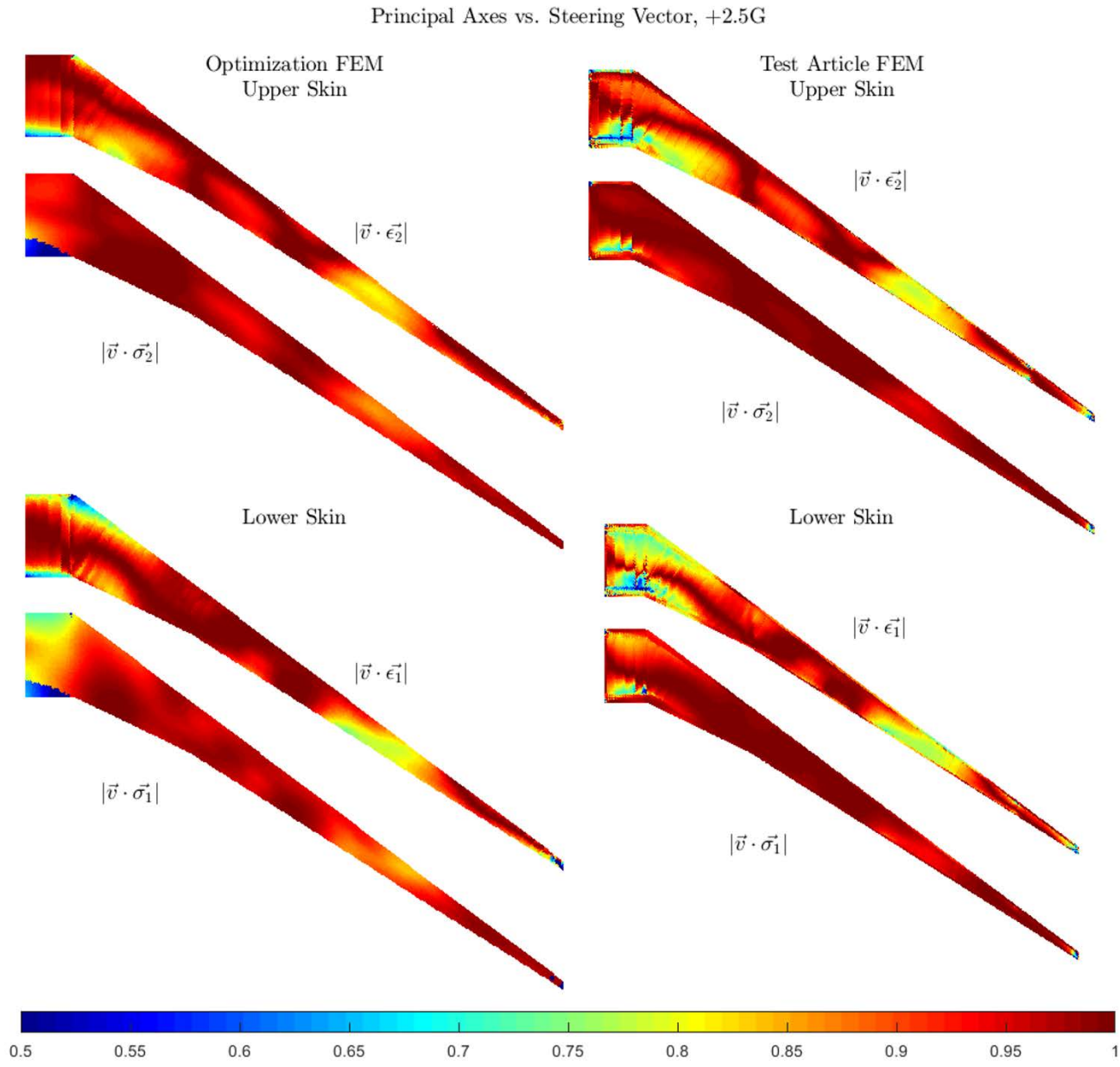

Figure 6.10. Correlation between fiber (tow-steering) direction and principal strain and principal stress axes for +2.5G load case.

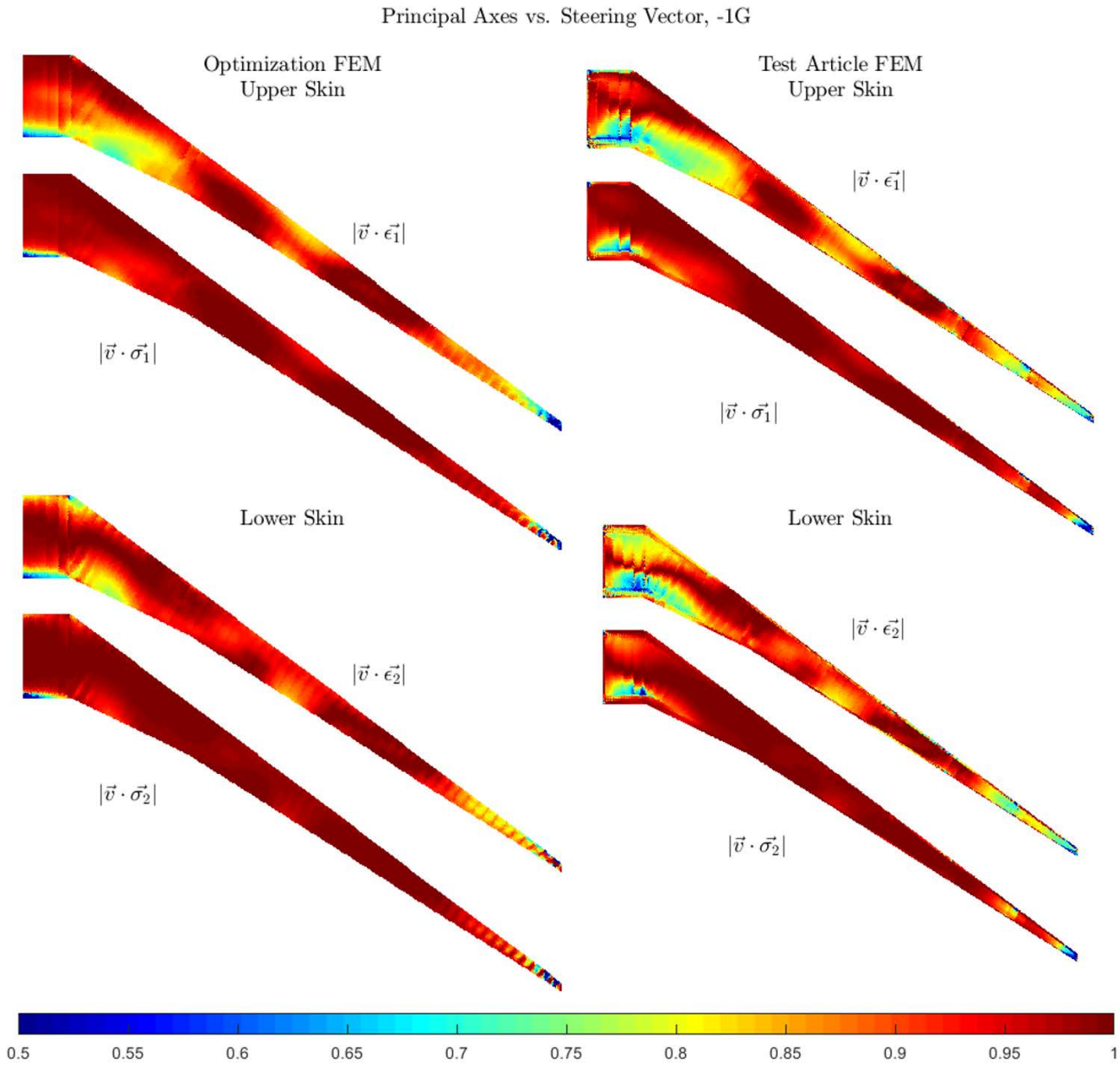

Figure 6.11. Correlation between fiber (tow-steering) direction and principal strain and principal stress axes for -1G load case.

7 Testing & Correlation

7.1 Ground Vibration Testing (GVT)

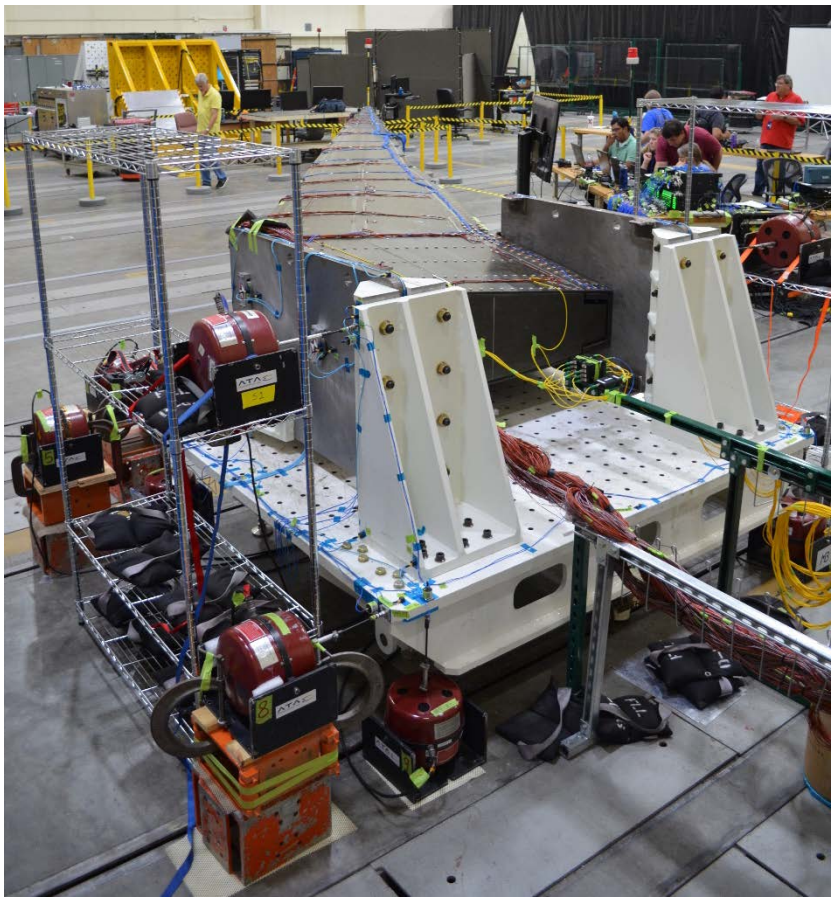

Figure 7.1. Test Article rigged for GVT (shakers at outboard, upper reaction plate corners not shown).

Low-amplitude ground vibration testing (GVT) was performed at AFRC FLL July 2018, as shown in Figure 7.1. The Fixed Base Correction [28] was utilized to mathematically constrain the desired boundary conditions using measured data, thus overcoming errors that would otherwise be attributed to compliant boundary conditions. The data used for correlation below are taken from the ATA-provided GVT test report, which are compiled from a combination of the "T15, Configuration 1" and "T16, Configuration 2" test data, which utilizes 14 shakers to excite the test article. The primary difference in the two configurations is that the wing tip shaker was oriented primarily horizontally for the T15 test, but was moved to a more vertical orientation for the T16 test and slightly higher shaker forces were utilized to better capture wing torsion. Data were collected via three-axis accelerometers bonded to the test article at the boundary conditions and along the span of the wing along the leading and trailing edges. Seismic-grade axial accelerometers were utilized at the shakers to provide the reference data for the fixed-base correction method.

For correlation purposes, the boundary conditions of the FEM were updated to correlate to the boundary conditions imposed as part of the fixed-base correction method. The resulting FEM constraints are depicted in Figure 7.2: the AFRC table triangular brackets that bolt to the load table are completely fixed. Since the BCs applied to the triangular brackets completely isolates the wing from the test table, additional constraints on the test table were not required. Additional constraints in the global-X direction were applied directly to the upper, outboard corner of the steel reaction plates to account for shakers and associated fixed-base corrections at those locations.

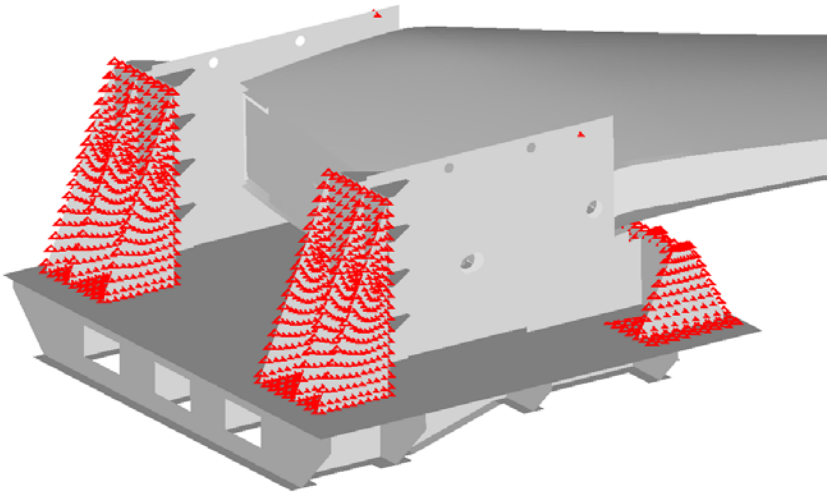

Figure 7.2. GVT prediction FEM boundary condition locations.

GVT frequency results for the first ten modes are compared to two FEM configurations in Table 13. The 'with skin offset' FEM configuration included offsets for skin elements to account for the as-built wing geometry and tends to correlate better to GVT test results than the 'no skin offset' FEM. The 'with skin offset' FEM predicted frequencies within 5.5% for the first ten mode shapes, while the 'no skin offset' FEM underpredicted the first, eighth, and tenth frequencies by more than 10% due to its increased compliance, particularly for the out-of-plane and bending modes. It is noted that in-plane bending is not significantly affected by the out-of-plane skin offsets, which is why these modes continue to correlate well with test data for the 'no skin offset' FEM.

Modal assurance criteria, which measures the degree of correlation between two mode shapes, is provided in Figure 7.3. As with the frequency data, the mode shapes of the 'with skin offset' FEM showed better correlation than the 'no skin offset' FEM, with the first six modes of the 'with skin offset' FEM showing a 97% correlation or better based on the modal assurance criteria (MAC), while the correlation drops to 88% and 83% for the 5th and 6th modes of the 'no skin offset' FEM. It is noted that torsion modes (modes 7 & 8) do show some signs that the torsion / bending behavior may begin to converge and/or swap between modes. It is interesting (but perhaps coincidental) to note that while the 'no skin offset' FEM continues to underpredict the frequency of modes 7 & 8 to a greater extent than the 'with skin offset' FEM, it does show slightly higher degree of mode shape correlation – 82% for the 'no skin offset' FEM vs 68% and 73% for the 'with skin offset' FEM, which outperformed in nearly all cases considered.

Table 13. GVT results comparison.

Mode	Test Freq (Hz)	'With skin offset' FEM (Hz)	Error	'No skin offset' FEM (Hz)	Error	Test Mode Shape
1	3.48	3.38	-2.93%	3.07	-11.60%	1st Bending
2	10.05	10.36	3.05%	9.32	-7.00%	2nd Bending
3	11.02	11.14	1.05%	11.08	1.49%	1st In-Plane Bending
4	21.22	22.37	5.42%	19.95	-5.56%	3rd Bending
5	30.15	30.91	2.52%	30.32	1.72%	2nd In-Plane Bending
6	35.23	36.86	4.62%	33.26	-4.74%	4th Bending
7	52.20	51.94	-0.50%	47.00	-9.69%	5th Bending with 1st Torsion
8	56.67	55.02	-2.92%	49.67	-11.97%	2nd Torsion with slight 5th Bending
9	59.08	61.58	4.23%	60.98	5.08%	3rd In-Plane Bending
10	77.40	76.03	-1.77%	68.87	-10.11%	6th Bending

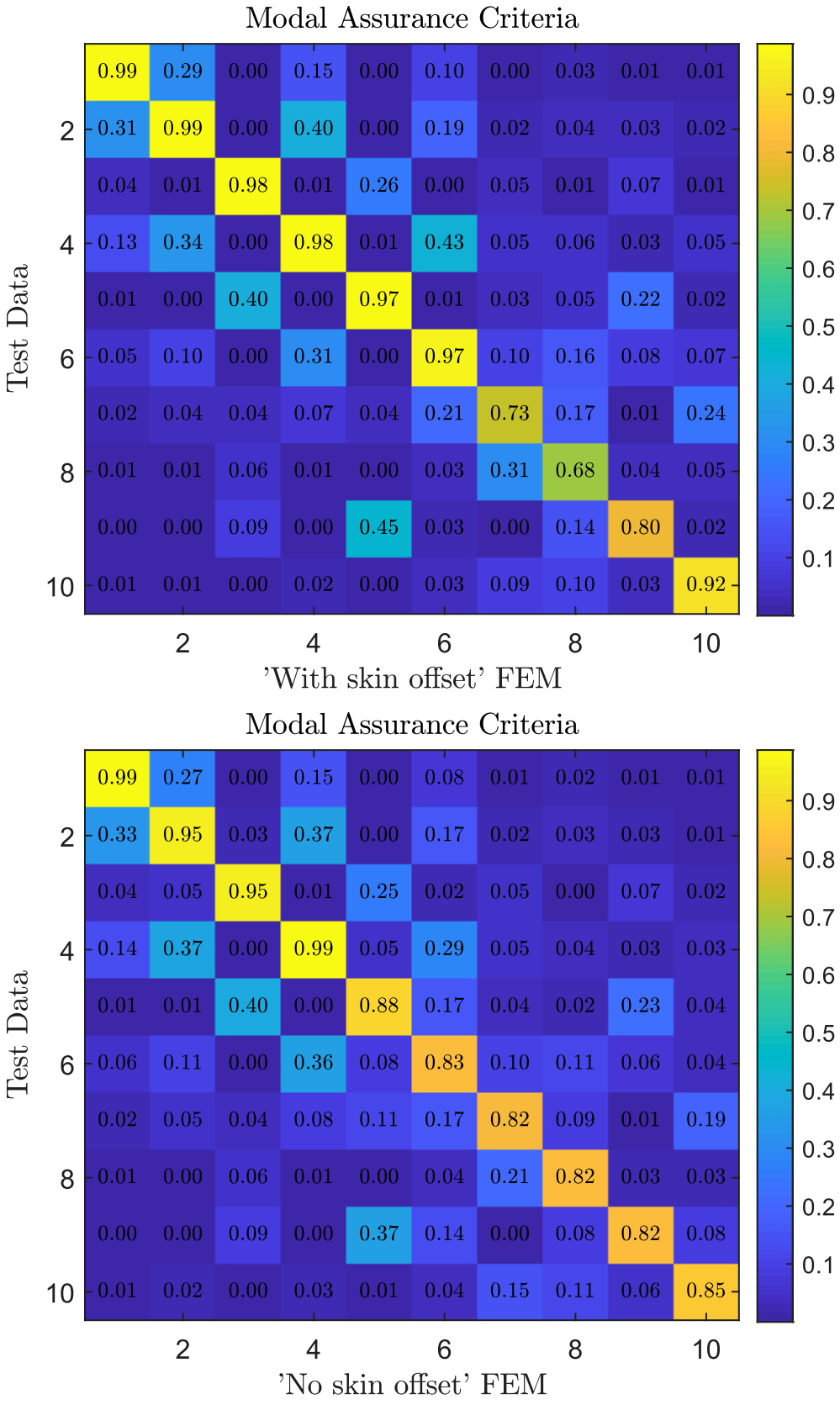

Figure 7.3. Modal assurance criteria comparisons for test data vs. FEM predictions for "With skin offset" FEM (top) and "no skin offset" FEM (bottom) configurations.

Mode shape comparisons between the test and predicted mode shapes are provided in Appendix D. It is noted that the test result mode shape shows a more predominant bending than torsion behavior in Mode 7, whereas Mode 8 appears to show a heavier component of torsion than bending; whereas FEM predictions show mode 7 & 8 to have blended torsion/bending behavior. Because the lower-order out-of-plane bending modes tend to correlate well to predictions, the larger participation of torsion in Mode 7 may suggest that the wing was either slightly more flexible in torsion relative to bending, or, that the torsional mass inertia was slightly greater than modeled relative to bending mass inertia.

7.2 Static Testing

7.2.1 Test Setup & Execution

Static testing was conducted by AFRC FLL in September 2018 for the -1G and flexural axes load cases, and October 2018 for the +2.5G test case. For static testing, the test article was mounted in the AFRC FLL self-reacting load fixture as shown in Figure 7.4. The reaction table was instrumented to measure the total reaction forces and moments. An overhead loading fixture with actuated pulley locations was provided to introduce true follower-forces to the three outboard load stations for the +2.5G test. Hydraulic actuators mounted to the floor beams of the self-reacting load fixture provided load at the four inboard load stations for the +2.5G test, and for all seven load stations for the -1G test. Loads for the +2.5G and -1G tests are provided in Table 14 and Table 15, respectively. Note that the Fx, Fy and Fz loads defined in Table 14 and Table 15 correspond to the load vectors in the designed 2.5G and -1G flight shapes, respectively.

Two flexural axis tests were conducted: a hydraulic flexural axis and a ‘shotbag’ test. The hydraulic flexural axis test utilized the outboard four load stations (a total of eight load application points: 4A-7A and 4B-7B) and independently applied the -1G load for each of those load locations, measuring the resulting wing response in each case. The ‘shotbag’ flexural axis test mounted a beam spanning to leading and trailing edge load points, which extended forward of the wing. A weight was hung from the beam and progressively moved forward, recording the resulting wing twist at each location.

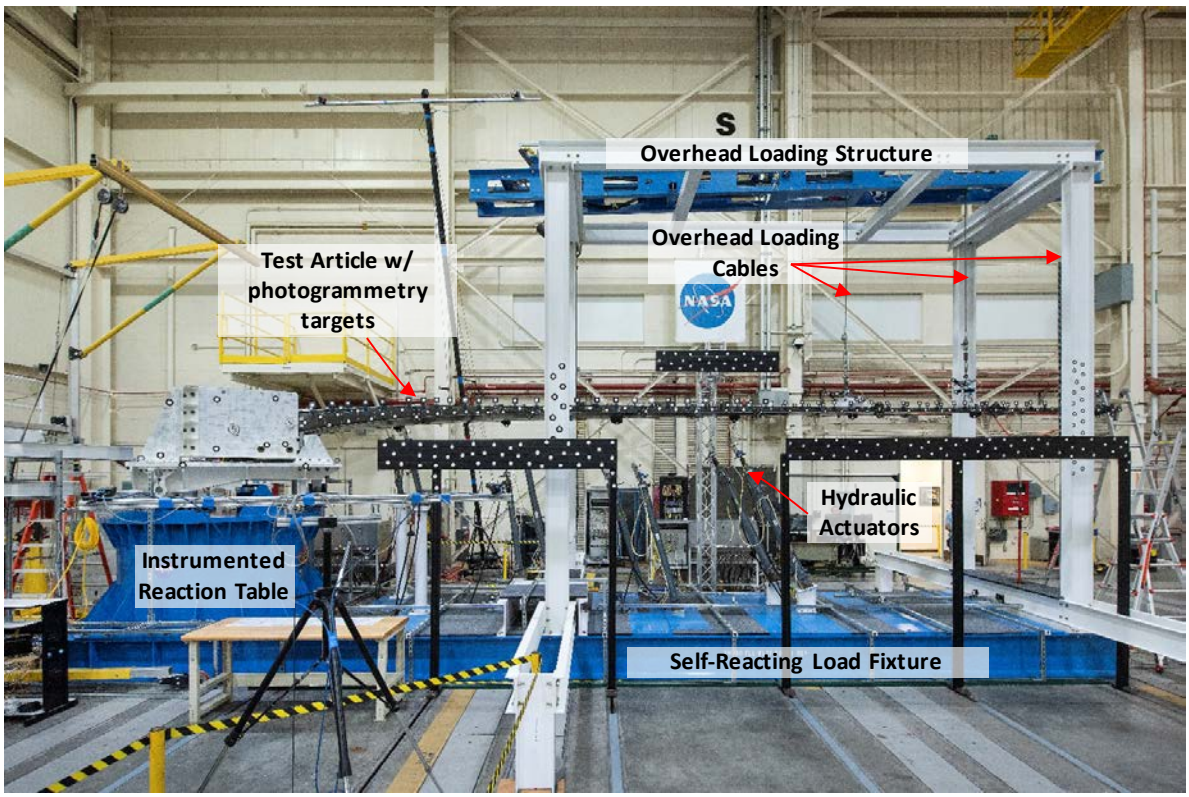

Figure 7.4. AFRC FLL test setup for -1G, +2.5G and flexural axis testing.

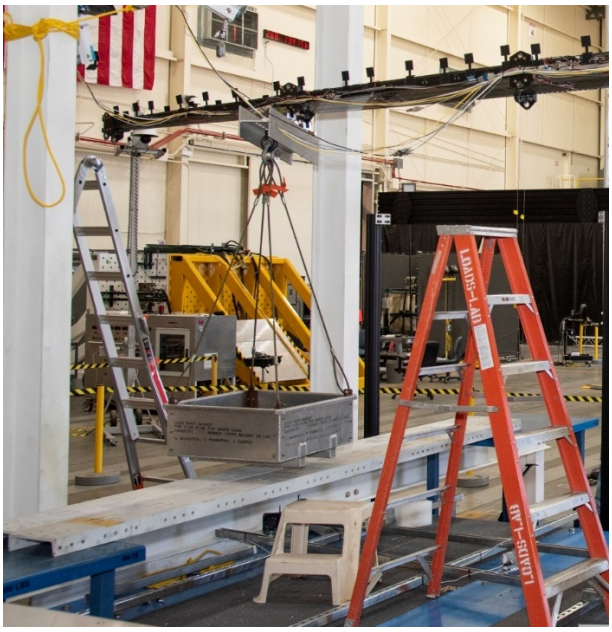

Figure 7.5. Testing hardware for 'shotbag' flexural axis testing.

Comprehensive details on instrumentation type, location, and orientation are available in a NASA-provided data package and are not repeated in this document.

Table 14. +2.5 loads.

Load Station	X (in)	Y (in)	Z (in)	Fx (lb)	Fy (lb)	Fz (lb)	Resultant (lb)
1A (LE)	302.58	83.89	40.33	-71.07	-123.09	3661.50	3664.26
2A (LE)	340.10	134.07	42.88	67.99	117.76	-1506.77	1512.89
3A (LE)	377.05	183.48	43.69	-222.56	-385.48	2740.76	2776.67
4A (LE)	415.03	234.27	44.37	-286.59	-496.38	2447.95	2514.16
5A (LE)	451.96	283.66	45.36	-213.43	-369.68	1351.17	1417.00
6A (LE)	488.80	332.94	45.19	-157.50	-272.79	882.04	936.60
7A (LE)	525.35	381.70	44.87	-37.48	-64.91	205.98	219.19
1B (TE)	347.84	82.79	42.22	-53.27	-92.26	2241.09	2243.62
2B (TE)	374.30	132.68	44.19	-389.52	-674.67	6628.02	6673.65
3B (TE)	405.16	181.61	44.98	-174.94	-303.00	1933.71	1965.11
4B (TE)	436.11	230.68	44.60	-163.65	-283.45	1281.80	1322.93
5B (TE)	468.65	282.29	45.20	-184.53	-319.61	1124.96	1183.95
6B (TE)	499.94	331.90	44.94	-122.05	-211.39	681.37	723.77
7B (TE)	531.42	381.93	45.22	11.78	20.41	-64.56	68.73

Table 15. -1G loads.

Load Station	X (in)	Y (in)	Z (in)	Fx (lb)	Fy (lb)	Fz (lb)	Resultant (lb)
1A (LE)	302.58	83.89	40.33	-8.53	-14.77	-1906.07	1906.15
2A (LE)	340.10	134.07	42.88	-7.30	-12.65	-749.00	749.14
3A (LE)	377.05	183.48	43.69	-26.91	-46.61	-1793.66	1794.47
4A (LE)	415.03	234.27	44.37	-28.80	-49.88	-1460.96	1462.09
5A (LE)	451.96	283.66	45.36	-24.53	-42.49	-1077.58	1078.70
6A (LE)	488.80	332.94	45.19	-15.15	-26.24	-591.33	592.10
7A (LE)	525.35	381.70	44.87	-7.05	-12.21	-313.70	314.02
1B (TE)	347.84	82.79	42.22	1.04	1.80	229.61	229.62
2B (TE)	374.30	132.68	44.19	-6.23	-10.78	-604.31	604.43
3B (TE)	405.16	181.61	44.98	8.98	15.56	621.55	621.81
4B (TE)	436.11	230.68	44.60	13.38	23.18	693.17	693.68
5B (TE)	468.65	282.29	45.20	16.36	28.34	725.15	725.89
6B (TE)	499.94	331.90	44.94	10.17	17.61	400.78	401.30
7B (TE)	531.42	381.93	45.22	4.69	8.13	234.45	234.64

Testing for the -1G and +2.5G case was largely executed as planned. During the +2.5G testing, an instability in the hydraulic load system was encountered at approximately 90% load, which resulted in a halt in testing and load dump. The instability was immediately preceded by an audible ‘pop’ and subsequent evaluation of strain gauge data revealed small step-changes in strains, primarily at gauge locations adjacent to the four 3” diameter pin locations mounting the spar webs to the steel reaction plates, which suggests that a sudden internal load redistribution triggered the hydraulic load system instability. The authors speculate that the most likely source of event was a propagation of the leading edge spar web nonstructural shim delamination (see Figure 5.3), which is located at the faying surface of the spar web and steel reaction plate pin joint, however, no definitive cause can be ascertained without a detailed disassembly and inspection of the test article assembly. In the following sections, test results for the +2.5G load case are reported at the 89% load level (just prior to the instability) and FEM predictions are scaled accordingly.

7.2.2 Test Correlation

7.2.2.1 Rigid Body Rotation

Rigid body rotation of the wing was both anticipated and observed during the testing. Rigid body rotation came from both nonlinear and linear sources. The primary contribution to nonlinear rigid body rotation was pin hole clearance. For the +2.5G case, the pin-hole clearance in the steel ‘reaction plates’ that were pinned to the spar webs, was the primary contributor. Pin hole clearances in the AFRC reaction table also provide contributions to rigid body rotation for both load cases. The majority of linear rigid body rotation was due to the flexure of the AFRC reaction table and its supporting structure. It was noted that the FEM model does not account for nonlinear rigid body rotations and while the AFRC table itself was modeled, additional compliance in the load cells and underlying pedestal was not modeled (e.g., boundary condition compliance).

The rigid body rotations of the wing were calculated by comparing the root inclinometers, rtROT*, which is located at on test axis origin at the center of the AFRC reaction table, and wROT*00, which is located on the upper wingskin, directly above rtROT* (* indicates two channels for each inclinometer, corresponding to global X and Y axes).

To assess the degree of rigid body rotation due to both pin hole clearance, which manifests as a near step-change in rotation, and increased boundary condition compliance, which manifests as a more compliant (larger) rotation/load slope, a coordinate transformation was applied to the global X and Y aligned data to compute the rotation about the test axis that was rotated -30° about the Z axis (i.e., a 30° sweep angle).

The results are depicted in Figure 7.6 for both the +2.5G case (corresponding to positive rotations) and the -1G case (negative rotations) as well as the FEM predictions for the AFRC reaction table and wing root rotations. The nonlinear rigid body rotation of the wing root was observed at approximately the 2% load level – this is characterized as a step-change in rotation between the wing (blue curve) and AFRC reaction table (green) of 0.27° for the +2.5G case. It is noted that this rotation was not observed for the -1G case; this was expected, as the rigid body rotation occurs when the up-loading overcomes the weight of the wing and causes a local reversal of load at the boundary conditions. As the -1G case loads in the wing in the direction of gravity, no load reversal occurs at the boundary conditions. As a result, the rigid body rotation of the wing root section is nearly identical to that of the AFRC table for the -1G case, as indicated by the overlaying data curves.

For both the +2.5G and -1G cases, a smaller rigid body rotation was observed at the AFRC table: 0.016° at approximately 9% load for the +2.5G case and -0.0089° at approximately 20% load for the -1G case.

The effects of AFRC reaction table boundary condition compliance was obtained by comparing the slope of the rotation vs. load curves compared to FEM predictions. By utilizing a linear least-square fit to the test over the 30-80% load range of Figure 7.6, the slope of the rotation curves was calculated, which was used to extrapolate the total rotation at 100% load that is due to the linear flexure of the AFRC reaction table and its boundary conditions. These results are tabulated in Table 16. For the +2.5G case, the predicted rotation of the AFRC reaction table was 0.0464°, however, the linear contribution observed during testing corresponds to a 0.1901° rotation, a 310% increase. This additional compliance in the reaction table and boundary conditions accounts for 0.129° of the total wing rotation discrepancy between test data and prediction at 90% load for the +2.5G case. Similarly for the -1G case, the AFRC reaction structure is approximately 421% more compliant than predicted. These differences were attributed to compliant boundary conditions: the AFRC reaction table FEM was rigidly pinned at the load cell locations; however, the load cells and underlying structure were not perfectly rigid and contributed to the overall compliance of the system.

The slope of the 30-80% linear fit for root wing rotation for the +2.5G load case is 0.259°, of which 0.069° is due to the flexure between the AFRC table and the wing root inclinometer. The corresponding FEM estimate for this flexural contribution is 0.052°. The additional compliance accounts for 0.015° of the total wing rotation discrepancy between test data and predictions at 90% load for the +2.5G case.

For the +2.5G case, a small amount of nonlinearity is observed in both the AFRC table rotations as well as the wing rotations above the 80% load level as compared to a linear extrapolation of the 30-80% load data. At 89% load, a total wing root rotation angle of 0.529° is observed, compared to 0.517° based on a linear extrapolation of the 30-80% data. Of this 0.012° nonlinearity observed at the wing, 0.007° is due to the nonlinearity observed at the AFRC table (0.192° observed vs. 0.185° linear extrapolation). This nonlinear behavior is attributed to follower load effects, which are not accounted for in the linear FEM analysis.

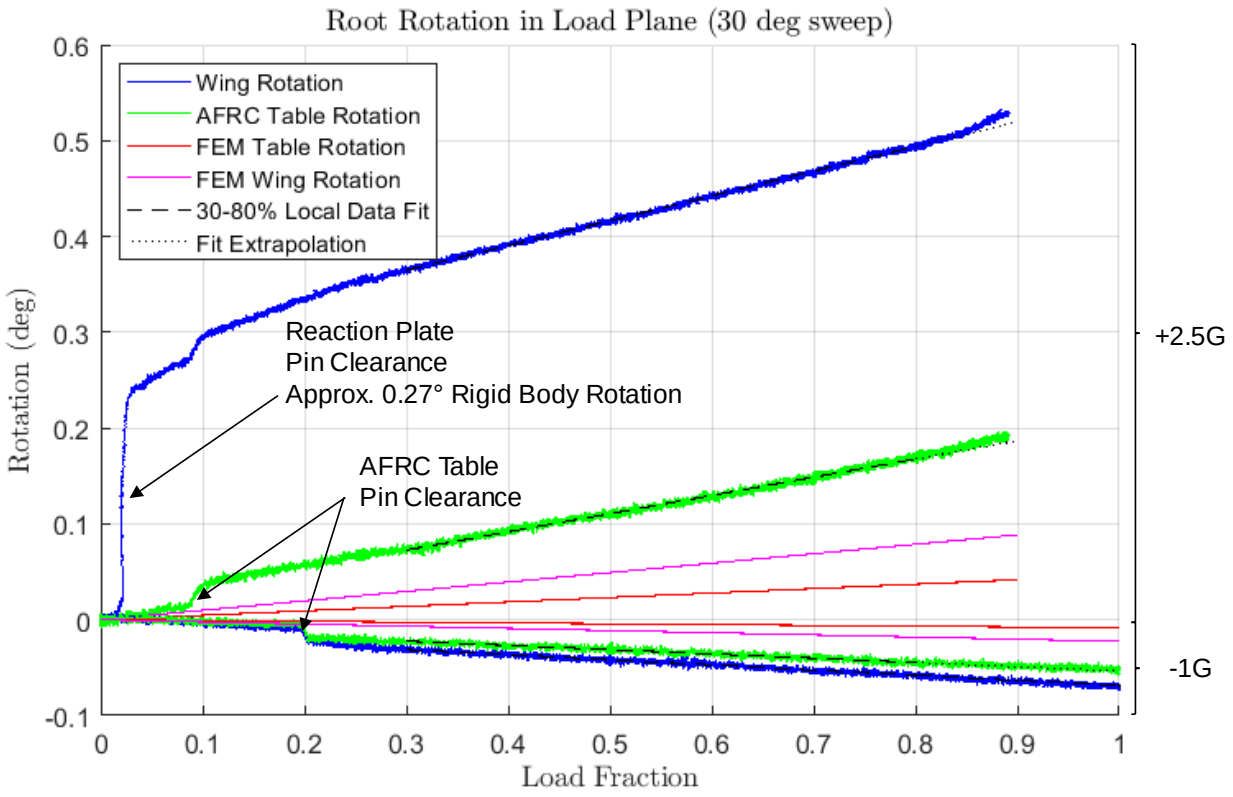

Figure 7.6. Rigid body rotations at wing root and AFRC reaction table.

Table 16. Rotation at 100% load due to linear AFRC table flexure (extrapolated for +2.5G case).

Load Case	Predicted Rotation	Test Rotation	% Difference
+2.5G	0.0464°	0.1901°	310%
-1.5G	-0.00858°	-0.0447°	421%

The various contributions to the wing rotation discrepancy for the +2.5G case at 90% load is summarized in Table 17. The total rotation at the wing root observed for the +2.5G test is 0.53° at the 90% load level, almost a factor of 6 over the FEM prediction of 0.09°. The difference (0.44°) corresponded to an increased tip deflection of 3.38 inches over predictions. Similarly for the -1G case, the total root rotation observed is -0.07°, compared to a prediction of -0.023°, corresponding to a difference in tip deflection of -0.36 inches.

Table 17. Sources of wing rotation error (test data relative to FEM) for +2.5G Load Case at 90% Load.

Source	Test Rotation	FEM Rotation	Rotation Error
AFRC pin clearance	0.016°	0°	0.016°
Reaction pin clearance	0.27°	0°	0.27°
AFRC table & BC linear flexure	0.1711°	0.0417°	0.129°
Wing to table mounting fixture linear flexure	0.0617°	0.0469°	0.015°
AFRC table & BC nonlinear flexure	0.007°	0°	0.007°
Wing to table fixture nonlinear flexure	0.005°	0°	0.005°
Total	**0.53°**	**.09°**	**0.44°**

7.2.2.2 Deflection and Rotation

Deflection data from stringpots (circles) and photogrammetry targets (squares) are provided in Figure 7.7 compared to two FEM predictions: the 'no skin offset' configuration (solid lines) and a 'with skin offset' FEM that implements offsets to skin elements to account for excess liquid shim thickness, which results in a stiffer prediction. Note that no corrections were made for rigid body rotation (which accounts for approximately 3.4 in. deflection at the tip) or stringpot angular error (up to 0.3 in.), as discussed below.

As the wing deforms, the stringpots will begin to deviate slightly from vertical due to span-shortening, introducing a sine error into the vertical measurement. Using photogrammetry data from the tip to estimate the span-shortening, the total error can be estimated. At the tip, the worst-case deviation from vertical is 3.5 degrees, corresponding to a total vertical error of approximately 0.3 in. (the preceding stringpot measurements could overpredict the vertical component by this amount). An initial stringpot height of 90 in. at zero load was used for this estimate. It is noted that the photogrammetry data are plotted at the deflected (not original) span location, and therefore, includes the effect of span shortening, which is 9 in. (measured along the global y-axis) at the tip for the +2.5G case at 89% load.

At the trailing edge tip there is a 2 in. discrepancy between the photogrammetry and stringpot vertical deflection data at 89% load, which is not fully explained by span shortening effects or typical instrumentation errors associated with photogrammetry or stringpots. One possible source of discrepancy considered is the local offset of the

photogrammetry targets from the wing center to preserve visual line of sight to the camera system. For targets offset above the wing, local rotations will cause the photogrammetry targets to overpredict span shortening and underpredict vertical deflection. Similarly, stringpots (including those at the tip) were attached to the bottom of the load lugs, which are offset from wing center by 3.6 in., which results in a slight overprediction of vertical deflection by the stringpots. However, these effects still do not fully explain the 2" discrepancy between instrumentation systems (it is noted for example, that the photogrammetry target at the TE tip was mounted near the wing neutral axis, therefore, this particular target would not suffer from offset rotation effects). A second possible source of error, which is difficult to quantify, is a potential misalignment between the photogrammetry coordinate system to the test axis coordinate system.

It is interesting to note that measured deflections tended to fall closer to the 'no skin offset' configuration than to the revised predictions that accounted for the skin offsets due to liquid shim offsets, even after considering the rigid body rotation contribution. Both the +2.5G (Figure 7.7) and -1G (Figure 7.11) load cases were consistent in showing larger deflections than predicted by the 'with skin offset' model. Table 18 provides a comparison of tip deflection data with and without corrections for rigid body rotation.

Two possible explanations exist. The first explanation is that the liquid shim thickness was overestimated during the inspection process. Because the assembly jig cradles did not provide simultaneous access to both skins, each skin surface was profiled independently, with a 'best fit' alignment to the wing jig shape taken for each skin. The movement of the wing and realignment to the measurement system was a source of error for the skin profiling. The second possible explanation is that the increased nonstructural liquid shim distance between the skin and spars/ribs resulted in a more compliant joint than modeled (no modification to joint stiffness was made). Each of these could be explored further: the wing could be remeasured, utilizing the load application points to jack the wing into the jig shape, and the FEM could be 'tuned' by altering individual fastener stiffness to account for additional joint compliance.

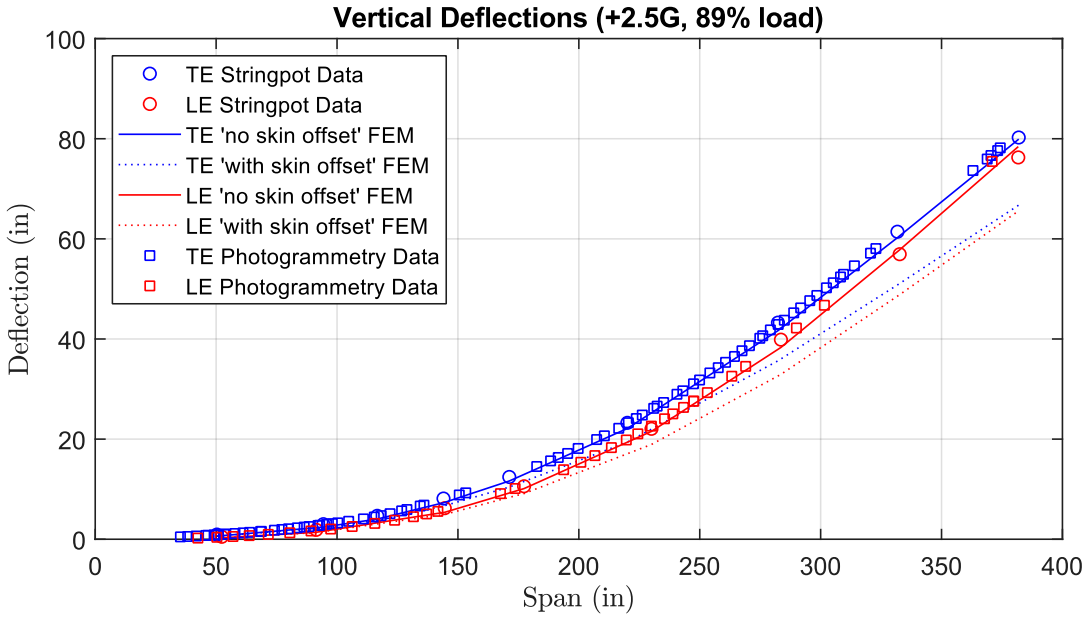

Figure 7.7. Deflection measurements vs. predictions for +2.5G load case.

To facilitate further postprocessing of the photogrammetry data set, a spanwise curve fit was obtained for the photogrammetry data along the leading and trailing edges, as shown in Figure 7.8 for the +2.5G case and Figure 7.12 for the -1G case. A fourth-order polynomial was selected to provide a smooth fit to the data, particularly in the midspan region. It is noted that due to the relative sparsity and noise of the data near the tip, the curves are only trusted for span locations less than 330 in. The curve fits are subsequently used to compute the test article's mean twist and bending rotations as a function of span. The computed rotation and twist data are subsequently differentiated to obtain curvature rates presented in the following section.

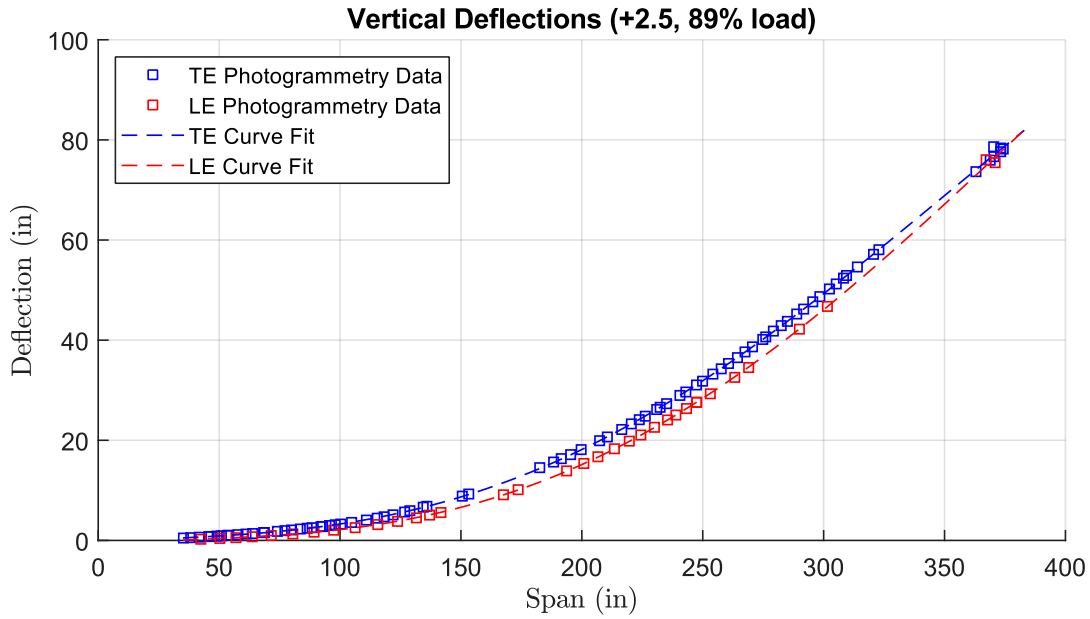

Figure 7.8. Fourth-order polynomial fits to photogrammetry +2.5G deflection data.

It is noted that in this report, all bending and twist angles are taken about the global coordinate system axes (X aft; Y outboard), consistent with those utilized in Figure C.1. The twist angle (taken about the global Y axis) is therefore directly comparable to the local change in angle of attack.

The rotation data follows similar trends as to the deflection data. As shown in Figure 7.9, the inclinometer rotation data (circles) about the global X-axis (bending angle) correlates closely to the 'no skin offset' FEM (solid lines). The black dashed line is the bending angle computed from the photogrammetry curve fits shown in Figure 7.8.

The high frequency nonsmoothness of the FEM prediction rotation data is attributed to local deformations of the skin edges due to discrete fastener connection points. The larger discontinuities (most notably observed in the Figure 7.14 FEM predictions) are due to discrete loading along the span. Other discontinuities may be observed at the sweep breaks located at approximately y =40" and y = 120", which introduce local 'kick' loads into the skins as the load path changes direction.

The wing rotation about the global Y-axis (twist) is provided in Figure 7.10. The twist data tends to correlate well to the ‘no skin offset’ FEM in the root and midspan region but begins to trend between the ‘no skin offset’ and ‘with skin offset’ predictions near the tip.

For the -1G load case, the bending angle test data tends to fall between the ‘with skin offset’ and ‘no skin offset’ predictions (Figure 7.13).

The difference in twist predictions for the -1G between the two predictions sets is generally small, and the test data tends to be larger than both predictions (Figure 7.14).

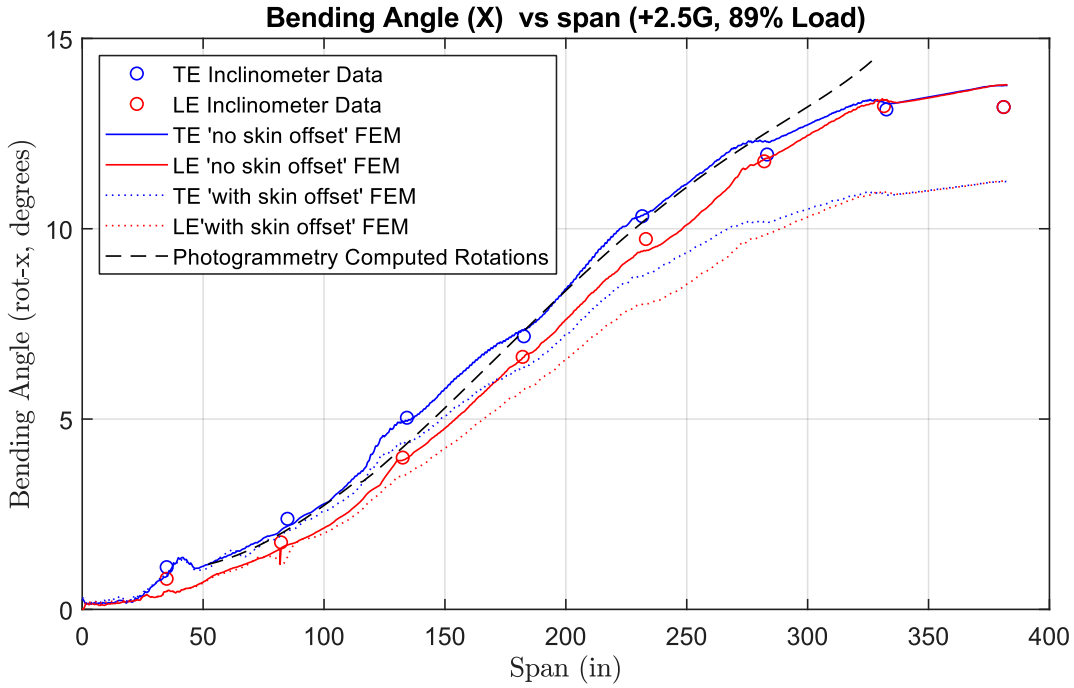

Figure 7.9. Bending rotation (about global X-axis) for +2.5G load case.

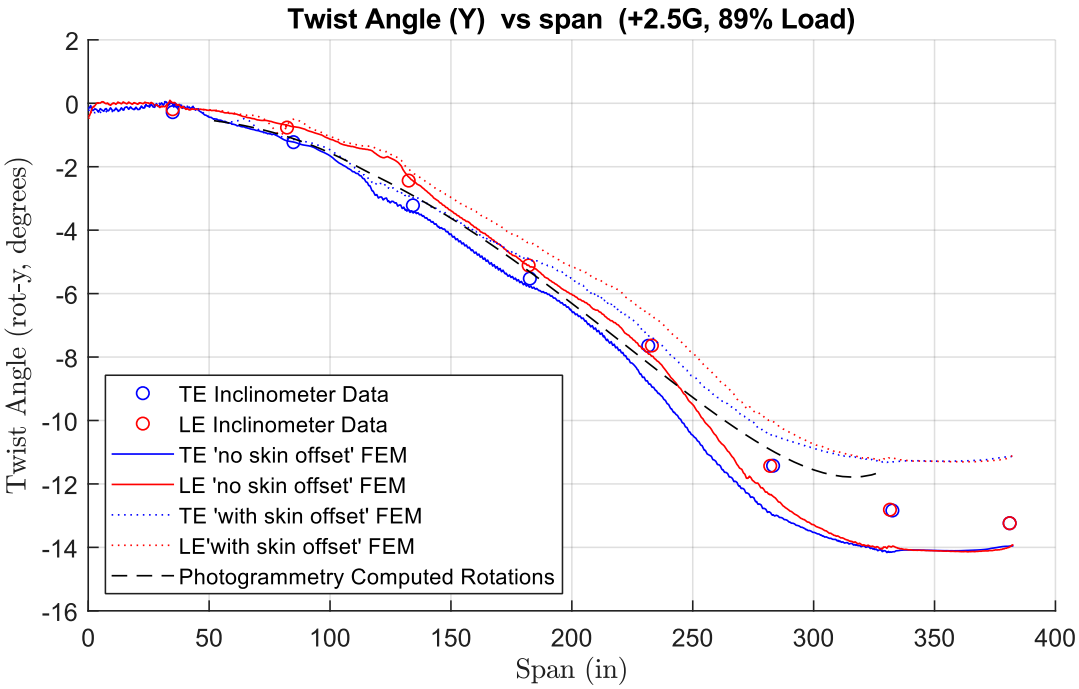

Figure 7.10. Twist rotation (about global Y-axis) for +2.5G load case.

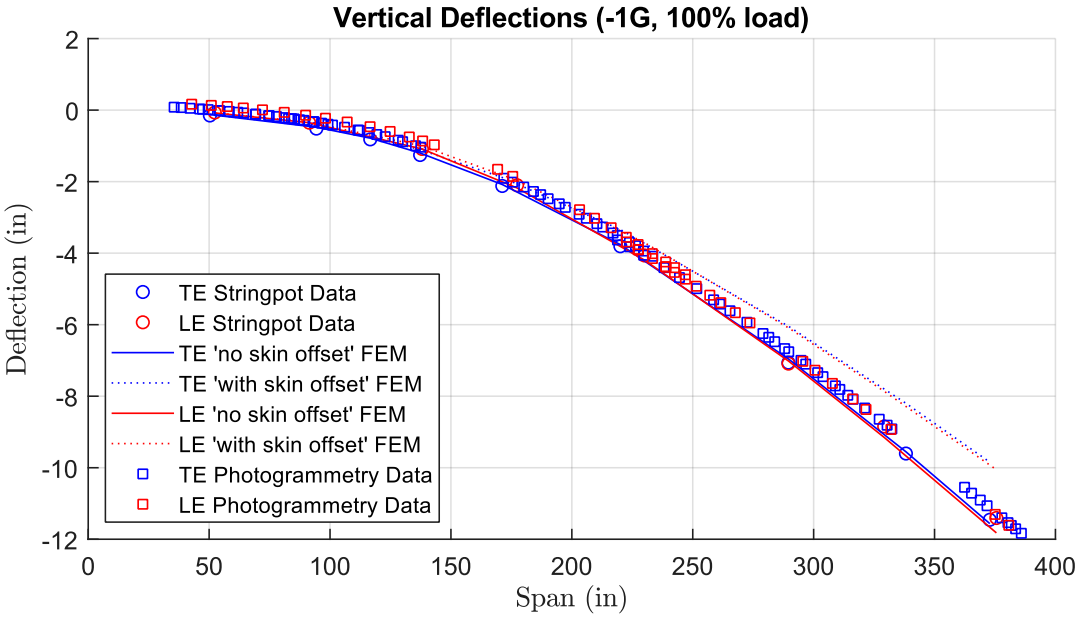

Figure 7.11. Deflection measurements vs. predictions for -1G load case.

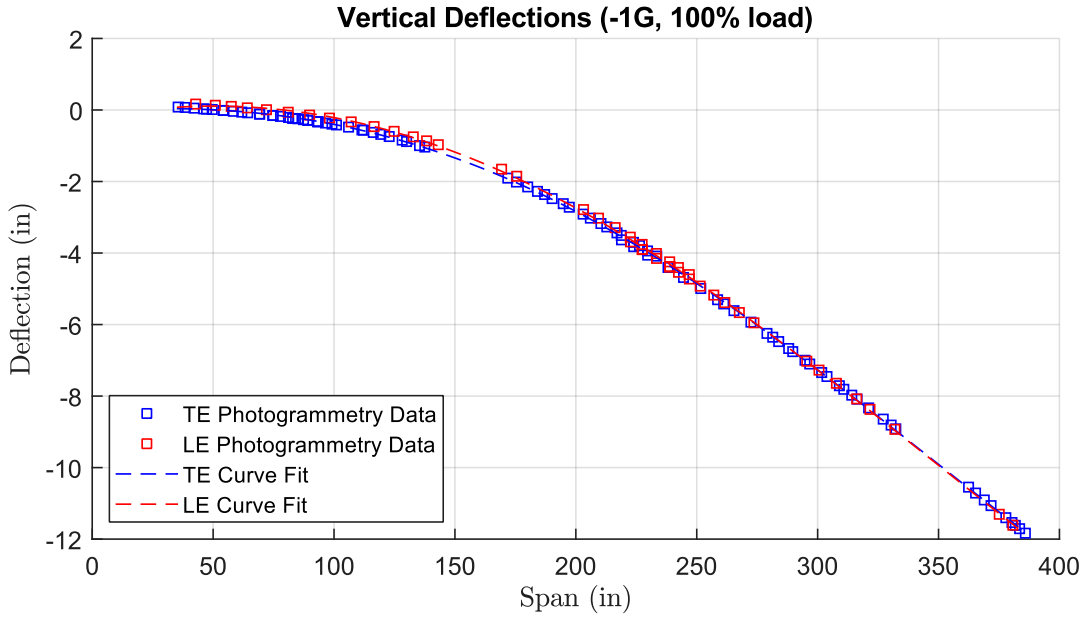

Figure 7.12. Fourth-order polynomial fits to photogrammetry -1G deflection data.

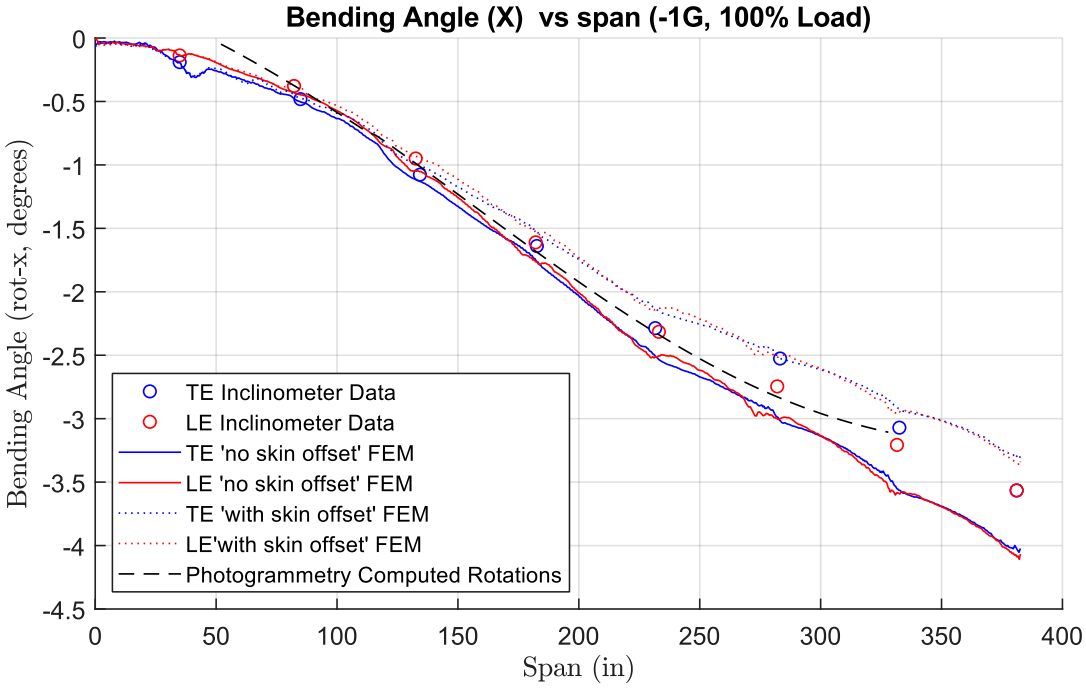

Figure 7.13. Bending rotation (about global X-axis) for -1G load case.

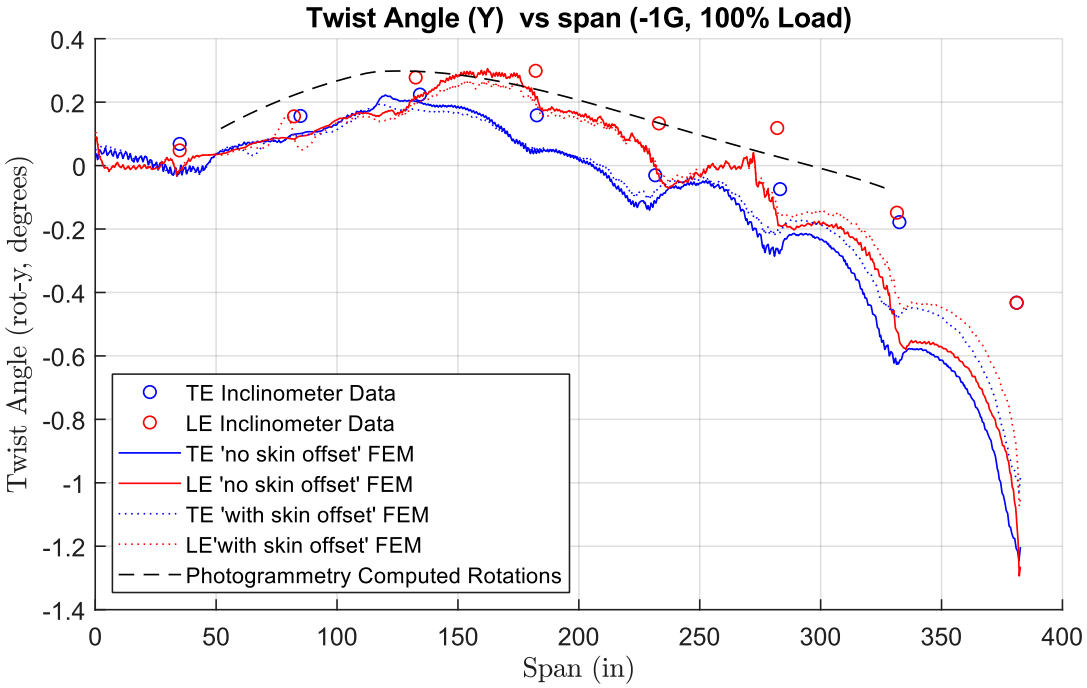

Figure 7.14. Twist rotation (about global Y-axis) for -1G load case.

Table 18. Summary of vertical tip deflection prediction and test data, with and without rigid body corrections.

		FEM Predictions		As measured		Corrected for Rigid Body Motion	
Load	Spar	With Skin Offset	No Skin Offset	Photo-grammetry	Stringpots	Photo-grammetry	Stringpots
+2.5G (89%)	TE	66.74	79.92	78.18	80.24	74.80	76.86
	LE	65.55	78.42	75.46	76.26	72.08	75.04
-1G (100%)	TE	-8.76	-10.29	-11.06	-11.46	-10.7	-11.1
	LE	-8.95	-10.52	-11.3	-11.41	-10.94	-11.05

7.2.2.3 Curvature & Twist Rate

Spanwise bending and twist curvatures were computed via central difference method based on data presented in the preceding section. Data for both predictions and curves fitted to photogrammetry models were sampled on a coarse basis consistent with the density of inclinometer data; the coarse basis also reduced noise due to numerical differentiation. Comparisons for the +2.5G load case for bending and twist curvature are provided in Figure ***7.15*** and Figure ***7.16***, respectively. Figure 7.17 and Figure 7.18 provide the corresponding plots for the -1G load case.

Figure ***7.15*** shows that the “with skin offset” FEM predicts lower curvatures than the ‘no skin offset’ model, particularly in the midspan region. Consistent with displacement and rotation data, the curvatures calculated with test data tend to agree with the ‘no skin offset’

predictions in these regions. The test-data-based twist curvature (twist rate) generally falls between the prediction sets for the +2.5G case (Figure ***7.16***).

Both bending and twist curvature test data for the -1G load case tend to fall between the 'with skin offset' and 'no skin offset' prediction data sets.

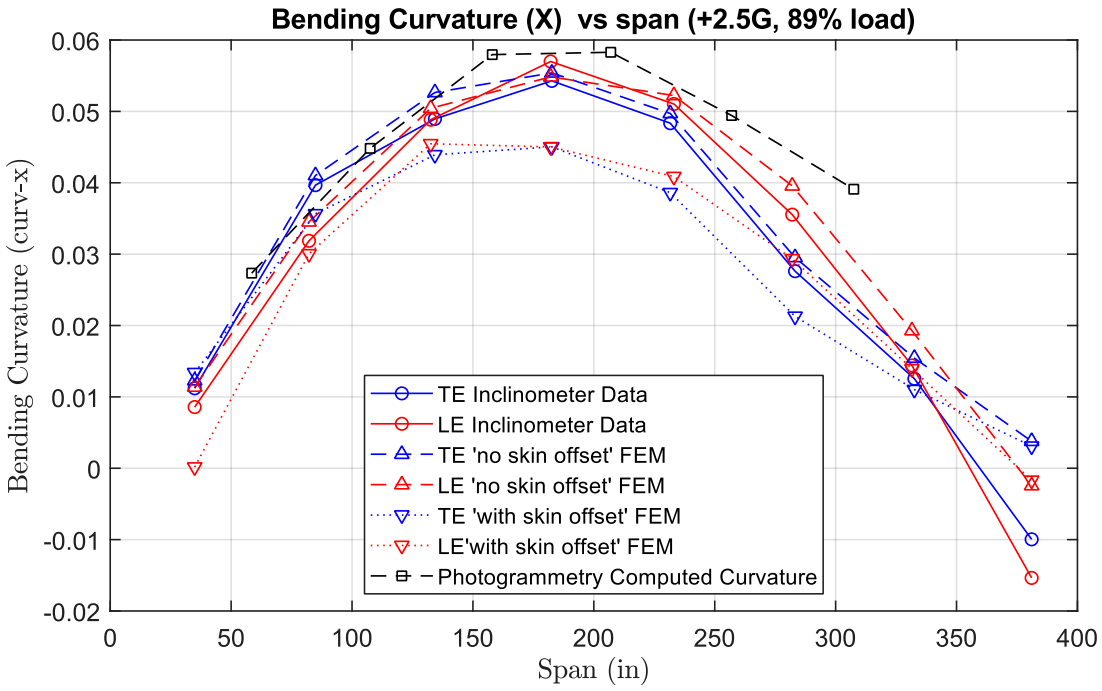

***Figure** 7.15. Bending curvature vs predictions for +2.5G load case.*

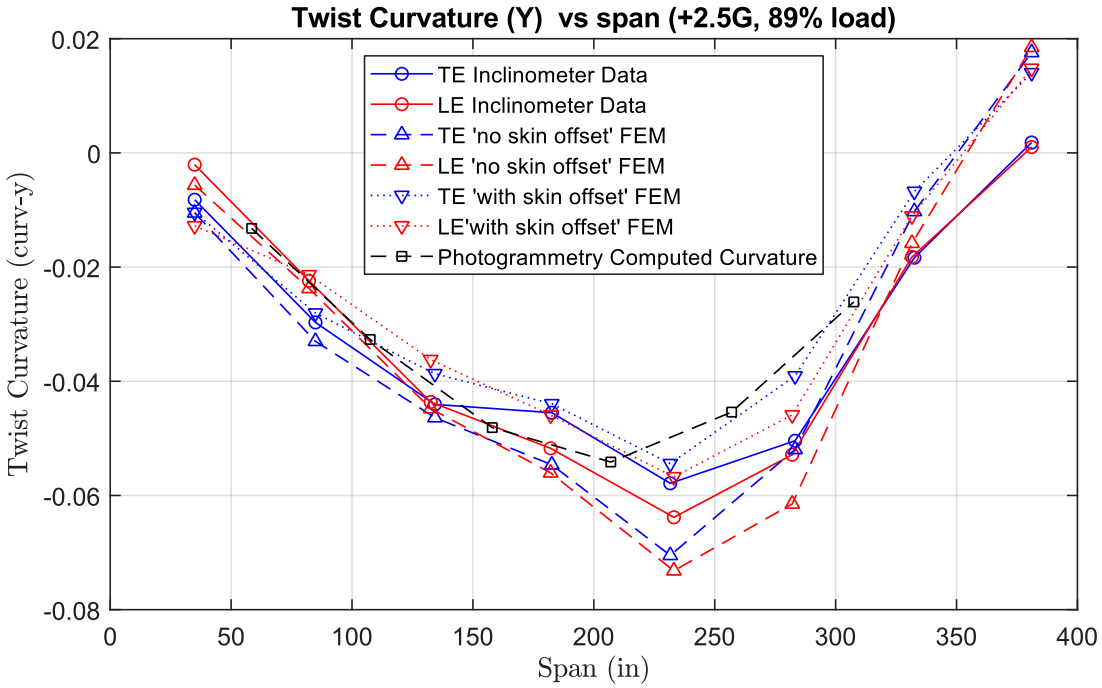

***Figure** 7.16. Twist curvature (spanwise twist rate) vs predictions for +2.5G load case.*

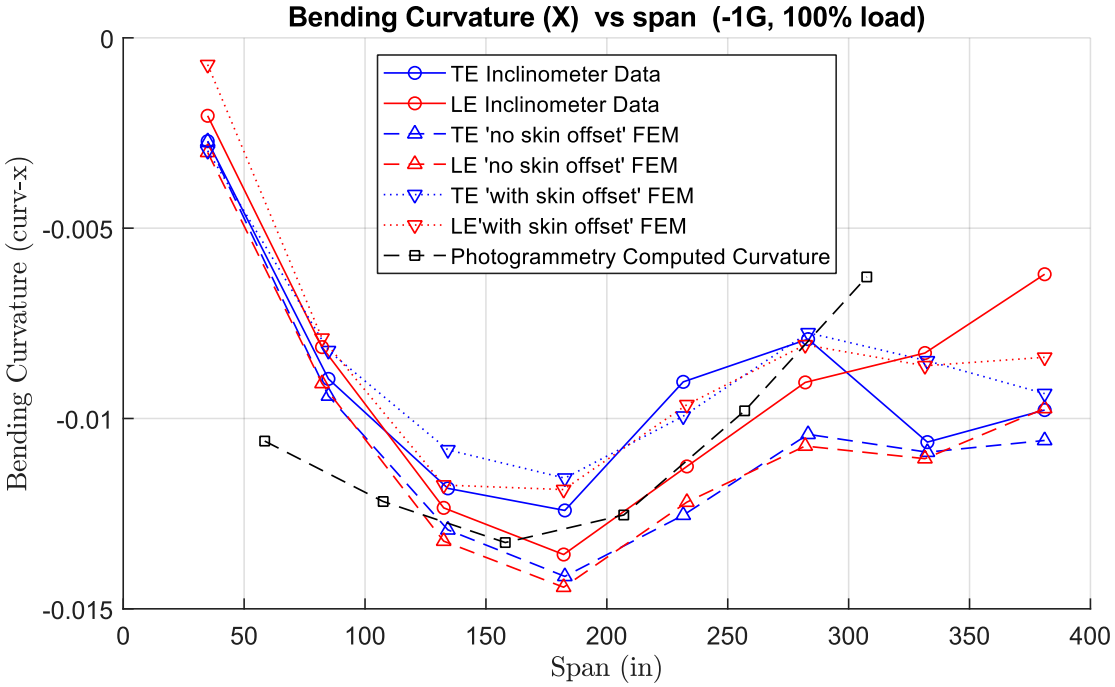

Figure 7.17. Bending curvature vs predictions for -1G load case.

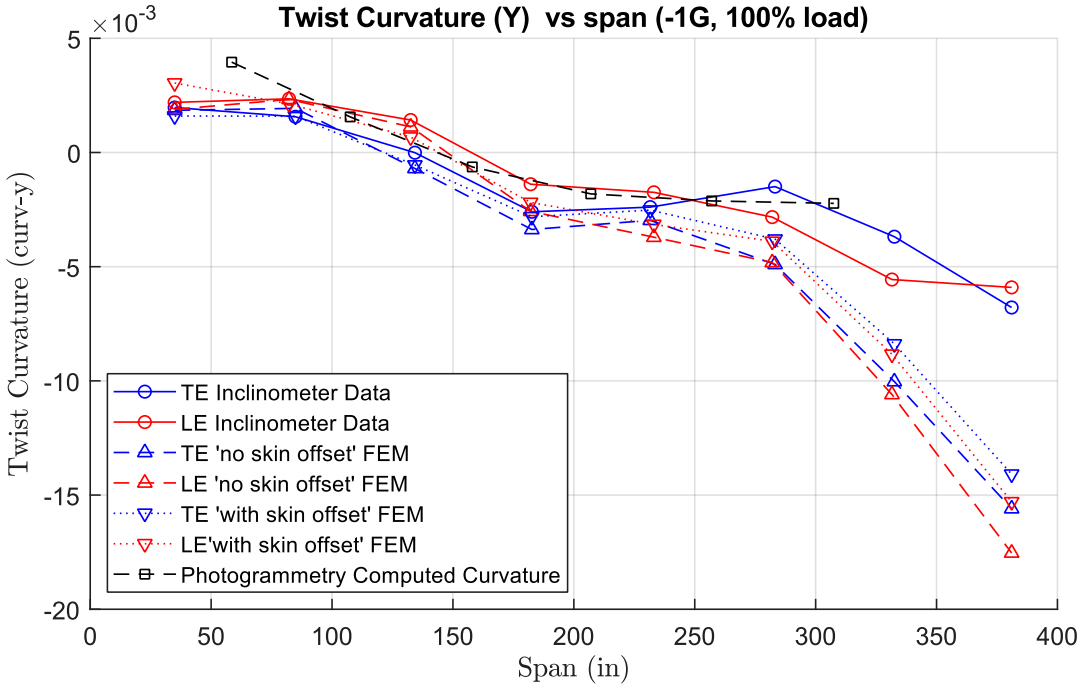

Figure 7.18. Twist curvature (spanwise twist rate) vs predictions for +2.5G load case.

7.2.2.4 Strain

7.2.2.4.1Skin Strains

For the +2.5G load case, the upper skin strain measured along the fiber optic strain sensing (FOSS) fibers generally correlated closer to the 'no skin offset' FEM as shown in C.3, which was generally consistent with the trends observed from the deflection data. However, the lower skin appeared to correlate closer to the 'with skin offset' FEM in most regions. It is noted that correlation was not consistent along the span – for example, the upper skin FOSS results tended to align closer to the 'with skin offset' FEM from approximately y = 240" to y = 280" while the lower skin FOSS results aligned closer to the 'no skin offset' FEM at y = 300" and exceeded both FEMs at approximately y = 330" to the tip.

In most regions, the degree of difference between the 'with skin offset' and 'no skin offset' FEMs tended to be less pronounced for the -1G case than the +2.5G case, and the FOSS data for the -1G case generally fell between the two FEM predictions, as observed in Figure C.5 and Figure C.6.

In general, however, the FOSS data trends showed strong correlation to predictions, matching both global trends as well as local minima and maxima behavior due to rib spacing, for example.

Strain gauge data along the span of the wing matched well with the FOSS trends, except for a few outliers. Like the FOSS data, the strain gauge data for the upper skin correlates closer to the 'no skin offset' FEM except for the gauges located from y = 250" to y = 280", which fell closer to the 'with skin offset' FEM, as observed in Figure C.7. The lower skin strain gauge data aligned more closely with the 'with skin offset' FEM for regions outboard of y = 150" as shown in Figure C.8, consistent with the FOSS data.

Upper and lower skin shear strains, as observed in Figure C.11 and Figure C.12 correlated better with the 'with skin offset' FEM for the +2.5G load case, particularly in outboard sections of the wing. The same was generally true for the -1G case, although the lower skin tended to correlate closer to the "no skin offset" FEM in the outboard regions.

Chordwise strains, as shown in Figure C.15 through Figure C.18 generally show greater deviation from prediction than the spanwise strain. However, it is noted that the chordwise strains were typically low (generally less than 1000 microstrain for the +2.5G and less than 500 microstrain for the -1G case) as no significant external chordwise load was applied in either the -1G or +2.5G load cases. The most significant chordwise strain occurs near the trailing edge root, particularly near the spar kink, which introduces local chordwise loading ('kick' loads) due to the geometric discontinuity.

Principal strain plots depicting the major principal strain, minor principal strain and the minor or major principal strain angle are provided in Figure C.19 through Figure C.30. The strain angle shown in these plots corresponds to the major principal strain angle for the lower skin in the +2.5G case and the upper skin in the -1G case (these skins are predominantly in tension due to bending) and the minor principal strain angle for the upper

skin in the +2.5G case and the lower skin in the -1G case (these skins are predominantly in compression due to bending). On the principal strain angle plots, the local tow-steering angle is provided as a reference; however, correlation of the tow-steering angle to principal strain angle was neither observed nor expected for the reasons discussed in Section 6.1.

It is noted that the strain gauge principal strains correlated better for the principal value oriented in the dominant loading direction (major principal for a skin in tension; minor principal for a skin in compression) than in the orthogonal direction. For example, for the midchord gauges in the +2.5G load, the major principal strain of the lower skin and minor principal strain of the upper skin tend to correlate better than the orthogonal direction (where no significant external load is applied).

In general, the principal strain angle plots show little difference in the predicted strain angle between the 'no skin offset' FEM and the 'with skin offset' FEM, furthermore, the principal strain angles observed during the testing correlate well to predictions. This suggests that while the liquid shim thickness and/or effective joint compliance may impact the strain (and therefore deflection) magnitudes, the strain directionality of the tow-steered skins is relatively unaffected by these factors and remains well-predicted with the current modeling techniques.

In general, the degree to which test data correlated with one FEM or the other varied for a given location or test case. While there could be several reasons why this is the case, one possibility could be the variability in the measurement data used to apply the skin offsets in the 'with skin offset' FEM. In addition to the measurement uncertainty in the total liquid shim thickness, there was also a degree of measurement uncertainty in the specific liquid shim thickness of the upper vs. lower skin at a given location. This uncertainty in liquid shim thickness measurements could account for some discrepancy between the 'with skin offset' FEM strain predictions and test data.

7.2.2.4.2 Spar Web Strains

Spar web shear strain data are depicted in Figure 7.19 and Figure 7.20 for the +2.5G and -1G test cases, respectively. FEM data were sampled from the spars approximately midbay (between ribs) to avoid near-field strain effects due to rib intersections (consistent with the strain gauge placement strategy).

Shear strain as measured by the rectangular rosettes was computed according to Eq. 18 of Appendix C, to provide a strain measurement consistent with the FEM data.

While the strain gauge data are sparse, the test data correlated well to predicted trends. Web shear strains appeared to be at or slightly less than strain values predicted for the +2.5G, while the web shear strains observed for the -1G load case appeared to be at or slightly above predicted values. It is noted that in the -1G load case, while the direction of loading is predominantly negative, all loads on the trailing edge spar except for load station 2 are upward, which accounts for the positive shear strain.

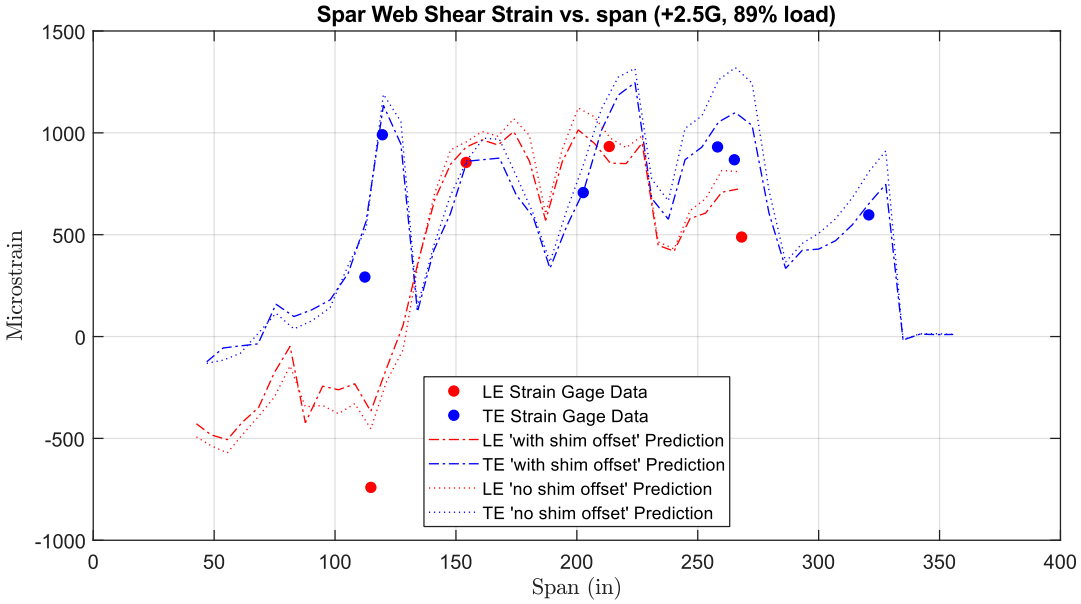

Figure 7.19. Spar web shear strain (+2.5G).

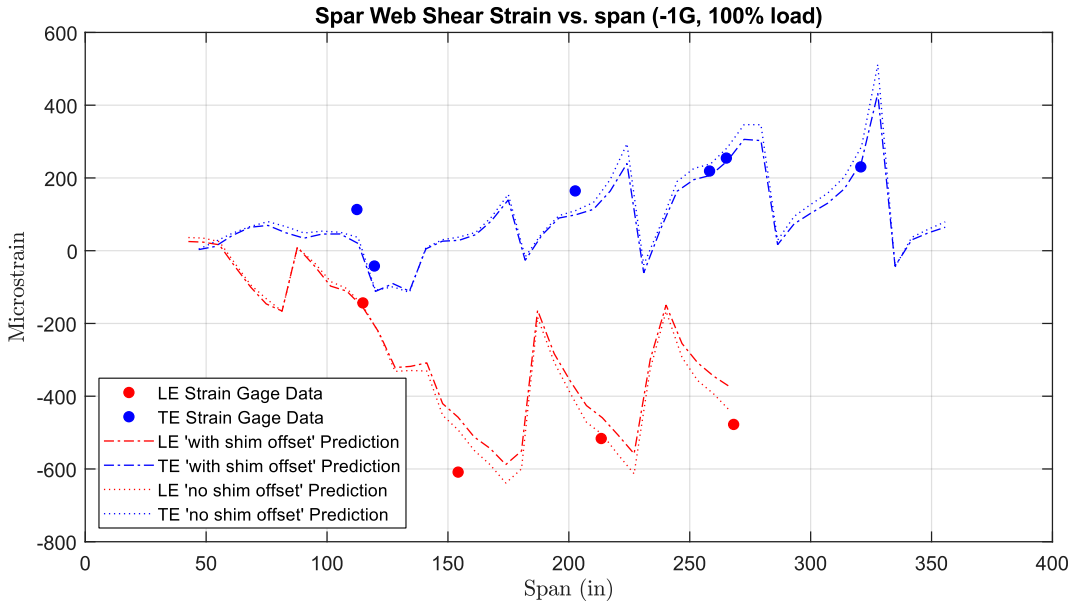

Figure 7.20. Spar web shear strain (-1G).

7.2.2.4.3 **Skin and Rib Bending Strains**

Seven locations on the upper skin and eight ribs were instrumented with back-to-back strain gauges to obtain local bending and membrane strains. The intent of this instrumentation was to capture any local nonlinear behavior (e.g., buckling) that develops prematurely during testing.

Since the linear static FEM predictions utilized in other sections of this report cannot capture nonlinear crushing loads due to bending (Brazier effect) on ribs or buckling behavior if it were to occur, a nonlinear FEM, based on the 'with skin offset' linear FEM was evaluated to provide a basis of comparison for the skin bays and ribs instrumented for local bending. The model was identical to the linear version, except that true follower loads were applied, and fastener stiffnesses were reduced from $1x10^6$ to $1x10^5$ (see discussion on joint stiffness as a possible source of deflection discrepancy in Section 7.2.5).

The bending strains for most of these locations remained linear as shown in Figure 7.21, however, a couple locations, particularly the skin gauge at Rib Bay 19 (derived channel benS19A), and Rib 31 (derived channel benR31A) exhibited a mildly nonlinear response. It is noted that skin bays 11 and 14 showed a similar behavior, however, to a much lesser extent: the total bending strain at these locations remained below 250 microstrain and the nonlinear behavior remained mild, while adjacent skin bays 12 and 13 behavior remained nearly linear. For rib 19, it is noted that in addition to its location just inboard of the Yehudi break, this rib bay also had a local minimum in the applied skin offset due to liquid shim thickness as compared to neighboring rib bays, which is apparent in Figure 6.6. This local decrease in skin offset created a local eccentricity giving rise to an increased bending load locally.

Similarly, vertical bending and membrane strains for Ribs 18, 31 and 33 are shown in Figure 7.22, which exhibited the largest or most nonlinear strains for back-to-back instrumented ribs. Membrane strains remained very low, as predicted – generally within 50 microstrain, with the nonlinearly increasing compressive strain being attributed to the nonlinear compressive loads that develop from wing bending. Rib 31 showed the most nonlinear bending strain and is approximately 37% higher than predicted but in absolute terms remained relatively low (less than 250 microstrain). Similar to the skin, the bending strain was attributed to geometric eccentricities and/or prestress in the rib from the installation process, rather than a buckling event that would have shown a strongly nonlinear behavior with a sharper increase in bending strain rate at the onset of buckling.

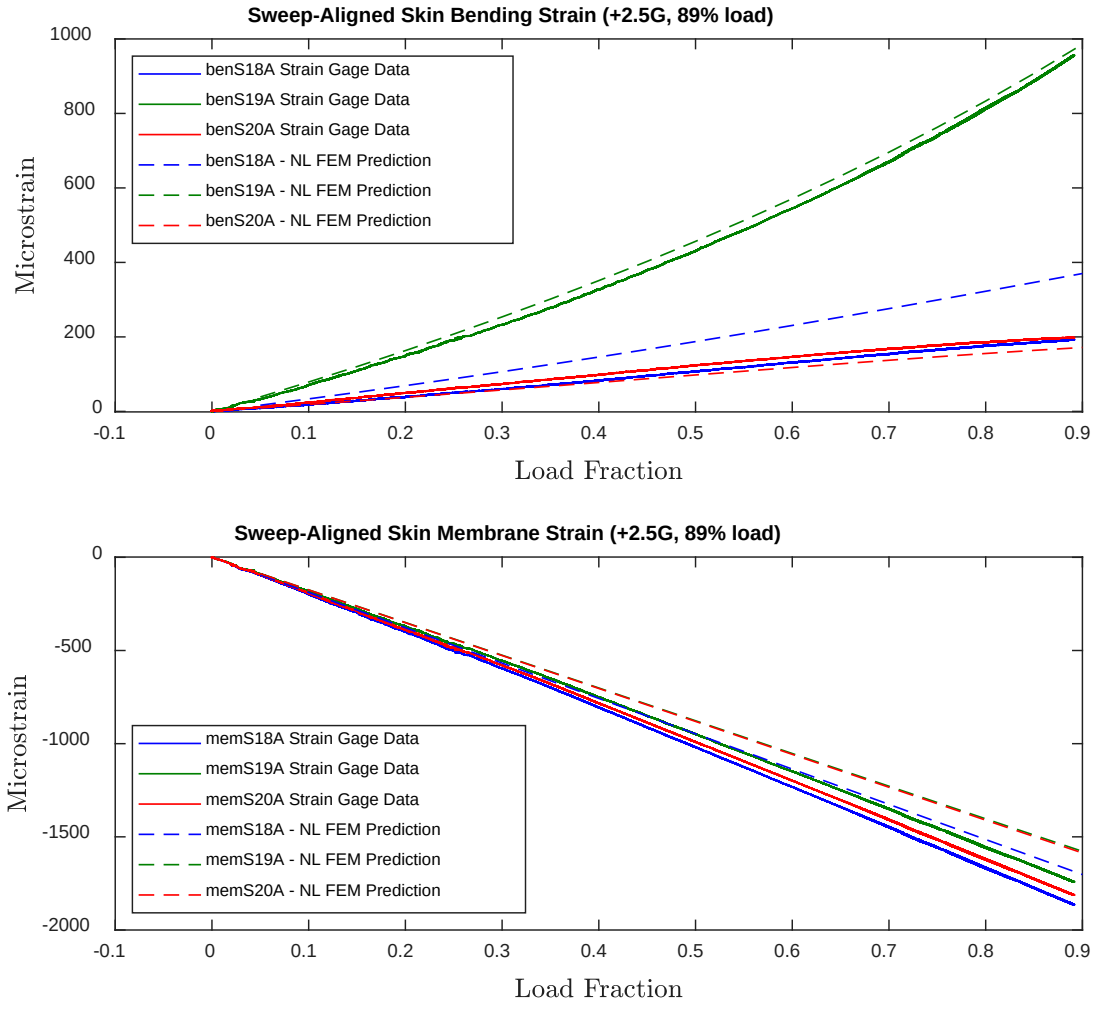

Figure 7.21. Bending and membrane strains for skin bays 18-20.

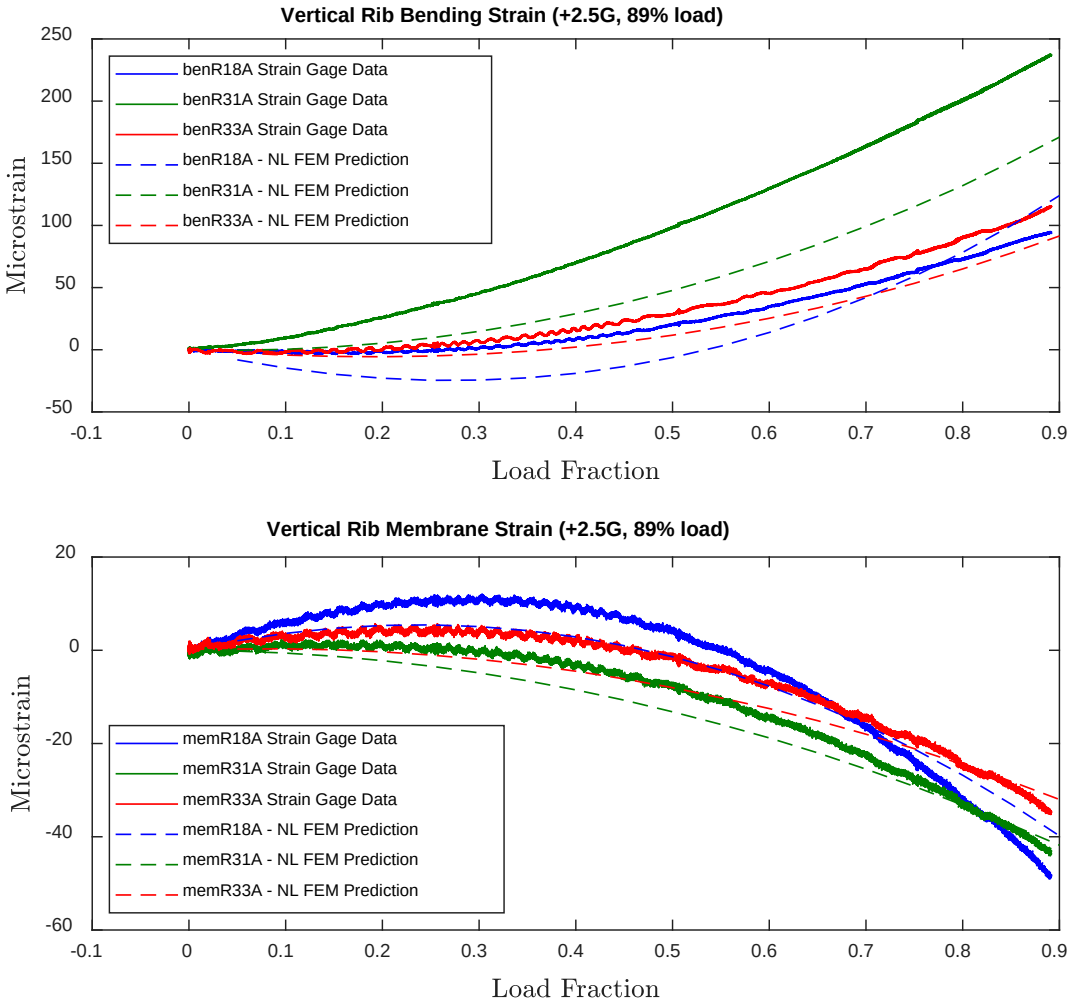

Figure 7.22 Bending and membrane strain for ribs 18, 31 and 33.

7.2.3 Flexural Axis

The flexural axis of the wing was determined both experimentally and numerically for a given station by independently applying loads at the leading and trailing edges and monitoring the location wing twist. Given the two independent sets of applied loads and resulting rotations for a given station, the flexural axis location was determined by solving two equations arising from the standard torsion-twist equation, $M = k\theta$, where $k = \frac{GJ}{L}$. In this case, the torsional constant was eliminated from the equation, and the resulting equation utilized to calculate the flexural axis location was:

$$L = \frac{-F_2 w}{\left(F_2 - \frac{\theta_2 F_1}{\theta_1}\right)}, \tag{11}$$

where F_1 and F_2 were the loads independently applied at the leading and trailing edges, respectively, θ_1 and θ_2 were the corresponding twist angles, and *w* was the chordwise distance between the leading and trailing load application points (as measured along the global x-axis), and L was the distance of the flexural axis location from the leading edge, as shown in Figure 7.23.

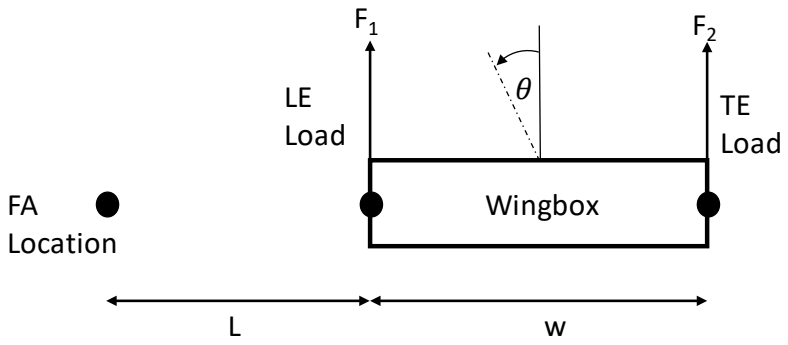

Figure 7.23. Flexural axis calculation approach.

For the hydraulic load cases, the mean applied load was found and the corresponding twist (about Y-axis) as computed by a rotation of the midchord (MC) inclinometer to align with global axes was utilized for the preceding calculation. To find the mean load, the test data were filtered to retain all values that were greater than 99% of the peak load. Corresponding twist values were also averaged to find the mean twist. Data were also corrected to rezero the data prior to the load commencing, and the inclinometer data were adjusted to remove rigid body twist that develops due to pin clearance in the mounting structure. The rigid body twist was computed by taking the difference of the observed twist at the upper skin wing root (as measured by inclinometer channel wROTY00) and the predicted twist from the 'with skin offset' FEM. At each load station, the test was repeated to generate two data sets. Resulting FA locations of these two data sets were averaged for results shown in Figure 7.24 and Table 19.

Flexural axis locations are calculated and presented for both September 2018 and February 2019 testing. The February testing was performed to observe whether the difference in results of the shotbag test at load station 7 was influenced by either a change of instrumentation at that location (a lower resolution inclinometer was used for shotbag and February tests) or by any hysteresis that may have been incurred as a result of the static loads testing. Load station 4 was also repeated as a control case (instrumentation was unchanged at this location). It is noted that the FA location predicted by the February test at load station 4 is 1.2" aft of the location predicted, however, the spread between the two FA location points for the February data is 1.8" while the spread between the two September data points is only 0.17". This suggests that the primary discrepancy between the February and September test data at load station 7 may be explained by the hysteresis within the February test data itself, rather than hysteresis due to the static load testing.

The approach described by Eq. 11 was utilized to calculate the flexural axis location for both FEM analysis as well as the experimental results obtained by independently applying load to each of the outboard load stations via a hydraulic actuator. Additionally, AFRC

also conducted a shotbag test wherein a beam was attached to both LE and TE load application points and extended forward of the wing. A shotbag weight was hung from the beam and the resulting twist angle recorded. The process was repeated at multiple locations increasingly forward of the wing. The flexural axis location was then determined by interpolating the twist angle data to find the location at which applying the shotbag load did not result in wing twist. The shotbag test data depicted in this report are obtained from NASA AFRC report "Passive Aeroelastic Tailored Wing Flexural Axis Location Verification Utilizing Shotbag Weights," Revision 5. Station 4 and 6 results were based on 'Test 1' while Station 5 and 7 results are based on the 'Test 3' data (Test 2 data were only reported for Station 7 and Stations 4 and 6 were not included in Test 3).

The resulting flexural axis locations are depicted in Figure 7.24. The measured flexural axis locations generally correlate well to predictions for Stations 4-6. Station 7 exhibited the greatest deviation from predictions. This may partially be due to difficulties that arise from instrumenting the tip, which has a chord length of approximately 6", which did not provide sufficient space to install and align three inclinometers at the LE, MC and TE as was done at other load stations. Furthermore, the shorter moment arm between the leading and trailing edge at the tip compared to inboard stations amplifies the effects of any measurement error, therefore, the effective resolution for accurately measuring the tip location is less than at locations with a larger moment arm.

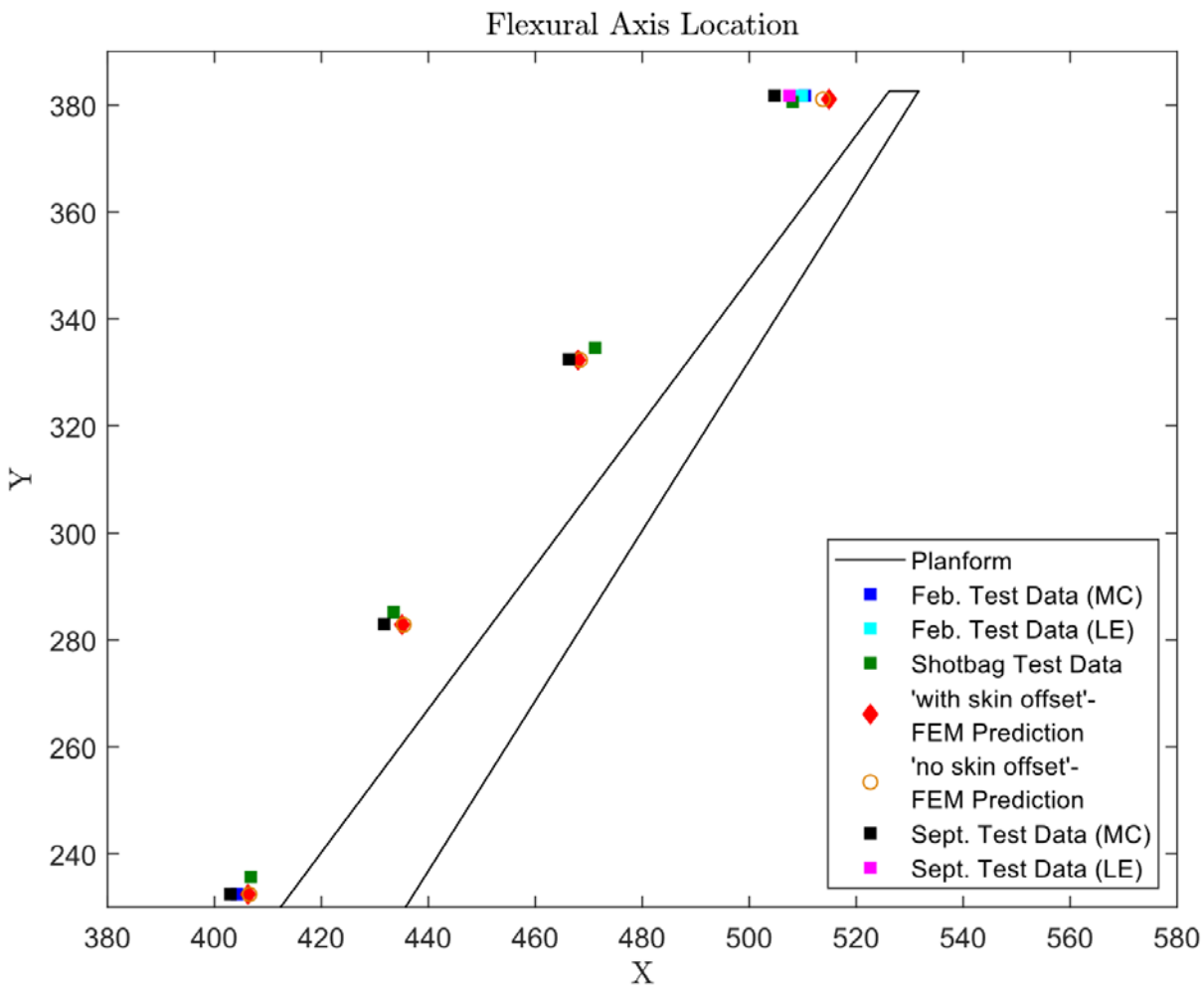

Figure 7.24. Flexural axis locations.

Table 19. Flexural axis location data.

		FEM 'no skin offset'	FEM 'with skin offset'	Shotbag Data	Sept. Data MC	Sept. Data LE	Feb. Data MC	Feb. Data LE
Station 4	X coord	406.55	406.27	406.80	402.97	-	404.21	-
	From LE	8.48	8.76	8.23	12.06	-	10.82	-
	Spread	-	-	-	0.17	-	1.83	-
Station 5	X coord	435.39	435.08	433.49	431.73	-	-	-
	From LE	16.57	16.89	18.48	20.24	-	-	-
	Spread	-	-	-	0.11	-	-	-
Station 6	X coord	468.37	467.99	471.18	466.29	-	-	-
	From LE	20.43	20.80	17.62	22.51	-	-	-
	Spread	-	-	-	0.21	-	-	-
Station 7	X coord	513.78	514.92	508.12	504.71	507.51	510.41	509.84
	From LE	11.46	10.32	17.12	20.53	17.73	14.83	15.40
	Spread	-	-	-	1.10	1.10	0.49	0.28

It is also noted that at all locations, some error may be introduced due to the TE and LE load locations not being perfectly aligned spanwise: the station 4 load locations are offset approximately 3.6” spanwise, station 5 by 1.3”, station 6 by 1.0” and station 7 by 0.2”. While the method employed herein calculates the flexural axis at the mean span location of the LE and TE load application points (approximately in line with the inclinometer location), no additional steps were taken to adjust the predictions to account for the staggered load locations. Because all methods, including both tests as well as FEM predictions should be equally affected, the relative comparison of calculated flexural axis locations is still valid.

If future research is contemplated that requires a more accurate prediction of the true flexural axis location from the existing test data, then one method of quantifying and possibly correcting the error due to staggered load points is to repeat the calculation outlined above with data projected to the most inboard load point (in this case the trailing edge location). For the LE data, no correction is required as the inclinometer, which is placed outboard of the LE load location, will register the same twist angle as if it were aligned with the LE (since there is no moment acting outboard of the LE station for that load case, no change in twist angle occurs). For the TE case, the twist angle must be estimated at the span location corresponding to the LE load location. This can be done either by interpolating the data set (photogrammetry data may provide a denser basis for this calculation), or, the inclinometer reading can simply be scaled geometrically assuming a constant torsional stiffness (while this assumption isn’t generally valid, it may be sufficient for small correction ratios).

7.2.4 Strain Gauge Data Anomalies and Corrections

Three strain gauge locations exhibit anomalies when compared with FEM predictions and/or adjacent Fiber Optic Strain Sensing (FOSS) instrumentation data, which suggest that certain strain gauge data channels may have been switched or mislabeled at the Data Acquisition System (DAS). Of these three suspect strain gauge anomaly locations, rK11111 and rK25104 are located adjacent to a FOSS ‘virtual rosette’, which provides an independent strain measurement that is used to cross-correlate the reported strain gauge values and potential corrections. Figure 7.25 and Figure 7.26 depict the layout of strain gauges rK11111 and rK25104, respectively, along with the adjacent FOSS sensor ID locations. Each of the FOSS ‘virtual’ rosettes consists of a total of three sensor locations from two separate fibers. Two of the sensor locations are taken from a fiber arranged in a sawtooth pattern such that the sensors are oriented at 90° from one another (such as Grating IDs 64 and 70 from Fiber 2 depicted in Figure 7.25). For correlation purposes, these legs align directly with the ‘A’ and ‘C’ legs of the adjacent rosette strain gauges and can therefore be compared directly. The third sensor location is taken from the second fiber, which is located near the sawtooth vertex and oriented at 45° from each of first the two sensor locations (such as Grating ID 138 from Fiber 1 in Figure 7.25).

A third strain gauge anomaly location, rK21110 is not co-located with a FOSS virtual rosette. The nearest FOSS fiber is located approximately 3.8 in. away as depicted in Figure 7.27, is aligned with the rosette leg ‘A’, which is NOT one of the channels suspected of being switched, and is therefore of little value in cross-correlating to rK21110.

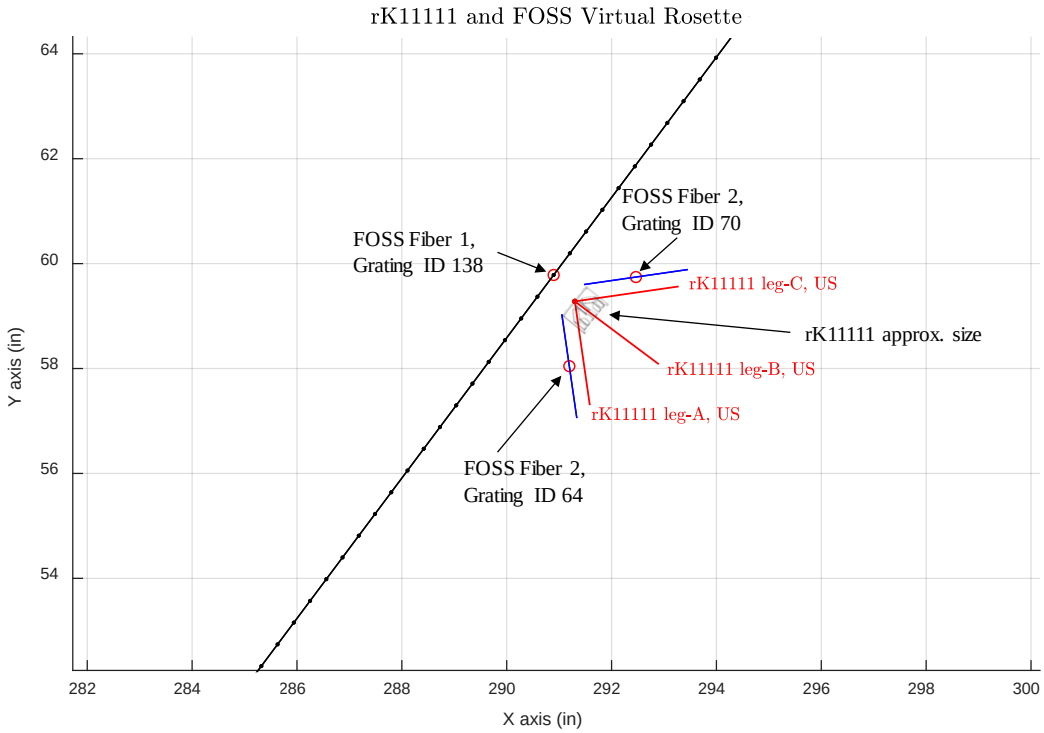

Figure 7.25. Layout schematic for rK11111 strain gauge and adjacent Fiber Optic Strain Sensing.

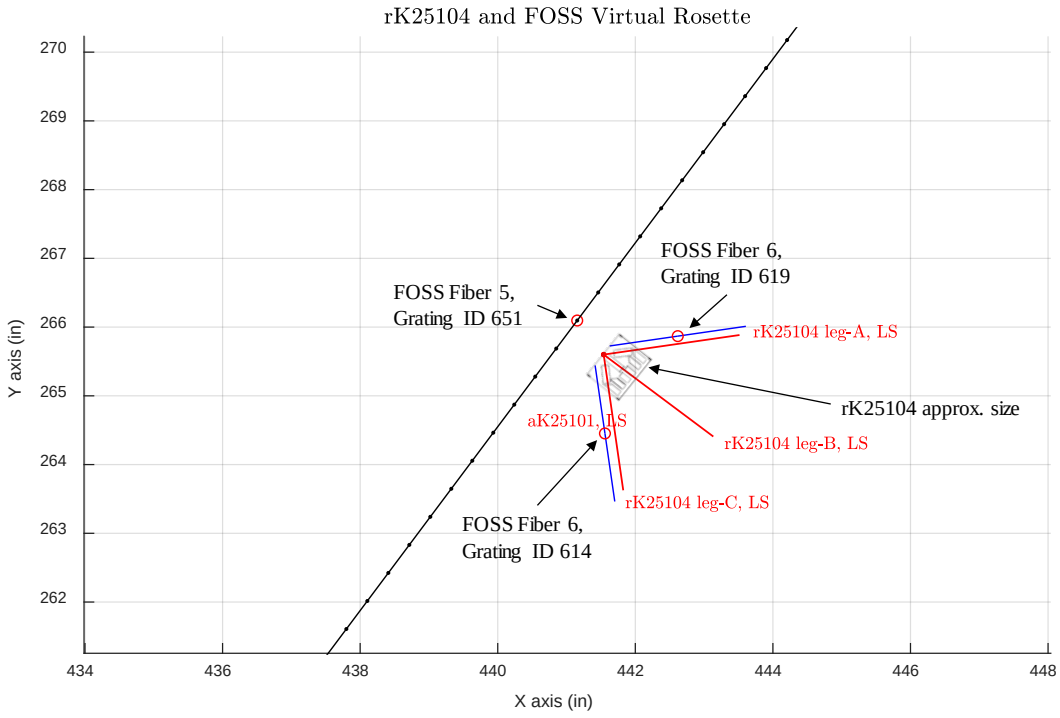

Figure 7.26. Layout schematic for rK25104 strain gauge and adjacent Fiber Optic Strain Sensing.

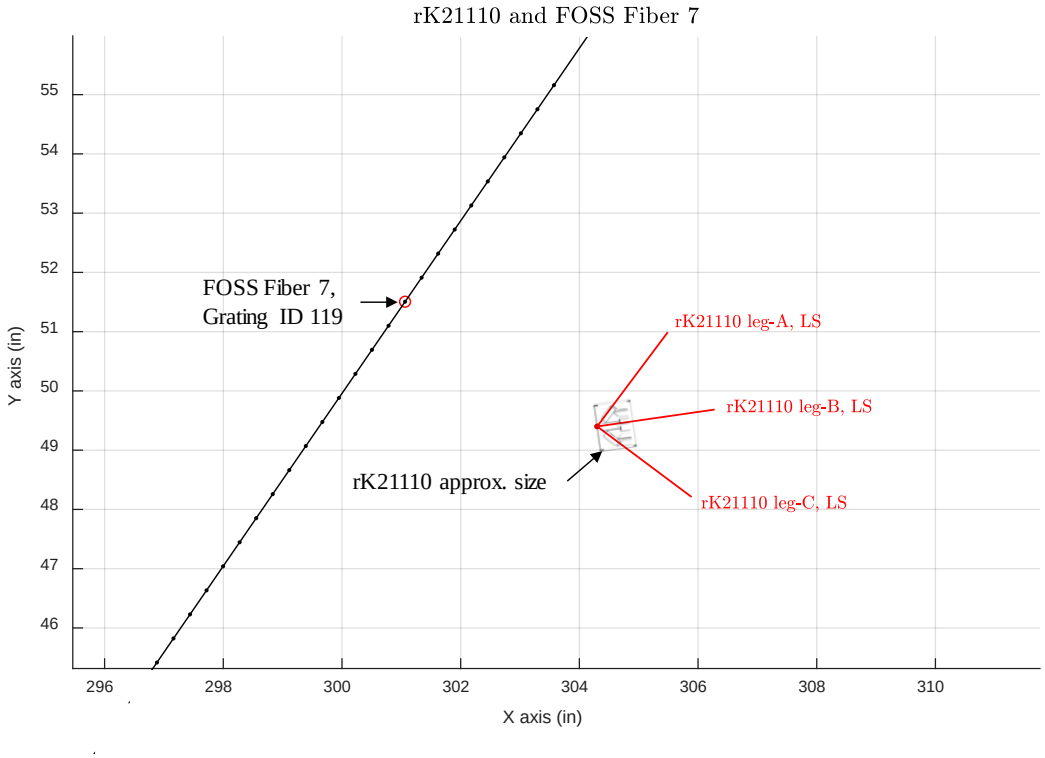

Figure 7.27. Layout schematic for rK21110 strain gauge and nearest Fiber Optic Strain Sensing.

Table 20 - Table 22 provide comparisons for the rK11111, rK25104 and rK21110 strain gauge locations, respectively, with corresponding FOSS data and FEM predictions. For each rosette, both the original data reported by the DAS as well as the proposed correction ('DAS corrected') are presented.

For rK11111, which is located on the upper skin leading edge at Rib Bay 9 (at span station y = 59.28), channels B and C are suspected of be switched. It is noted that FOSS Fiber 2, Grate 70 is expected to correlate to rK11111C, however, as shown in Table 20, rK11111C exhibits -116.1% and -110.8% error relative to the FOSS measurements for the +2.5G and -1G load cases as reported by the DAS. After switching channels B and C, these errors decrease to -3.8% and -9.6%, respectively. The uncorrected strain gauge data also exhibits -70° and 87° total angular error for the computed principal strain angle relative to FOSS virtual rosette computations for the +2.5G and -1G load cases, respectively. After switching the B and C channels, these errors decrease to 1° and -2°, respectively. The uncorrected data exhibits an error of -23.6% for the +2.5G minor principal strain and -43.4% for the -1G major principal strain, while the errors for the corrected data decrease to -2.1% and -10.6%, respectively. Corrected strain gauges values also tend to improve correlation to FEM predictions, as shown in Table 20.

For rK25104, which is located on the lower skin leading edge at Rib Bay 40 (at span station y = 265.6), channels A and B are suspected of be switched. It is noted that FOSS Fiber 6, Grate 619 is expected to correlate to rK25104A, however, as shown in Table 21, rK25104A exhibits –233.5% error relative to the FOSS measurement for the +2.5G load case as reported by the DAS while the corrected data (switched channels A and B) result

in 0.9% error. While the error for the -1G load case does increase from -1.6% for the uncorrected data to 20.9% for the corrected data, the total error remains small at 33 microstrain, therefore, more weight is given to the +2.5G case given the larger magnitude of strain involved.

The rK25104 uncorrected strain gauge data exhibits 86° total angular error for the computed principal strain angle relative to FOSS virtual rosette computations for the +2.5G load case, which improves to a -1° total angular error for the corrected data. The principal strain angle error for the -1G load case is not appreciably affected (-1° and 3° for the uncorrected and corrected cases, respectively). The uncorrected data exhibits an error of -55.3% for the +2.5G major principal strain and 15.5% for the minor principal strain, while the errors for the corrected data decrease to -4.9% and 2.3%, respectively, which strongly supports the theory that these channels have been switched. Corrected strain gauges values also tend to improve correlation to FEM predictions, as shown in Table 21.

For rK21110, which is located on the lower skin midchord of Rib Bay 9 (at span station y = 49.4), channels B and C are suspected of being switched. However, evaluating the possibility of the rK21110B and rK21110C channels being switched at the DAS is more challenging than for rK11111 and rK25104, as no adjacent instrumentation is available to correlate these channels. Furthermore, both the FEM predictions and data exhibit similar strains for both channels in the -1G case, leaving only the +2.5G FEM prediction to provide a basis for evaluating a possible correction. Uncorrected DAS data exhibits -86.0% and 191.7% error for the rK21110B and rK21110C channel compared to FEM predictions for the +2.5G case. Switching these channels decreases the error to -26.0% and 44.8%, respectively. Similarly, the major principal strain error decreases from 30.9% for the uncorrected data to -14.1% for the corrected data, while the principal strain angle error decreases from 48° to 6° for the +2.5G load case, as provided in Table 22. While these significant reductions in errors relative to predicted values do support the theory that the rK21110B and rK21110C channels were switched at the DAS, the relatively high residual error coupled with limited correlation data leaves greater uncertainty than in the cases of rK11111 and rK25104.

Because the adjacent FOSS instrumentation provides strong support for the theory that the rK11111 and rK25104 data anomalies were due to switched instrumentation channels, corrected data for these locations are utilized for plots provided in Appendix C. Use of corrected data is annotated by a separate legend entry. While corrected data for rK21110 do tend to correlate better to FEM predictions, evidence of switched instrumentation is not obvious, and because it cannot be correlated to adjacent instrumentation, no correction is applied for data presented in Appendix C. Use of data from suspect channels rK21110B and rK21110C is annotated by a separate legend entry.

Table 20. Comparison of Strain Gauge rK11111 and corresponding FOSS and FEM data.

						As Report by DAS				With channels B&C switched			
						Relative to FOSS		Relative to FEM		Relative to FOSS		Relative to FEM	
	Data	DAS	DAS Corrected	FOSS	FEM	Total Error	Percent Error	Total Error	Percent Error	Total Error	Percent Error	Total Error	Percent Error
89% 2.5G	rK11111A / F2G64	98	98	75	69	23	31.1%	30	43.0%	23	31.1%	30	43.0%
	rK11111B	-1099	184		-51	NA	NA	-1048	2045.2%	NA	NA	236	-460.0%
	rK11111C /F2G70	184	-1099	-1142	-1375	1326	-116.1%	1560	-113.4%	43	-3.8%	276	-20.1%
	Maj. Prin. Angle (deg)	52	123	122	118	-70		-66		1		5	
	Maj. Prin. microstrain	1382	409	373	287	1010	270.9%	1096	382.0%	37	9.8%	122	42.7%
	Min. Prin. microstrain	-1100	-1410	-1440	-1593	340	-23.6%	494	-31.0%	30	-2.1%	183	-11.5%
	F1G138 (ref only)			-1205									
100% -1G	rK11111A / F2G64	76	76	78	126	-2	-2.2%	-50	-39.7%	-2	-2.2%	-50	-39.7%
	rK11111B	145	-17		22	NA	NA	123	568.1%	NA	NA	-39	-179.9%
	rK11111C /F2G70	-17	145	160	178	-177	-110.8%	-195	-109.7%	-15	-9.6%	-33	-18.6%
	Maj. Prin. Angle (deg)	132	46	45	48	87		85		0		-2	
	Maj. Prin. microstrain	154	243	272	285	-118	-43.4%	-131	-46.0%	-29	-10.6%	-42	-14.8%
	Min. Prin. microstrain	-95	-22	-34	19	-61	182.3%	-114	-595.0%	12	-35.1%	-41	-213.8%
	F1G138 (ref only)			266									

Table 21. Comparison of Strain Gauge rK25104 and corresponding FOSS and FEM data.

						As Report by DAS				With channels A&B switched			
						Relative to FOSS		Relative to FEM		Relative to FOSS		Relative to FEM	
	Data	DAS	DAS Corrected	FOSS	FEM	Total Error	Percent Error	Total Error	Percent Error	Total Error	Percent Error	Total Error	Percent Error
89% 2.5G	rK25104A / F6G619	-1434	1083	1074	2071	-2508	-233.5%	-3504	-169.2%	9	0.9%	-987	-47.7%
	rK25104B	1083	-1434	NA	-1219	NA	NA	2302	-188.9%	NA	NA	-215	17.6%
	rK25104C /F6G614	17	17	14	-60	3	23.6%	77	-128.9%	3	23.6%	77	-128.9%
	Maj. Prin. Angle (deg)	132	46	46	40	86		92		-1		5	
	Maj. Prin. microstrain	1225	2605	2738	3472	-1513	-55.3%	-2247	-64.7%	-133	-4.9%	-867	-25.0%
	Min. Prin. microstrain	-2641	-1504	-1650	-1461	-991	60.1%	-1180	80.8%	146	-8.8%	-43	3.0%
	F5G651 (ref only)			2673									
100% -1G	rK25104A / F6G619	157	192	159	88	-2	-1.6%	68	77.7%	33	20.9%	104	118.3%
	rK25104B	192	157	NA	125	NA	NA	67	53.5%	NA	NA	31	25.0%
	rK25104C /F6G614	-263	-263	-235	-220	-28	11.8%	-43	19.7%	-28	11.8%	-43	19.7%
	Maj. Prin. Angle (deg)	163	168	165	163	-1		1		3		6	
	Maj. Prin. microstrain	270	262	249	179	20	8.2%	90	50.2%	13	5.2%	83	46.1%
	Min. Prin. microstrain	-376	-333	-325	-311	-51	15.5%	-65	20.9%	-7	2.3%	-22	7.0%
	F5G651 (ref only)			-247									

Table 22. Comparison of Strain Gauge rK21110 and corresponding FOSS and FEM data.

						As Report by DAS				With channels B&C switched			
						Relative to FOSS		Relative to FEM		Relative to FOSS		Relative to FEM	
	Data	DAS	DAS Corrected	FOSS	FEM	Total Error	Percent Error	Total Error	Percent Error	Total Error	Percent Error	Total Error	Percent Error
89% 2.5G	rK21110A / F7G119	1543	1543	1786	1761	-243	-13.6%	-218	-12.4%	-243	-13.6%	-218	-12.4%
	rK21110B	182	964		1302			-1120	-86.0%			-338	-26.0%
	rK21110C	964	182		331			634	191.7%			-148	-44.8%
	Maj. Prin. Angle (deg)	91	49		43			48				6	
	Maj. Prin. microstrain	2363	1551		1806			557	30.9%			-255	-14.1%
	Min. Prin. microstrain	144	175		286			-142	-49.6%			-111	-38.8%
100% -1G	rK21110A / F7G119	-269	-269	-342	-317	73	-21.5%	48	-15.2%	73	-21.5%	48	-15.2%
	rK21110B	-49	-70		-119			71	-59.2%			49	-41.0%
	rK21110C	-70	-49		-121			51	-42.0%			73	-59.8%
	Maj. Prin. Angle (deg)	169	163		167			2				-3	
	Maj. Prin. microstrain	-13	-18		-79			66	-83.3%			62	-77.7%
	Min. Prin. microstrain	-326	-300		-359			33	-9.2%			59	-16.4%

7.2.5 Discussion & Possible Sources of Prediction Discrepancy

While most data did correlate very strongly with predicted models, the discrepancy between the tip deflection and the 'with skin offset' FEM was unexpected, even after correcting for rigid body rotation and considering the small angle errors that may develop in stringpot data. The 'with skin offset' FEM captured the geometric effects of increased shim thickness beneath the skins, thus resulting in increased second moment of area, and therefore, a prediction of a stiffer response. It is noted that the test results did indicate that the wing was stiffer than the 'no skin offset' model predicts, which indicated some stiffening of the wing as compared to the 'no skin offset' FEM. It is noted that the deflection data did remain bounded by the two predictions.

In evaluating the discrepancy in deflection measurements vs predictions, two sources of error are quantifiable. The first, and largest, is the rigid body rotation, which develops at the boundary condition. By measuring the rotation of the wing root and comparing to the predicted rotations, the net rigid body rotation not accounted for in the FEM was found. These greater-than-predicted rotations account for approximately 3.38 in. of deflection at the tip for the +2.5G case, and 0.36 in. of deflection for the -1G case. The second source of error is the small angle error that develops at the stringpots due to span shortening. For the +2.5G case, this can account for up to 0.3 in. error (as an overmeasurement).

The most likely source of discrepancy in the tip deflection model was in the fastener joint stiffness. While the skins were offset due to increased liquid shim thickness, no correction was applied to account for increased joint thickness / compliance resulting for the thicker nonstructural shim. In fact, all fasteners were modeled with an arbitrarily high stiffness value ($1x10^6$ lb/in) to simulate a near-rigid fastener joint. The increased joint thickness likely resulted in a more compliant joint, which may admit greater shear deformation between the skins and spars. Greater than anticipated shear deformation of the wing could have contributed to larger deflections than modeled.

It is noted that spar web shear strains do not deviate significantly from predictions – the +2.5G case shows strains at or slightly below predicted values, while the -1G test data shows shear strains at or slightly greater than predictions. Therefore, if additional shear deformation occurred in the test article, it is likely to have occurred at the skin/spar interface, rather than at the spar webs. It is also noted that both FEM predictions were consistent in spar web shear strain predictions, as the skin offsets did not significantly affect shear load distribution because the wing shear stiffness was not affected by the offset. Unfortunately, no instrumentation to measure the shear motion of the skins relative to the spars was present.

While the 'with skin offset' FEM appeared to underpredict static deflections by approximately 13% in the +2.5G test case, the ground vibration testing results correlated very well. Typically, a 13% overprediction of stiffness (as observed in the static loads testing) would correspond to a 6% overprediction in natural frequency, yet this is not observed in the GVT results. One possible explanation that is consistent with the fastener/joint compliance hypothesis is that for the small deflections and loads associated with the GVT were not sufficient to overcome the static friction in the joints.

An evaluation of the fastener stiffnesses may be performed by modifying each fastener stiffness to a more realistic value. Huth stiffness calculations are recommended as a starting point, and subsequent tuning could be performed to see if the model can be 'tuned' to achieve the measured tip deflection while maintaining reasonable values for fastener stiffnesses.

A second factor that may contribute to modeling errors is the wing thickness measurement error. Because the wing skins were profiled in jig shape, it was necessary to perform the measurement in two different positions as simultaneous access to both skins was not available due to the geometry of the jig cradles. Once the lower skin was profiled (while the wing was resting on the upper skin cradle), the wing was flipped into the lower skin cradle, the laser measurement system realigned to the wing, and the upper skin was profiled. While it was expected that each skin profile was individually accurate within typical laser tracker error, it is possible that an additional, larger measurement error of the skins relative to each may have been incurred due to the realignment process. This hypothesis could be ascertained by repeating the skin measurements in a single setup. The AFRC test fixture would provide an ideal fixture for conducting this measurement, as the 14 hydraulic load locations could be utilized to maintain jig shape while affording simultaneous access to both skins.

Two additional explanations were also considered but are considered unlikely to be primary contributors to increased tip deflection. The first explanation that was considered is softening due to local skin bending or buckling. However, no significant buckling was observed during the test. Of the skin bays and ribs instrumented with back-to-back strain gauges, the local bending strains generally remained low and relatively linear. Locations showing a nonlinear trend were readily explained by nonlinear analysis without a corresponding increase in global tip deflection. The second explanation considered to be unlikely is lower than modeled material moduli. Material moduli are based on unnotched tension coupon test data for representative laminates (for the tow-steered skin) or the NCAMP database (for the ribs and spars). It is noted that one potential source of error is the difference in tensile and compressive modulus. For this effort, the modulus used for the skin laminate was based on the unnotched tensile coupon test results (12.446 msi in the longitudinal direction). However, it is noted that the unnotched compressive modulus (10.764 msi) was found to be 13.5% lower than the tensile modulus. It is noted that lower material modulus generally results in higher than predicted skin strains, which is not significantly observed.

8 Recommendations for Future Research

This project has demonstrated the feasibility of utilizing high-fidelity MDAO architecture to achieve a tow-steered skin design that achieves improved performance compared to an unsteered wing for static aeroelastic load conditions. It was further demonstrated that the resulting designs are manufacturable and largely behave as predicted using traditional FEM techniques with spatially varying material orientations to represent the tow-steering topology. In parallel, significant progress has been made toward advancing the state-of-the-art in high-aspect ratio topology optimization.

The following are suggested areas for continued research:

1. Tuning of the Test Article FEM to match observed tip deflection

While most test data correlated closely to predictions, the FEM most representative of the as-built geometry underpredicted the tip deflection. While some of the discrepancy is attributed to rigid body rotation near the boundary conditions, it is likely that there was additional compliance in the model that was not currently modeled. One likely explanation is that the fastener joints were more compliant than modeled due to the increased liquid shim thickness. It may be possible to tune the FEM by adjusting individual fastener stiffnesses until the test article tip deflection is obtained. Huth fastener stiffness are suggested to be used as a starting point. Alternatively, it may be possible to reinstrument the wing to directly measure relative shear motion between the skins and spar webs. Additionally, a nonlinear material model could be utilized to account for typical reductions of laminate modulus in compression.

2. Advancements in Aircraft Optimization & System Level Benefits

2.1. Implementation of Flutter Constraints and Gust Response for Tow-Steering Optimization

The current optimization only considers static aeroelastic load conditions (+2.5G, 1G cruise, -1G), however, dynamic aeroelastic constraints such as flutter and gust response are important to consider for realistic aircraft designs. During this project, advancements in implementing flutter constraints in a high-fidelity aerostructural optimization framework have been developed [25], which should be compatible with the present tow-steering optimization.

It is recommended that the tow-steering optimization studies be performed again with active flutter and gust constraints, as these conditions may further differentiate the performance benefits of tow-steering technology compared to traditional designs.

2.2. Assessment of Tow-Steering with Complementary Technologies

The present study only considered the benefit of tow-steering in the absence of other related technology for load alleviation. Compounding benefits may be obtained by combining tow-steering technologies with other wing technologies, such as active load alleviation. By coupling both technologies in a single optimization, an accurate assessment of the combined performance, limitations, and relative benefits can be obtained.

Similarly, tow-steering has only been considered as part of the wing skins, however, tow-steering may be broadly applicable to other aerostructures. In general, any structure in which the principal load direction changes spatially may benefit by maintaining fiber alignment with the load direction. Tow-steering may be beneficial to structural members such as spars or fuselages subject to bending loads where the fiber could be oriented for shear stress at the neutral axis (e.g., spar web, fuselage waist) and steered to align with tensile or compressive fiber stresses at the spar caps or fuselage crown/keel. Tow-steering may also be beneficial in carrying load around cutouts such as access panels, windows and doors.

3. Advancement of Tow-Steering Manufacturing Technologies

The tow-steered coupons and test articles were fabricated with traditional Automated Fiber Placement equipment and pushed the limits of functionality of existing COTS software to program the desired steering paths. However, significant room for improvement exists in improving the current constraints (steering radius) and undesired features (laps/gaps and puckers). One promising technology is continuous tow-shearing, largely being developed by researchers at the University of Bristol, which enable tight-radius steering patterns to be fabricated while largely avoiding problems with puckers and significantly mitigating convergence zones. While advancements have been made in achieving production rates, this technology does require new hardware, representing a significant cost barrier to widespread adoption.

Additional research should also be performed to assess whether tow-steering utilizing traditional AFP equipment can be optimized. Possible areas for improvement include both the material (fiber, resin) and processing parameters (rates, compaction pressure, heating elements, debulk sequences, etc..) as well as a study of tow-path generation and resulting machine code, which may benefit from being included earlier in the optimization process so that the resulting tow-steering pattern is optimized not only for design, but also for fabrication.

4. Research of Tow-Steering Analysis, Test, and Certification

While the present study shows promising benefits for tow-steering, any new technology must be certified before its benefits may be realized on an operational aircraft. Tow-steered laminates introduce particular challenges in the test and certification process compared to traditional AFP laminates, due to the larger degree to which laps and gaps and puckers can develop. If these features cannot be eliminated from the manufacturing process through additional M&P development, then they must be addressed during the

analysis, test and certification process. Techniques to accurately and reliably predict the occurrence and effects of these features is required. Because the tow-steering process so significantly opens the design space, it is anticipated that traditional composite material testing matrices will quickly become intractable. Therefore, advancements in the analysis and cost-effective testing must be developed prior to certification.

5. Through Thickness Optimization

The present study has made significant advancements in developing state-of-the-art tools for large scale 3D topology optimization, which has resulted in the solution of some of the largest stress and frequency-constrained problems attempted. While significant progress has been obtained toward an ambitious goal, additional research and development is required to efficiently optimize highly resolved, high-aspect ratio wing topologies.

9 Acknowledgements

Substantial contributions to this project were made by subcontractors at the University of Michigan for tow-steering and aeroelastic analysis and general design and testing support; and Georgia Institute of Technology for topology optimization. In particular, Dr. Joaquim Martins, Dr. Carlos Cesnik, Timothy Brooks and Christopher Lupp performed the tow-steering optimization, aeroelastic analysis and made contributions to the design, analysis and testing of the uCRM-13.5 test article. Computational resources for the tow-steering optimization were provided by Extreme Science and Engineering Discovery Environment (XSEDE), which is supported by the National Science Foundation grant number ACI-1053575. Funding for the later tow-steering optimization studies was provided by the University of Michigan.

Dr. Graeme Kennedy, Ting Wei Chin, and Mark Leader performed the topology optimization work at Georgia Institute of Technology.

10 References

[1] T. R. Brooks, Design Optimization of Flexible Aircraft Wings Using Tow-steered Composites, Ann Arbor, MI: PhD thesis, University of Michigan, 2018.

[2] T. R. Brooks, J. R. R. A. Martins and G. J. Kennedy, "High-fidelity aerostructural optimization of tow-steered composite wings," *Journal of Fluids and Structures,* vol. 88, pp. 122-147, 2019.

[3] J. Vassberg, "Introduction: Drag Prediction Workshop," *Journal of Aircraft,* vol. 45, no. 6, pp. 737-737, 2008.

[4] T. R. Brooks, G. K. W. Kenway and J. R. R. A. Martins, "Benchmark Aerostructural Models for the Study of Transonic Aircraft Wings," *AIAA Journal,* vol. 56, pp. 2840-2855, 2018.

[5] M. L. Bucalem and K.-J. Bathe, "Higher-order MITC general shell elements," *International Journal for Numerical Methods in Engineering,* vol. 36, no. 21, pp. 3729-3754, 1993.

[6] G. J. Kennedy and J. R. R. A. Martins, "A parallel aerostructural optimization framework for aircraft design studies," *Structural and Multidisciplinary Optimization,* vol. 50, no. 12, pp. 1079-1101, 2014.

[7] G. K. W. Kenway, G. J. Kennedy and J. R. R. A. Martins, "Scalable Parallel Approach for High-Fidelity Steady-State Aeroelastic Analysis and Derivative Computations," *AIAA Journal,* vol. 52, no. 5, pp. 935-951, 2014.

[8] Z. Lyu, G. K. Kenway, C. Paige and J. R. R. A. Martins, "Automatic Differentiation Adjoint of the Reynolds-Averaged Navier--Stokes Equations with a Turbulence Model," in *21st AIAA Computational Fluid Dynamics Conference*, p. 2581, 2013.

[9] C. A. Mader, G. Kenway and J. R. R. A. Martins, "Towards High-Fidelity Aerostructural Optimization Using a Coupled ADjoint Approach," in *Proceedings of the 12th AIAA/ISSMO Multidisciplinary Analysis and Optimization Conference*, p. 5968, 2008.

[10] G. J. Kennedy and J. R. R. A. Martins, "A Parallel Finite-Element Framework for Large-Scale Gradient-Based Design Optimization of High-Performance Structures," *Finite Elements in Analysis and Design,* vol. 87, no. 9, pp. 56-73, 2014.

[11] L. Uyttersprot, Inverse Distance Weighting Mesh Deformation, M. Sc. Thesis, Delft University of Technology, 2014.

[12] S. A. Brown, "Displacement Extrapolation for CFD+CSM Aeroelastic Analysis," in *Proceedings of the 35th AIAA Aerospace Sciences Meeting*, p. 1090, 1997.

[13] P. E. Gill, W. Murray and M. A. Saunders, "SNOPT: An SQP algorithm for large-scale constrained optimization," *SIAM Review,* vol. 47, no. 1, pp. 99-131, 2005.

[14] R. E. Perez, P. W. Jansen and J. R. R. A. Martins, "pyOpt: A Python-Based Object-Oriented Framework for Nonlinear Constrained Optimization," *Structural and Multidisciplinary Optimization,* vol. 45, no. 1, pp. 101-118, 2012.

[15] A. B. Lambe, J. R. R. A. Martins and G. J. Kennedy, "An Evaluation of Constraint Aggregation Strategies for Wing Box Mass Minimization," *Structural and Multidisciplinary Optimization,* vol. 55, no. 1, pp. 257-277, 2017.

[16] G. Kreisselmeier and R. Steinhauser, "Application of Vector Performance Optimization to a Robust Control Loop Design for a Fighter Aircraft," *International Journal of Control,* vol. 37, pp. 251-284, 1983.

[17] W. J. Stroud and N. Agranoff, "Minimum-mass design of filamentary composite panels under combined loads: Design procedure based on simplified buckling equations," NASA TN D-8257, Washington, DC, Oct 1976.

[18] G. J. Kennedy, G. K. W. Kenway and J. R. R. A. Martins, "High Aspect Ratio Wing Design: Optimal Aerostructural Tradeoffs for the Next Generation of Materials," in *Proceedings of the AIAA Science and Technology Forum and Exposition (SciTech)*, p. 0596, 2014.

[19] G. J. Kennedy, G. K. Kenway and J. R. R. A. Martins, "A Comparison of Metallic, Composite and Nanocomposite Optimal Transonic Transport Wings," NASA CR–2014-218185, 2014.

[20] T. R. Brooks and J. R. R. A. Martins, "On Manufacturing Constraints for Tow-steered Composite Design Optimization," *Composite Structures,* vol. 204, pp. 548-559, 2018.

[21] G. K. W. Kenway and J. R. R. A. Martins, "Multipoint High-Fidelity Aerostructural Optimization of a Transport Aircraft Configuration," *Journal of Aircraft,* vol. 51, no. 1, pp. 144-160, 2014.

[22] T. W. Sederberg and S. R. Parry, "Free-form Deformation of Solid Geometric Models," *SIGGRAPH Comput. Graph.,* vol. 20, no. 4, pp. 151-160, 1986.

[23] Federal Aviation Administration, *Federal Aviation Regulations, Part 25 --- Airworthiness Standards: Transport Category Airplanes,* 2009.

[24] O. Stodieck, J. E. Cooper, P. M. Weaver and P. Kealy, "Aeroelastic Tailoring of a Representative Wing Box Using Tow-Steered Composites," *AIAA Journal,* vol. 55, no. 4, pp. 1425-1439, 2017.

[25] E. Jonsson, C. A. Mader, J. R. R. A. Martins and G. J. Kennedy, "Computational Modeling of Flutter Constraint for High-Fidelity Aerostructural Optimization," in *AIAA Scitech 2019 Forum*, p. 2354, 2019.

[26] B. K. Stanford and C. V. Jutte, "Comparison of curvilinear stiffeners and tow steered composites for aeroelastic tailoring of aircraft wings," *Computers & Structures,* vol. 183, pp. 48-60, 2017.

[27] G. K. W. Kenway and J. R. R. A. Martins, "Buffet Onset Constraint Formulation for Aerodynamic Shape Optimization," *AIAA Journal,* vol. 55, no. 6, pp. 1930-1947, 2017.

[28] K. L. Napolitano and N. C. Yoder, "Fixed Base FRF Using Boundary Measurements as References: Analytical Derivation," *Topics in Modal Analysis I,* vol. 5, pp. 299-308, 2012.

[29] M. H. Shirk, T. J. Hertz and T. A. Weisshaar, "Aeroelastic tailoring - Theory, practice, and promise," *Journal of Aircraft,* vol. 23, no. 1, pp. 6-18, 1986.

[30] K. S. Raju and J. S. Tomblin, "AGATE STATISTICAL ANALYSIS PROGRAM," National Institute for Aviation Research, 2004 - Version 1. [Online]. Available: http://www.niar.wichita.edu/agate/Documents/Materials/ASAP_2004_v1.xls.

11 Attachments

The following Aurora proprietary attachments have been provided to NASA as part of the final report documentation:

1. Aurora Flight Sciences, "Rib Defect, Disposition and Repair Report," Aurora Flight Sciences, Manassas, VA, February 20, 2017.
2. Aurora Flight Sciences, "PAT LE Spar NDI Indication List and PAT 203 NDI Indication Map," Aurora Flight Sciences, Manassas, VA, 2017.
3. Aurora Flight Sciences, "Discrepancy Report (DR) & Disposition Instructions (DI)," Aurora Flight Sciences, Manassas, VA, February 13, 2018
4. Aurora Flight Sciences, "Spar MRB Discrepancy Report (DR) & Disposition Instructions (DI)," Aurora Flight Sciences, Manassas, VA, December 8, 2017
5. Aurora Flight Sciences, “Rib 42-47 MRB Discrepancy Report & Disposition Instructions,” Aurora Flight Sciences, Manassas, VA, December 12, 2017
6. Aurora Flight Sciences, “MASS Properties Bill of Material,” Aurora Flight Sciences, Manassas, VA, March 2, 2018
7. Aurora Flight Sciences, “Tow-Steering Mechanical Coupon Test Results,” Aurora Flight Sciences, Manassas, VA, March 31, 2016

Appendix A. Bend-twist Coupling Quantification

When comparing the amount of passive load alleviation introduced into the design through material bend-twist coupling, it is useful to define a metric to measure the local degree of coupling in the wing. It is well-known from classical laminate theory CLT that the bend-twist coupling in a laminate structure is closely related to the laminate bending stiffness matrix, $\boldsymbol{D}$. This stiffness matrix relates the midplane bending curvatures of a laminate panel, $\boldsymbol{\kappa}$, to the moment resultants, $\boldsymbol{M}$, as shown below:

$$\begin{bmatrix} M_{xx} \\ M_{yy} \\ M_{xy} \end{bmatrix} = \begin{bmatrix} D_{11} & D_{12} & D_{16} \\ D_{12} & D_{22} & D_{26} \\ D_{16} & D_{26} & D_{66} \end{bmatrix} \begin{bmatrix} \kappa_{xx} \\ \kappa_{yy} \\ \kappa_{xy} \end{bmatrix} \tag{12}$$

where D_{11}, D_{66}, D_{16}, and D_{26} are components of the bending stiffness matrix, $\boldsymbol{D}$. The degree of spanwise bend-twist coupling is determined by the magnitude and sign of the off-diagonal term, D_{16}. The typical way of increasing this term is by using increasingly unbalanced ply orientations in the laminate layup.

Shirk et al. [29] introduced a nondimensional coupling parameter to measure the magnitude of this term given by:

$$\psi_1 = \frac{D_{16}}{\sqrt{D_{11}D_{66}}}. \tag{13}$$

This parameter was originally derived for the aeroelastic analysis for a cantilevered composite plate. We extend this for the case of a thin-walled wing box by treating it as a "sandwich" structure. This allows the effective bending stiffness matrix, $\boldsymbol{D}^{\text{eff}}$, to be computed for each pair of wing skin panels along the span of the wing box, as shown in Figure A.1

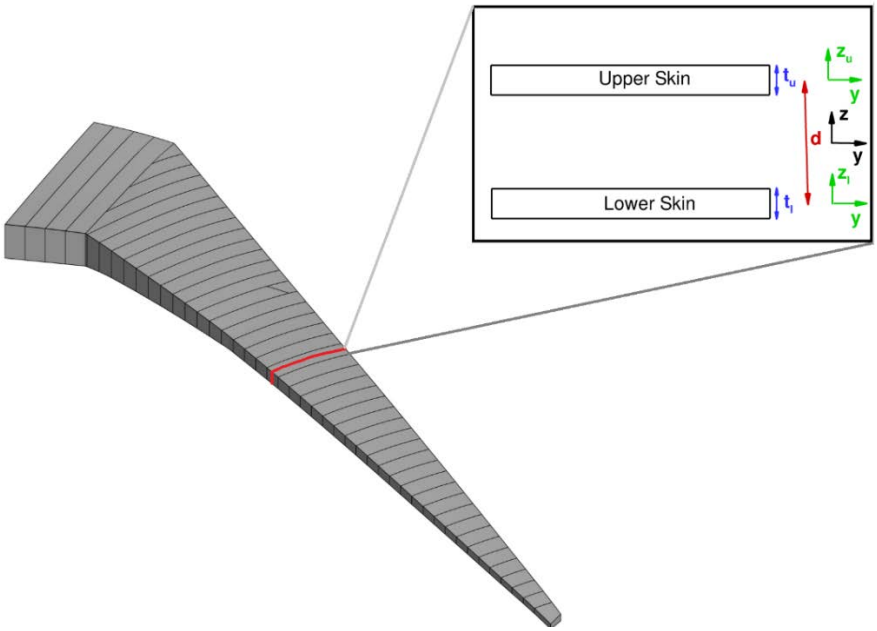

Figure A.1. Cross-sectional view of typical wing box skin panels.

The bending stiffness matrix for a sandwich structure is

$$\boldsymbol{D}^{eff} = \left(\frac{d}{2}\right)^2 (\boldsymbol{A}_u + \boldsymbol{A}_l) \tag{14}$$

where $\boldsymbol{A}_u$ and $\boldsymbol{A}_l$ are the membrane stiffness matrices for each spanwise pair of upper and lower skin panels, respectively, and d is the local wing box depth at each location. In this calculation, the effect of the spars and ribs are neglected. This is acceptable, since the spars and ribs (which are made of balanced plies) make no contribution to the bend-twist coupling of the wing.

The components of $\boldsymbol{D}^{eff}$ can be substituted into Equation 8, and then the effect of the wing box depth, d, cancels out, yielding

$$\psi_1 = \frac{A_{u_{16}} + A_{l_{16}}}{\sqrt{(A_{u_{11}} + A_{l_{11}})(A_{u_{66}} + A_{l_{66}})}}. \tag{15}$$

This means that ψ_1 ultimately only depends on the components of the membrane stiffness of each skin panel, $\boldsymbol{A}_u$ and $\boldsymbol{A}_l$. Because in this study the panel thickness and ply orientation vary within the panel, and thus so do $\boldsymbol{A}_u$ and $\boldsymbol{A}_l$, the membrane stiffness for each panel is approximated by averaging the values in each panel. Computing the coupling parameter at each spanwise wing box section allows one to identify regions of the wing box design for which the optimizer is taking advantage of the additional aeroelastic tailoring offered by anisotropy.

Appendix B. Normalized Tow-Steering Coupon Test Data

Tow-steering coupon test results are aggregated in Table 23 – Table 31. Strengths and elastic moduli were normalized to the corresponding unsteered laminate value for comparison, i.e., a relative strength or stiffness value of 1.0 is shown for all unsteered laminates. The b-basis estimate for strength was based on the statistical calculation provided by the Advanced General Aviation Transport Experiments (AGATE) Statistical Analysis Program (ASAP) calculator [30] for the indicated population (single batch, single environment). In cases where multiple tow-steering groups were tested (e.g., divergence, curvature, or neutral), a combined group was also reported that combines all tow-steered coupons for that test. Due to the increased population size of the combined group, the b-basis estimated strength was often greater than the individual results due to greater confidence. When comparing the b-basis values, it is important to consider the number of samples as well as coefficient of variance since both factors heavily influence the estimate.

The largest difference in performance between tow-steered and unsteered laminates was observed in the longitudinal unnotched tension results. As shown in Table 23, the mean strength of the steered divergence group was less than 75% of that of the unsteered laminates. Coupons taken from moderate-curvature/moderate-divergence regions of tow-steering had slightly greater strength with a mean of approximately 85% of the unsteered strength. Both tow-steered groups exhibited high coefficients of variation, depressing the estimated b-basis strengths. Overall, modulus was relatively unaffected with the mean tow-steering values within 2% of the unsteered samples and relatively low coefficient of variation. It was noted that the high-divergence group had lower mean strength and higher variation than the moderate-curvature, moderate-divergence group.

The difference in relative strength was less pronounced in the transverse direction, as indicated in Table 24. The coefficient of variation of the transverse unnotched specimens was also lower than for the longitudinal case. As with the longitudinal case, the modulus values remained with 6% of the unsteered laminate values.

Table 23. Longitudinal unnotched tension results.

Panel I.D.	Steered - Divergence	Steered - Neutral	Unsteered	Steered (Combined)
No. of Specimens tested	5	5	4	10
Mean Strength (normalized)	0.747	0.847	1.000	0.797
Coeff. Of Var. (%)	17.67	12.49	3.57	15.62
Modulus (normalized)	1.005	0.985	1.000	0.995
Coeff. Of Var. (%)	2.81	2.89	1.28	2.89
b-basis Est. Strength (normalized)	0.259	0.521	1.000	0.624

Table 24. Transverse unnotched tension results.

Panel I.D.	Steered - Divergence	Steered - Neutral	Unsteered	Steered (Combined)
No. of Specimens tested	5	5	4	10
Mean Strength (normalized)	0.939	0.945	1.000	0.942
Coeff. Of Var. (%)	6.45	8.23	3.73	6.99
Modulus (normalized)	1.030	1.058	1.000	1.044
Coeff. Of Var. (%)	2.41	3.06	0.66	2.96
b-basis Est.Strength (normalized)	0.882	0.800	1.000	0.999

Table 25. Longitudinal unnotched compression results.

Panel I.D.	Steered - Neutral	Unsteered
No. of Specimens tested	5	5
Mean Strength (normalized)*	0.977	1.000
Coeff. Of Var. (%)*	9.98	4.53
Modulus (Tool Side) (normalized)	0.923	1.000
Coeff. Of Var. (%)	16.86	2.54
Modulus (Bag Side) (normalized)	0.971	1.000
Coeff. Of Var. (%)	3.89	1.85
b-basis Est.Strength* (normalized)	0.709	1.000

*includes data from invalid failure modes for compression

Table 26. Transverse unnotched compression results.

Panel I.D.	Steered - Divergence	Steered - Neutral	Unsteered	Steered (Combined)
No. of Specimens tested	5	5	5	10
Mean Strength (normalized)	0.984	1.018	1.000	1.001
Coeff. Of Var. (%)	7.37	4.71	9.24	6.06
Modulus (Tool Side) (normalized)	1.073	1.016	1.000	1.044
Coeff. Of Var. (%)	4.94	4.74	2.60	5.38
Modulus (Bag Side) (normalized)	0.965	0.957	1.000	0.961
Coeff. Of Var. (%)	2.86	6.91	2.01	4.99
b-basis Est.Strength (normalized)	1.106	1.323	1.000	1.375

Tow-steering effects appeared to be less pronounced for the unnotched compressive coupons. For unnotched longitudinal compression, the mean strength values of the steered coupons were within 3% of the unsteered values, albeit with higher coefficient of variance, as indicated in Table 25 (it is noted that several specimens within this group failed via end-brooming; an invalid failure mode for determining strength). The transverse compression values (Table 26) were even closer, with the mean strength with 2% of the unsteered coupons, and generally lower coefficients of variation.

Open hole tension test results generally exhibited less variation than the unnotched test results. Tow-steered coupons dominated by high curvature achieved 93.5% of the mean tensile strength of unsteered laminates, while high-divergence steered laminates achieved a mean strength of 96.2% of the unsteered control group, as shown in Table 27. As with the unnotched laminates, the high-divergence group had greater coefficient of variation.

For the transverse open hole tension results, as shown in Table 28, the mean strengths for the tow-steered values remained near the unsteered mean strengths, with the curvature-dominated coupons averaging 107% of the unsteered coupons and the divergence-dominated coupons averaging almost 96% of the unsteered strengths. It was noted that for the transverse OHT results, the curvature-dominated specimens exhibited higher coefficient of variance than the divergence-dominated specimens, opposite of the findings for the transverse case. This difference may be partially explained by the correlation between divergence and curvature for orthogonal plies; the transverse plies in a high-curvature, low-divergence region (as measured by the longitudinal plies) was actually low curvature, high divergence.

Table 27. Longitudinal open hole tension results.

Panel I.D.	Steered - Curvature	Steered - Divergence	Unsteered	Steered (Combined)
No. of Specimens tested	4	4	5	8
Mean OHT Strength (normalized)	0.935	0.962	1.000	0.948
Coeff. Of Var. (%)	6.31	12.60	5.37	9.43
Modulus (normalized)	0.976	1.003	1.000	0.989
Coeff. Of Var. (%)	2.02	6.03	1.84	4.45
b-basis Est.Strength (normalized)	0.759	0.329	1.000	0.904

Table 28. Transverse open hole tension results.

Panel I.D.	Steered - Curvature	Steered - Divergence	Unsteered	Steered (Combined)
No. of Specimens tested	4	4	4	8
Mean OHT Strength (normalized)	1.072	0.959	1.000	1.016
Coeff. Of Var. (%)	6.67	3.06	3.69	7.77
Modulus (normalized)	1.008	0.949	1.000	0.978
Coeff. Of Var. (%)	2.61	0.56	1.12	3.68
b-basis Est.Strength (normalized)	0.836	1.004	1.000	1.019

Table 29. Longitudinal open hole compression results.

Panel I.D.	Steered - Curvature	Steered - Divergence	Unsteered	Steered (Combined)
No. of Specimens tested	5	5	5	10
Mean OHC Strength (normalized)	0.930	1.079	1.000	1.005
Coeff. Of Var. (%)	4.66	12.85	9.40	12.39
Modulus (normalized)	0.993	0.967	1.000	0.980
Coeff. Of Var. (%)	1.72	4.93	0.97	3.72
b-basis Est.Strength (normalized)	1.225	0.830	1.000	1.143

Table 30. Transverse open hole compression results.

Panel I.D.	Steered - Curvature	Steered - Divergence	Unsteered	Steered (Combined)
No. of Specimens tested	5	5	5	10
Mean OHC Strength (normalized)	1.027	0.977	1.000	1.002
Coeff. Of Var. (%)	8.16	4.26	4.23	6.76
Modulus (normalized)	0.988	0.915	1.000	0.951
Coeff. Of Var. (%)	9.52	8.81	6.99	9.59
b-basis Est.Strength (normalized)	0.826	0.975	1.000	1.013

For the longitudinal open hole compression, as provided in Table 29, the curvature-dominated tow steered coupons achieved 93% of the mean strength found in the unsteered coupons, while the divergence-dominated specimens achieved nearly 108% strength, albeit with higher coefficient of variation. The transverse open hole compression specimens performed more closely to the unsteered laminates. The high-curvature specimens exhibited nearly 103% of the unsteered mean strength and the divergence-dominated specimens achieved almost 98% strength, as shown in Table 30. The same trend was observed in the open hole tensile specimens as in the open hole compression specimens: the curvature-dominated specimens underperformed the divergence-dominated specimens in longitudinal tests but outperformed in transverse tests.

Table 31. Combined (T12 and T21) v-notch shear results.

Panel I.D.	Steered - Curvature	Steered - Divergence	Unsteered	Steered (Combined)
No. of Specimens tested	10	10	10	20
Mean Shear Strength (normalized)	0.961	0.987	1.000	0.974
Coeff. Of Var. (%)	3.35	5.24	5.49	4.5175
Shear Modulus (normalized)	1.045	1.017	1.000	1.031
Coeff. Of Var. (%)	6.00	6.42	7.94	6.1972
b-basis Est.Strength (normalized)	1.019	0.994	1.000	1.026

V-notch shear testing (results provided in Table 31), showed little variation between steered and unsteered specimens: curvature-dominated specimens achieved 96% of the unsteered mean strength, although with *lower* coefficient of variation, while divergence-dominated specimens achieved almost 99% of the mean strength, with a similar coefficient of variation.

Figure B.1 shows examples of unnotched tensile coupons after testing; Figure B.2 shows examples of open hole tension coupons after testing. In both cases, the directionality of splintering reveals the dominant fiber direction; longitudinal coupons exhibited greater splintering in the 0° direction, while transverse coupons exhibited splintering in the 90° direction.

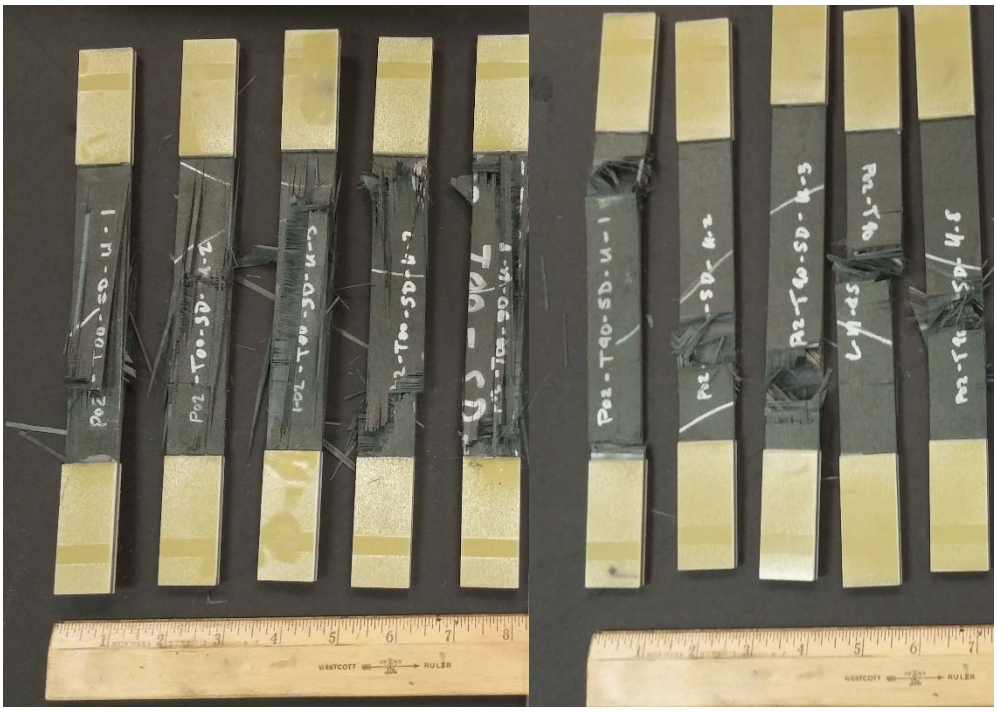

Figure B.1. Longitudinal (left) and transverse (right) unnotched tension coupons from divergence-dominated tow-steering panels.

Figure B.2. Longitudinal (left) and transverse (right) OHT coupon from curvature-dominated tow-steering panels.

Appendix C. Strain Correlation

The following correlation plots compare the predicted strain from FEM models to the measured strain during static +2.5G and -1G testing. FEM predictions are provided for both the “with skin offset” and “no skin offset” models, as described in Section 6. The test data were taken at 100% load for the -1G case, and at 89% load for the +2.5G.

For correlation to FOSS test data, results from the FEMs were linearly interpolated along the FOSS reference line locations shown in Figure C.1, which correspond to the fiber optic strain sensing (FOSS) locations. Strains were transformed from the global coordinate system to a local coordinate system, where the ‘spanwise’ direction is locally aligned to the FOSS fiber direction. The FOSS correlation reference lines were utilized for the FEM data presented in C.3 thru Figure C.6. While strain gauge data are also provided in the FOSS correlation plots, it is noted that in general, the strain gauges may be a few inches away from the FOSS fiber and were generally oriented differently, particularly for the trailing edge gauges, which may contribute to differences in FOSS and strain gauge measurements.

For correlation to strain gauge data, FEM results were linearly interpolated along strain gauge reference lines shown in Figure C.2 to more closely align to actual strain gauge locations. For strain gauge correlation predictions, the FEM data are transformed from the global coordinate system to a local coordinate system aligned with the strain gauge axis. For data in the root section, inboard of y = 32”, no transformation was applied; the “spanwise” remained aligned to global-Y and the “chordwise” direction remained aligned to global-X. For data outboard of y = 32”, strain predictions were transformed to align with the LE sweep angle, so that “spanwise” data followed the LE spar, and the “chordwise” direction was 90 degrees orthogonal, aligning roughly with rib orientation. The strain gauge correlation reference lines were utilized for the FEM data presented in C.11 thru Figure C.30.

While the strain gauge correlation reference lines generally intersected the strain gauge vertices, not all strain gauges used for correlation were located exactly on the reference lines. For strain gauges used for correlation, the following gauges were located more than 0.5” off the correlation lines:

Upper Skin:
rK12102 – at y = 117.4; 6.6” from MC correlation line (towards TE)
aK11201 – at y = 64.77, 1.1” from MC correlation line (towards TE)
aK11103 – at y = 44.08, 0.6” from MC correlation (towards TE)
rK11121 – at y = 30.34, 1.8” from TE correlation line (towards TE)

Lower Skin:
rK21119 – at y = 45.49, 1.9” from TE correlation line (towards LE)

For principal strain angle results, the angle is reported relative to global X-axis, as depicted by θ in Figure C.2. It is further noted that the principal angle reported corresponds to the major principal strain if the skin is predominantly in tension (e.g., the lower skin for +2.5G and the upper skin for -1G) or the minor principal strain direction if

the skin is predominantly in compression (the upper skin for +2.5G and the lower skin for -1G).

Strain transformations were applied utilizing a rotation matrix, as described by Equation 16.

$$[A] = \begin{bmatrix} \cos^2\theta & \sin^2\theta & 2\cos\theta\sin\theta \\ \sin^2\theta & \cos^2\theta & -2\cos\theta\sin\theta \\ -\cos\theta\sin\theta & \cos\theta\sin\theta & \cos^2\theta - \sin^2\theta \end{bmatrix}$$

$$[R] = \begin{bmatrix} 1 & 0 & 0 \\ 0 & 1 & 0 \\ 0 & 0 & 2 \end{bmatrix} \tag{16}$$

$$\begin{bmatrix} \varepsilon_x{}' \\ \varepsilon_y{}' \\ \gamma_{xy}{}' \end{bmatrix} = [R][A][R]^{-1} \begin{bmatrix} \varepsilon_x \\ \varepsilon_y \\ \gamma_{xy} \end{bmatrix}$$

Principal angles and strains were calculated according to Equation 17. It is noted that after the major and minor principal strains (ε_1 and ε_2, respectively) were computed, they were checked to ensure that the customary ordering $\varepsilon_1 > \varepsilon_2$ was intact, else θ_ε was incremented by 90° and the principal strains swapped.

$$\theta_\varepsilon = \frac{1}{2}\tan^{-1}\frac{\gamma_{xy}}{\varepsilon_x - \varepsilon_y}$$

$$[Q] = \begin{bmatrix} \cos\theta_\varepsilon & \sin\theta_\varepsilon \\ -\sin\theta_\varepsilon & \cos\theta_\varepsilon \end{bmatrix} \tag{17}$$

$$\begin{bmatrix} \varepsilon_1 & \\ & \varepsilon_2 \end{bmatrix} = [Q] \begin{bmatrix} \varepsilon_x & \frac{\gamma_{xy}}{2} \\ \frac{\gamma_{xy}}{2} & \varepsilon_y \end{bmatrix} [Q]^{-1}$$

Finally, it is noted that while the extensional strain values corresponding to strain gauge grids aligned to a normal strain direction of interest (e.g., spanwise or chordwise) were used directly, the shear strain value was computed based on all three legs of rosette strain gauge. For a rectangular rosette where the 'B' leg bisects the orthogonal 'A' and 'C' legs corresponding to the local x- and y- axes, respectively, the shear strain was computed according to Equation 18.

$$\gamma_{xy} = 2\varepsilon_B - \varepsilon_A - \varepsilon_C \tag{18}$$

It is noted that the skin rosette strain gauges were generally (but not always) placed with the 'A' leg in the local sweep-aligned spanwise direction and the 'C' leg in the relative chordwise direction, such that the right-handed normal direction points outward from the skin OML. The FEM normal direction, however, points *inward* from the skin IML, therefore, the FEM Z1 skin surface results are used to correlate to OML strain gauges (the Z2 skin surface results correlates to IML strain gauges) and the sign corresponding to shear

strains (e.g., γ_{xy}) is flipped for the FEM data for both skins. Both of these nuances are corrected for in the following results.

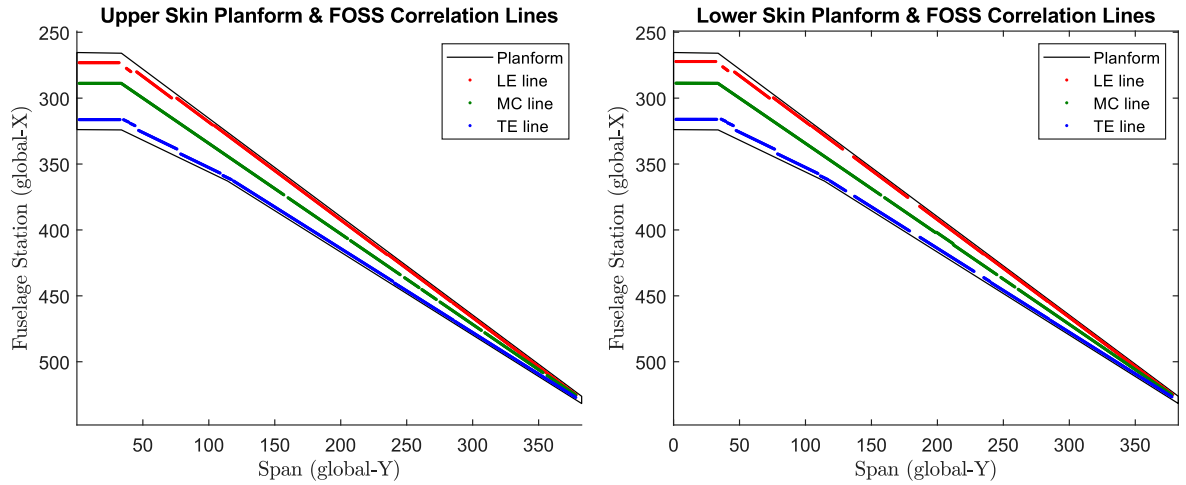

Figure C.1. Test article planform, FOSS reference lines and global axes directions. **FOSS predictions are aligned to local FOSS direction.**

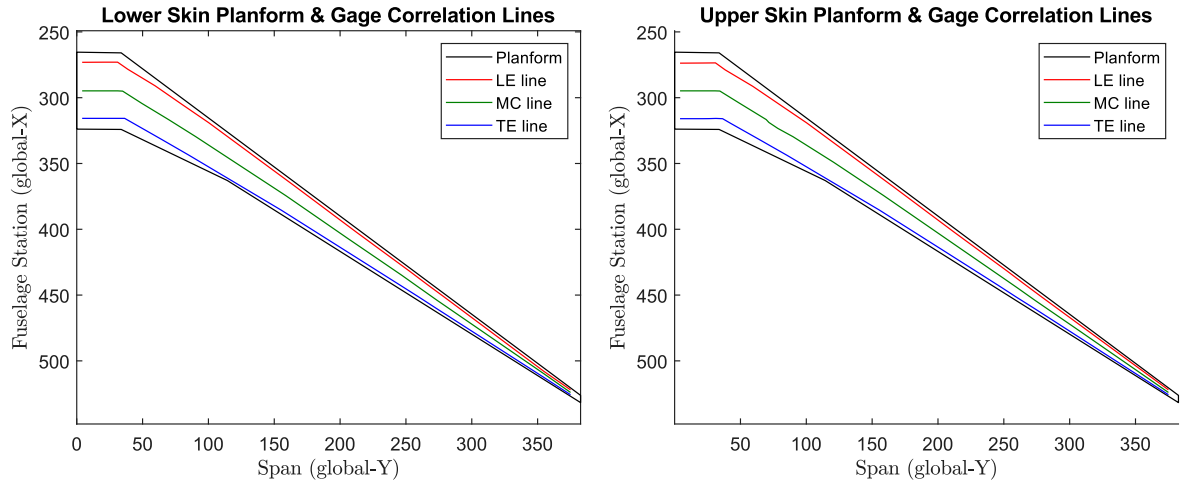

Figure C.2. Test article planform, strain gauge correlation lines and global axes directions. **Strain gauge predictions are aligned to the local LE spar.**

In accordance with the discussion in Section 7.2.4 pertaining to the strain gauge anomalies at rK11111, rK25104 and rK21110, any quantity relying on strain gauge data from rK11111B, rK11111C, rK25104A, or rK25104B is labeled as “Corrected Strain Gauge Data” and any quantity relying on strain gauge data from rK21110B or rK21110C is labeled as “Suspect Strain Gauge Data.”

FOSS Strain Plots

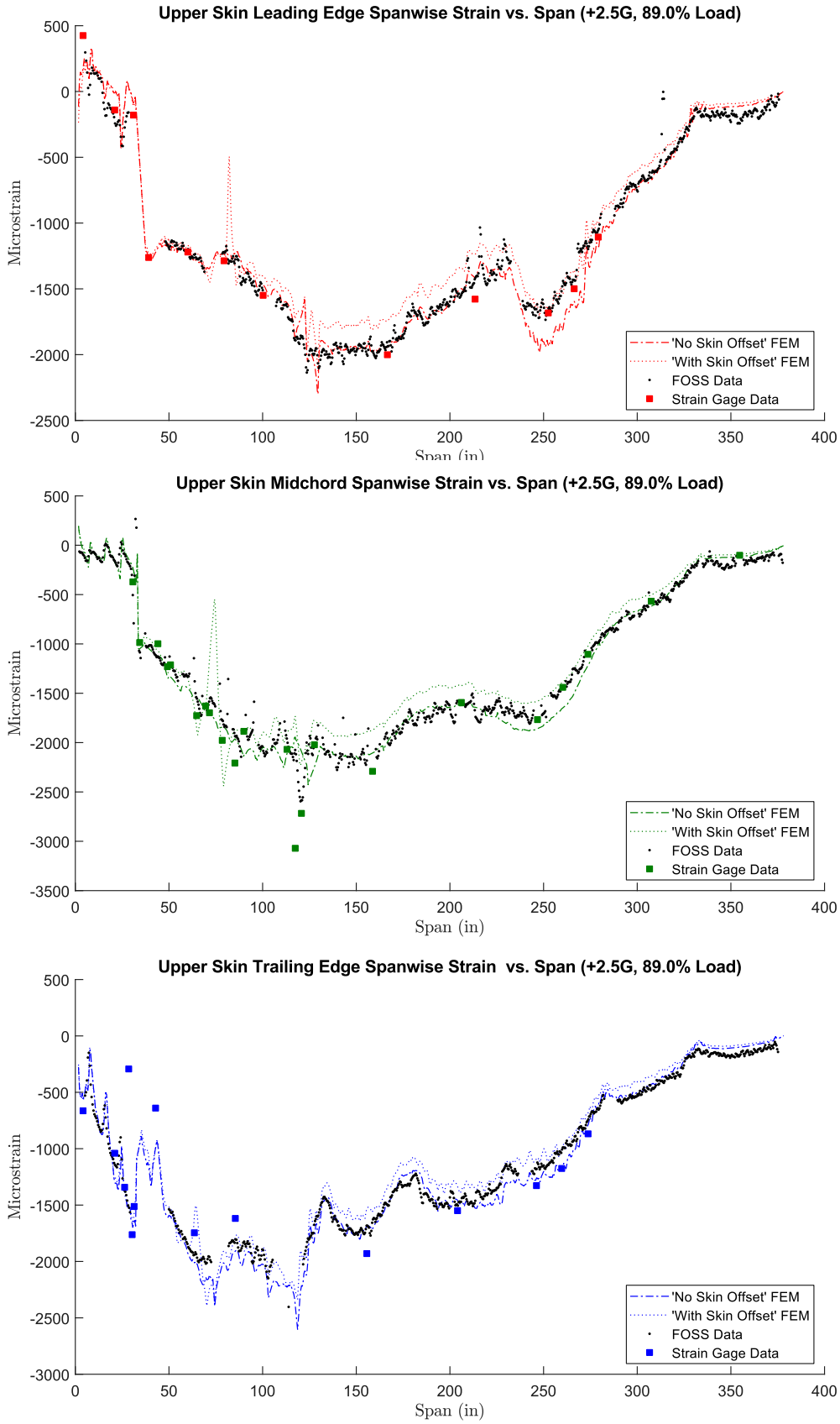

Figure C.3. Upper skin spanwise strains for +2.5G load case for leading edge (top), midchord (middle) and trailing edge (bottom).

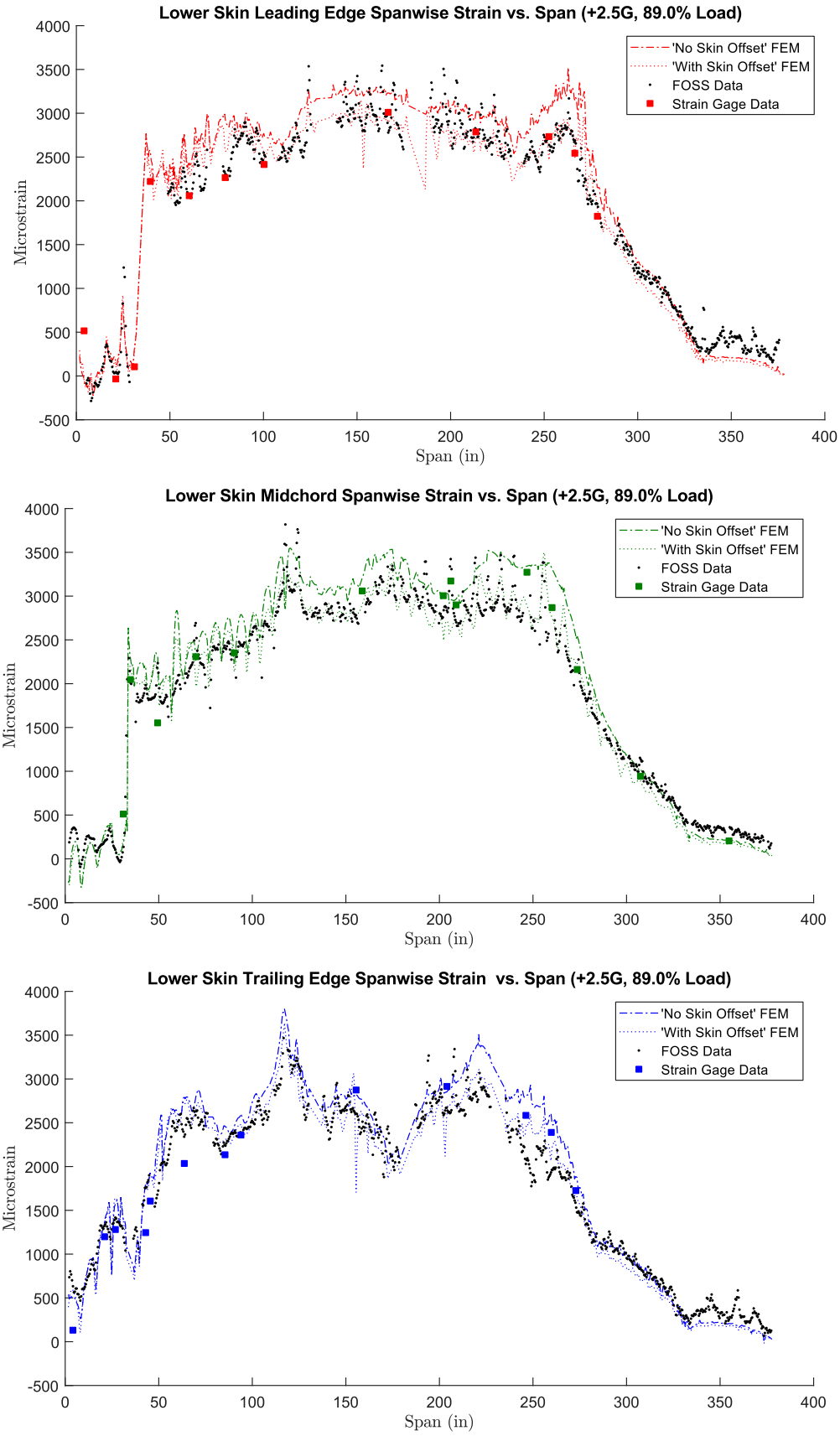

Figure C.4. Lower skin spanwise strains for +2.5G load case for leading edge (top), midchord (middle) and trailing edge (bottom).

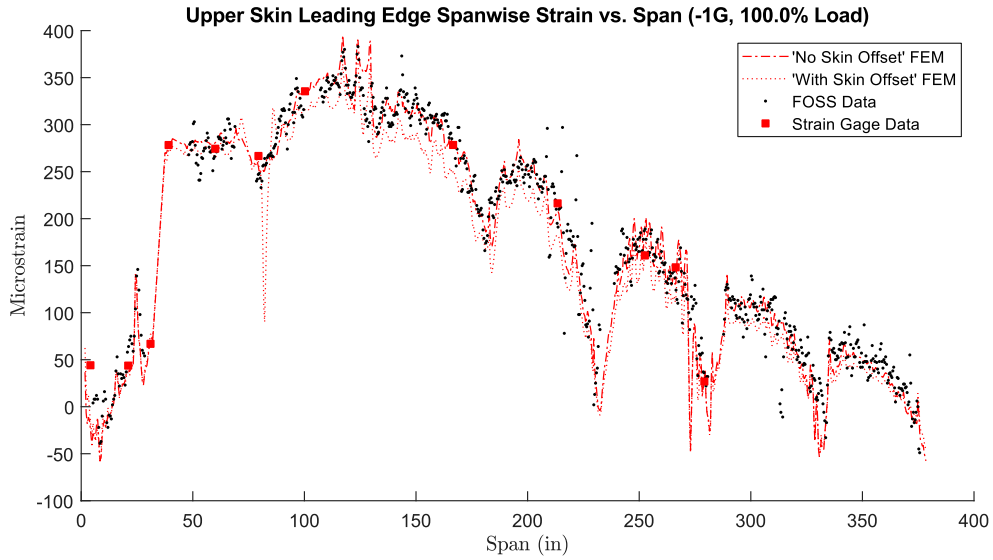

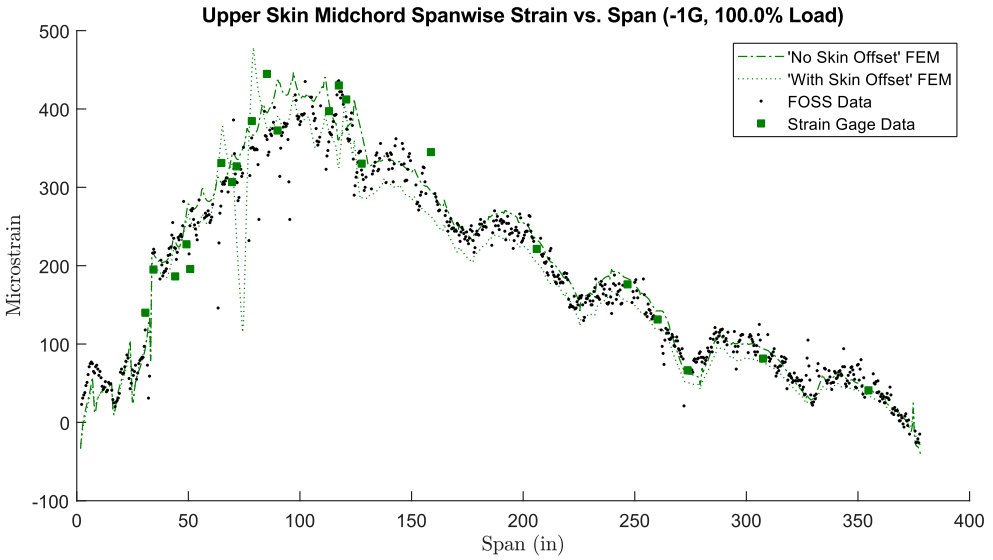

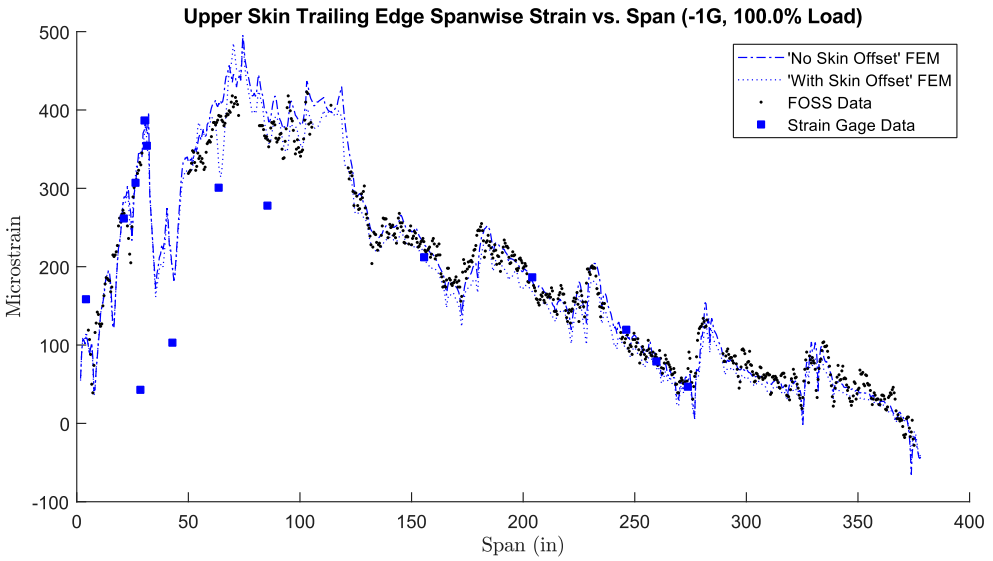

Figure C.5. Upper skin spanwise strains for -1G load case for leading edge (top), midchord (middle) and trailing edge (bottom).

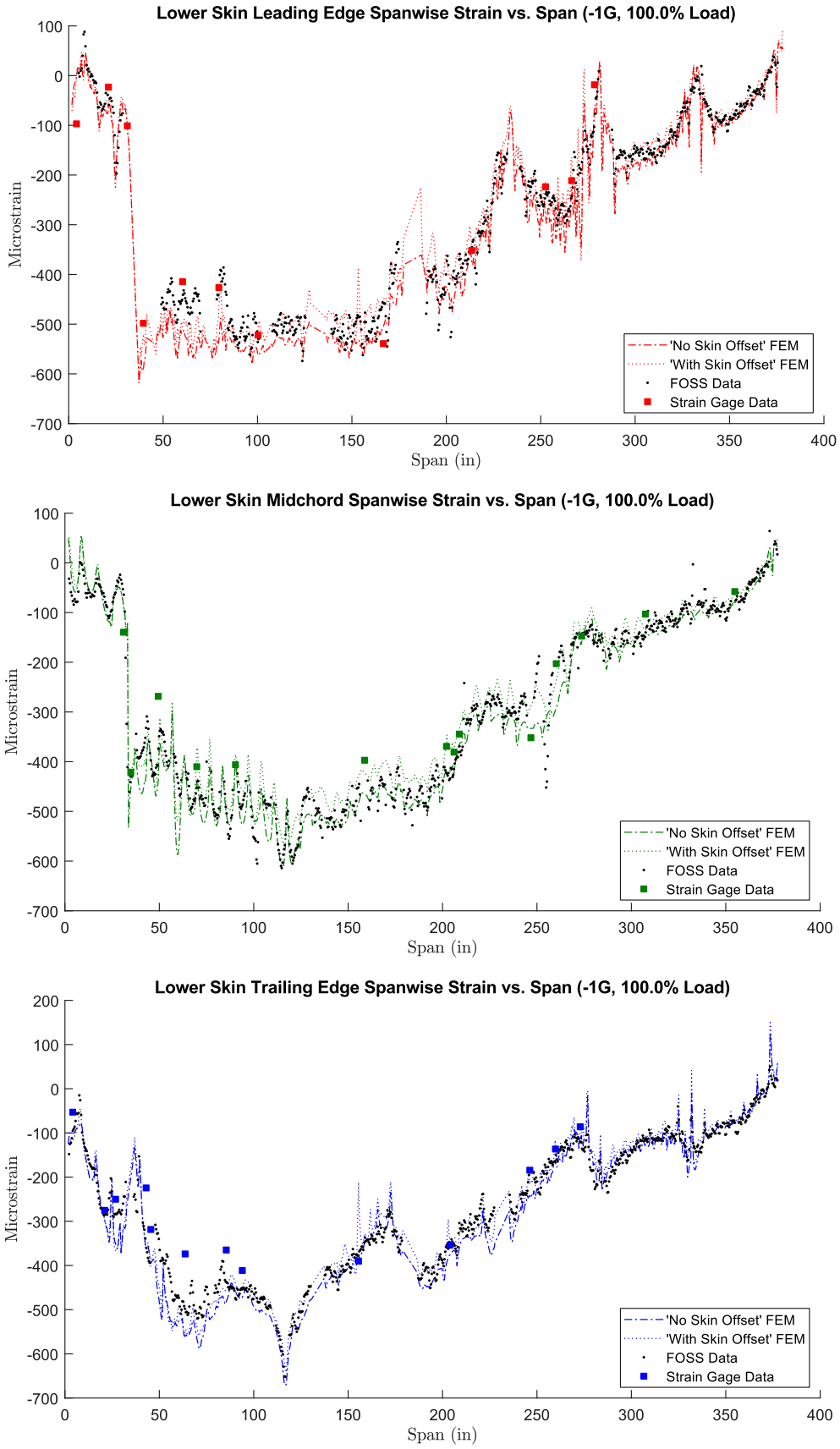

Figure C.6. Lower skin spanwise strains for -1G load case for leading edge (top), midchord (middle) and trailing edge (bottom).

Spanwise Strain Plots

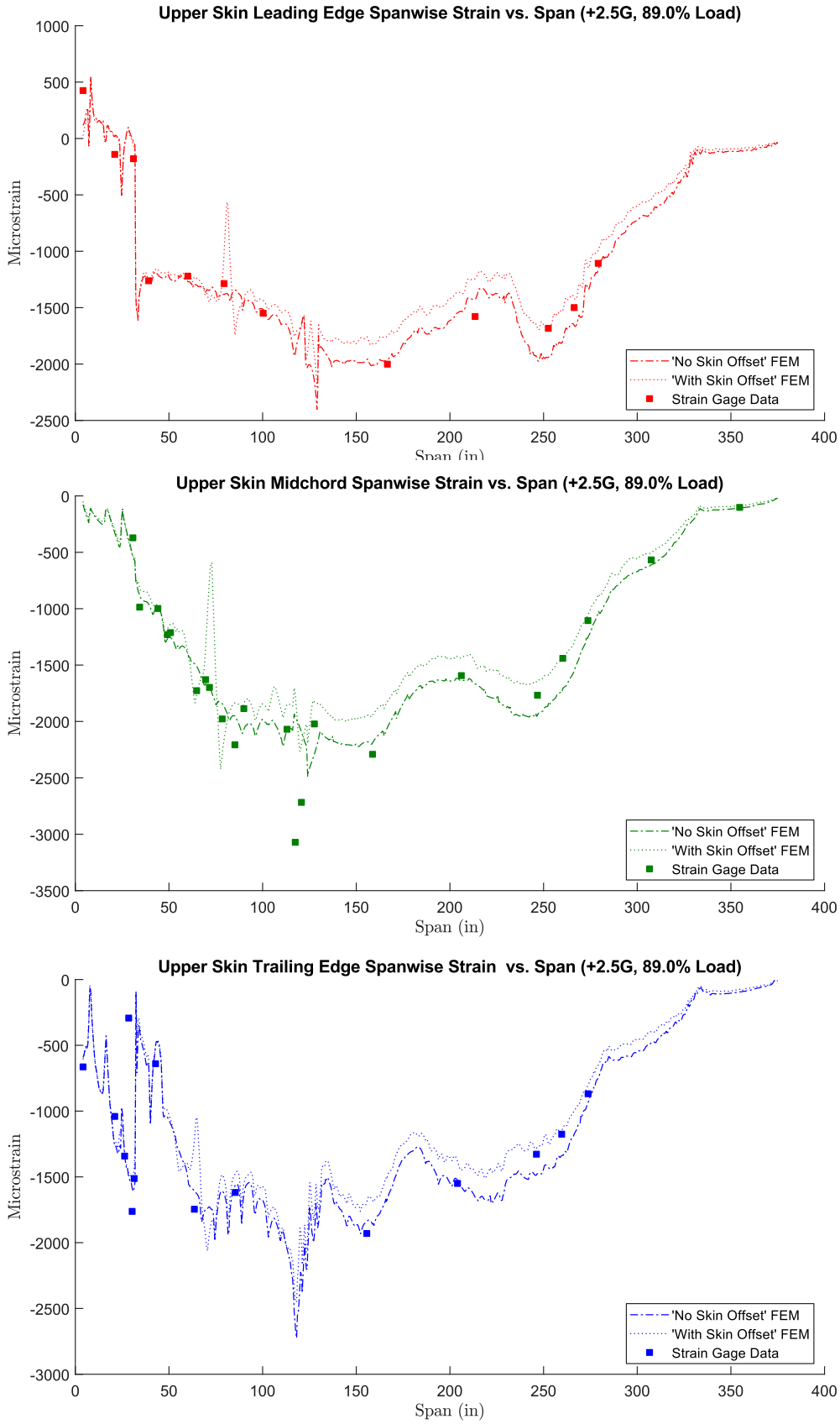

Figure C.7. Upper skin spanwise strains for +2.5G load case for leading edge (top), midchord (middle) and trailing edge (bottom).

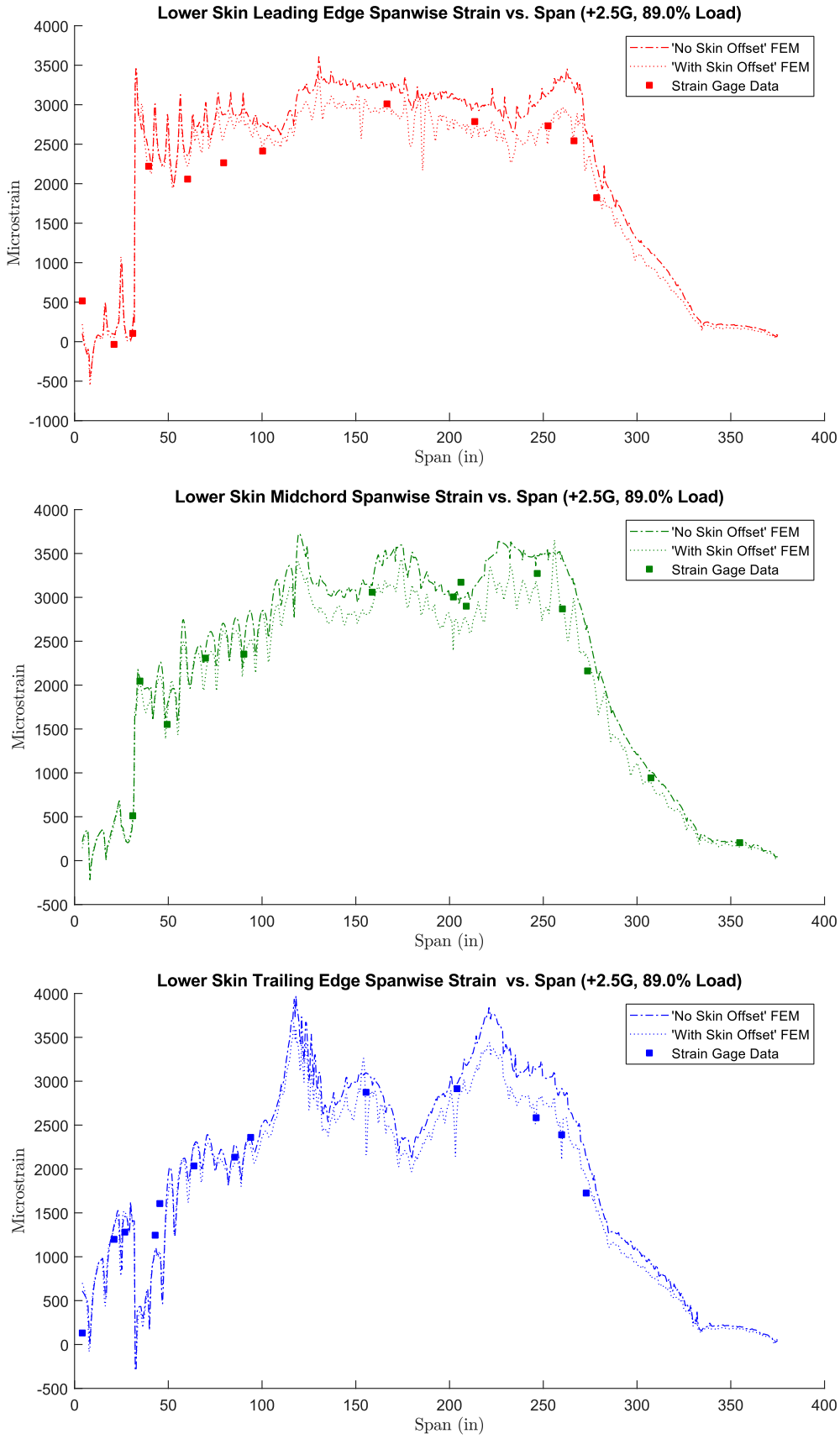

Figure C.8. Lower skin spanwise strains for +2.5G load case for leading edge (top), midchord (middle) and trailing edge (bottom).

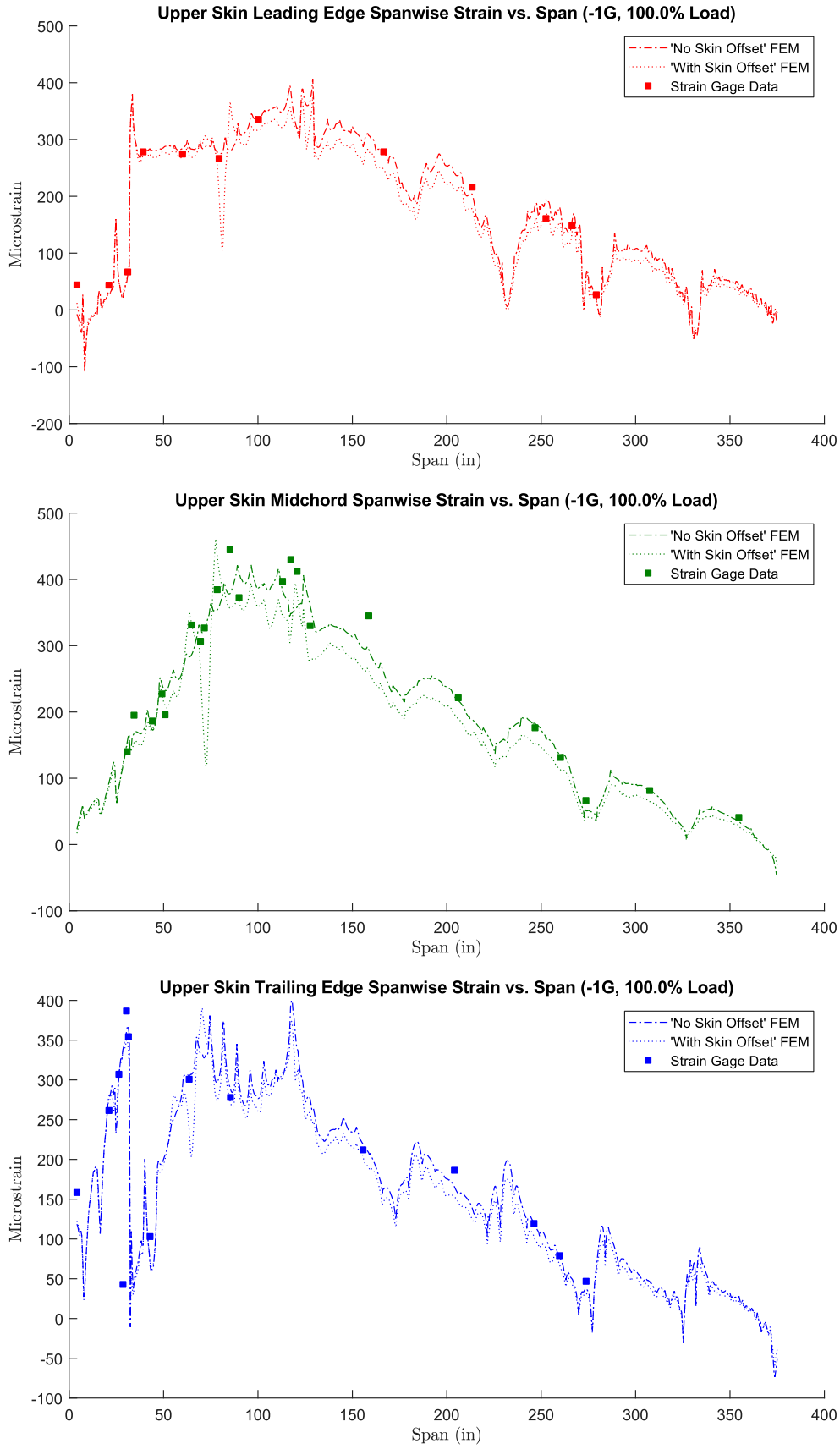

Figure C.9. Upper skin spanwise strains for -1G load case for leading edge (top), midchord (middle) and trailing edge (bottom).

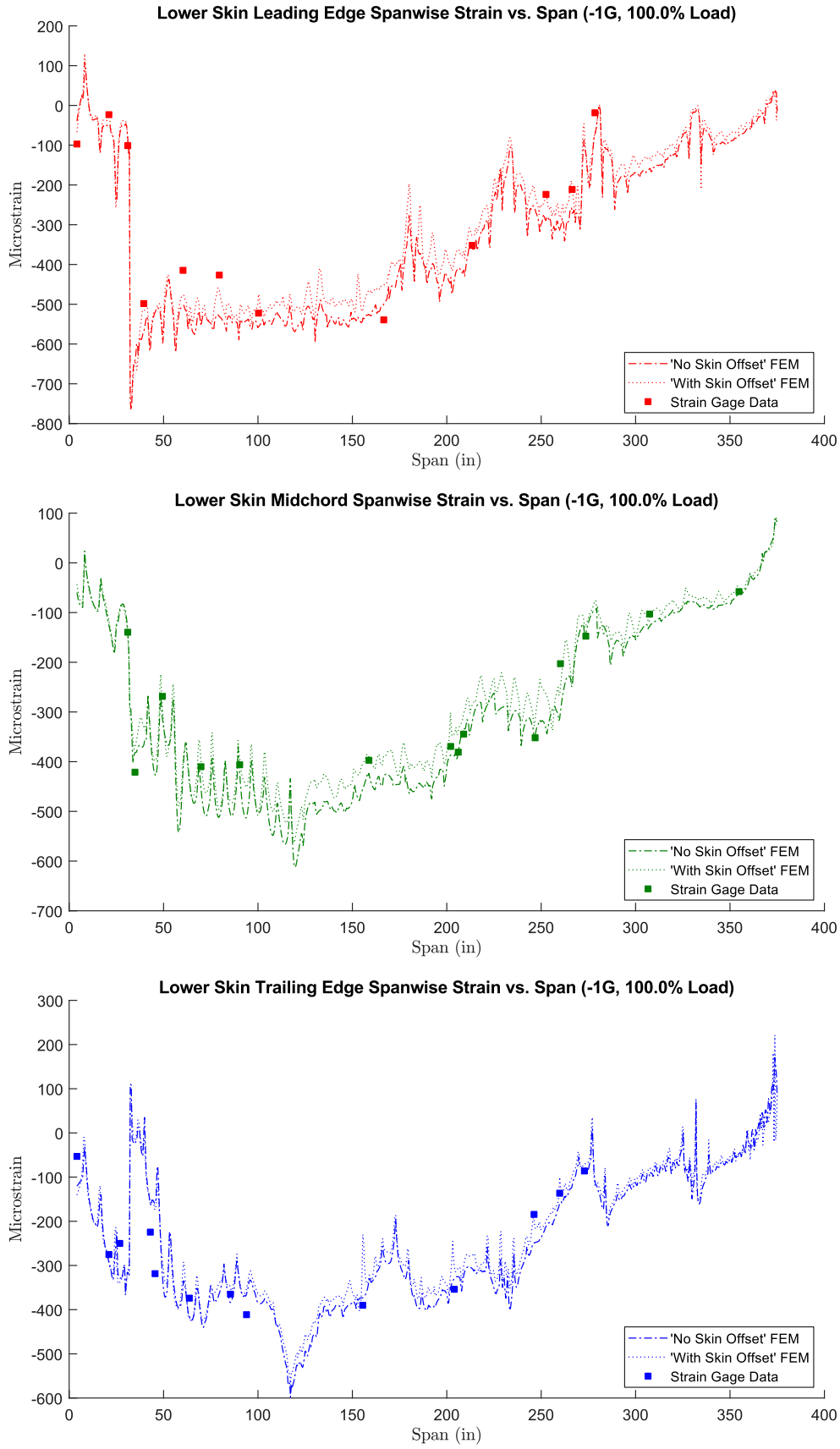

Figure C.10. Lower skin spanwise strains for -1G load case for leading edge (top), midchord (middle) and trailing edge (bottom).

Shear Strain Plots

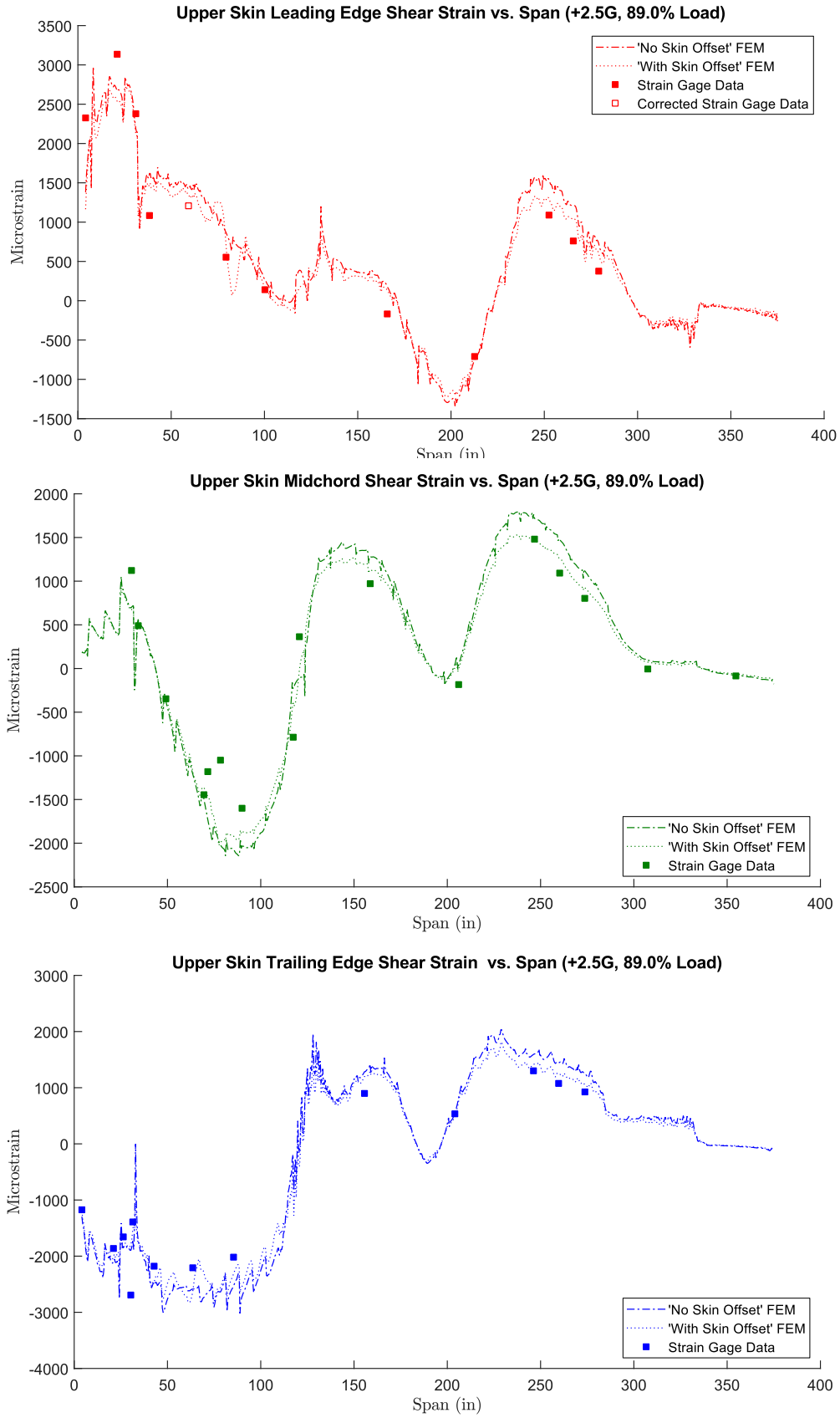

Figure C.11. Upper skin shear strains for +2.5G load case for leading edge (top), midchord (middle) and trailing edge (bottom).

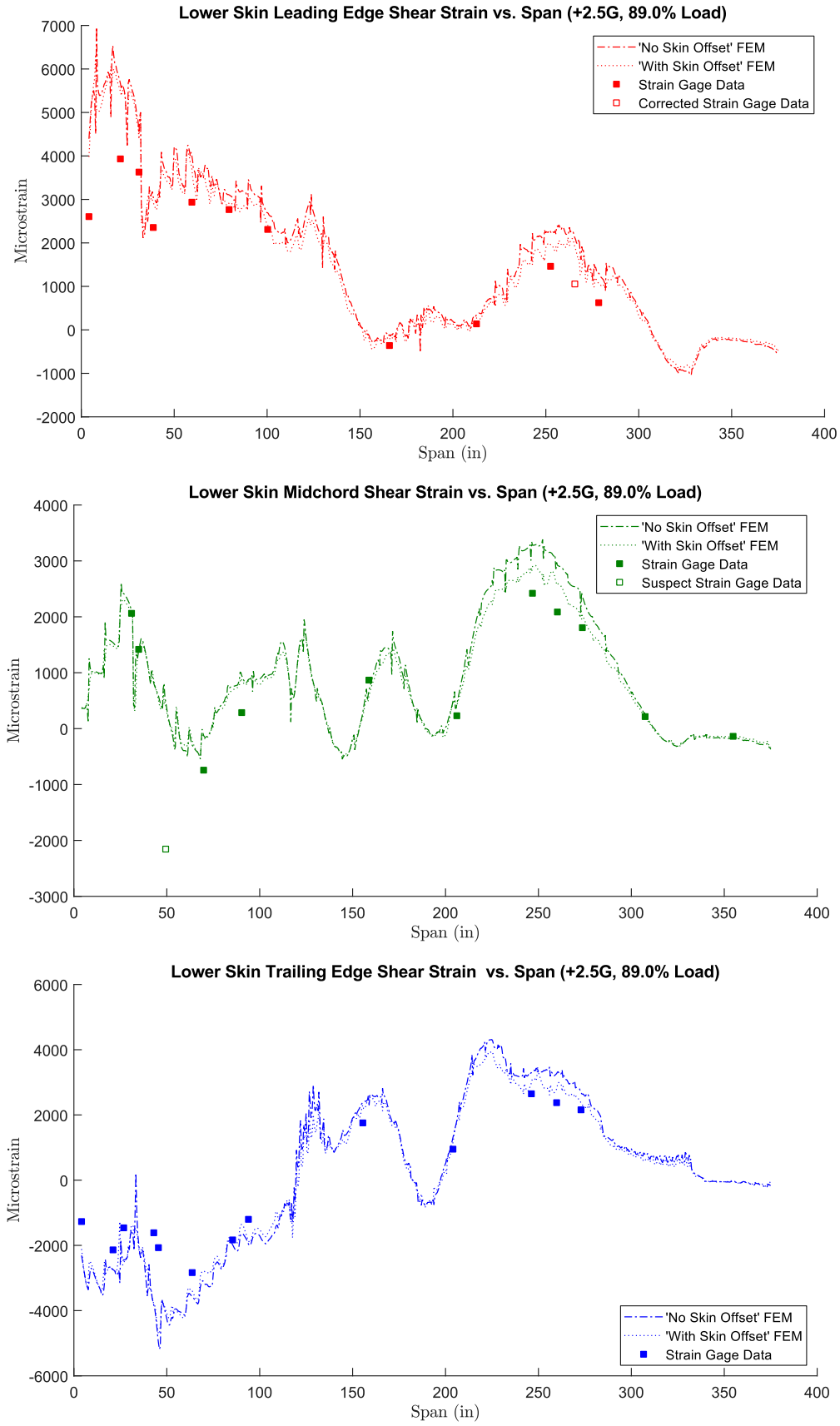

Figure C.12. Lower skin shear strains for +2.5G load case for leading edge (top), midchord (middle) and trailing edge (bottom).

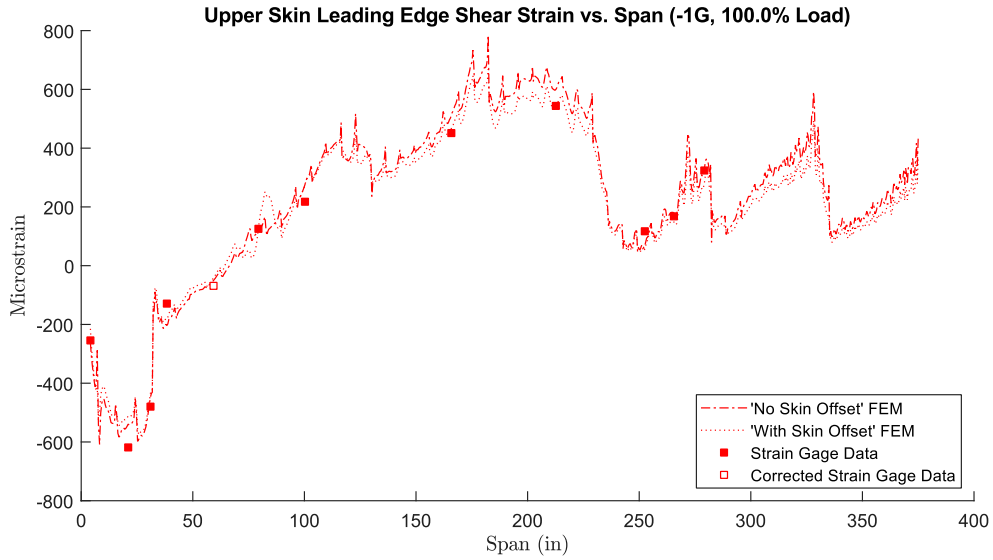

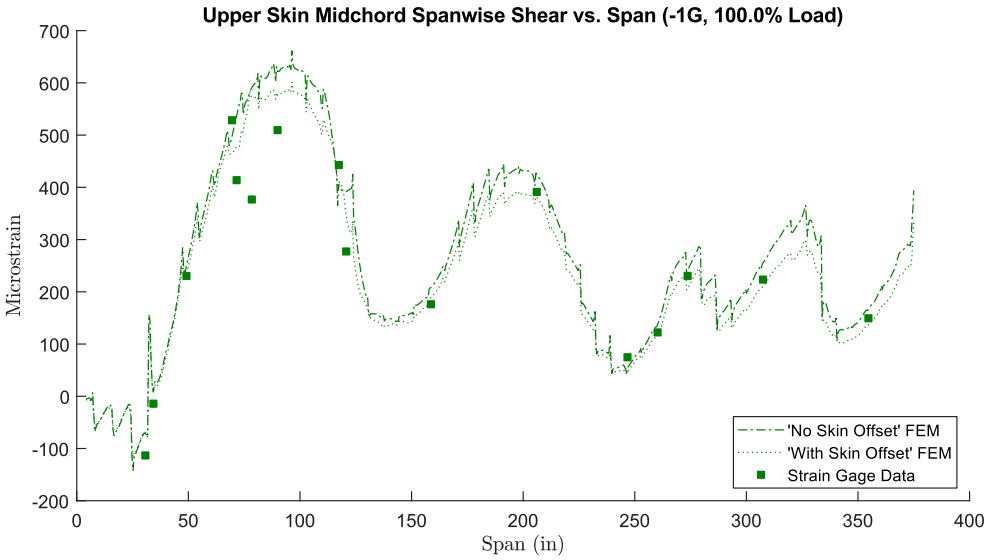

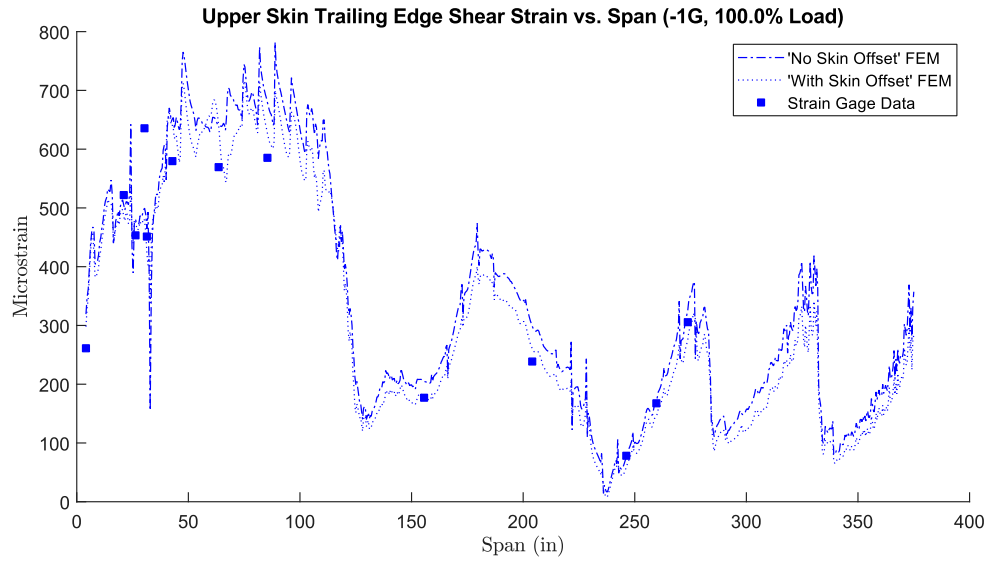

Figure C.13. Upper skin shear strains for -1G load case for leading edge (top), midchord (middle) and trailing edge (bottom).

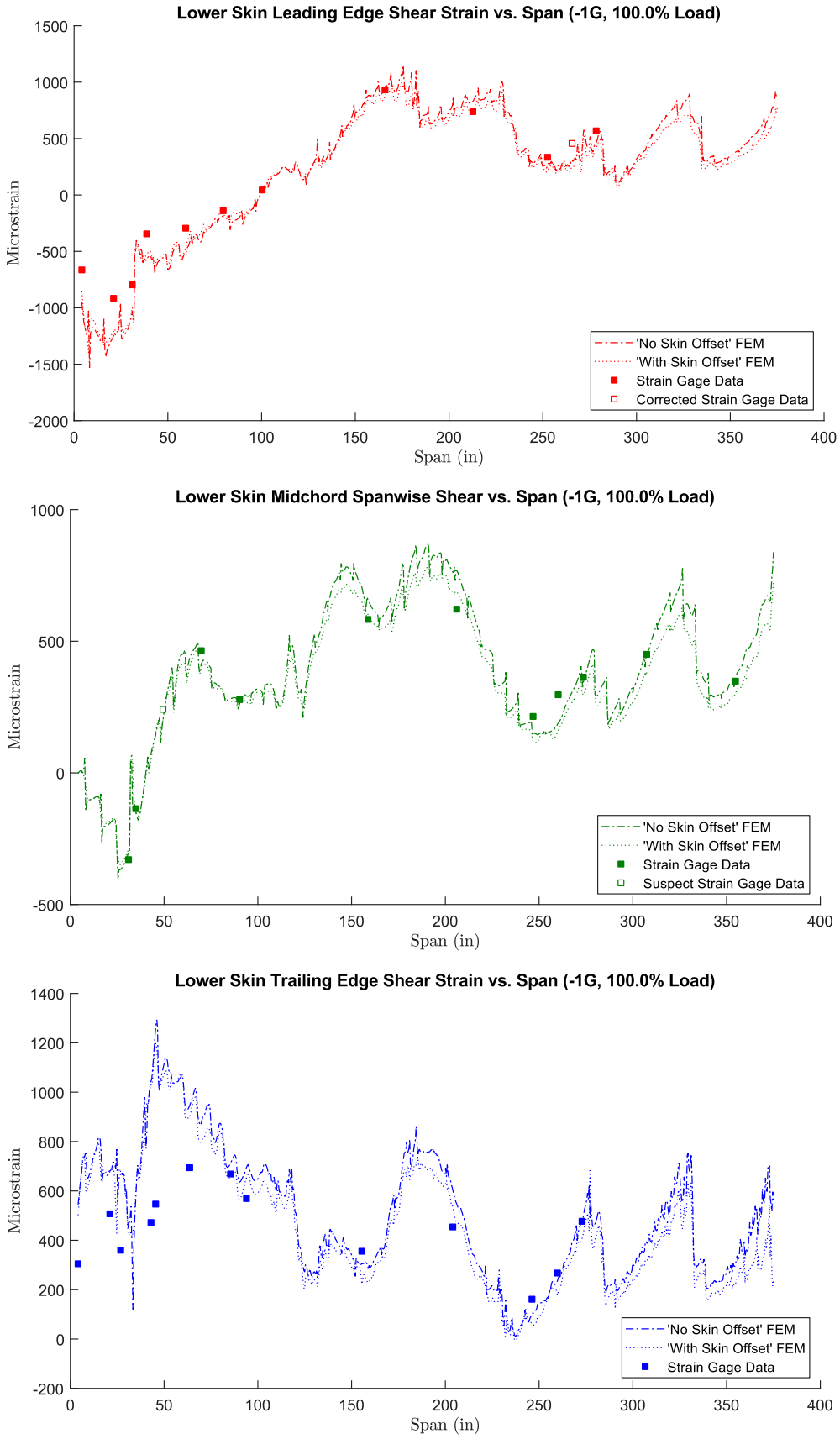

Figure C.14. Lower skin shear strains for -1G load case for leading edge (top), midchord (middle) and trailing edge (bottom).

Chordwise Strain Plots

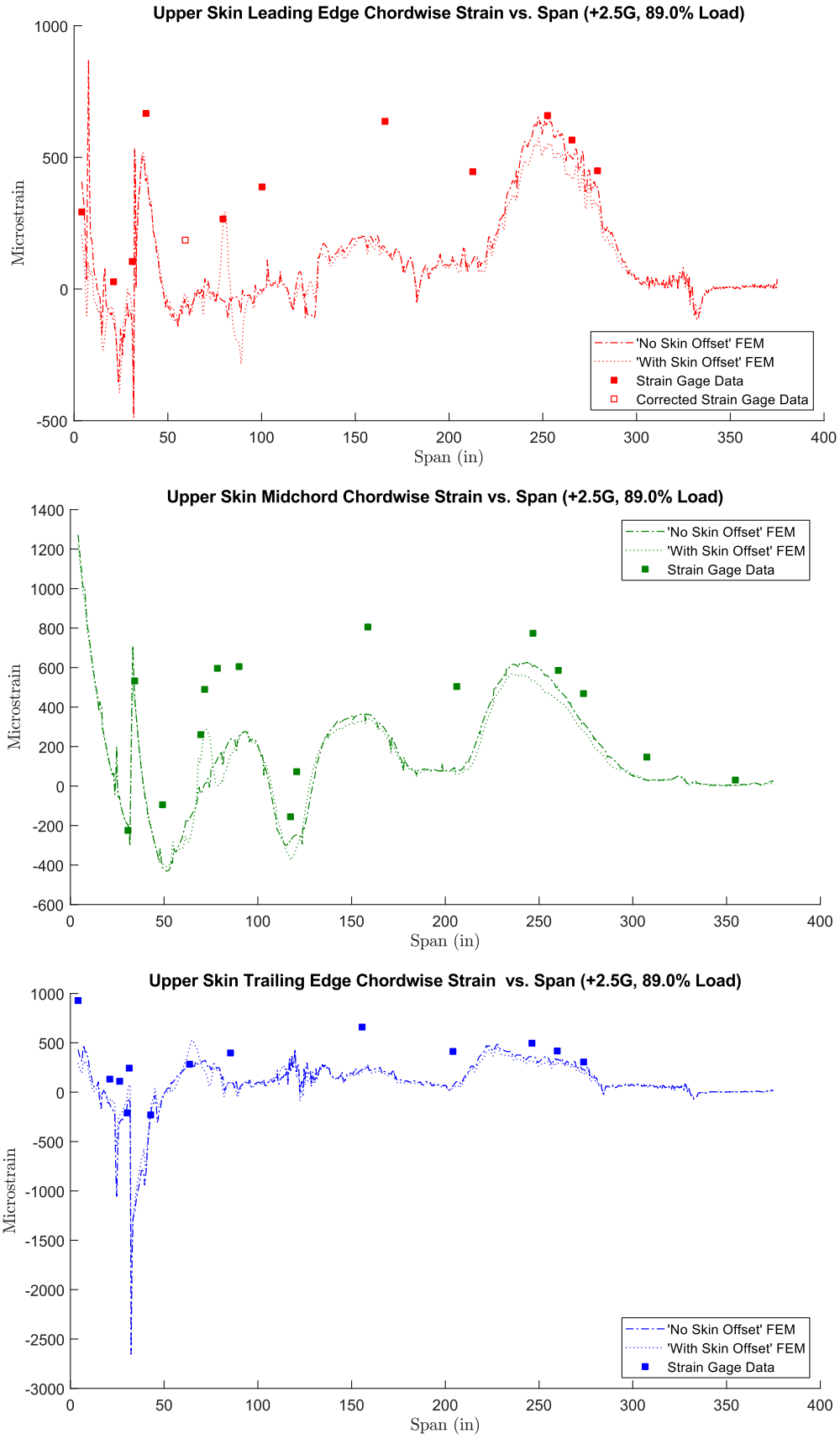

Figure C.15. Upper skin chordwise strains for +2.5G load case for leading edge (top), midchord (middle) and trailing edge (bottom).

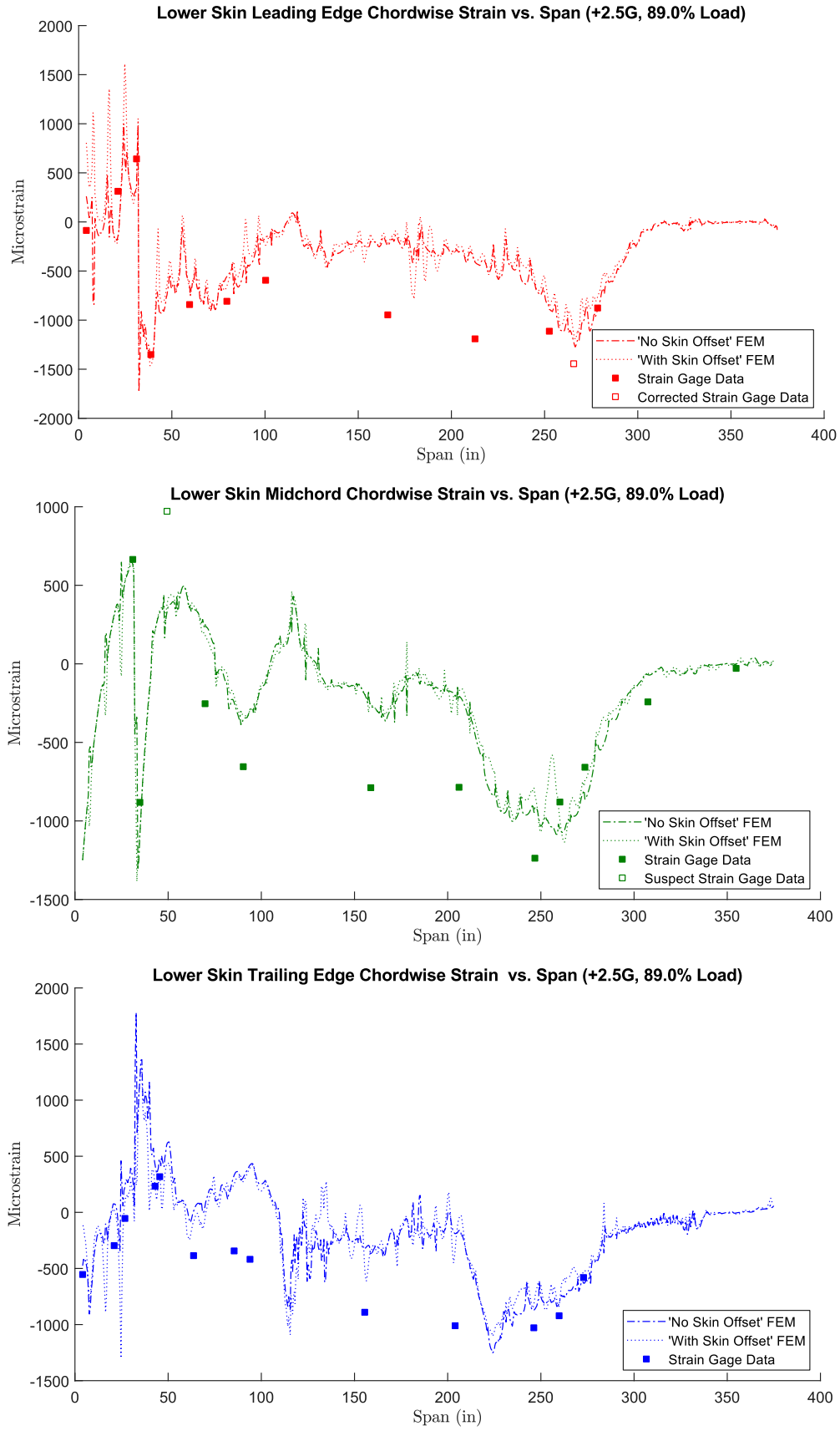

Figure C.16. Lower skin chordwise strains for +2.5G load case for leading edge (top), midchord (middle) and trailing edge (bottom).

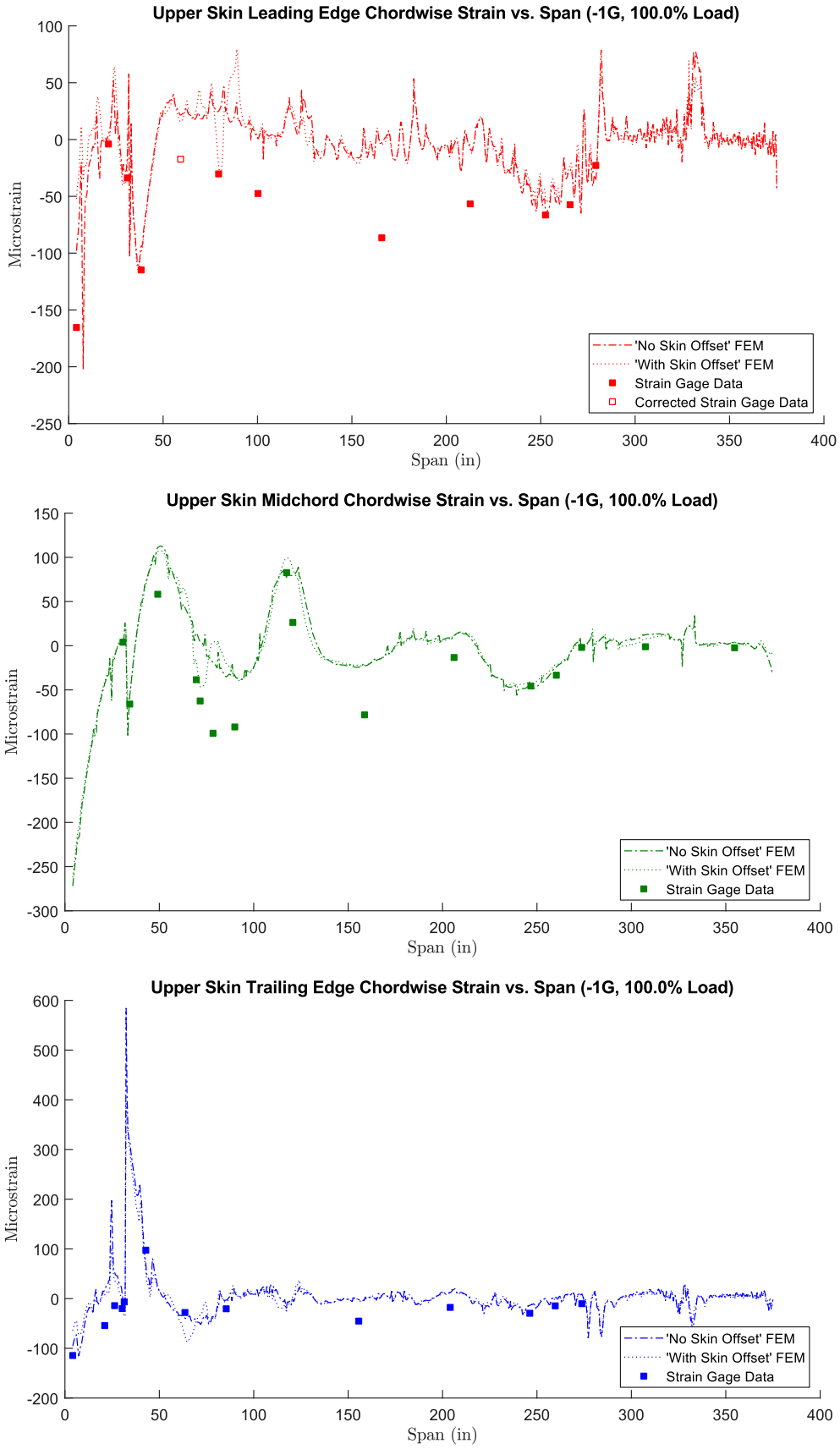

Figure C.17. Upper skin chordwise strains for -1G load case for leading edge (top), midchord (middle) and trailing edge (bottom).

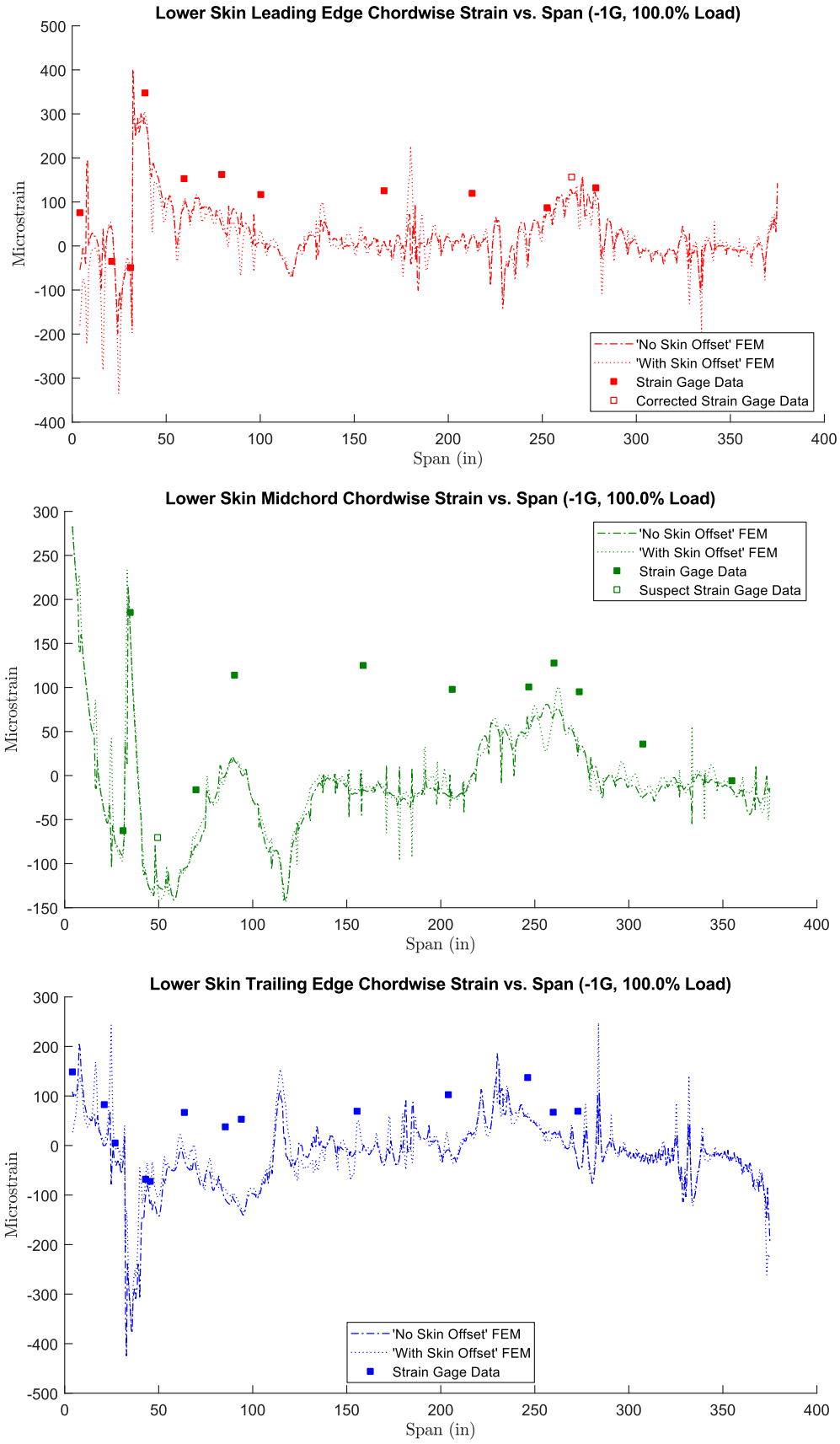

Figure C.18. Lower skin chordwise strains for -1G load case for leading edge (top), midchord (middle) and trailing edge (bottom).

Principal Strain Plots

Figure C.19. Principal strains for lower skin mid-chord, +2.5G: major, minor and minor angle.

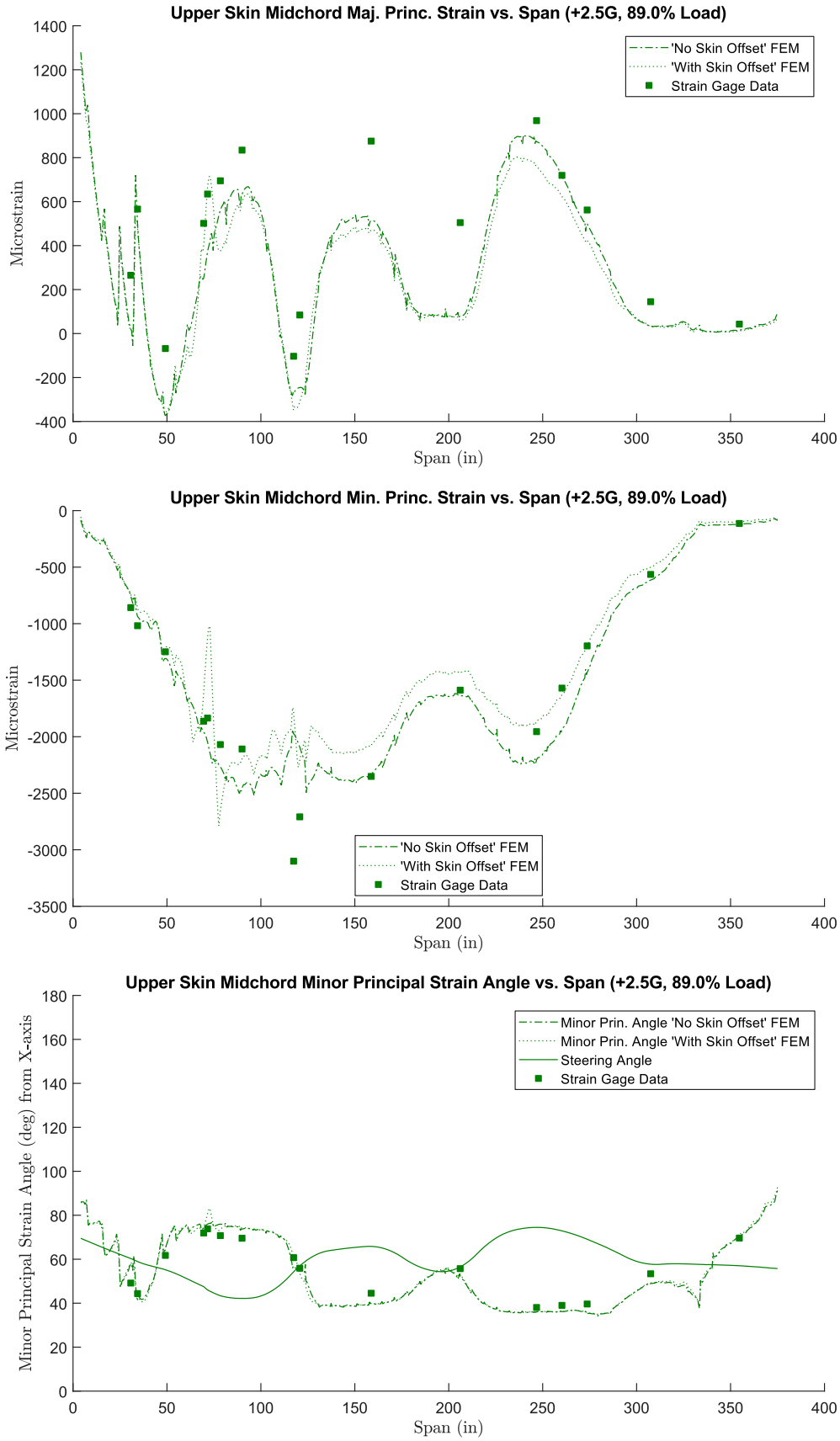

Figure C.20. Principal strains for upper skin mid-chord, +2.5G: major, minor and minor angle.

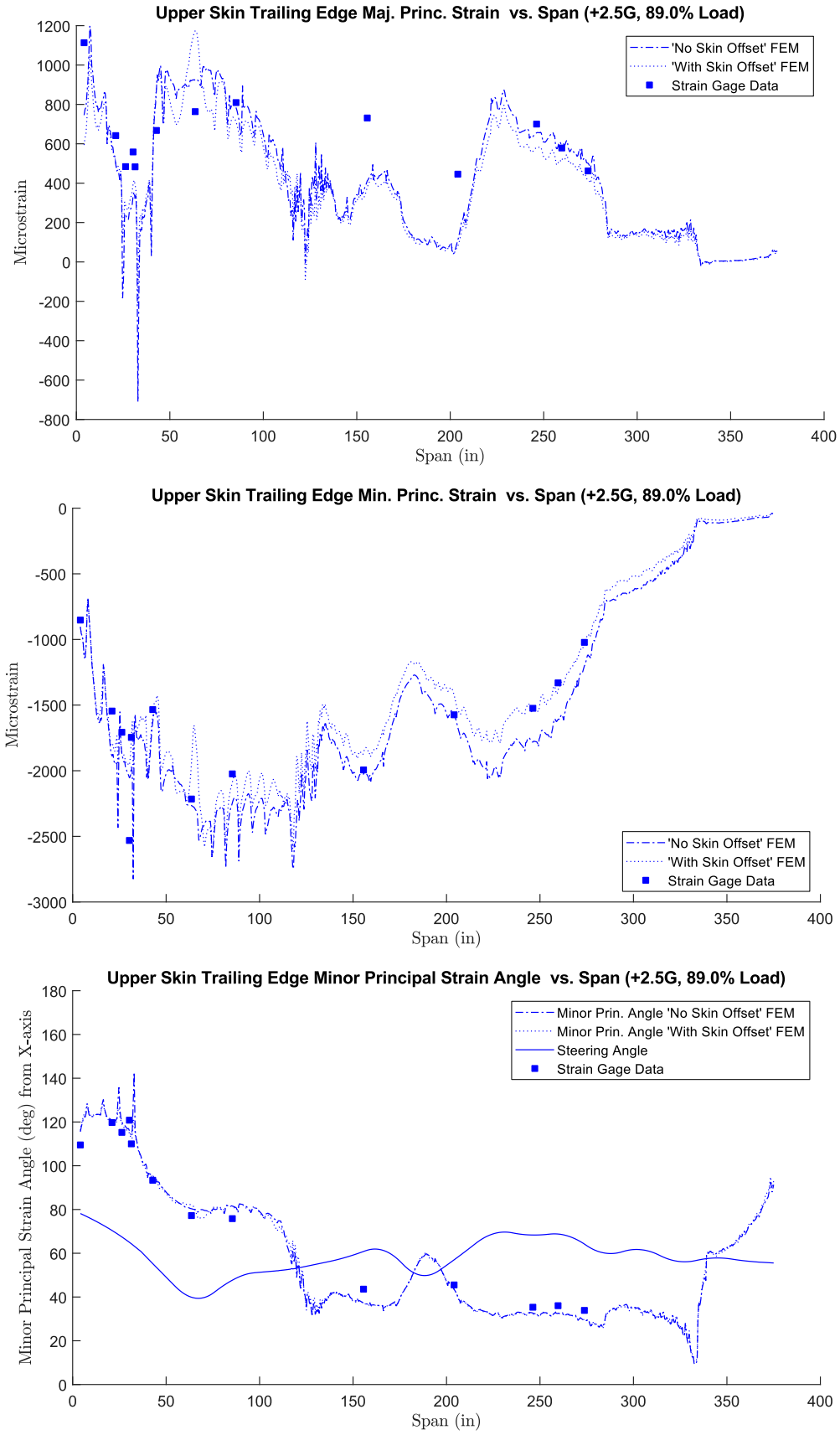

Figure C.21. Principal strains for upper skin trailing edge, +2.5G: major, minor and minor angle.

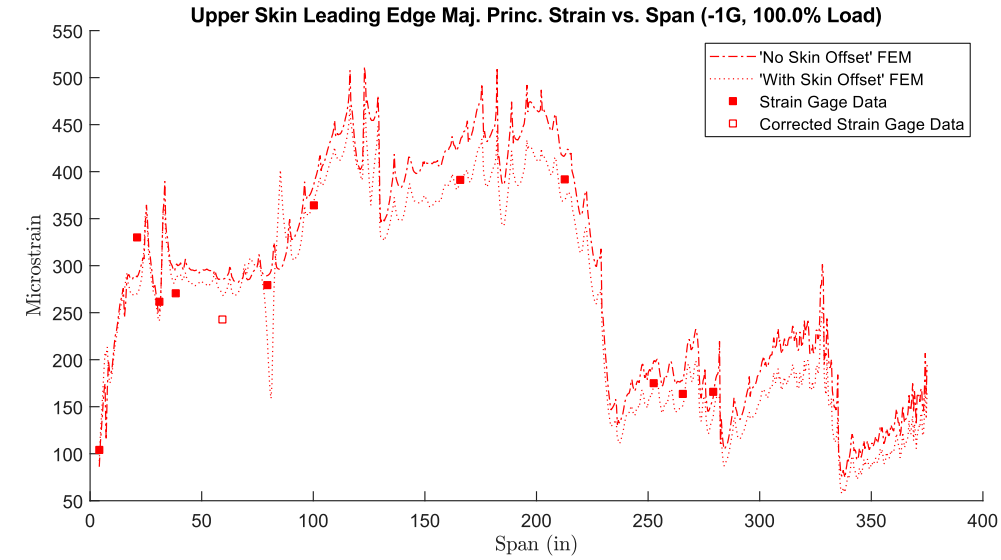

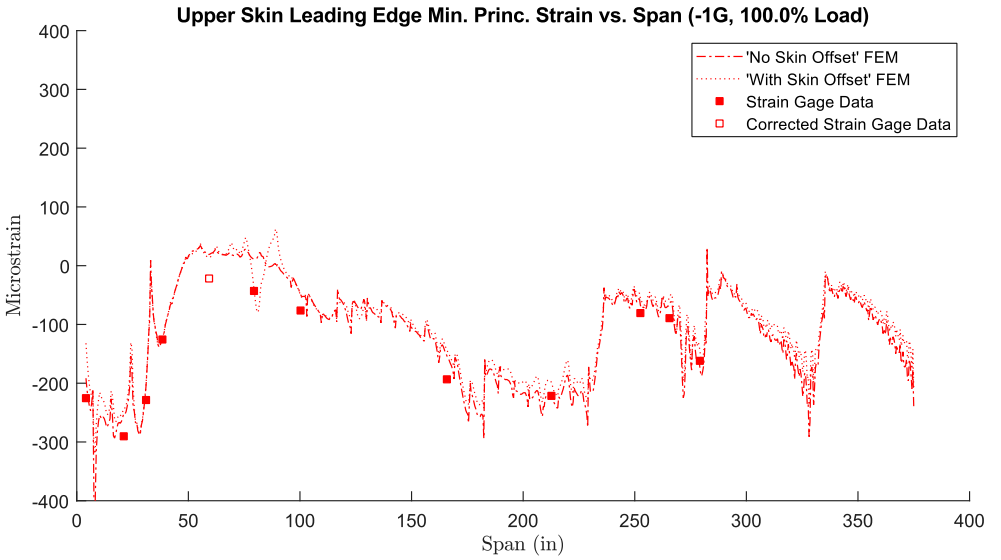

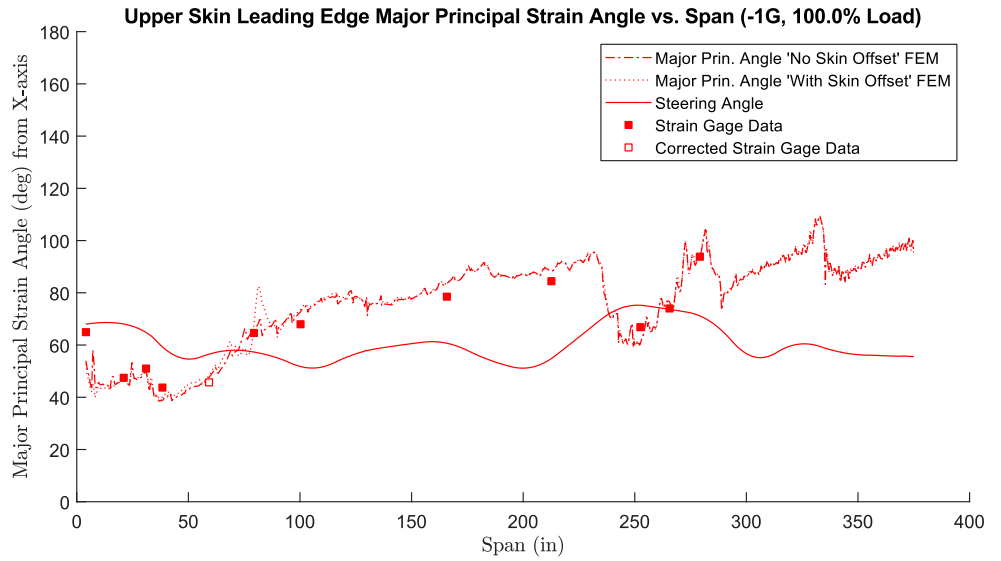

Figure C.22. Principal strains for upper skin leading edge, -1G: major, minor and major angle.

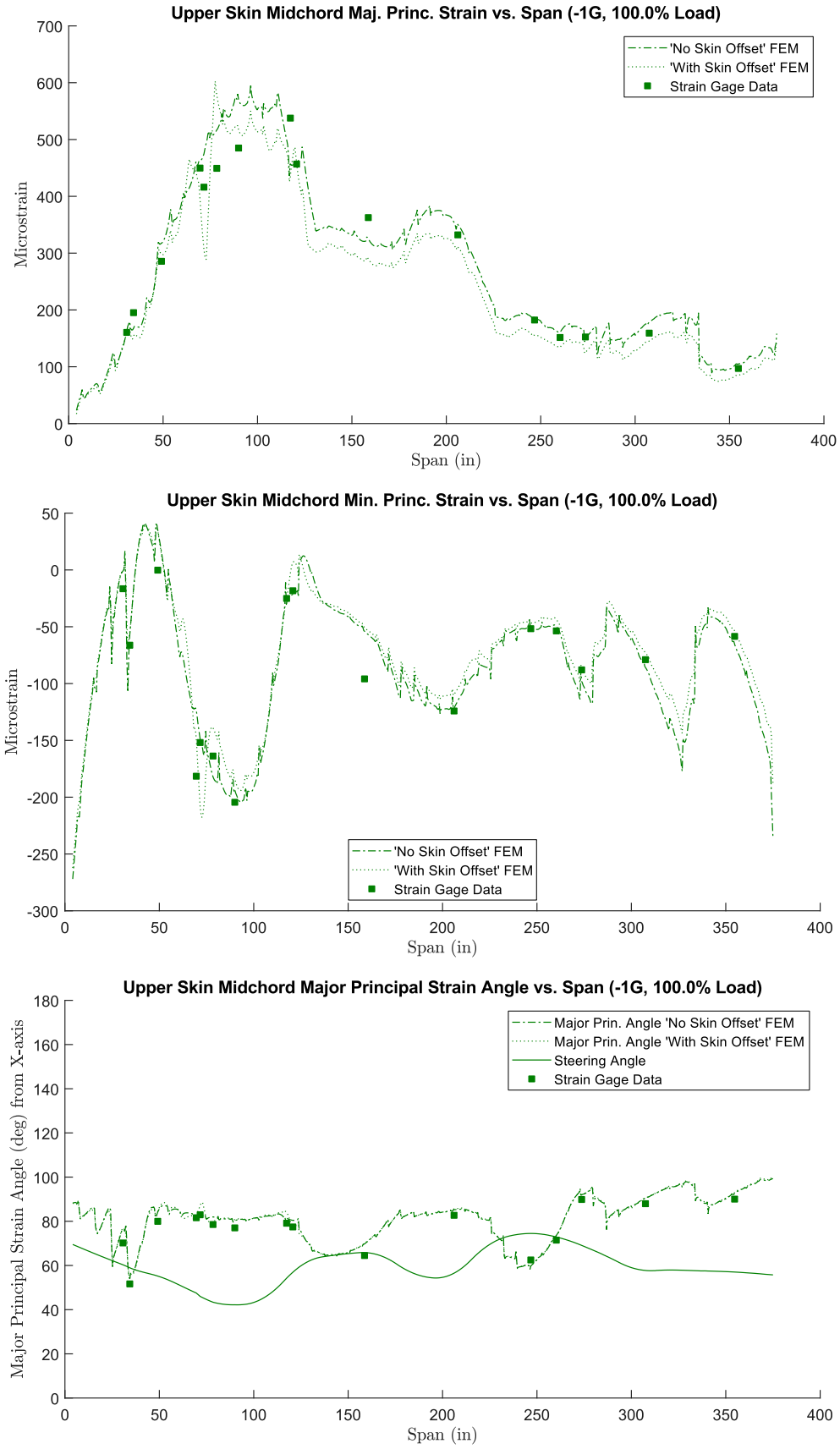

Figure C.23. Principal strains for upper skin mid-chord, -1G: major, minor and major angle.

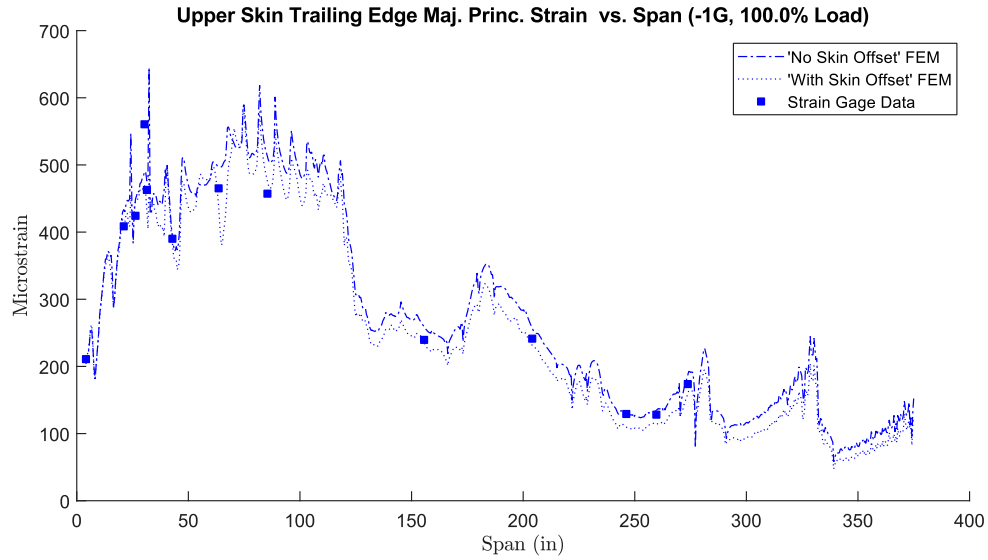

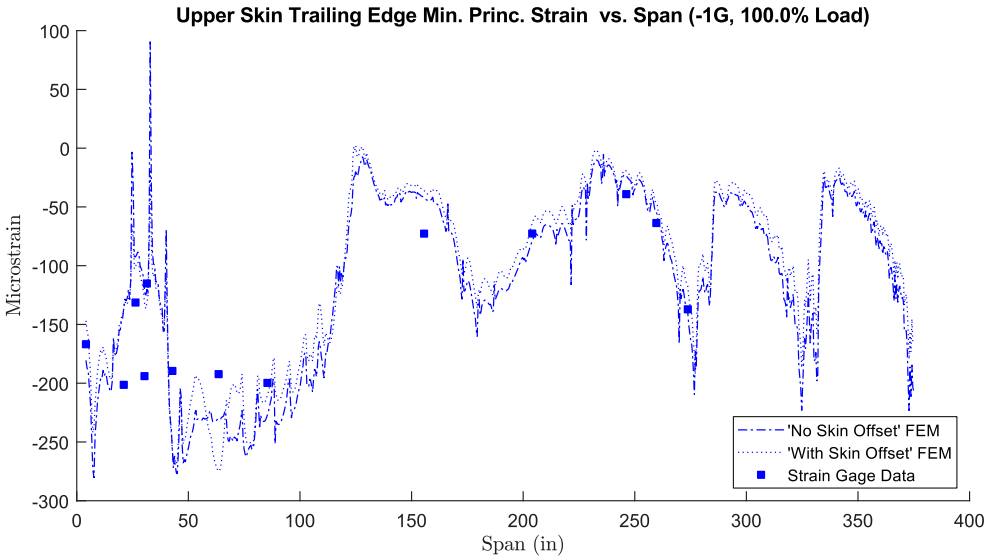

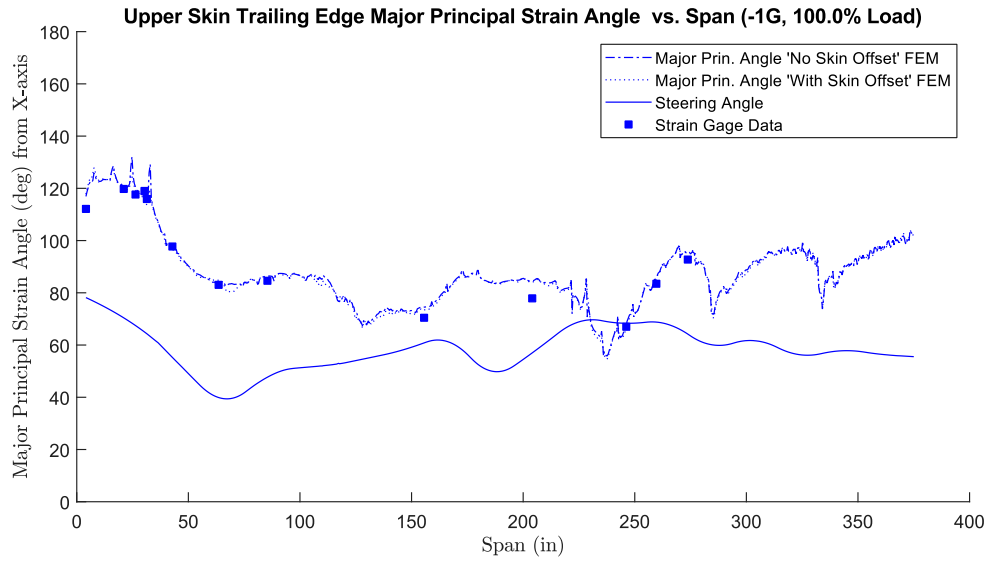

Figure C.24. Principal strains for upper skin trailing edge, -1G: major, minor and major angle.

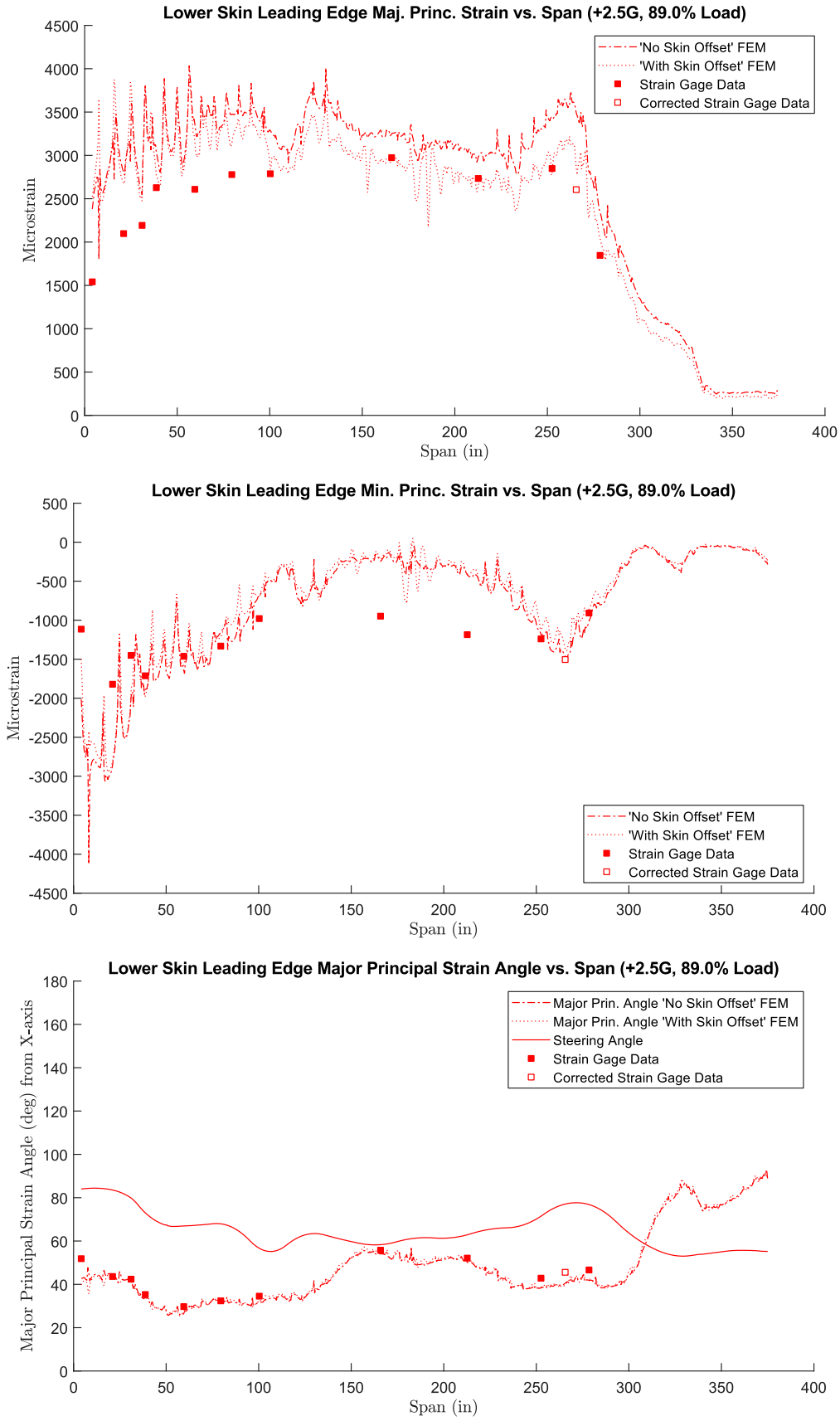

Figure C.25. Principal strains for lower skin leading edge, +2.5G: major, minor and major angle.

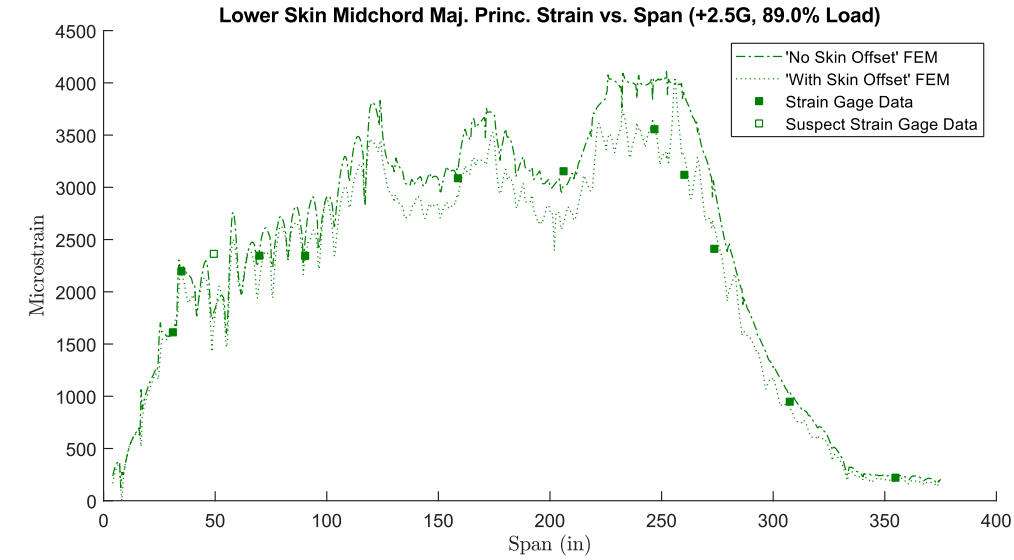

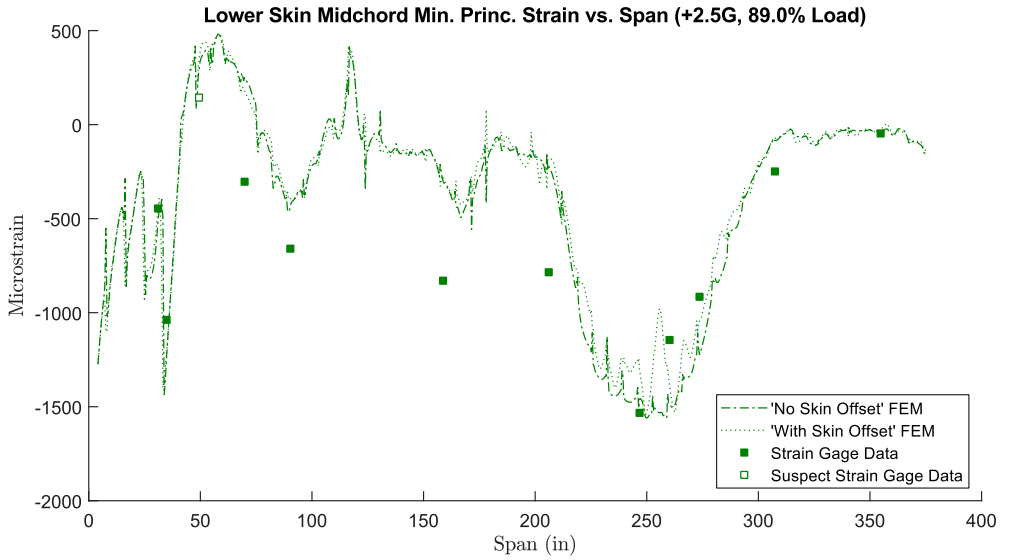

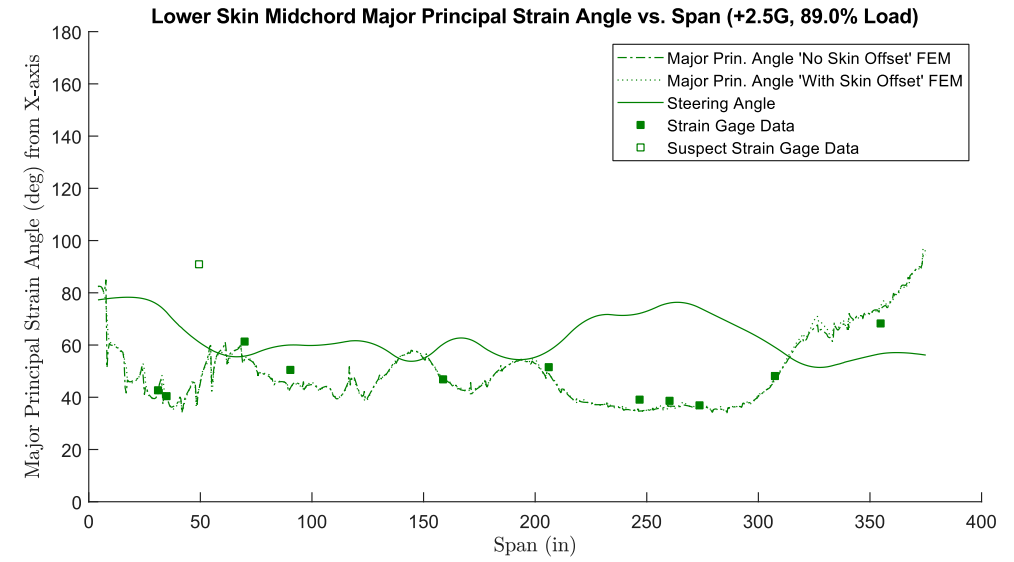

Figure C.26. Principal strains for lower skin mid-chord, +2.5G: major, minor and major angle.

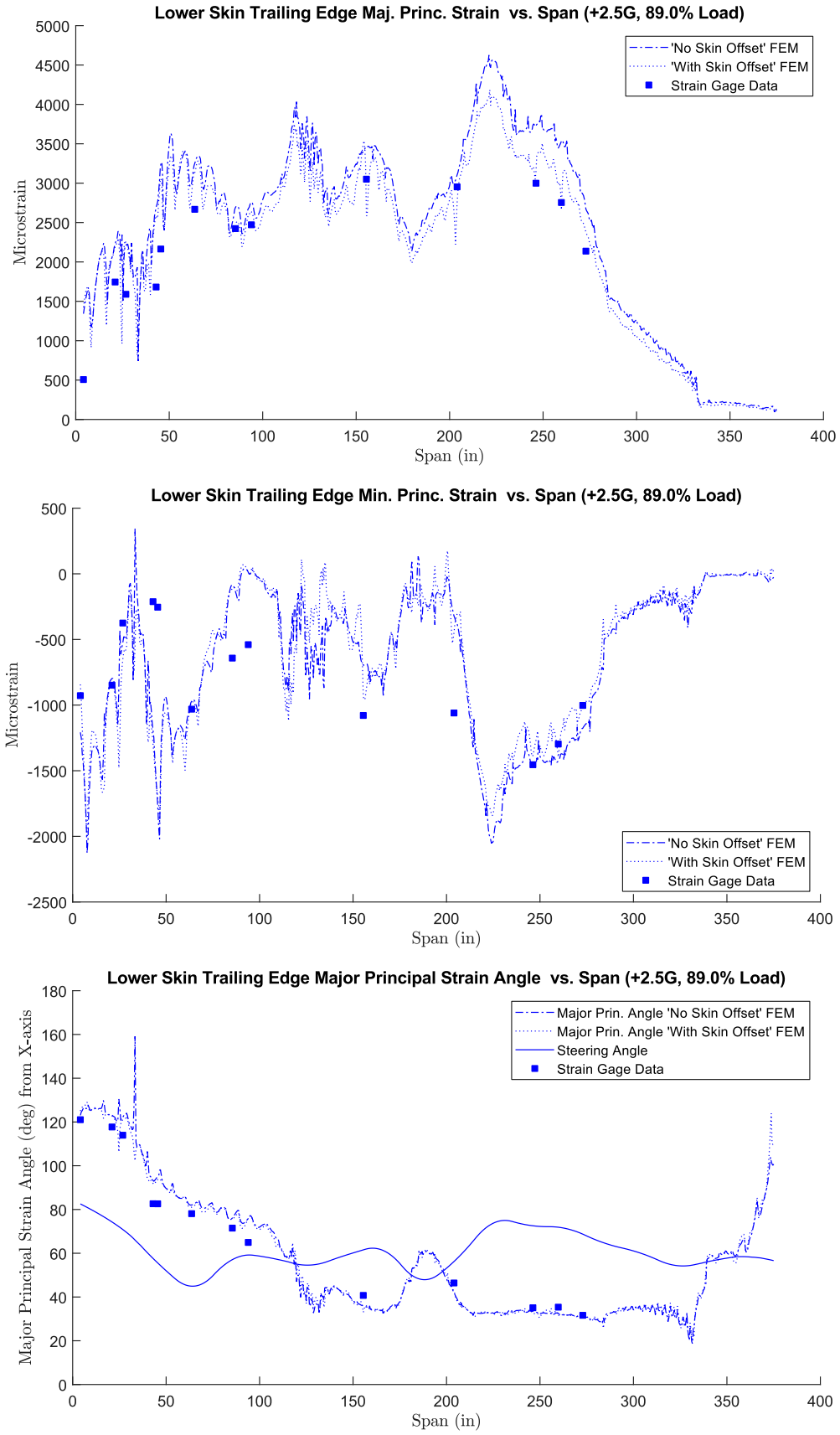

Figure C.27. Principal strains for lower skin trailing edge, +2.5G: major, minor and major angle.

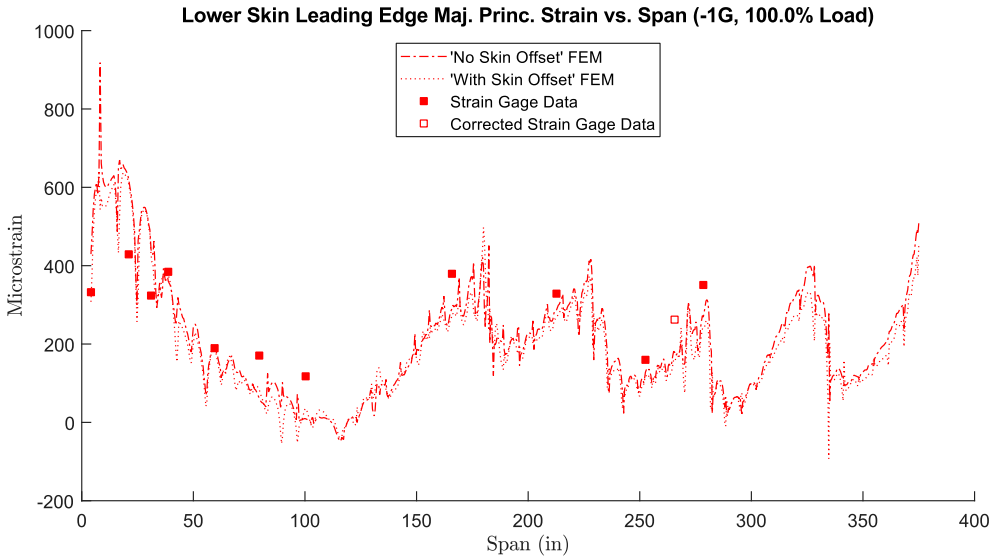

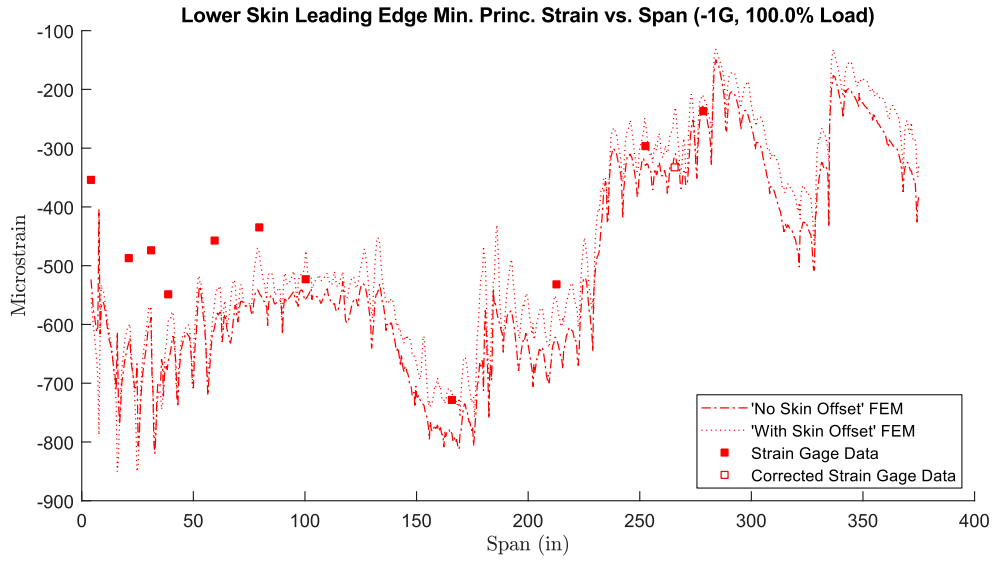

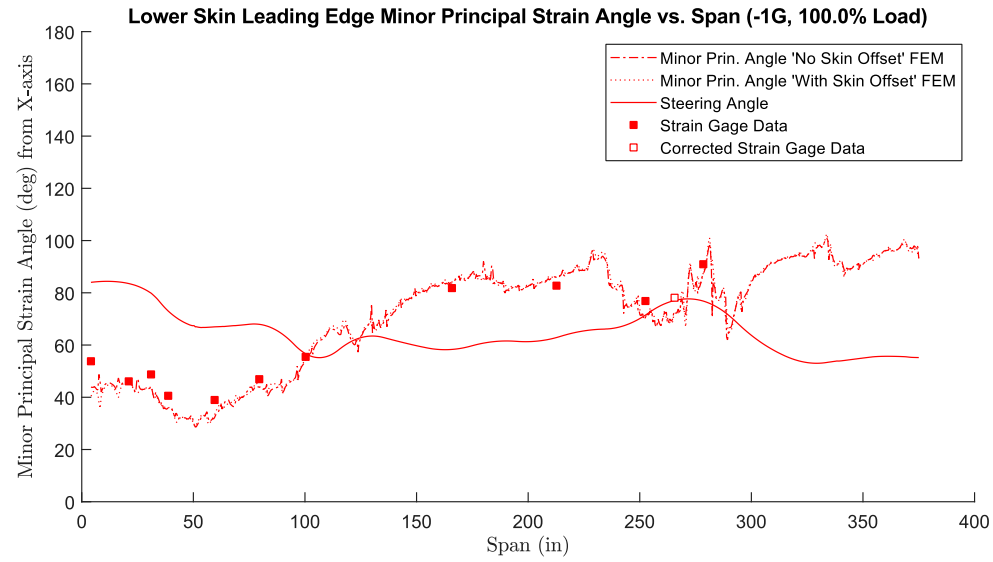

Figure C.28. Principal strains for lower skin leading edge, -1G: major, minor and minor angle.

Figure C.29. Principal strains for lower skin mid-chord, -1G: major, minor and minor angle.

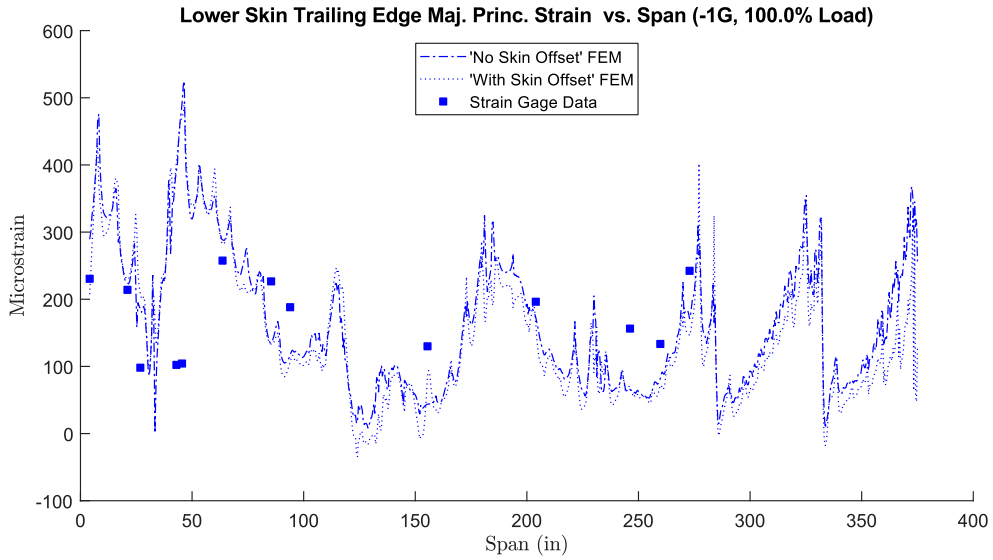

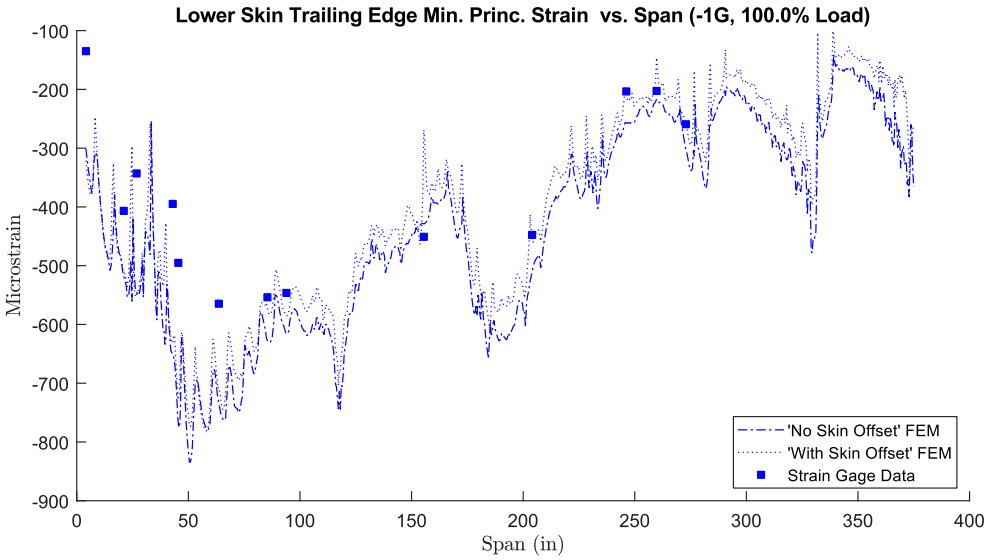

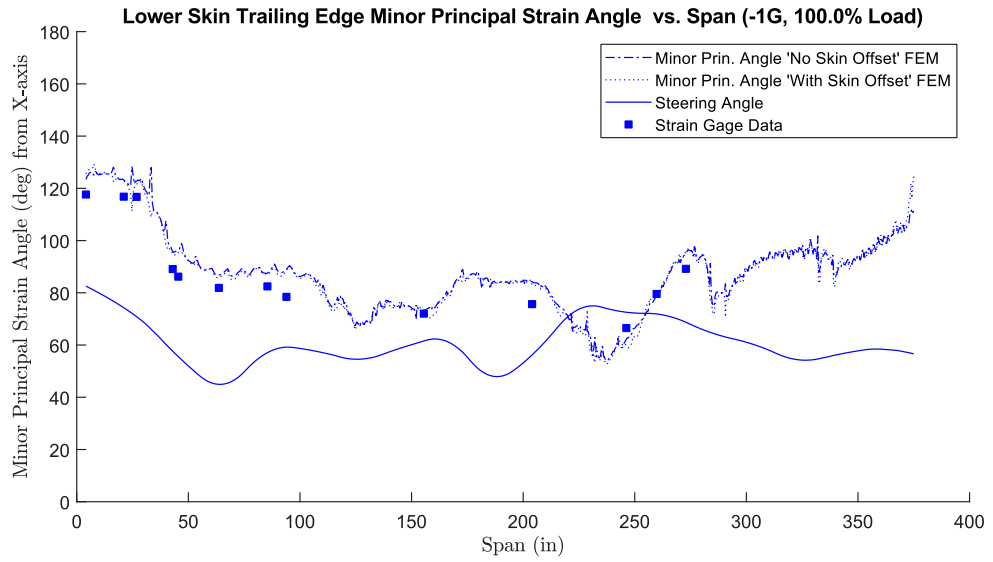

Figure C.30. Principal strains for lower skin trailing edge, -1G: major, minor and minor angle.

Appendix D. Mode Shape Comparison Plots

The following plots compare FEM mode shape predictions with measured mode shapes from GVT. Note that due to differences in plotting software, the GVT and FEM scale factors and colormaps are slightly different, therefore, only qualitative assessments should be drawn from the following mode shape comparisons.

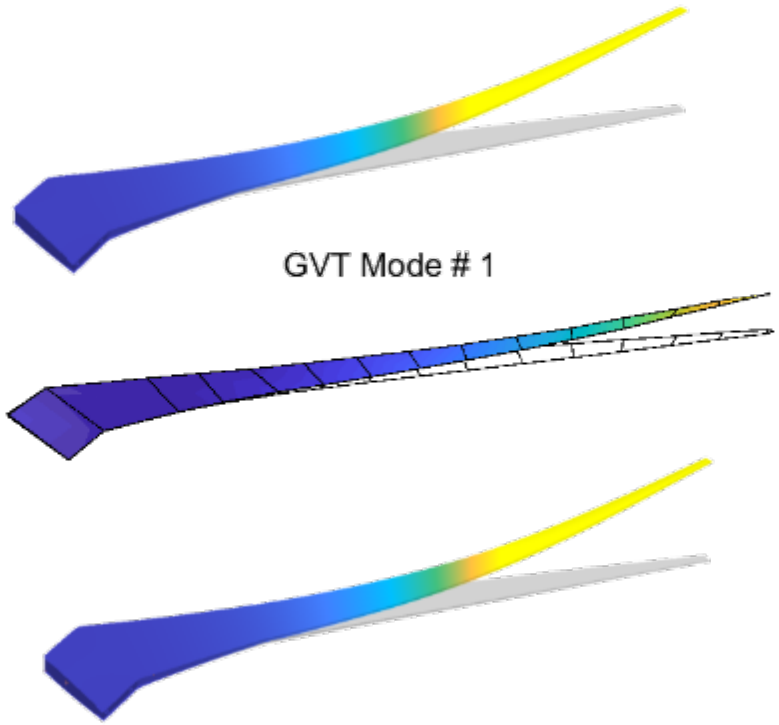

Figure D.1. Mode Shape 1 (1st bending) Comparison. "With skin offset" FEM (top), GVT Result (middle) and "no skin offset" FEM (bottom).

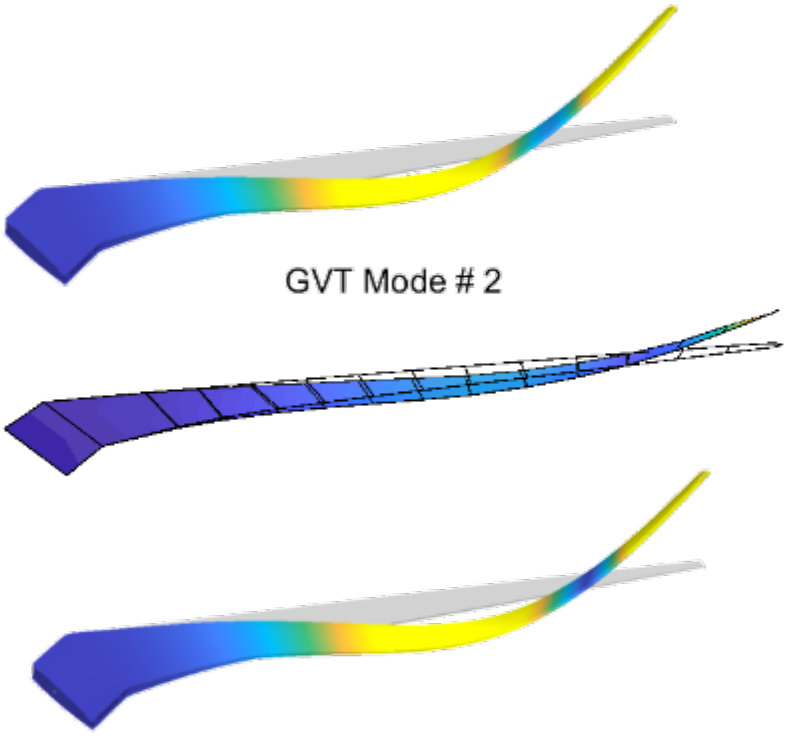

Figure D.2. Mode Shape 2 (2nd bending) Comparison. "With skin offset" FEM (top), GVT Result (middle) and "no skin offset" FEM (bottom).

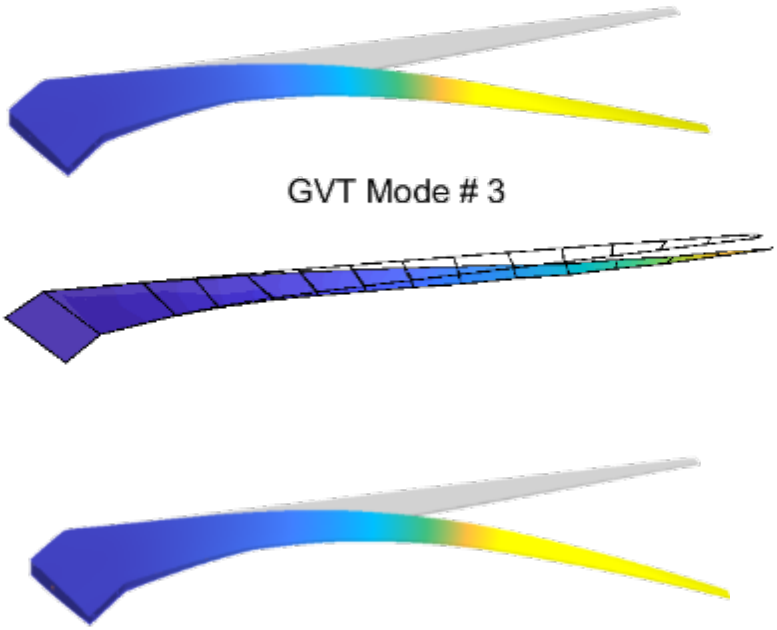

Figure D.3. Mode Shape 3 (1st in-plane bending) Comparison. "With skin offset" FEM (top), GVT Result (middle) and "no skin offset" FEM (bottom).

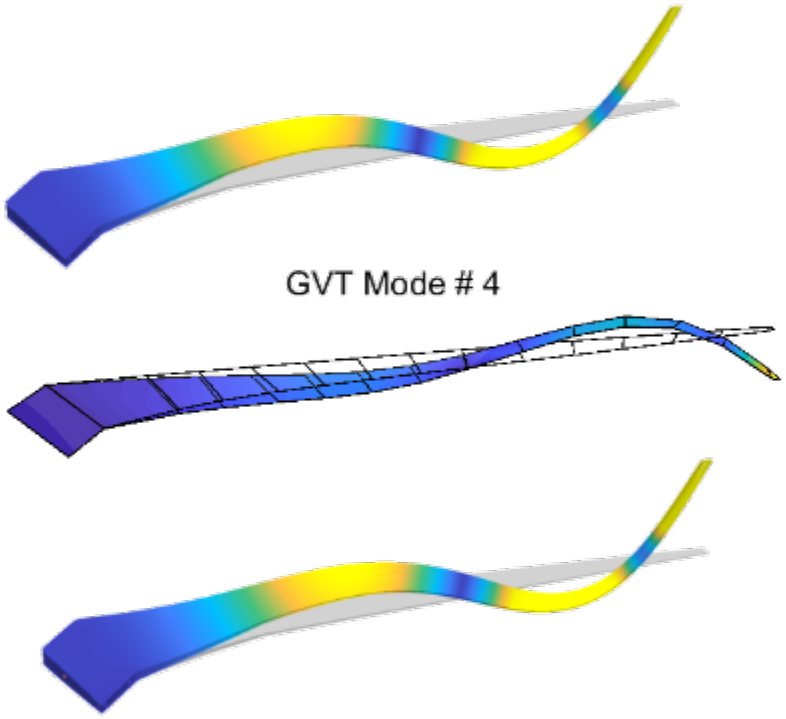

Figure D.4. Mode Shape 4 (3rd bending) Comparison. "With skin offset" FEM (top), GVT Result (middle) and "no skin offset" FEM (bottom).

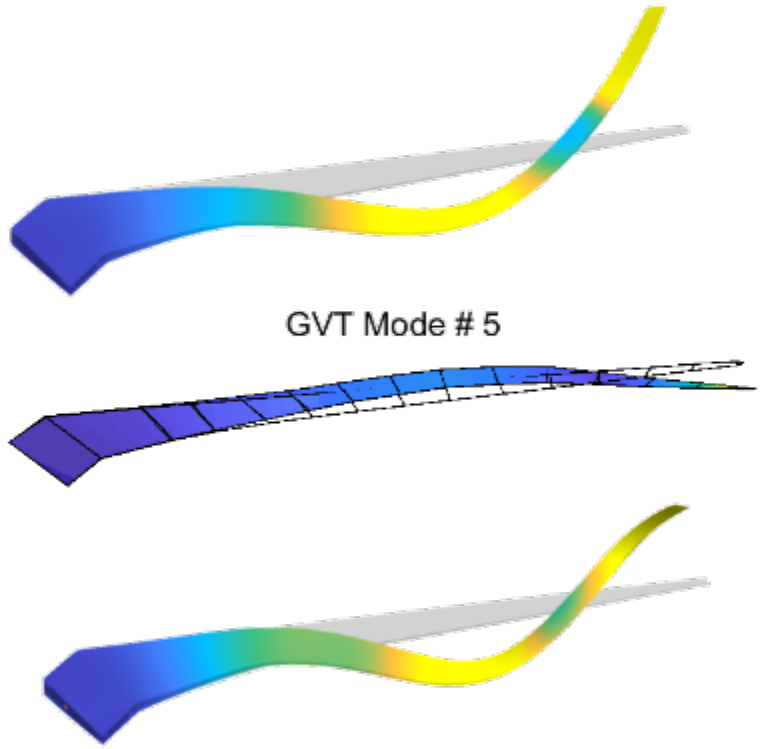

Figure D.5. Mode Shape 5 (2nd in-plane bending) Comparison. "With skin offset" FEM (top), GVT Result (middle) and "no skin offset" FEM (bottom).

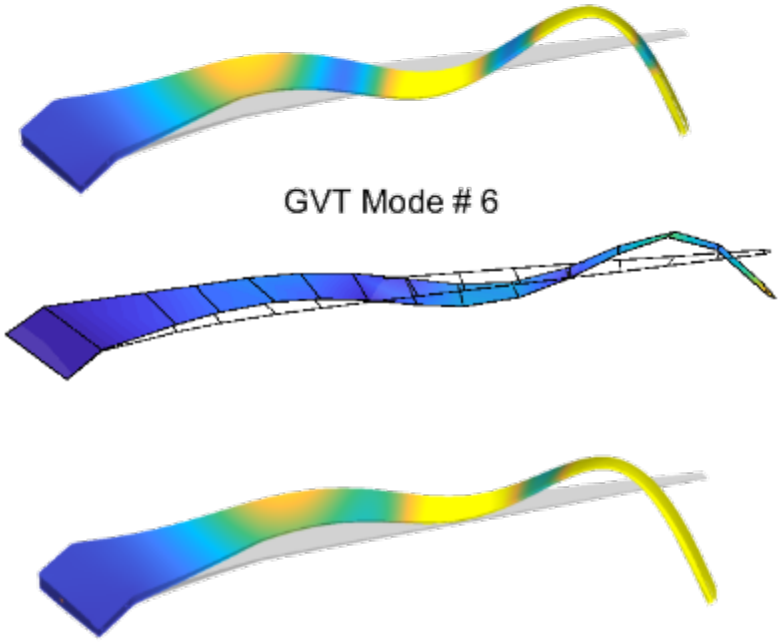

Figure D.6. Mode Shape 6 (4th bending) Comparison. "With skin offset" FEM (top), GVT Result (middle) and "no skin offset" FEM (bottom).

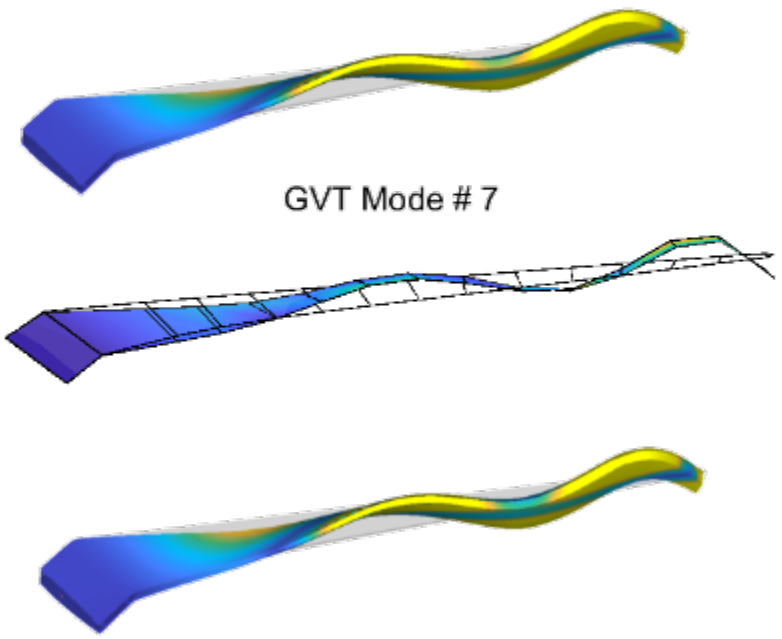

Figure D.7. Mode Shape 7 (5th bending with 1st torsion) Comparison. "With skin offset" FEM (top), GVT Result (middle) and "no skin offset" FEM (bottom).

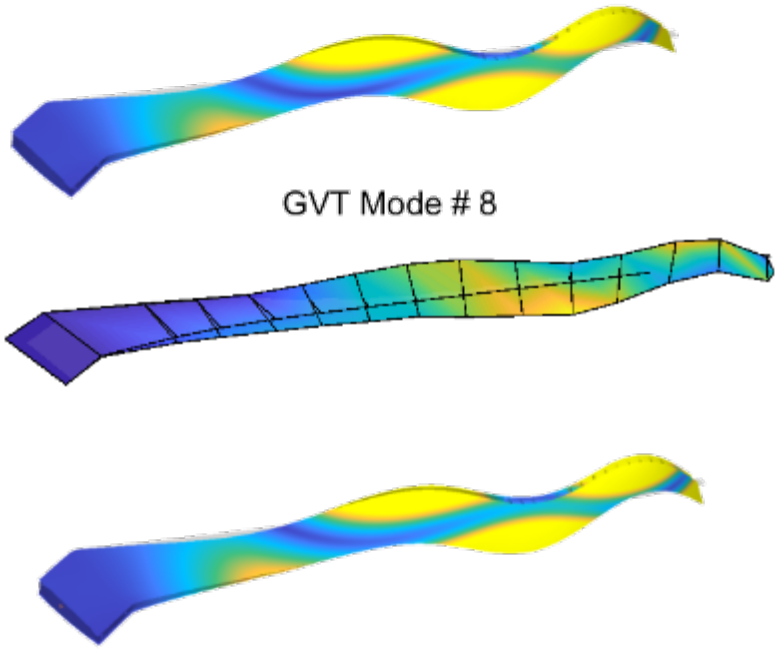

Figure D.8. Mode Shape 8 (2nd torsion with slight 5th bending) Comparison. "With skin offset" FEM (top), GVT Result (middle) and "no skin offset" FEM (bottom).

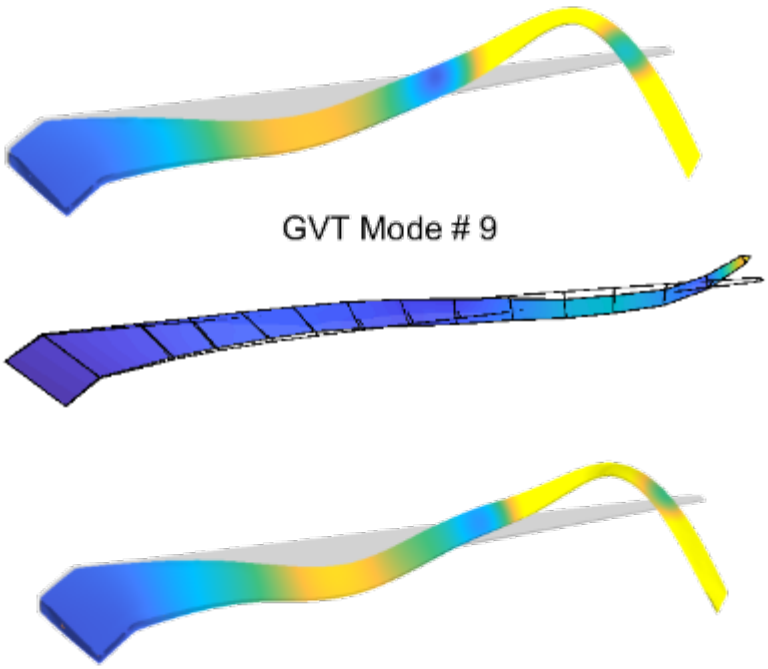

Figure D.9. Mode Shape 9 (3rd in-plane bending) Comparison. "With skin offset" FEM (top), GVT Result (middle) and "no skin offset" FEM (bottom).

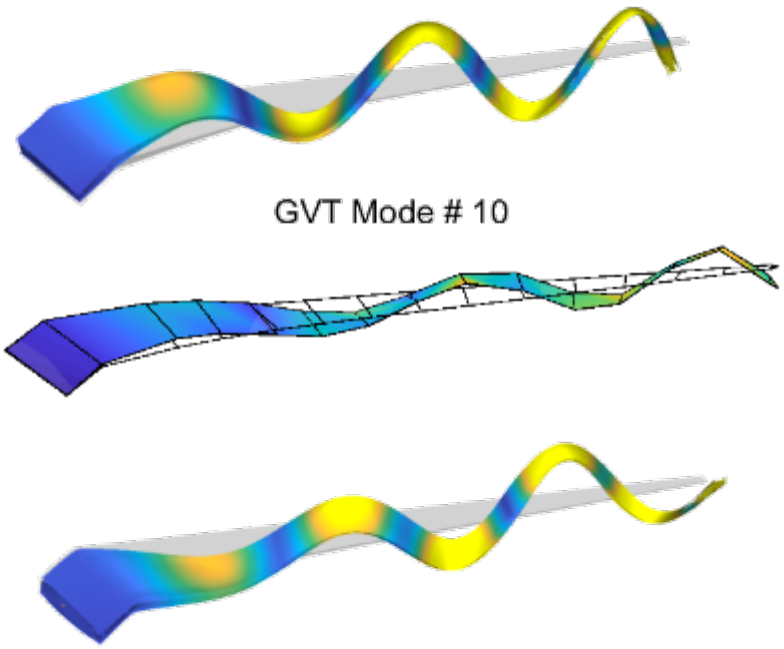

Figure D.10. Mode Shape 10 (6th bending) Comparison. "With skin offset" FEM (top), GVT Result (middle) and "no skin offset" FEM (bottom).

Appendix E. Through Thickness Topology Optimization

Passive Aeroelastic Tailoring of High-Aspect Ratio Wings: Through-thickness Topology Optimization

Mark Leader, Ting Wei Chin, and Graeme J. Kennedy
Georgia Institute of Technology

Contents

1 Introduction

This document provides a summary of the work performed under the Passive Aeroelastic Tailoring of High-Aspect Ratio Wings project at the Georgia Institute of Technology. The goal of this part of the project was to explore the potential benefits of utilizing novel through-thickness topology optimized wing structures to achieve passive aeroelastic tailoring. This is a challenging technical task due to the large design space opened up by allowing arbitrary through-thickness topology in the depth of the wing. Large-scale design and analysis problems are produced when applying conventional topology parametrization strategies to the through-thickness topology problem. These problems require specialized, state-of-the-art computational methods developed specifically to leverage high-performance computing resources in order to achieve the necessary resolution. In addition, a full spectrum of structural design criteria must be considered to achieve a realistic design, including stress-based strength criteria, structural stability, and natural frequency requirements. Each of these criteria were addressed within the scope of the project, as described below.

This project undertook a first step towards this ambitious goal of through-thickness topology wing design by considering a variety of modeling strategies and fidelities. Initial work examined compliance minimization, using both a static tip load as well as a steady aerodynamic load. Buckling constraints applied to the wing skins were also explored. These results are summarized in Section 2. Next, to achieve large-scale, detailed through-thickness topologies, we developed a geometry and meshing tool called TMR. TMR allowed us to efficiently generate very large meshes and perform adaptive mesh refinement to improve the structural resolution in the designs while reducing overall computational costs. Section 3 provides more detail on TMR and our meshing capabilities. Section 4 illustrates some of the compliance minimization results using the meshes generated through TMR. In order to create more practical designs, we needed to shift to using a stress-constrained mass minimization formulation for topology optimization. This problem formulation is considerably more difficult than compliance minimization, and Section 5 details how we treated stress constraints to be more suitable for large-scale topology optimization problems. Next, we developed an approach to handle natural frequency constraints for these very large through-thickness topology optimization problems. While still relevant to the design problem on their own, natural frequency constraints are similar to buckling constraints in that they both require solving eigenvalue problems, and consideration of multiple eigenvalues. However, the natural frequency eigenvalue problem is somewhat easier to solve due to numerical challenges of generalized buckling eigenvalue problem. Section 6 describes in detail our approach for efficiently applying natural frequency constraints for large-scale topology optimization problems. The slender geometry of the uCRM provides an additional challenge for topology optimization, as a very large number of elements are required to generate sufficient detail through the thickness of the wing. For this reason, we also explored two different, simpler geometries when developing our current capabilities. Section 7 provides results using these simpler geometries for three different problem formulations: compliance minimization, stress-constrained mass minimization, and stress- and frequency-constrained mass minimization. At the end of the same section, we provide our most recent results for topology optimization with the uCRM geometry. Finally, we provide some closing remarks in Section 8.

The overall framework, the connections between its components, and the solution process flow are illustrated in Figure 1. The process of solving a topology optimization problem begins with a CAD geometry definition that is imported from a STEP file into TMR, our open source mesh

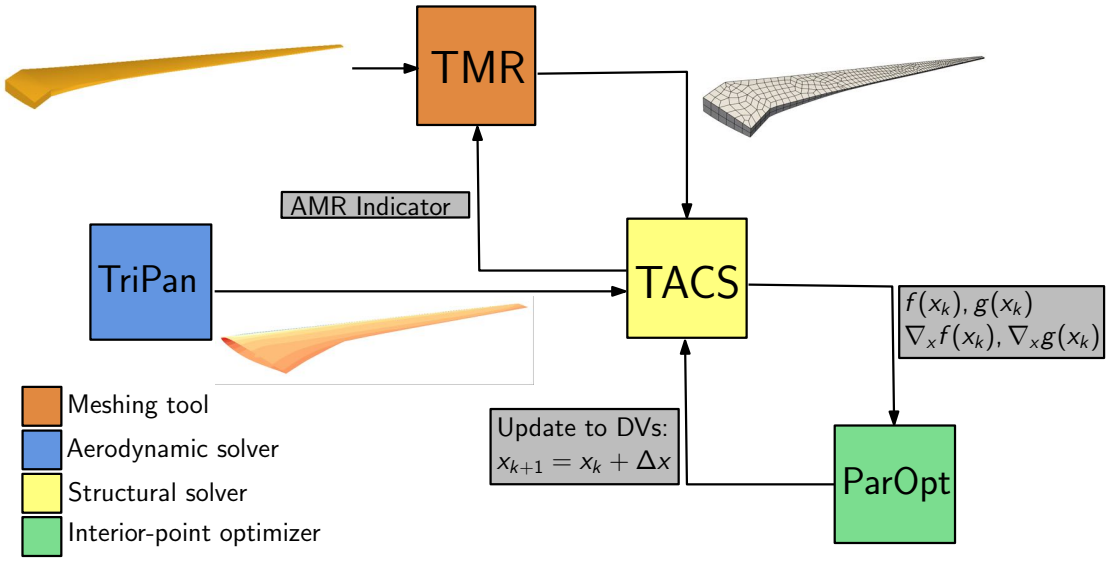

Figure 1: Topology optimization framework.

generation and adaptive-mesh refinement tool[1]. TMR generates a hierarchy of hexahedral meshes of the domain that are well-suited for geometric multigrid methods. TMR is also used to define the boundary conditions, material properties, and topology design variables. The node locations, element connectivity, and boundary conditions are passed from TMR to our open source structural solver called TACS [11][2]. TACS evaluates the objective and constraint functions, such as the structural mass and aggregate stress, and their derivatives with respect to design variables, which are then passed to our open source optimizer ParOpt[3]. ParOpt is a parallel optimization toolkit that takes the objective and constraint functions and their gradients as inputs. TACS and ParOpt iterate until a convergence criterion is satisfied. Finally, when mesh adaptation is used, a local indicator drives the generation of a new mesh and the process repeats.

2 Aerostructural Optimization with the 2.5D Model

In this section, we present the details of the initial work on this project, focusing on results from the mass-constrained compliance minimization and mass-constrained buckling optimization problems. All results utilize a spatial filter to alleviate any numerical instabilities or checkerboard patterns [23].

2.1 uCRM-9 and uCRM-13.5 Wingbox Designs

Figure 2 shows the optimized design for uCRM-9 wingbox under static aerodynamic load, while Figure 3 shows the optimized design for the 10% scale uCRM-13.5 wingbox subjected to a point load at the tip.

[1] https://github.com/gjkennedy/tmr
[2] https://github.com/gjkennedy/tacs
[3] https://github.com/gjkennedy/paropt

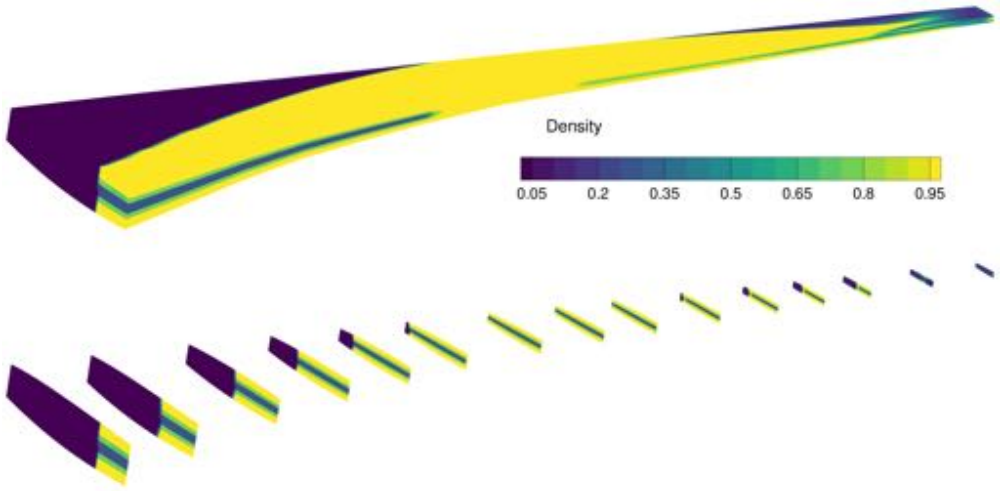

Figure 2: uCRM-9 wingbox optimized for static aerodynamic loading.

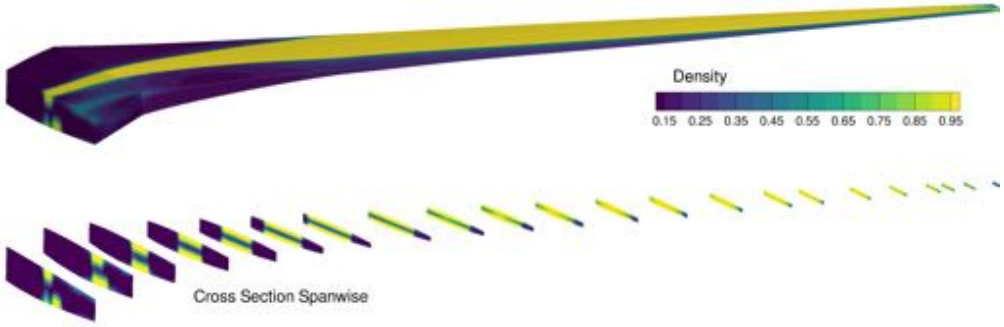

Figure 3: uCRM-13.5 wingbox optimized for tip point loading.

The results illustrate the effect of the loading on the final optimized designs. For the design under static aerodynamic loading, most of the material distribution is placed inboard of the wing, given that the loading on the surface is the largest at the root. On the other hand, the optimized uCRM-13.5 design has more material placed near the tip of the wing due to the location of the point load. In both cases, the optimized wingbox designs are not discrete 0-1 solutions. The through-thickness distribution of material in both wingboxes mimics a composite structure. The internal intermediate stiffness material acts in a similar manner to a soft-core with the top and bottom surfaces acting as stiffer face-sheets. This configuration maximizes the bending stiffness of the wing for a given fixed mass.

2.2 Optimized Design of Flat Plate and uCRM-13.5 Skin

Next, we consider the results from buckling optimization of the wingbox skin. The buckling optimization formulation includes a number of eigenvalues within the KS aggregation function. To ensure that the design is not sensitive to the number of eigenvalues, we first investigate how the optimized design changes as the number of aggregated eigenvalues increases.

Figure 4 shows the number of function evaluations required for the optimization and the final designs obtained as the number of aggregated eigenvalues increases. For designs with less than

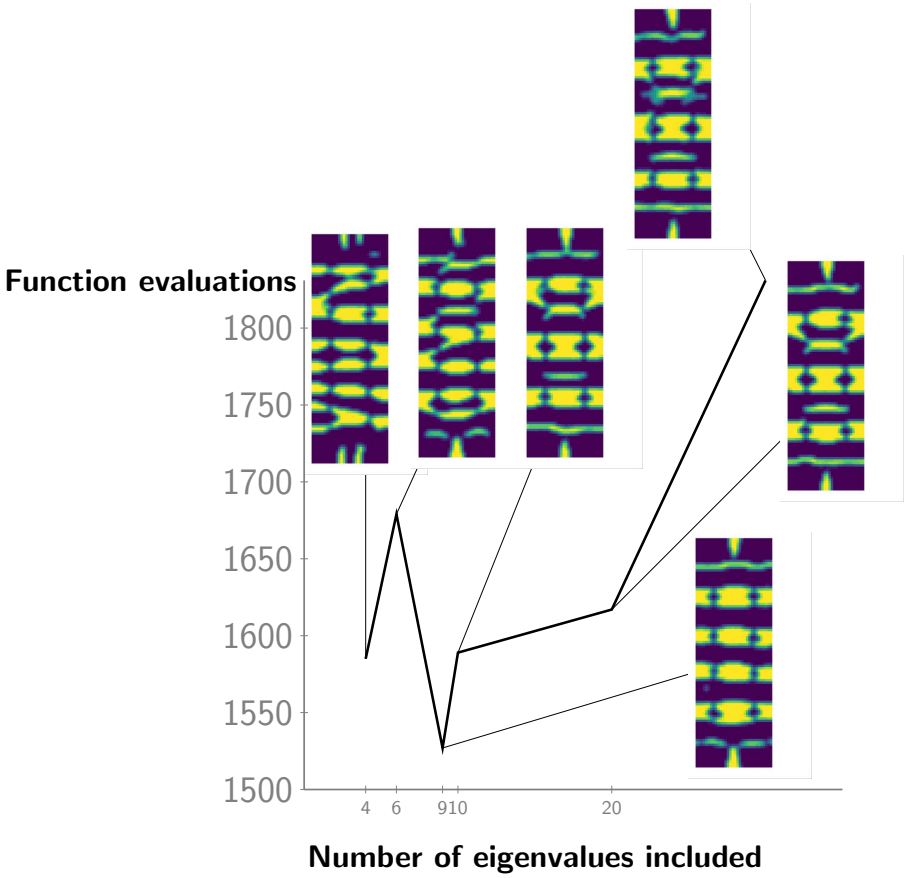

Figure 4: Design changes drastically for less than 10 eigenvalues included.

ten eigenvalues, the number of axial members varies. Once the number of aggregated eigenvalues exceeds ten, the number and shape of the members in the optimized design remains relatively fixed. Furthermore, increasing the number of eigenvalues beyond ten results in a greater number of function evaluations required to obtain the optimized design. Therefore, the buckling optimization problems presented here, both for the flat plate as well as the uCRM skin, include the ten lowest eigenvalues.

Figure 5 shows the optimized design for the flat plate subjected to both buckling and shear displacement boundary conditions, as well as the buckling mode for the optimized design. Since the mass constraint fixes the total plate mass at the average of the two candidate thicknesses, the final design consists of equal areas of both candidate thicknesses. Furthermore, the thicker candidate material is placed parallel to the compressive load.

Figure 6 shows the optimized design for the uCRM skin segment. The skin segment is extracted from the top skin of the uCRM-13.5 wingbox as shown in Figure 7 and Figure 8. The skin segment is subjected to both buckling and shear displacement boundary conditions. Due to the geometric skew of the skin and the curvature of the segment, the optimized design is different from the previous flat plate design.

Lastly, Figure 9 shows the results for buckling optimization with stress constraints for the flat plate and uCRM skin segment. Due to the stress constraint that smooths out any stress concentra-

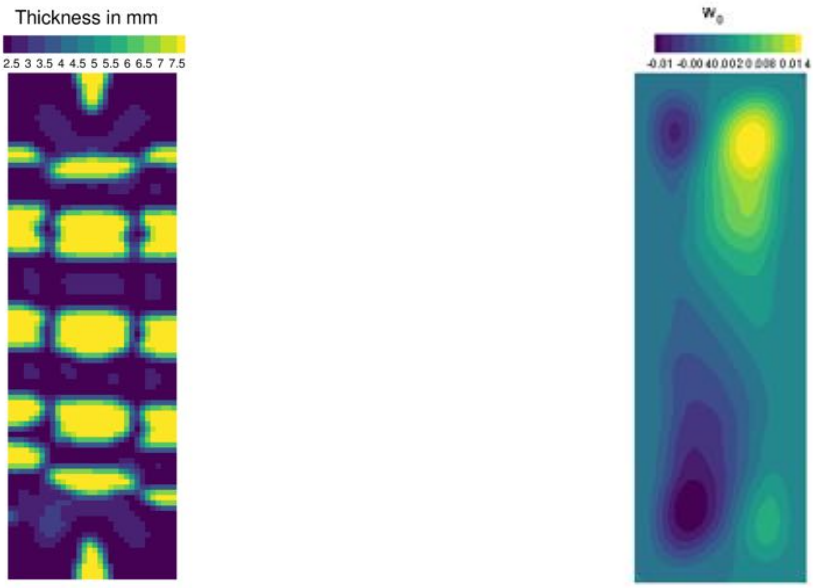

(a) Optimized design obtained after 500 iterations. (b) First buckling mode of optimized design.

Figure 5: Optimized design of flat plate and its first buckling mode.

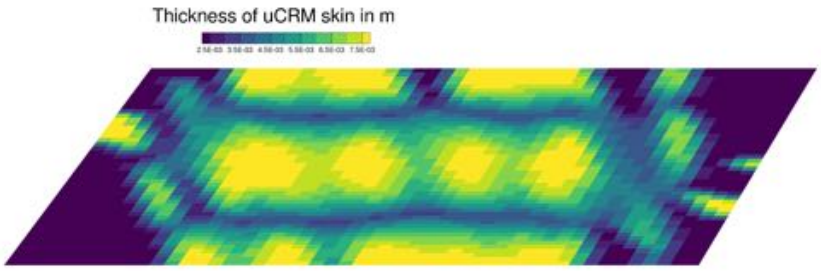

Figure 6: Optimized design of uCRM skin.

tion, we see different thickness distribution compared to Figures 5 and 6.

2.3 Segmentwise Topology Optimization

The results from Section 7 illustrate the demanding computational requirements needed to obtain an optimized wingbox topology on a full-scale mesh with sufficient resolution to obtain through-thickness structural features. In this section, we present an alternate segmentwise approach that seeks to address these challenges.

Figure 10 illustrates the segmentwise topology optimization approach. In this method, the full-scale wingbox is divided into segments that are optimized independently. As shown in Figure 11, loads on each segment of the wingbox can be estimated independently since the overall wing is statically determinant. This segment-based load determination procedure is illustrated below for an elliptic lift distribution. The extension of this procedure to general, nonelliptic lift distributions poses no difficulty.

Figure 7: Optimized design of uCRM skin on a wing.

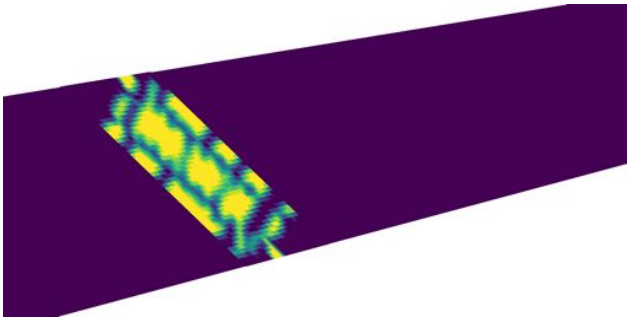

Figure 8: Enlarged view of optimized skin segment.

The elliptic lift distribution over a wing can be expressed as follows:

$$L'(y) = \frac{\pi}{4} L \sqrt{1 - \left(\frac{2y}{b}\right)^2} \tag{1}$$

where L is the lift, $L'(y)$ is the lift per unit span, and $b/2$ is the semi-span. The moment, torque and shear acting at a station y_0 can be determined by integrating the lift distribution as follows:

$$\begin{aligned} M_x(y_0) &= \int_{y_0}^{b/2} (y - y_0) L'(y) dy \\ T_y(y_0) &= \int_{y_0}^{b/2} (y - y_0) \tan(\Lambda) L'(y) dy \\ V_z(y_0) &= \int_{y_0}^{b/2} L'(y) dy \end{aligned} \tag{2}$$

where $M_x(y_0)$, $T_y(y_0)$, and $V_z(y_0)$ are the moment, torque, and shear, respectively, and Λ is the sweep of the wing.

Instead of treating the moment, torque and shear resultants as distributed loads, we impose them as point forces. While the shear loads can be applied directly to the segment, the moment and torque resultants must be resolved into equivalent point forces, as shown in Figure 12. Figure 12 also illustrates the boundary conditions, which are applied to the segment to remove rigid body

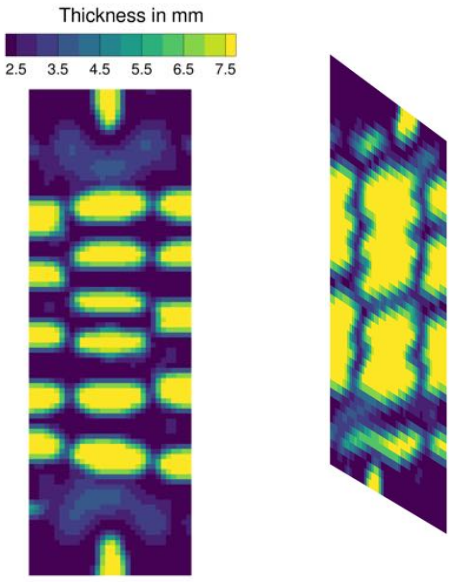

Figure 9: Optimized design with stress constraints of flat plate and uCRM skin segment, respectively.

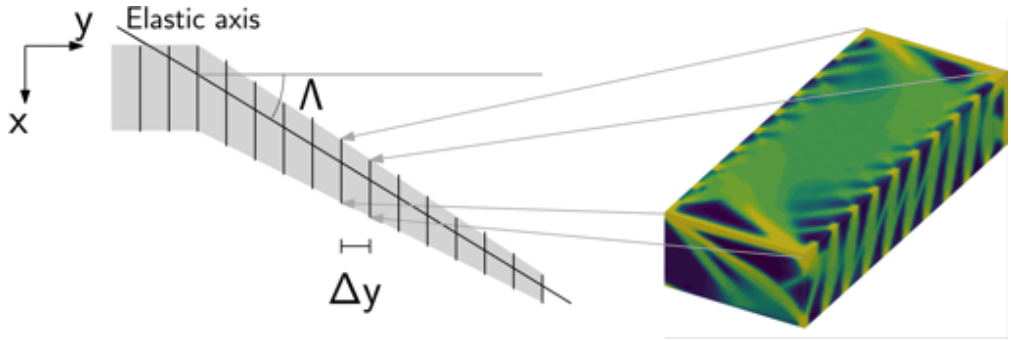

Figure 10: Illustration of Segmentwise Topology Optimization.

translation and rotation. Lastly, crushing loads are applied as shown in the figure to simulate the effects of aerodynamic loading.

Each segment in the wingbox is discretized with 128 chordwise elements, 64 spanwise elements and 64 through thickness elements, resulting in a mesh with just over 600 000 elements. A single material formulation is used as described above. The compliance-minimization formulation is with the mass constraint at 20% of the total solid domain.

The results from the topology optimization of a single segment are shown in Figure 13. The segment-based design method clearly enables better-resolved through thickness structural features with truss-like structure.

Figures 14, 15 and 16 show the internal structure in the chordwise, spanwise and through-thickness directions, respectively. The optimized design has material distributed primarily to the surfaces of the wingbox segment, with no internal structure. Figure 14 clearly shows truss-like structures formed at either ends of the segment, while the center remains void in the chordwise direction. Similarly, Figure 15 shows that the spanwise direction has interesting features at each

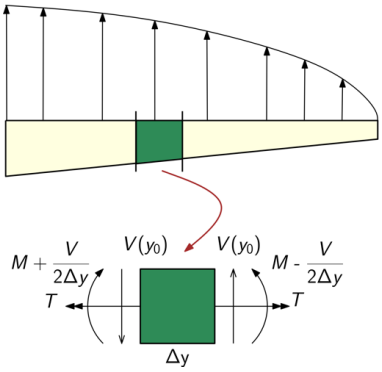

Figure 11: Lift distribution model on uCRM-13.5 wing.

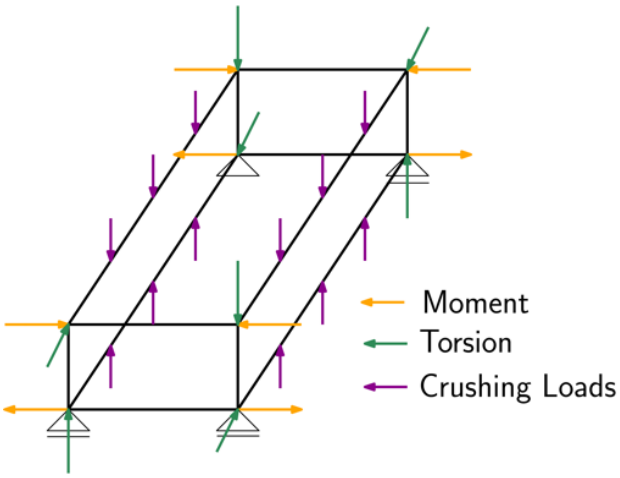

Figure 12: Application of loads to wing segment.

end of the segment due to the crushing aerodynamic loads. Finally, Figure 16 shows that the optimizer has placed most of the material at the top and bottom surface, forming a skin-like structure for maximum bending stiffness.

2.4 2.5D Sandwich Model

In this approach, we seek an alternate finite element model for topology optimization by modeling the wingbox as a sandwich-type structure. The benefits of this model are two-fold:

1. The model has a significantly smaller number of design variables and degrees of freedom in the finite-element model when compared to full three-dimensional models.

2. Stress and buckling constraints are easier to impose within the model, including the effect of the through-thickness core. The model consists of a shell model for the upper and lower surface with a 3D through-thickness volume element. Stress constraints are imposed in the skins and include the geometric stiffness from the through-thickness elements in the buckling calculation. The goal of this is approach is to obtain optimal rib/spar layouts that include buckling criteria as well as a fully-sized skin.

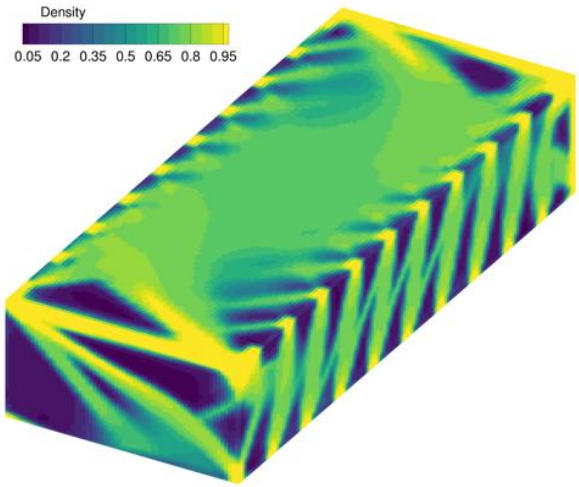

Figure 13: Segmentwise Optimized Design.

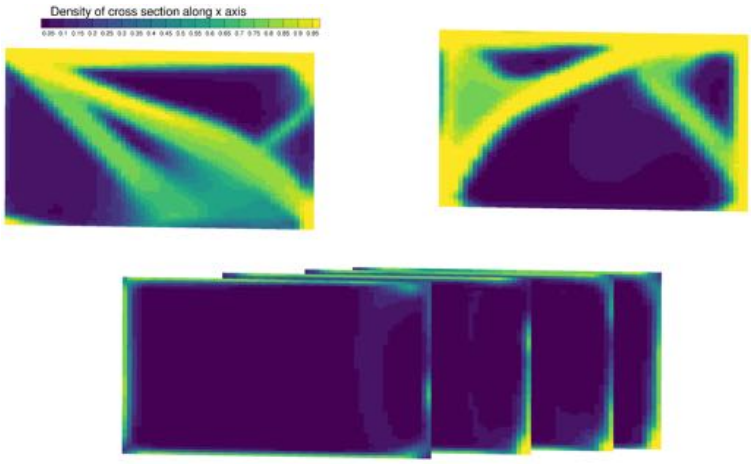

Figure 14: Chordwise Optimized Design.

Based on the results from our compliance minimization work, the model has an upper and a lower skin connected through a sandwich core. The finite-element model uses a 3D sandwich structure where the individual elements within the volume mesh are analogous to an extended high-order sandwich panel theory (for instance EHSAPT). Instead of discretizing the volume mesh through the thickness, we create volume elements that extend from the top skin to the bottom and discretizing them in both the spanwise and chordwise directions. In this finite element model, as shown in Figure 17, we assume a displacement that is a cubic function of the through-thickness direction, with 4 quadrature points through the thickness. This allows us to capture any shear stresses in the core of a sandwich structure.

This sandwich modeling approach eliminates the difficulty of obtaining a through-thickness topology for uCRM wingbox using on a 3D solid element. MITC shell elements are used for the upper and lower surfaces of the wingbox. This finite element formulation reduces the computational cost so that we can employ aerostructural optimization with stress, buckling as well as

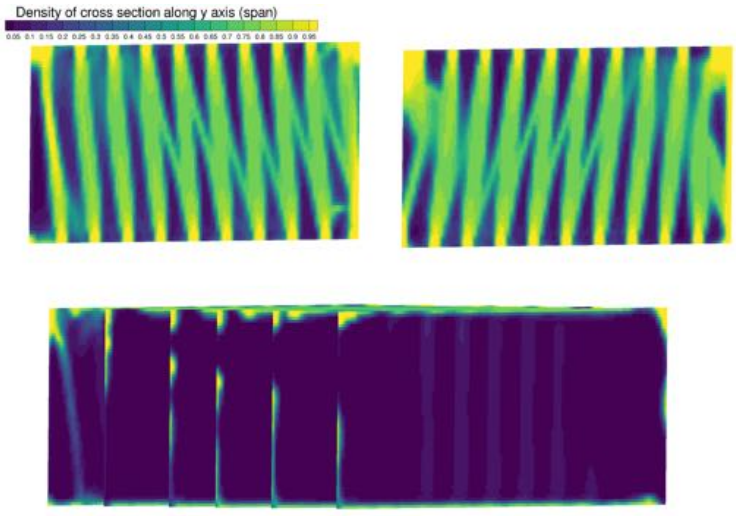

Figure 15: Spanwise Optimized Design.

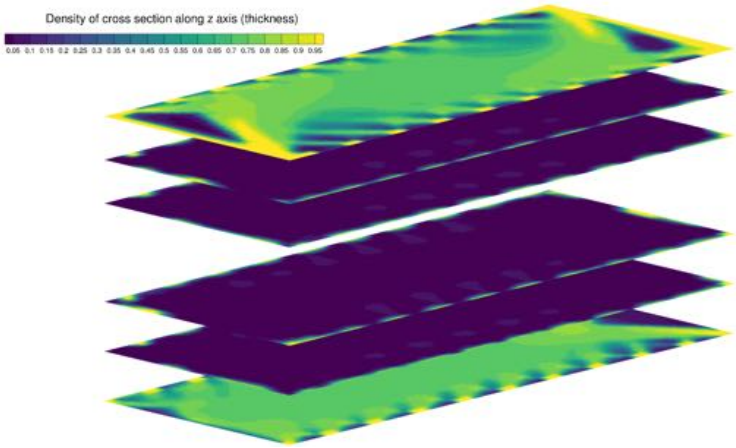

Figure 16: Thicknesswise Optimized Design.

aeroelastic constraints on the entire wingbox.

First, we examined a structural mass-minimization problem with 2.5g static load, with both stress and buckling constraints. The buckling constraint is applied to the wing and analyzed using a linearized eigenvalue buckling analysis. The optimization problem is summarized in Table 1 and the result is shown in Figure 18.

From Figure 18, we observed the formation of an elongated spar-rib-like structure in the core that extends from the leading edge of the wing near the tip to the trailing edge of the wing near the root. This is likely formed to resist failure in the core due to the wing deflection. The thickness distribution of the top skin towards the root is also thicker than that of the bottom skin, which is likely to overcome buckling on the top skin due to the upward deflection of the wing.

Additionally, we have added a -1.0g load case to the design problem with additional stress and buckling constraint to evaluate its effect on the final design. Figure 19 shows the obtained result.

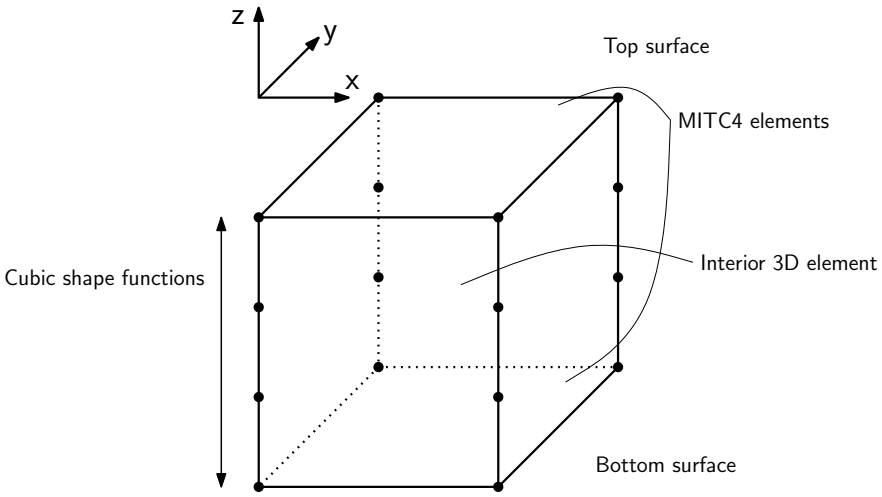

Figure 17: Proposed element under development. Note that the element has bilinear inplane displacements and cubic-through thickness displacements.

Table 1: Static aerodynamic buckling optimization problem description for mass minimization

	Variable/function	Description	Quantity
Minimize	Mass	Structural mass	
with respect to	x	Design variables for the core	3401
	t	Thickness for the top and bottom skin	6802
		Total number of design variables	**10203**
Subject to	$KS_{stress} < 1.0$	Yield Stress	1
	$KS_{buckling} > 1.5$	Buckling constraint on the structure	1
		Total number of constraints	**2**

Comparing the two designs, we see in the case of having both 2.5g and -1.0g loading, the "rear spar" present in Figure 18 was moved forward. The skin thickness distribution in both cases are similar except for some regions in the dual loading case where the thickness is larger.

In addition, we have investigated the effect of skin thickness and core density distribution, on the aerostructural optimization problem for minimum TOGW. This characterization requires two separate aerostructural optimization formulations: one with only core density design variables and the other with only thickness design variables. These formulations are shown in Tables 2 and 3.

For the problem shown in Table 2, the resulting design is shown in Figure 20. We observed from Figure 20 that the design is similar to those shown in Figure 18 and 19, where there is a rib-spar structure extending from the leading edge of the wing to the trailing edge of the wing except in this case, the back spar and leading edge rib-spar is not connected. This can be due to the fact that the thicker top and bottom skins are providing uniform stiffness as well.

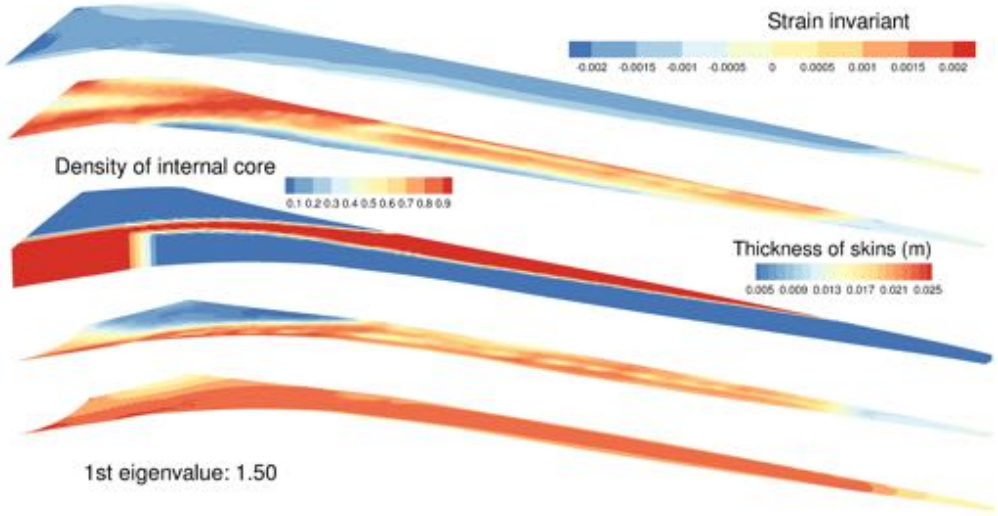

Figure 18: Result for static aerodynamic buckling optimization with stress constraints for mass minimization with 2.5g load

Table 2: Aerostructural optimization problem description for TOGW minimization with only core density design variables

	Variable/function	Description	Quantity
Minimize	TOGW	Takeoff Gross Weight	
with respect to	x	Design variables for the core	3401
	α	Angle of attack (for each flight condition)	2
		Total number of design variables	**3403**
Subject to	$KS_{stress} < 1.0$	Yield Stress	1
	L = nW	Load Factor (n depends on flight condition)	2
		Total number of constraints	**3**

For the problem shown in Table 3, the design derived is shown in Figure 21. Figure 21 shows the result for aerostructural optimization for TOGW with only the skin thickness as design variables and the core density distribution is fixed at 0.5. We see that without the core design variables, the distribution of the thickness is place further inboard of the wing as expected.

Lastly, we employed an aerostructural formulation to minimize the takeoff gross weight (TOGW) of the structure subjected to stress constraint. Table 4 below shows the mathematical formulation for the optimization process.

By varying the lowering core stiffness and density properties to around 20 GPa and keeping the skin stiffness at 70 GPa, we obtain the design shown in Figure 22. We observed that with the lower core stiffness, the optimizer choose to place more of the core structure in the middle of the wing.

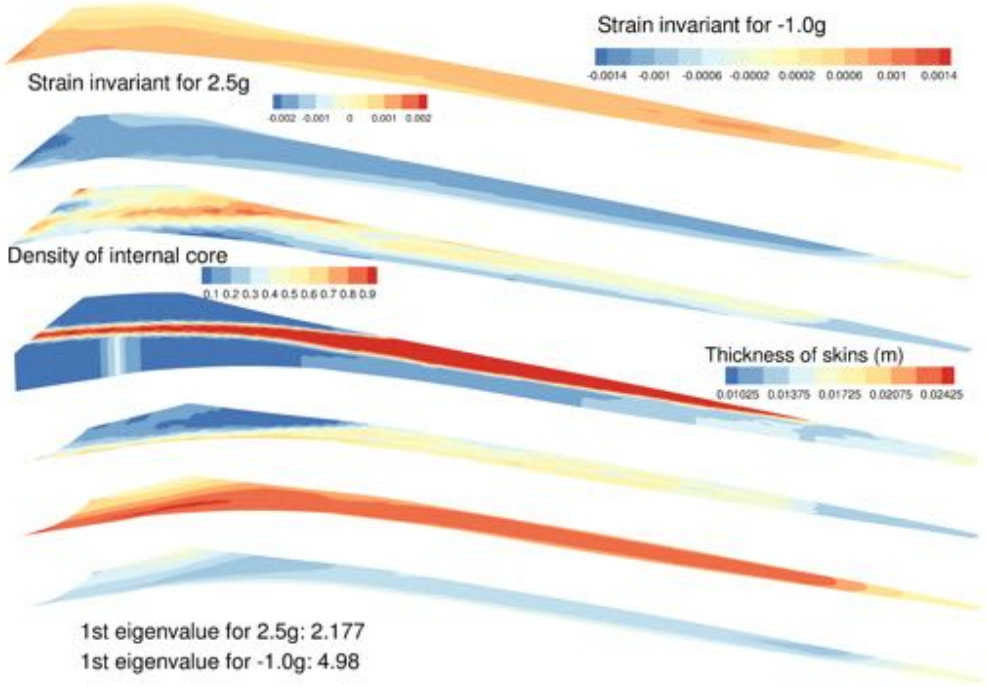

Figure 19: Mass minimization with stress and buckling constraints at 2.5g and -1.0g

2.5 Cellular Lattice Core Structure

A separate effort was made to map the variable density core designs to a cellular lattice core structure. Using this mapping, the wingbox core could be reconstructed with the chosen fixed angle cellular lattice structure. The stiffness and density distribution is given as an input to the mapping. The resulting lattice structure would consist of cells of a fixed size but varying interior density given by the topology optimized core structure.

For the FEM model, we were able to improve on the dummy wingbox model that was generated previously. The top and bottom CQUAD skin elements are modelled as PSHELLS and the core CHEXA brick elements are modelled as PSOLID. Since NASTRAN does not have a suitable sandwich element for the core, we increased the number of through thickness brick- elements to properly model the behavior of the core. We also used the mapping to convert the core density distribution to a cell size distribution with fixed angles and thicknesses. They were used to compute the orthotropic properties of the lattice structure. The resulting properties are then used to compute the orthotropic constitutive property MAT12 for the BDF format.

For the CAD model, we generate the in-plane lattice structure distribution based on the density distribution. In this case, to simplify the process, we divided the wing into 12 different segments spanwise and in each segment, the average density of the core in the region is used to calculate the lattice cell size in those segments. The higher the average density of the region, the smaller and more compact the lattice structure becomes in the corresponding segment. Figure 23 shows a possible spanwise lattice structure distribution based on the spanwise density distribution.

For the generation of the CAD file, we used OpenCASCADE to produce the lattice core struc-

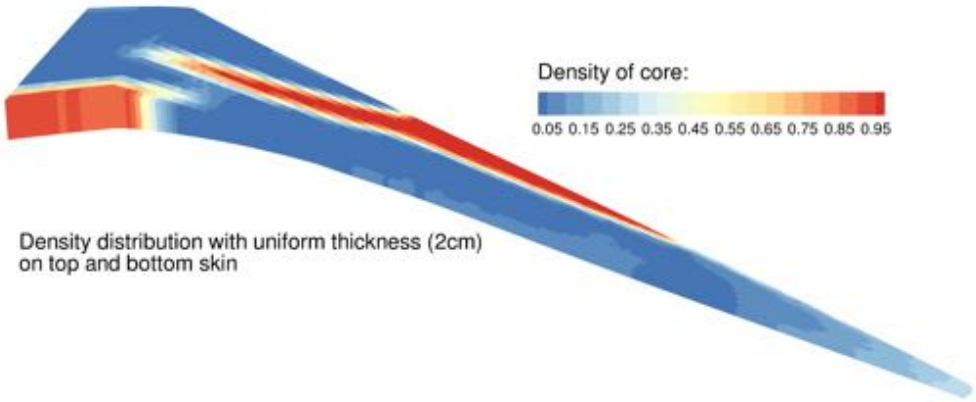

Figure 20: Aerostructural optimization with discrete through thickness topology for fixed upper and lower skin thickness

Table 3: Aerostructural optimization problem description for TOGW minimization with only skin thickness design variables

	Variable/function	Description	Quantity
Minimize	TOGW	Takeoff Gross Weight	
with respect to	t	Thickness for the top and bottom skin	6802
	α	Angle of attack (for each flight condition)	2
		Total number of design variables	**6804**
Subject to	$KS_{stress} < 1.0$	Yield Stress	1
	L = nW	Load Factor (n depends on flight condition)	2
		Total number of constraints	**3**

ture. The wingbox is generated by extruding the desired planform onto the top and bottom surfaces of the wing as provided by the IGES file. A mapping between the core density and the lattice structure was calculated analytically and used to convert the optimized core density distribution to the desired lattice structure. Through this mapping, we compute the nodal locations as well as the connectivity for the lattice structure through the planform. To do so, we divided the planform into 12 different segments spanwise and computing the average density distribution in each region. Each segment will consist of lattice structure with the same cell size. A comparison between the original core structure and the lattice structure is shown in Figure 24. Through OpenCASCADE, we can project the points onto the top and bottom surface such the lattice structure is contained within the wingbox. A STEP file of the structure can be produced as a result.

To generate the lattice structure in the core of the wingbox, we turned to OpenCASCADE, an open source geometry generation tool which is able to read in IGES/STEP files and interact with its generated geometry and output them in the IGES/STEP formats. In our case, we were able to read in the input uCRM-13.5 IGES surface file and generate the planform of the wingbox as well as the lattice structure spanwise distribution. What remains to be done is to trim the excess lattice

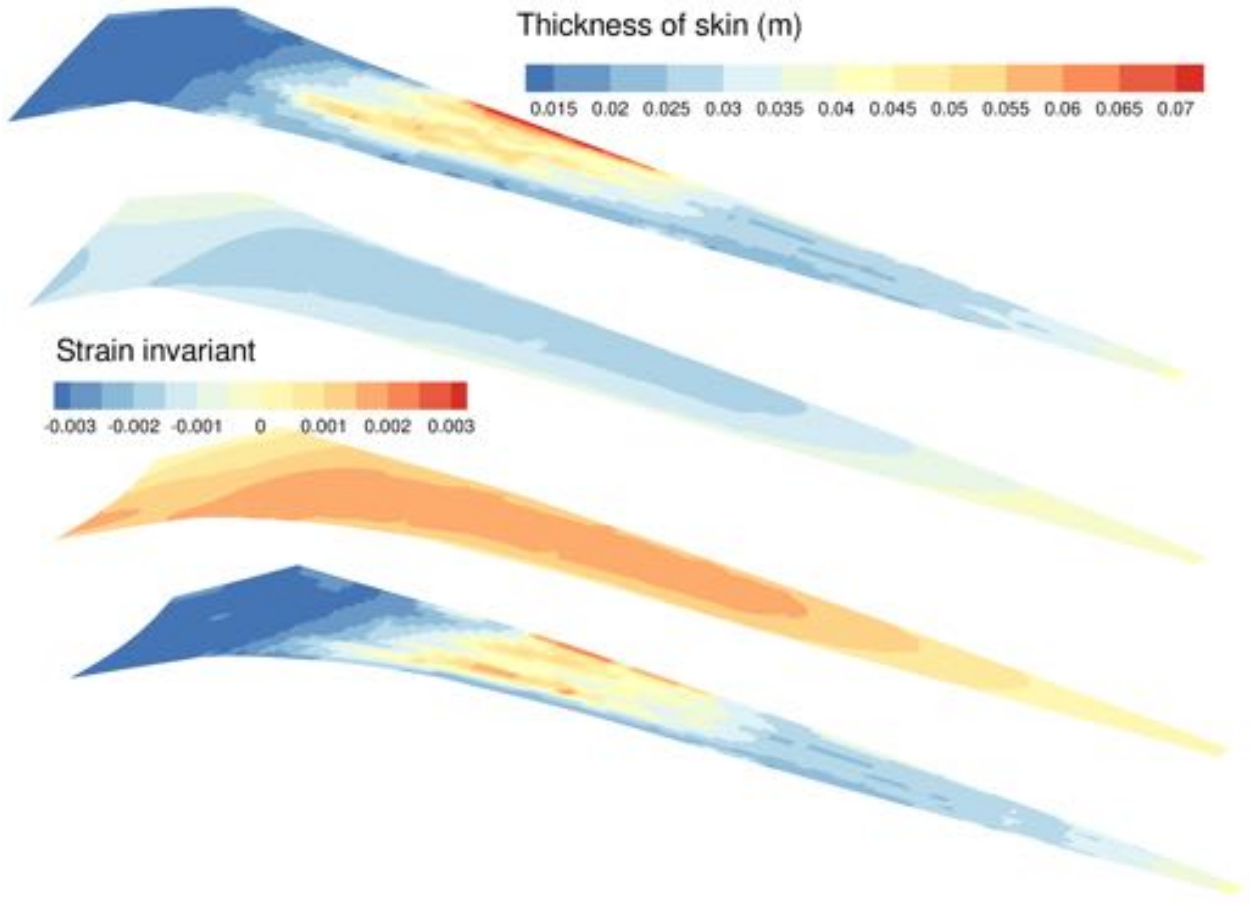

Figure 21: Aerostructural optimization with only skin thickness as design variables

structure such that it fits into the uCRM-13.5 wingbox geometry. Another alternative that is under consideration is to generate untrimmed planform and lattice structure distribution as STEP files and post process it through commercial CAD software. Figures 25 and 26 show the progress in OpenCASCADE.

3 Geometry and Meshing

To achieve the objective of creating through-thickness topology optimized structural designs for the uCRM 13.5 wing, we developed a geometry and meshing tool called TMR. TMR is a parallel adaptive mesh generation tool that is capable of efficiently meshing complex geometries with hundreds of millions of hexahedral elements using a semistructured octree method. These high-resolution meshes are created by first generating an initial coarse hexahedral mesh and subsequently refining the mesh using an octree on each coarse element [9, 3]. The initial coarse hexahedral volume mesh can be either generated in TMR using a swept-mesh method or taken as input from external hexahedral meshing tools. The swept-mesh technique results in a hexahedral mesh that is unstructured on the source and target faces, but structured in the swept direction [16]. The source quadrilateral mesh is generated using the Blossom-Quad algorithm [19]. This algorithm generates an even

Table 4: Aerostructural Optimization Problem Description for TOGW minimization

	Variable/function	Description	Quantity
Minimize	TOGW	Takeoff Gross Weight	
with respect to	x	Design variables for the core	3401
	t	Thickness for the top and bottom skin	6802
	α	Angle of attack (for each flight condition)	2
		Total number of design variables	**10205**
Subject to	$KS_{stress} < 1.0$	Yield Stress	1
	L = nW	Load Factor (n depends on flight condition)	2
		Total number of constraints	**3**

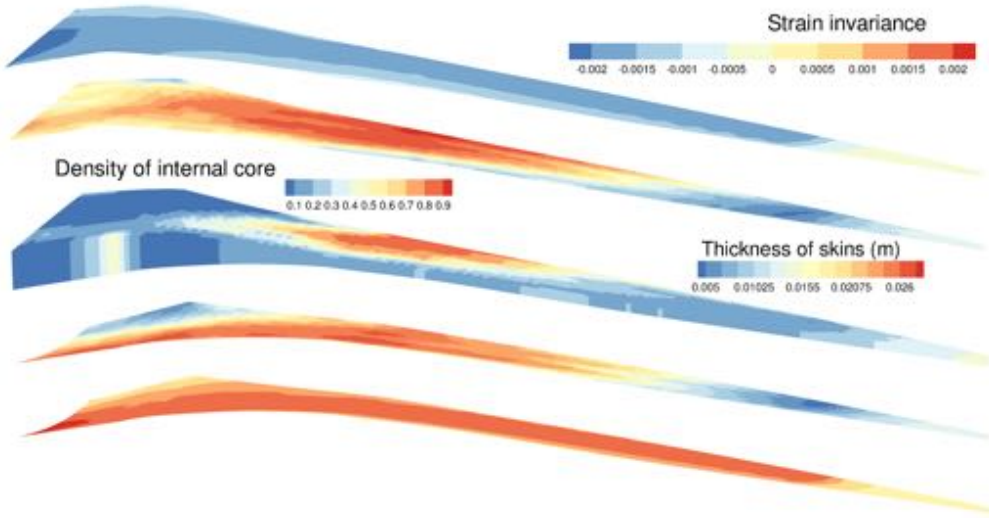

Figure 22: TOGW-optimized design with E_{core} = 20.0 GPa

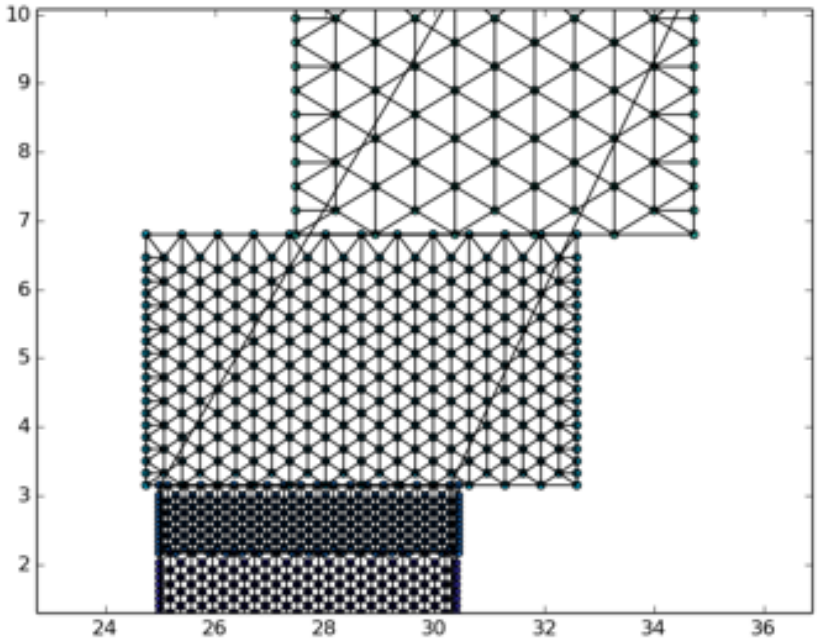

Figure 23: Differing lattice size distribution for differing average density

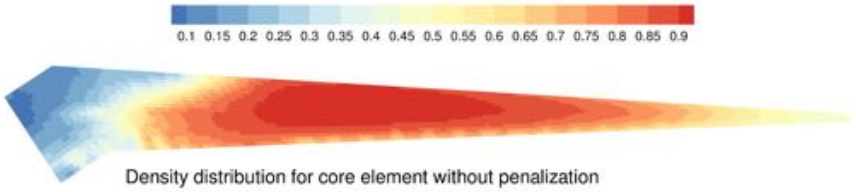

(a) Optimized core structure without penalization

(b) Mapped lattice structure

Figure 24: Comparison between the original core structure and the mapped lattice structure

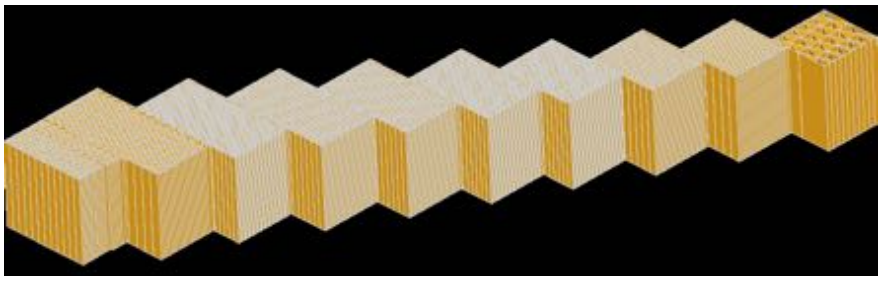

Figure 25: Untrimmed lattice structure design for the core

Figure 26: Top and bottom surface of the wingbox

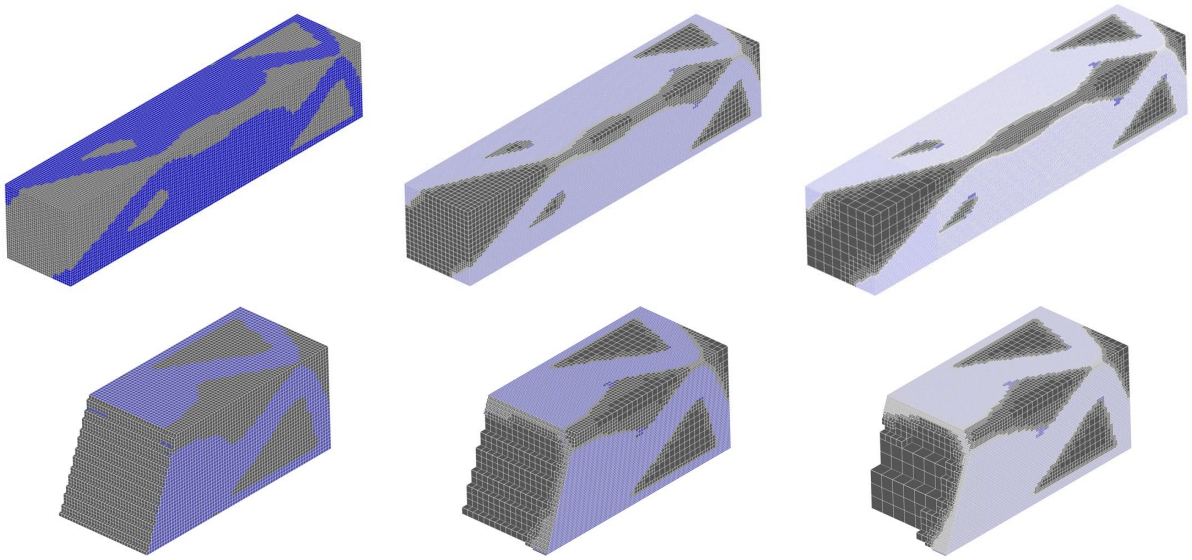

(a) Design on initial uniform mesh

(b) One cycle of adaptive mesh refinement

(c) Two cycles of adaptive mesh refinement

Figure 27: Feature-based adaptive mesh refinement process. Full domain (top), exposed cut (bottom).

number of triangular elements, and then recombines triangles into quadrilaterals by computing an optimal pairing [7] based on a quality function for each possible quadrilateral. TMR uses the Blossom V implementation of the Blossom algorithm [13].

A key feature of TMR is the ability to locally refine elements, utilizing the underlying octree structure. This is especially important for structures with low volume fractions, like a wingbox, because we can locally refine the mesh for higher resolution where there is material, and coarsen the mesh where there are voids. Figure 27 below illustrates this concept. The left figures show structure that has formed from topology optimization on an initially uniform mesh. The figures in the center column show the mesh after one cycle of adaptive mesh refinement. Where material has formed, the elements are refined by one level, and elements with low values of the design variable have been coarsened by one level. TMR also performs element balancing when refinement is done, so that there is no greater than one level of refinement difference between the elements. The top row shows the full design domain, while the bottom row shows an exposed cut so that the internal volume mesh can be seen.

4 Compliance Minimization

Figure 28 below shows compliance minimization results for the uCRM wingbox. The case shown here uses one cycle of adaptive mesh refinement, resulting in a mesh with 6.4 million elements and 20 million degrees of freedom. In this case, the results resemble those structures formed in the early 2.5D model studies and early aeroelastic optimization results. Unfortunately, this design contains large unsupported regions of wing skin and would likely be highly susceptible to buckling. Furthermore, no strength criteria were imposed within the design optimization formulation.

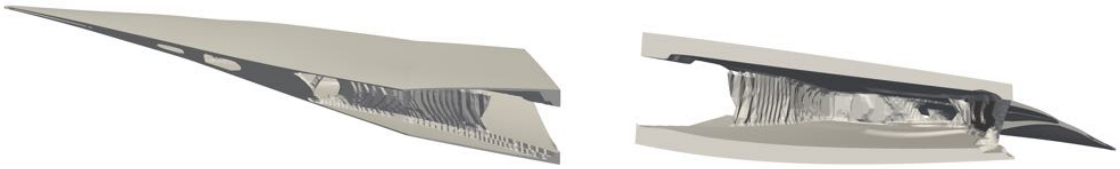

Figure 28: uCRM wingbox compliance minimization results. Leading edge (left), wing root (right).

5 Stress Constraints

Stress constraints within topology optimization pose two primary challenges: first, the well-known stress-singularity issue that affects the stress in areas of vanishing density [4, 5, 14], and second, the problem of imposing a bound on the pointwise stress everywhere within the domain [6]. Our approach to the stress-singularity issue is standard: we utilize an ε-relaxation approach [5, 14] and define a local relaxed stress ratio in element i as follows

$$s_r = \frac{\xi_i}{1-\varepsilon(1-\xi_i)}\frac{\sigma_{vM}}{\sigma_y}, \tag{3}$$

where ξ_i is the interpolated element density, σ_{vM} is the von Mises stress computed from the finite-element solution, σ_y is the design von Mises stress, ε is the stress relaxation parameter. By construction, the relaxed stress ratio (3) vanishes as the local interpolated density vanishes, $\xi_i \to 0$, but achieves the full stress ratio at an interpolated density value of $\xi_i = 1$. Note that the relaxed stress ratio is a function of both the design variables and the finite-element state vector.

To bound the stress everywhere within the structure, we aggregate the relaxed stress ratio using a single KS aggregation functional [1, 10]. The aggregated stress constraint is formulated as

$$c_{KS}(\mathbf{x},\mathbf{u}) = s_r^{\max} + \frac{1}{\rho_{KS}}\ln\left[\int_\Omega e^{\rho_{KS}(s_r - s_r^{\max})}d\Omega\right] \leq \beta, \tag{4}$$

where $c_{KS}(\mathbf{x},\mathbf{u})$ is the KS functional, $s_r^{\max}$ is the maximum relaxed stress ratio in the domain Ω, and ρ_{KS} is the KS parameter. The constraint (4) provides a smooth approximation of the maximum stress in the domain. Here we employ the KS functional, rather than the discrete KS function, which is nonconservative but exhibits mesh independence [10]. The use of the KS functional, rather than a discrete aggregate, ensures that the design problem formulation is consistent between meshes. The parameter β is chosen to be less than unity, due to the use of the nonconservative form of the KS functional, so that the resulting maximum stress is approximately equal to the yield stress. Typical values for β are between 0.5 to 0.7, depending on the value of the aggregation parameter, ρ_{KS}.

Stress-constrained topology optimization designs often exhibit mesh-sensitivity. This issue is more severe in stress-constrained applications compared to compliance design problems, since the local stress is predicted less accurately than the compliance. To address this challenge, we evaluate

the local stress using an elementwise reconstruction. The advantage of the reconstruction technique is that it achieves a less mesh-sensitive estimate of the true value of the stress aggregate (4) than without reconstruction. While different reconstruction methods have been utilized by other authors [27, 18], in this work, we evaluate the local element strain, and subsequently the stress, based on a reconstruction of the displacement field within each element. This approach is designed to be simple to implement and increases the smoothness of the constraint gradient. However, the proposed approach does not improve the asymptotic order of convergence of the stress aggregate itself. This deficiency, in most cases, is moot since the presence of stress singularities in the problem limits asymptotic accuracy.

The reconstruction technique proceeds by adding enrichment basis functions to fit the average displacement derivatives at the element nodes. This process is performed independently for each element, for each displacement component. For the x-component of the displacement, the enriched displacement field is interpolated as follows

$$u(\eta) = \mathbf{N}(\eta)^T \mathbf{u}_e + \bar{\mathbf{N}}(\eta)^T \bar{\mathbf{u}}_e, \tag{5}$$

where $u(\eta) \in \mathbb{R}$ is the interpolated displacement along the x-direction, $\eta \in [-1,1]^3$ are the coordinates in the computational domain, $\mathbf{N}(\eta) \in \mathbb{R}^8$ are the element shape functions, $\mathbf{u}_e \in \mathbb{R}^8$ are the x-component of the displacement at each element node, and $\bar{\mathbf{u}}_e \in \mathbb{R}^9$, are the enriched displacements. The enrichment basis functions, $\bar{\mathbf{N}}(\eta)$, are zero at the element nodes so that the nodal displacement values are not modified. For a trilinear hexahedral element, we utilize 9 enrichment functions for the displacement along each coordinate direction, as described in Appendix A.

The process to obtain the elementwise enriched displacements requires two steps. First, the approximate spatial derivatives of the displacements at each node in the mesh are obtained by averaging the derivatives from all elements that touch that node. Next, on an element-by-element basis, the enriched displacements, $\bar{\mathbf{u}}_e$, are obtained by solving a least-squares problem that minimizes the ℓ_2 norm of the difference between the averaged derivatives at the nodes of each element, $\mathbf{u}_{e,x} \in \mathbb{R}^{24}$, and the derivatives obtained from the elementwise displacement (5). This least-squares problem can be written in terms of the two matrices, $\mathbf{A}_x \in \mathbb{R}^{24\times 8}$ and $\bar{\mathbf{A}}_x \in \mathbb{R}^{24\times 9}$, which give the derivative of the displacement $u(\eta)$ along each coordinate direction at the nodes. These matrices are described in Appendix A. With these definitions, the least-squares problem can be written as

$$\min_{\bar{\mathbf{u}}_e} ||\mathbf{u}_{e,x} - \mathbf{A}_x \mathbf{u} - \bar{\mathbf{A}}_x \bar{\mathbf{u}}_e||_2. \tag{6}$$

The solution of the element-by-element problem (6) is

$$\bar{\mathbf{u}}_e = (\bar{\mathbf{A}}_x^T \bar{\mathbf{A}}_x)^{-1} \bar{\mathbf{A}}_x^T (\mathbf{u}_{e,x} - \mathbf{A}_x \mathbf{u}_e). \tag{7}$$

Note that the matrices, $\bar{\mathbf{A}}_x$ and $\mathbf{A}_x$, are independent of the displacement solution and only depend on the shape functions, the enrichment basis, and the geometry of the element.

Figure 29 illustrates the reconstruction process in two dimensions. Figure 29a shows a structured mesh in black and an associated displacement field in brown. The displacement derivatives at each node are denoted, $u^{+/-}_{i,x/y}$, with the subscripts indicating the node number and the direction of the derivative, and the superscript indicating whether the derivative is being taken from the positive or negative coordinate direction. Derivatives in the x-direction are shown in blue and derivatives

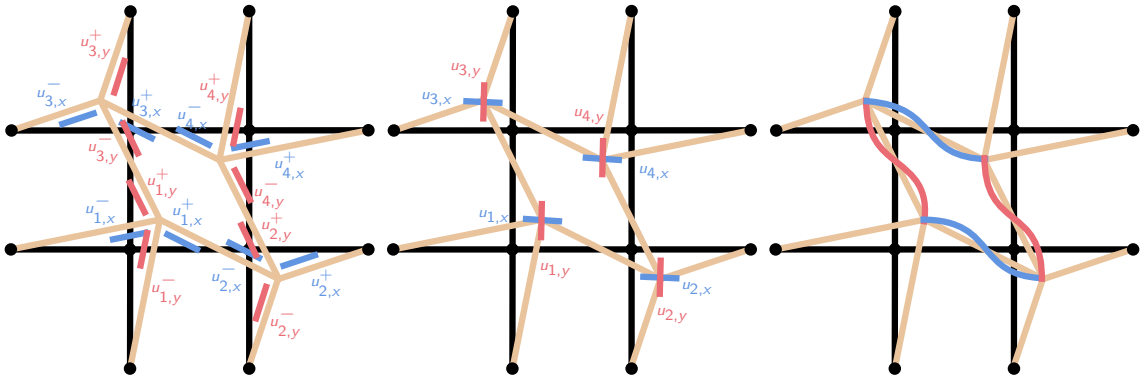

(a) Nodal displacement derivatives (b) Nodal displacement derivatives (c) Reconstructed displacement field

Figure 29: Reconstruction process

in the y-direction are shown in red to indicate that the reconstruction process occurs simultaneously and independently in each direction. Figure 29b shows the averaged nodal displacement derivatives, $u_{i,x/y}$. These averaged nodal derivatives are then used to compute the reconstructed displacement field shown in Figure 29c.

With the reconstruction, the derivative of the KS functional (5) with respect to element displacement involves the original nodal displacement values and contributions from the enriched displacement field

$$\frac{\partial c_{KS}}{\partial \mathbf{u}_e} = \frac{\partial c_{KS}}{\partial \varepsilon_{ij}} \frac{\partial \varepsilon_{ij}}{\partial \mathbf{u}_e} + \frac{\partial c_{KS}}{\partial \varepsilon_{ij}} \frac{\partial \varepsilon_{ij}}{\partial \bar{\mathbf{u}}_e} \left(\frac{\partial \bar{\mathbf{u}}_e}{\partial \mathbf{u}_e} + \frac{\partial \bar{\mathbf{u}}_e}{\partial \mathbf{u}_{e,x}} \frac{\partial \mathbf{u}_{e,x}}{\partial \mathbf{u}_e} \right), \tag{8}$$

where ε_{ij} is the element strain. The two terms in (8) involving the enriched displacement components, $\bar{\mathbf{u}}_e$, are functions of the terms from the least-squares reconstruction process and are computed as

$$\frac{\partial \bar{\mathbf{u}}_e}{\partial \mathbf{u}_e} = -(\bar{\mathbf{A}}_x^T \bar{\mathbf{A}}_x)^{-1} \bar{\mathbf{A}}_x^T \mathbf{A}_x,$$

and

$$\frac{\partial \bar{\mathbf{u}}_e}{\partial \mathbf{u}_{e,x}} = (\bar{\mathbf{A}}_x^T \bar{\mathbf{A}}_x)^{-1} \bar{\mathbf{A}}_x^T.$$

The derivative of the KS functional with respect to the finite-element solution vector is assembled from the contributions from each elements in the mesh.

5.1 Reconstruction Demonstration and Verification

To demonstrate the effect of this elementwise reconstruction, Figure 30 shows the von Mises stress field for a 3D crank problem using 8-node trilinear elements, with polynomial degree $p = 1$, and 27-node triquadratic elements, with polynomial degree $p = 2$, with and without computing the reconstruction. The von Mises stress obtained with reconstruction, $p = 1+$, is significantly smoother and exhibits better symmetry than the solution using trilinear shape functions with the standard approach, $p = 1$. The difference for the elements using triquadratic shape functions, $p = 2$ and $p = 2+$, is less significant but can still be observed near the areas of highest stress.

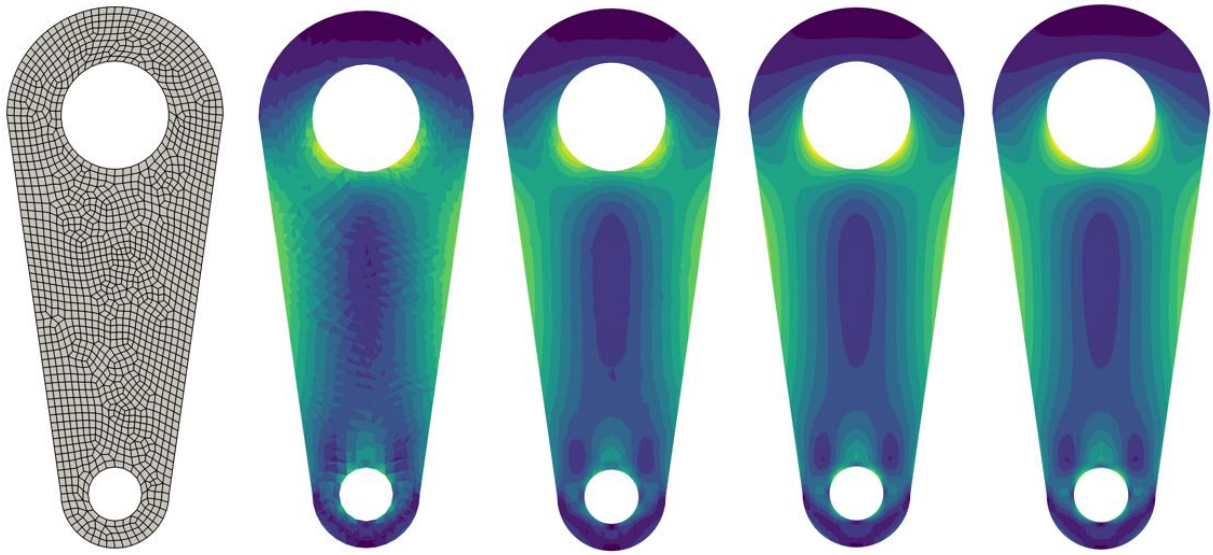

(a) Mesh (b) p = 1 (c) p = 1+ (d) p = 2 (e) p = 2+

Figure 30: Stress field comparison between solutions with and without reconstruction

As a further verification of the stress constraint, Figure 31 shows the design obtained from the solution of a stress-constrained mass minimization problem using a 3D analogue of the 2D L-bracket problem presented by Le et al. [14]. While Le et al. obtained results using 2D plane stress elements, the results shown here utilize the proposed 3D reconstruction process. The domain of the 3D problem consists of the same in-plane dimensions as the 2D problem, while the out-of-plane thickness is increased from 1 mm in the original problem, to 10 mm in the 3D problem, to allow through-thickness topology to be resolved. To account for the increased depth of the domain, a 18 N load is applied over the upper 5 mm of the top corner of the horizontal member to produce the same force per unit depth as the original problem. To emulate the formulation of Le et al. [14], these results employ SIMP penalization with $P = 3$, but use the proposed KS aggregation with $\rho_{KS} = 30$. Figure 31a shows the result from Le et al. [14], and Figure 31b shows the present result from two different views. Both the 2D and 3D designs share similarities with a deep rounded corner that avoids the re-entrant corner in the initial domain. However, the 3D topology has significant differences due to the ability to vary member dimensions in the through-thickness direction.

6 Frequency Constraints

Finding the natural frequencies of vibration requires the solution of the generalized eigenvalue problem

$$\mathbf{K}(\mathbf{x})\mathbf{u}_i = \lambda_i \mathbf{M}(\mathbf{x})\mathbf{u}_i, \tag{9}$$

where λ_i is the eigenvalue and $\mathbf{u}_i$ is the corresponding eigenvector. Throughout the remainder of this section, we omit the design vector arguments to the mass and stiffness matrices for ease of presentation.

In this work, the goal of the natural frequency constraint is to bound the fundamental natural frequency from below by a specified value, such that all natural frequencies are greater than

(a) Result from Le et al. [14] (b) Solution using reconstruction

Figure 31: Validation against the 2D L-bracket problem.

or equal to ω_0. There are two primary challenges when imposing this type of frequency constraint within the context of a topology optimization problem: first, the mathematical issue of mode switching, which makes the eigenvalues locally nondifferentiable [22], and second, the algorithmic issue of developing efficient and scalable eigenvalue solution procedures for large-scale problems. Mode switching occurs when the eigenmode associated with the lowest eigenvalue switches as the design changes. At the cross-over point, the minimum eigenvalue is not differentiable [22]. Authors have addressed this issue using the bound formulation with modal assurance techniques [12, 15], or using p-norm or KS aggregation strategies [25]. In this work, we perform KS aggregation on the r-lowest eigenvalues, $\lambda_1 \leq \lambda_2 \leq \ldots \leq \lambda_r$, resulting in the following constraint

$$c_{KS_\lambda}(\lambda_1, \ldots, \lambda_r) = \lambda_1 - \frac{1}{\rho_{KS_\lambda}} \ln \left[\sum_{i=1}^{r} e^{-\rho_{KS_\lambda}(\lambda_i - \lambda_1)} \right] \geq \omega_0^2, \tag{10}$$

where $\rho_{KS_\lambda} = 50$. In this way, if mode switching occurs, the KS-aggregation still identifies the approximate lowest eigenvalue, and therefore eigenmode tracking is not required.

Evaluating the eigenvalue aggregate (10) requires the solution of a large-scale generalized eigenvalue problem. Many eigenvalue solution methods utilize direct factorization techniques, making them too computationally expensive for high-resolution topology optimization problems. In this work, we develop a Jacobi–Davidson method [24] to compute the eigenvalues of the natural frequency problem (9). This method leverages the scalable geometric multigrid preconditioner used in the Krylov solution method for the finite-element governing equations. To accelerate the eigenvalue solution procedure, we propose two eigenvector recycling strategies, which utilize eigenvectors from the eigenproblem at the previous design iteration to provide an initial subspace. Eigenvector recycling has been used in the context of nonlinear eigenvalue problems [21], but have not been investigated in the context of topology optimization. Recycling methods for the solution of linear systems have been demonstrated for topology optimization in the context of mass-constrained compliance minimization [26, 17], but not, to the best of our knowledge, for eigenvalue problems. To compare the performance of the proposed method, we also solve the eigenproblem (9) using a conventional shift-and-invert Lanczos method [8].

6.1 Shift-and-invert Lanczos method

Shift-and-invert Lanczos techniques are commonly used in finite-element frequency and buckling analysis [8]. The shift-and-invert strategy preconditions the spectral properties of the eigenproblem (9) to promote separation of the eigenvalues close to a desired value, thereby accelerating the convergence of the Lanczos method. With a shift-and-invert strategy, the natural frequency eigenproblem (9) becomes

$$\mathbf{M}(\mathbf{K}-\sigma\mathbf{M})^{-1}\mathbf{M}\mathbf{u}_i = \mu_i\mathbf{M}\mathbf{u}_i, \tag{11}$$

where the transformed eigenvalues are $\mu_i = 1/(\lambda_i - \sigma)$ and the original eigenvalues that are close to the shift value σ become the extreme eigenvalues of the transformed eigenproblem. Shift-and-invert Lanczos methods have proven to be very effective when a full factorization of the matrix $\mathbf{K}-\sigma\mathbf{M}$ is available. However, for large-scale applications, a full factorization is not computationally feasible, and iterative solution methods are required instead. Unfortunately, shift-and-invert strategies require a tightly-converged solution for every application of the operator $(\mathbf{K}-\sigma\mathbf{M})^{-1}$, making them expensive when combined with iterative methods. In contrast, the Jacobi–Davidson method can be used with inexact solutions of a linear system without sacrificing the accuracy of the method.

6.2 Jacobi–Davidson method

The goal of the Jacobi–Davidson method is to find approximate solutions of the generalized eigenproblem (9) through an iterative technique that uses the Davidson approach of constructing an approximation to the eigenvector using a $\mathbf{M}$-orthogonal subspace, while using Jacobi's method to search for new vectors to add to this subspace [24]. A detailed description of the algorithm is shown in Appendix B in Algorithm 1.

At iteration k, the Jacobi–Davidson method uses an $\mathbf{M}$-orthogonal subspace of dimension k, denoted $\mathbf{V}_k \in \mathbb{R}^{n\times k}$ that satisfies the property

$$\mathbf{V}_k^T\mathbf{M}\mathbf{V}_k = \mathbf{I}.$$

The approximate eigenvalues and eigenvectors, called the Ritz values and Ritz vectors, are written as $\lambda_i \approx \theta_i$, and $\mathbf{u}_i \approx \mathbf{V}_k\mathbf{y}_i$. The Ritz values and vectors are obtained by enforcing a Galerkin orthgonality condition leading to the reduced eigenproblem

$$\mathbf{V}_k^T\mathbf{K}\mathbf{V}_k\mathbf{y}_i = \theta_i\mathbf{V}_k^T\mathbf{M}\mathbf{V}_k\mathbf{y}_i.$$

Introducing the matrix $\mathbf{A}_k \triangleq \mathbf{V}_k^T\mathbf{K}\mathbf{V}_k \in \mathbb{R}^{k\times k}$, and applying the $\mathbf{M}$-orthogonality property, this problem can be simplified as

$$\mathbf{A}_k\mathbf{y}_i = \theta_i\mathbf{y}_i. \tag{12}$$

Since the dimension of the subspace is small, such that $k \ll n$, a solution method for small dense eigenproblems can be used to solve (12). The Ritz value and vector are approximations, so the residual $\mathbf{r}_i = (\mathbf{K}-\theta_i\mathbf{M})\mathbf{V}_k\mathbf{y}_i$ is non-zero and an indicator of the accuracy of the approximation.

In our implementation of the Jacobi–Davidson method, for the first s iterations, we build $\mathbf{V}_k$ using recycled eigenvectors from previous eigenproblems. After this initial recycling phase, the subspace $\mathbf{V}_k$ is built using vectors generated from an inexact Newton solution. To motivate the

update scheme, consider the following Newton-step on the residuals of the i-th generalized eigenvalue appended with the $\mathbf{M}$-normality condition $\mathbf{u}_i^T\mathbf{M}\mathbf{u}_i = 1$

$$\begin{bmatrix} (\mathbf{K}-\theta_i\mathbf{M}) & \mathbf{M}\mathbf{u}_i \\ \mathbf{u}_i^T\mathbf{M} & 0 \end{bmatrix} \begin{bmatrix} \mathbf{t} \\ \Delta\lambda \end{bmatrix} = \begin{bmatrix} -(\mathbf{K}-\theta_i\mathbf{M})\mathbf{u}_i \\ \frac{1}{2}(\mathbf{u}_i^T\mathbf{M}\mathbf{u}_i - 1) \end{bmatrix} = \begin{bmatrix} -\mathbf{r}_i \\ 0 \end{bmatrix}, \tag{13}$$

which gives the update $(\mathbf{t}, \Delta\lambda)$ to the Ritz pair. Note that by construction the Ritz vector is in the span of the basis, $\mathbf{u}_i \in \operatorname{span}\{\mathbf{V}_k\}$, and the residual is orthogonal to the basis such that $\mathbf{r}_i^T\mathbf{V}_k = 0$. As a result, the approximate eigenvector $\mathbf{u}_i$ satisfies

$$\mathbf{u}_i^T\mathbf{r}_i = 0.$$

As a consequence of this identity $(\mathbf{I}-\mathbf{M}\mathbf{u}_i\mathbf{u}_i^T)\mathbf{r}_i = \mathbf{r}_i$. The second condition in the linear system (13) imposes $\mathbf{u}_i^T\mathbf{M}\mathbf{t} = 0$ such that $\mathbf{t} = (\mathbf{I}-\mathbf{u}_i\mathbf{u}_i^T\mathbf{M})\mathbf{t}$. Combining these two results, the Newton update (13) can be written as

$$(\mathbf{I}-\mathbf{M}\mathbf{u}_i\mathbf{u}_i^T)(\mathbf{K}-\theta_i\mathbf{M})(\mathbf{I}-\mathbf{u}_i\mathbf{u}_i^T\mathbf{M})\mathbf{t} = -\mathbf{r}_i. \tag{14}$$

Instead of solving for the update (14) to a tight tolerance, it can be beneficial to use a loose tolerance that requires fewer iterations. In this work, we utilize the same geometric multigrid preconditioner as the linear solver and use FGMRES(m) to loosely solve (14) where $m = 10$.

6.3 Recycling methods for Jacobi–Davidson method

Since the proposed Jacobi–Davidson method is used in a design optimization process, it will be repeatedly applied to a sequence of related eigenproblems. In particular, the eigenvectors will exhibit similar characteristics between optimization iterations, and the difference in the eigenvalues between iterations will converge to zero as the design converges. To take advantage of this property, the eigenvectors computed at the previous iterations can be recycled to accelerate the convergence of the next eigenproblem. The Jacobi–Davidson method is well suited to a variety of recycling strategies since the subspace vectors, $\mathbf{V}_k$, need only be $\mathbf{M}$-orthogonal. An $\mathbf{M}$-orthogonal set of vectors can easily be obtained from any set of vectors by applying the modified Gram–Schmidt algorithm [20].

The recycling technique starts by constructing a set of an initial set of s vectors, stored as columns in $\mathbf{R}_s \in \mathbb{R}^{n\times s}$ that are computed from the eigenvectors obtained in the previous iteration. We examine the following two strategies: (1) one recycled vector, $s = 1$, that is an equally-weighted linear combination of the eigenvectors from the previous solution, and (2) a number of recycled vectors, $s \leq r$, that are equal to the lowest eigenvectors from the previous solution. The first step in the recycling algorithm is to perform modified Gram–Schmidt to reorthogonalize the set of recycled vectors and store them in the first s-columns of the basis $\mathbf{V}_k \in \mathbb{R}^{n\times k}$, with $k = s$. Next, the algorithm forms the portion of the $\mathbf{A}_k \in \mathbb{R}^{k\times k}$ matrix formed by $\mathbf{A}_k = \mathbf{V}_k^T\mathbf{K}\mathbf{V}_k$. Finally, the regular Jacobi–Davidson method is started from iteration $k = s$.

6.4 Performance of shift-and-invert Lanczos and Jacobi–Davidson

To quantify the benefits of the Jacobi–Davidson method over shift-and-invert Lanczos, we perform a compliance-minimization study with mass and frequency constraints for a 3D beam problem

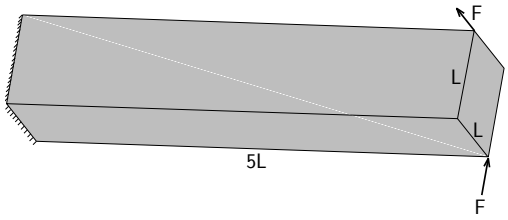

Figure 32: 3D cantilever beam with point loads

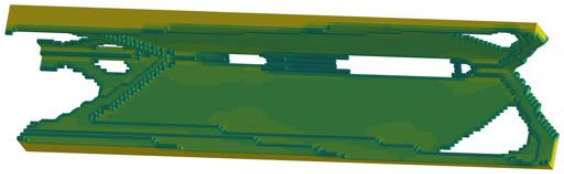

(a) Design obtained using 24 processors for mesh with 525,987 degrees of freedom.

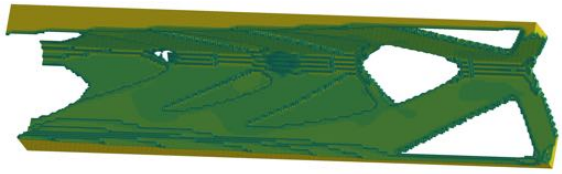

(b) Design obtained using 48 processors for mesh with 4 million degrees of freedom.

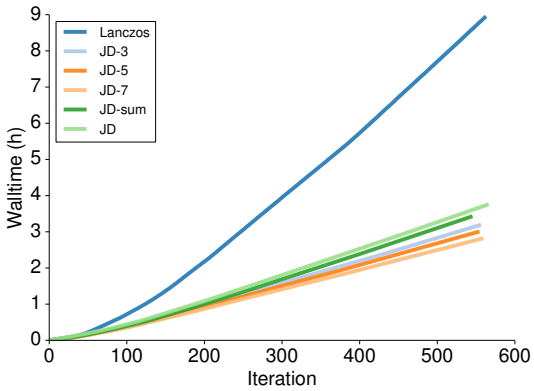

(c) Cumulative wall time using 24 processors for mesh with 525,987 degrees of freedom.

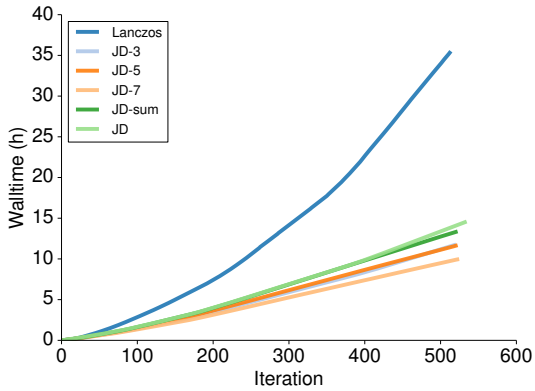

(d) Cumulative wall time using 48 processors for mesh with 4 million degrees of freedom.

Figure 33: Design and wall time for the different methods on different mesh sizes

as shown in Figure 32. The beam domain is $5 \times 1 \times 1$ and is discretized using two different mesh sizes, one having $32 \times 32 \times 160$ elements with 525,987 degrees of freedom and the other having $64 \times 64 \times 320$ elements with over 4 million degrees of freedom. The frequency constraint is evaluated by the shift-and-invert Lanczos or Jacobi–Davidson with different recycling strategies. The mass is constrained such that only 10% of the domain volume is occupied by material. The smaller mesh case was run on 24 processors, while the larger mesh case was run on 48 processors.

Figure 33 shows a summary of the topologies and computational times from this study. Figure 33c and Figure 33d show a comparison between between the total computational time using Lanczos and different variants of the Jacobi–Davidson for the small and large cases, respectively. For the smaller problem, the Jacobi–Davidson method required between 56 to 70% less computational time than the shift-and-invert Lanczos method. The larger problem exhibits similar time savings, with between 60 and 73% less computational time depending on the recycling strategy used for the Jacobi–Davidson method. The Jacobi–Davidson methods on both mesh sizes lie within the

same performance range even as the design evolves. Without using recycling schemes, Jacobi–Davidson, denoted by JD, does not perform as well as the JD variants that use recycling. This is expected since the method without recycling discards information about eigenvectors from the previous solution. The Jacobi–Davidson method that uses one recycled vector that is an equally-weighted linear combination of the eigenvectors from the previous solution, as denoted by JD-sum, only outperformed the Jacobi–Davidson method without any recycling. Lastly, JD-s, where s is the lowest s eigenvectors recycled from the previous solution, demonstrated better performance as the number of eigenvectors recycled from the previous solution increases. In this example, $s = 3$, 5, and 7 eigenvectors were recycled out of 10 total eigenvectors. Recycling 7 eigenvectors performed the best, and resulted in a 28 to 33% reduction in computational time when compared to the Jacobi–Davidson method without any recycling. From this example, we conclude that the benefits of the Jacobi–Davidson method with eigenvector recycling are clear, especially with high-resolution 3D structures.

7 Results

7.1 Problem Formulations

In this section, we describe the three different topology optimization problem formulations that we use in this work: (1) mass-constrained compliance minimization, (2) stress-constrained mass minimization, and (3) stress- and frequency-constrained mass minimization.

7.1.1 Mass Constrained Compliance Minimization

The mass-constrained compliance minimization problem is formulated as:

$$\begin{aligned} \text{minimize} \quad & c(\mathbf{x}) = \mathbf{f}^T \mathbf{K}(\mathbf{x})^{-1} \mathbf{f} \\ \text{with respect to} \quad & 0 \leq \mathbf{x} \leq 1 \\ \text{such that} \quad & m_{\text{fixed}} - m(\mathbf{x}) \geq 0 \end{aligned} \tag{15}$$

where $c(\mathbf{x})$ is the compliance of the structure, $\mathbf{u}$ are the state variables, and $\mathbf{f}$ is the force vector. Finally, $m(\mathbf{x})$ is the mass of the structure and the fixed mass value m_{fixed} given by:

$$m_{fixed} = f_v V \rho \tag{16}$$

where f_v is the volume fraction, V is the total volume of the structure, and ρ is the density of the solid material.

7.1.2 Stress Constrained Mass Minimization

The mass minimization problem with stress constraints is formulated as:

$$\begin{aligned} \text{minimize} \quad & m(\mathbf{x}) \\ \text{with respect to} \quad & 0 \leq \mathbf{x} \leq 1 \\ \text{such that} \quad & c_{KS}(\mathbf{x}, \mathbf{u}) \leq \beta \\ \text{governed by} \quad & \mathbf{K}(\mathbf{x})\mathbf{u} = \mathbf{f} \end{aligned} \tag{17}$$

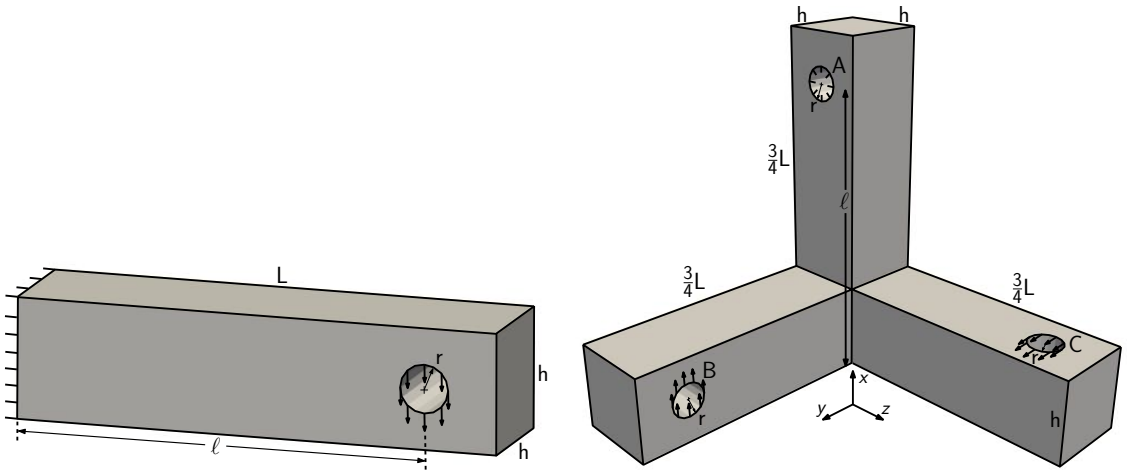

(a) Cantilever beam problem domain (b) Orthogonal bracket problem domain

Figure 34: Problem domains

where β is a value chosen to be less than or equal to 1 to account for the nonconservative nature of the continuous KS functional. The trivial solution, $\mathbf{x} = 0$, of problem (17) is avoided by starting the design problem from a point with $x_i = 0.95$ in all cases.

7.1.3 Stress and Frequency Constrained Mass Minimization

The mass minimization problem with stress and frequency constraints is formulated as:

$$\begin{aligned} \text{minimize} \quad & m(\mathbf{x}) \\ \text{with respect to} \quad & 0 \leq \mathbf{x} \leq 1 \\ \text{such that} \quad & c_{KS}(\mathbf{x},\mathbf{u}) \leq \beta \\ & c_{KS_\lambda}(\lambda_1,\ldots,\lambda_r) \geq \omega_0^2 \\ \text{governed by} \quad & \mathbf{K}(\mathbf{x})\mathbf{u} = \mathbf{f} \\ & \mathbf{K}(\mathbf{x})\mathbf{u}_i = \lambda_i \mathbf{M}(\mathbf{x})\mathbf{u}_i \end{aligned} \tag{18}$$

The minimum allowable natural frequency, ω_0, is specified based on the problem domain.

7.2 Problem Domains

We use two problem domains, shown in Figure 34, to demonstrate our proposed stress- and frequency-constrained topology optimization methods. These problem domains consist of a cantilever beam and an orthogonal bracket. For all cases, aluminum is used as the design material with a density value of $\rho = 2,600$ kg/m^3, a Young's modulus value of $E = 70$ GPa, a Poisson's ratio of $\nu = 0.3$, and a yield stress value of $\sigma_y = 276$ MPa.

7.2.1 Cantilever Beam Problem

Figure 34a shows a cantilevered beam with a hole cut out near the free end, with a downward traction applied throughout the hole. The geometry is nondimensional with values of $\ell/L = 0.85$,

$h/L = 0.25$, and $r/L = 0.05$. We also define nondimensional load and frequencies so that these results can be replicated independent of scale.

For the cantilever beam problem, the maximum stress in the beam based on Euler–Bernoulli beam theory is

$$\sigma_{\max} = \frac{6F\ell}{h^3}.$$

Substituting the material yield stress σ_y for $\sigma_{\max}$ and rearranging, a normalized load, $\bar{F}$, can be defined as

$$\bar{F} = \frac{F\ell}{6\sigma_y h^3}.$$

Using dimensional analysis, we define a nondimensional natural frequency as

$$\bar{\omega}_0 = \omega_0 L\sqrt{\rho/E}. \tag{19}$$

For the cantilever beam problem, we use $\bar{F} = 0.015$ and $\bar{\omega}_0 = 0.3$ as the nondimensionalized load and frequency values.

7.2.2 Orthogonal Bracket Problem

Figure 34b shows the orthogonal bracket domain, with 3 orthogonal beam members with holes cut near the free ends of each member. The holes are each cut in different directions. Hole A at the top of the vertical member is completely clamped, while traction loads of equal magnitude are applied to holes B and C. This has the effect of creating a bending moment in each of the horizontal members, and a combined bending and torsional load in the vertical member. Here, nondimensional length ratios shown in the diagram below are $\ell/L = 0.85$, $h/L = 0.25$, and $r/L = 0.05$.

In order to scale the loads for the orthogonal bracket, we compute the maximum von Mises stress in the beam and compare this value to the material yield stress. Because both loads act at a distance on the vertical member, the maximum stress will occur near the cutout in the vertical member. The loads on the horizontal members result in equivalent moments M_x and M_z, and equivalent point loads F_y and F_x. The axial stress $\sigma_{11}(y,z)$ is computed from the contributions from both M_z and F_x as

$$\sigma_{11}(y,z) = \frac{F_x}{A} - y\frac{M_z + F_y\ell}{\frac{1}{12}h^4} = \frac{-36F\ell}{h^3}\left(1 + y\frac{24\ell}{h^2}\right).$$

Computing the shear stresses in the beam from torsion is challenging due to warping caused by the square cross section. To do this, we use the closed-form approximation from Bauchau and Craig [2, p. 285]

$$\sigma_{12}(y,z) = \frac{36F\ell}{h^3}\left[\left(\frac{y}{h}\right)^2 - \frac{1}{4}\right]\left(\frac{z}{h}\right), \qquad \sigma_{13}(y,z) = \frac{-36F\ell}{h^3}\left(\frac{y}{h}\right)\left[\left(\frac{z}{h}\right)^2 - \frac{1}{4}\right].$$

There is an additional component of σ_{12} from the shear stress from F_y that is

$$\sigma_{12}(y,z) = \frac{3}{2}\frac{F}{h^2}\left(1 - \left(\frac{y}{h}\right)^2\right).$$

Table 5: Problem data for the cantilever beam stress constraint comparison

	Elements	DOF	m%	q	ε	Time (h)	n_{procs}
Reconstruction/symm.	8,101,863	23,722,908	34.95%	5	0.1	8.5	72
KS functional/symm.	8,056,188	23,586,873	35.15%	5	0.1	7.7	72
Discrete KS/symm.	8,072,498	23,631,708	34.87%	5	0.1	7.6	72
Reconstruction/nonsymm.	9,330,720	27,328,236	35.19%	5	0.1	9.5	72
KS functional/nonsymm.	9,171,624	26,872,533	34.90%	5	0.1	10.1	72
Discrete KS/nonsymm.	9,155,328	26,824,899	34.37%	5	0.1	10.2	72

Computing an estimate of the maximum von Mises stress based on these stress components gives

$$\sigma_{\max} = \frac{F}{h^2}\sqrt{\frac{819}{2}\left(\frac{\ell}{h}\right)^2 + 48\left(\frac{\ell}{h}\right) + \frac{307}{32}}$$

Substituting σ_y for $\sigma_{\max}$ and rearranging results in the following expression for normalized load:

$$\bar{F} = \frac{F}{\sigma_y h^2}\sqrt{\frac{819}{2}\left(\frac{\ell}{h}\right)^2 + 48\left(\frac{\ell}{h}\right) + \frac{307}{32}} \tag{20}$$

We use the same nondimensional expression for the frequency (19) as the cantilever beam case. For the orthogonal bracket problem, we use $\bar{F} = 1.0$ and $\bar{\omega}_0 = 0.18$ as the nondimensionalized load and frequency values.

7.3 Topology Optimization Results

7.3.1 Reconstruction and Stress Constraint Comparison

Before examining the full set of results, we first study the effect of the reconstruction technique presented in Section 5 on the optimized designs. For this study, we use the cantilever domain and compare designs obtained from stress-constrained mass minimization using the reconstruction with designs obtained without reconstruction, using both the KS functional and the discrete KS function. Additionally, we also examine the effect of using a nonsymmetric or symmetric mesh which are shown side-by-side in Figure 35a and Figure 35b for comparison. Note that twice uniformly coarsened versions of the full finite-element meshes are shown for clarity.

In each case, the optimization utilizes one cycle of adaptive mesh refinement, with 150 iterations on the initial mesh, and 150 iterations on the refined mesh. Table 5 summarizes the problem data for each constraint type for both symmetric and nonsymmetric meshes. Note that in all cases, the final volume fraction of structure is within 1% while the symmetric and nonsymmetric cases with reconstruction are within 0.25%. Figure 35 shows the optimized designs for each case, where the figures on the left show the nonsymmetric results, and the figures on the right show the symmetric results. The top figures show the solution when stress reconstruction is used, the middle row shows the case where no reconstruction is used, and the stress constraint is evaluated using the KS functional, and the bottom row shows the solutions without reconstruction, where the discrete KS function is used to evaluate the stress constraints. Overall the designs share many similarities with a

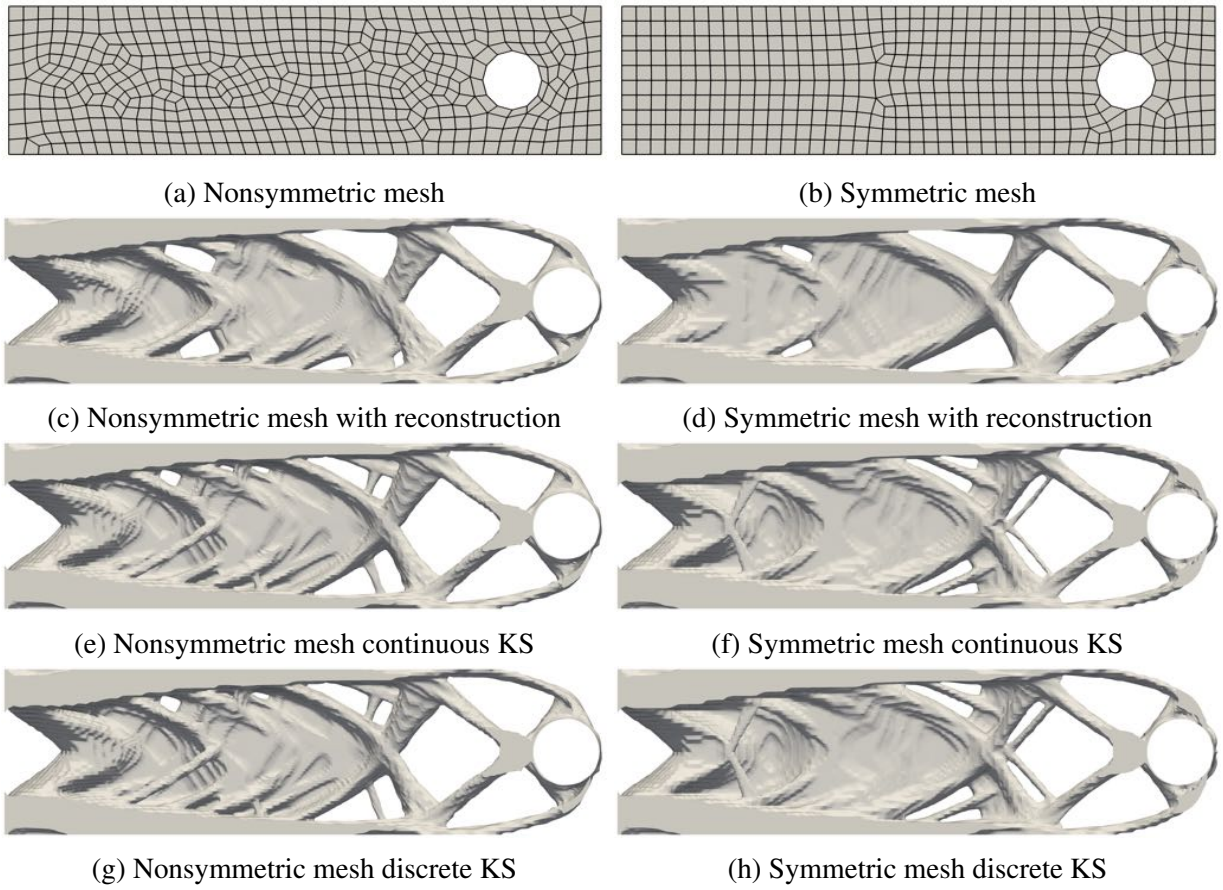

(a) Nonsymmetric mesh (b) Symmetric mesh

(c) Nonsymmetric mesh with reconstruction (d) Symmetric mesh with reconstruction

(e) Nonsymmetric mesh continuous KS (f) Symmetric mesh continuous KS

(g) Nonsymmetric mesh discrete KS (h) Symmetric mesh discrete KS

Figure 35: Stress constrained topology optimization results using different techniques to evaluate the stress constraint. The left column shows results generated on a nonsymmetric mesh, while the right column shows results using a symmetric mesh. The top row shows each mesh, the second row uses stress reconstruction with the continuous KS functional, the third row uses the KS functional without stress reconstruction, and the bottom row uses the discrete KS function without stress reconstruction.

top and bottom flange and web-like structure which transitions to an open truss at the load application point. The designs that employ reconstruction have a more consolidated geometry with fewer, thicker members, while the designs without reconstruction have more numerous slender members. We attribute these differences to the reconstruction technique that predicts higher stress in slender members represented by fewer finite-elements. The primary difference between the symmetric and nonsymmetric designs with reconstruction in Figure 35d and Figure 35c, respectively, is the additional attachment point between the lower flange and web structure at about 70% of the length from the root in the nonsymmetric result. Unlike the other web attachment points, this additional feature does not span the entire width of the web but is attached symmetrically on either side about the width. The single side view of the topology over-emphasizes the asymmetry in this case.

Table 6: Problem data for the cantilever beam domain

	Elements	DOF	m%	q	ε	$\sigma_{\max}/\sigma_y$	$\bar{\omega}_0$	Time (h)	n_{procs}
Compliance	14,350,202	42,738,516	35%	10, 10	—	—	—	16.1	72
Stress	14,068,319	41,534,952	34.9%	8, 10	0.1	1.03	—	63.3	72
Stress & frequency	13,401,506	40,108,296	34.4%	8, 10	0.1	1.02	0.3	202.2	72

Figure 36: Top, side, and rear views of the mass-constrained compliance minimization result for the cantilever beam problem

7.3.2 Cantilever Beam Results

Figure 36, Figure 37, and Figure 38 show the results for the compliance, stress-constrained, and stress- and frequency-constrained problems, respectively for the cantilever beam domain. For each problem, a top view, a side view, and a rear view from the cantilevered end are provided. Each of these problems uses one cycle of adaptive mesh refinement, resulting in a mesh size between 13.4 and 14.3 million elements, and between 40.1 and 42.7 million degrees of freedom (DOF), depending on the problem. Adaptive mesh refinement is performed for each problem after 500 iterations. The adaptation step produces a new design mesh and associated design parametrization. The old design point is interpolated to the new design space and all other optimization parameters are retained.

As a first step, we solve the stress-constrained mass minimization problem resulting in a structure with a mass fraction of 34.9% and a maximum stress of 103% of the yield stress. This small stress violation is due to the nonconservative nature of the KS functional itself, not due to a constraint violation in the optimization problem. Next, we solve the conventional mass-constrained compliance minimization problem with the mass fraction constrained to 35%, selected based on the stress-constrained result. Finally, we solve the stress- and frequency-constrained mass minimization problem with the lowest nondimensionalized natural frequency constrained to be greater than a value of $\bar{\omega}_0 = 0.3$. The resulting structure has a mass fraction of 34.4%, a maximum stress of 102% of the yield stress, and a nondimensionalized first natural frequency of $\bar{\omega}_1 = 0.46$. Note that the frequency constraint is not active at the final design point. Table 6 summarizes the problem data for the cantilever beam, including problem size, values of the RAMP penalization and stress relaxation, results, and computational cost.

The stress-constrained result, in Figure 37, and the compliance minimization result, in Figure 36, both form structures which resemble I-beams. However, the compliance minimization result and the frequency constrained result, shown in Figure 38, form closed boxes. The stress and frequency result has features resembling both the compliance based design and the stress based design. This is intuitive since compliance minimization is equivalent to stiffness maximization, and stiffer structures have higher natural frequencies for the same mass, in general. Applying stress

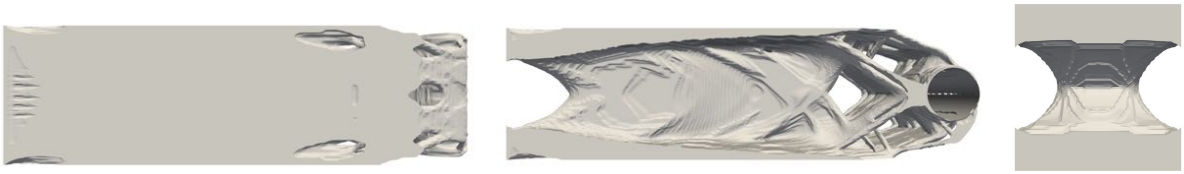

Figure 37: Top, side, and rear views of the stress-constrained mass minimization result for the cantilever beam problem

Figure 38: Top, side, and rear views of the stress- and frequency-constrained mass minimization result for the cantilever beam problem

and frequency constraints can then be thought of as increasing the stiffness of the structure while enforcing stress constraints. Note that the web structures formed in the stress-constrained case and in the compliance minimization case are hollow inside.

Figure 39, Figure 40, and Figure 41 show the material failure ratio for the compliance, stress-constrained, and stress- and frequency-constrained problems, respectively, with the topology side-by-side for reference. The stress-constrained mass minimization result is almost uniformly stressed everywhere. The compliance minimization case shows high stress concentrations at the top and bottom of the flange of the beam near the root. The stress- and frequency-constrained mass minimization case shows a region near the root of the beam along the sides with low stress.

Figure 42a shows the history of the stress and frequency constraints during the design. The constraint ratio is the ratio of the constraint value to the design limit, which for feasible designs, should be less than or equal to one for stress, and greater than or equal to one for frequency. The optimizer quickly satisfies both the stress and frequency constraints, but once the frequency constraint is satisfied, the first eigenvalue continues to increase, and the optimizer is then only concerned with finding the minimum mass solution which satisfies the stress constraint. Even though it is inactive during much of the design optimization, the frequency constraint has the effect

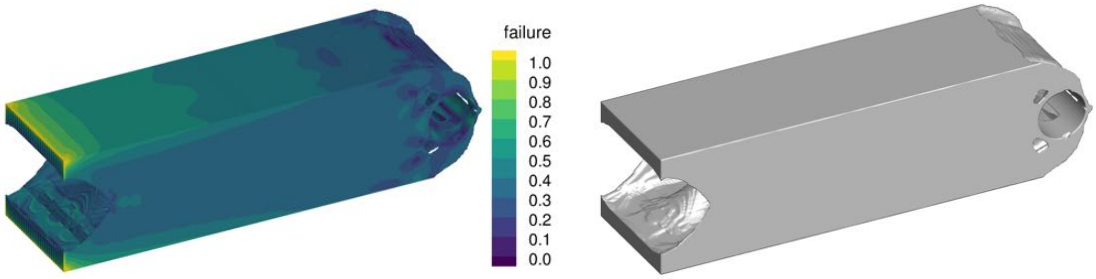

Figure 39: Failure (left) and topology (right) for the mass-constrained compliance minimization case of the cantilever beam problem

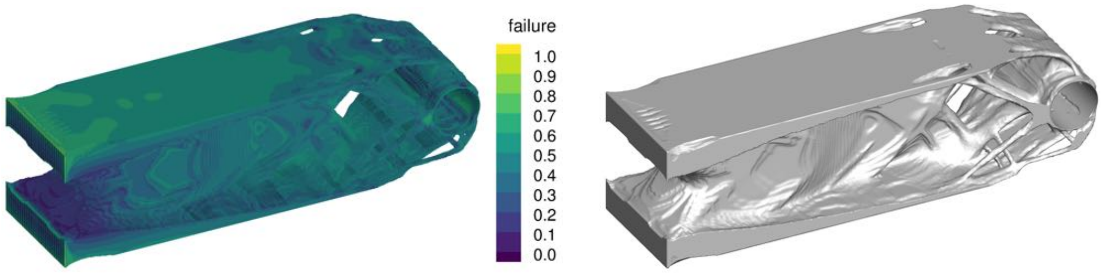

Figure 40: Failure (left) and topology (right) for the stress-constrained mass minimization case of the cantilever beam problem

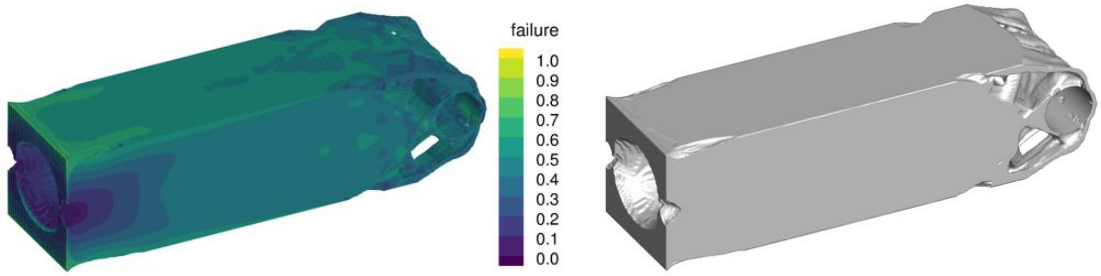

Figure 41: Failure (left) and topology (right) for the stress- and frequency-constrained mass minimization case of the cantilever beam problem

of closing off a portion of the design space where the stress-constrained minimum mass solution existed, resulting in a very different topology. Also note that the sudden change in the constraint values at 500 iterations occurs because that is the point at which the adaptive mesh refinement takes place.

Figure 42b shows the optimization history of the mass and the infeasibility, with designs highlighted at 35, 100, 500, and 1000 iterations. The design quickly becomes feasible at around iteration 36. By iteration 100, the design has largely converged, and changes after this point are relatively minor. It becomes infeasible again after the adaptive mesh refinement step but quickly recovers to a feasible point. Figure 43 shows the history of the first six beam eigenvalues as the design evolved. Initially, the first two natural frequencies, ω_1 and ω_2, are repeated, but over the course of the optimization they spread out and become distinct by the final design. In addition, at the initial design point, ω_4 and ω_5 are repeated natural frequencies, while and ω_3 and ω_6 are well-separated. At the final design point ω_3 and ω_4 as well as ω_5 and ω_6 have coalesced close to one another. At the final design, the normalized natural frequencies take values of $\bar{\omega}_1 = 0.46$, $\bar{\omega}_2 = 0.49$, $\bar{\omega}_3 = 1.12$, $\bar{\omega}_4 = 1.15$, $\bar{\omega}_5 = 1.35$, and $\bar{\omega}_6 = 1.38$.

7.3.3 Orthogonal Bracket Results

Figure 44, Figure 45, and Figure 46 show the results for the compliance, stress-constrained, and stress- and frequency-constrained problems, respectively, for the orthogonal bracket domain. Two views are provided: an isometric view, and a view from the top, looking down from the perspective of the vertical member. Again, one cycle of adaptive mesh refinement was used, resulting in meshes with between 4.7 and 5.3 million elements and between 14.1 and 16 million degrees of freedom.

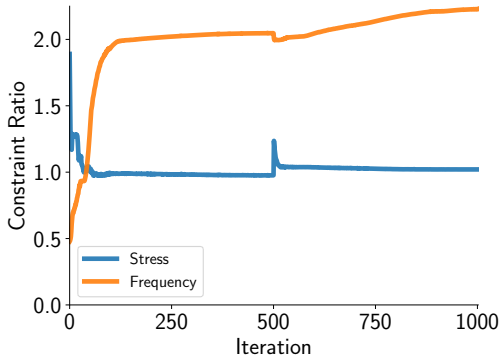

(a) Convergence of stress and frequency constraints

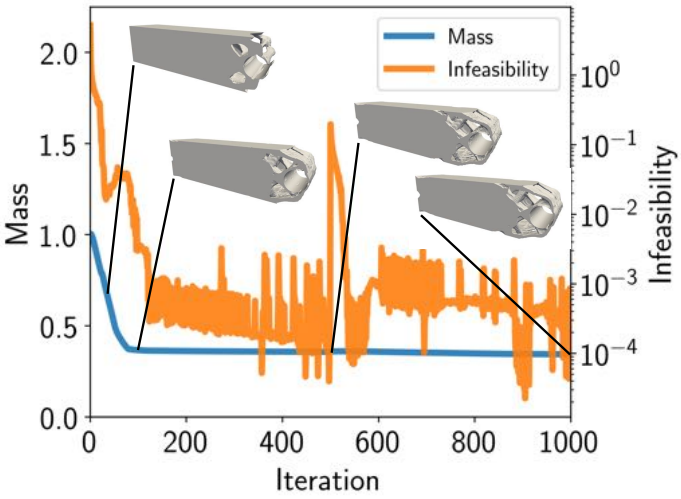

(b) History of objective and infeasibility

Figure 42: Optimization history of cantilever beam problem

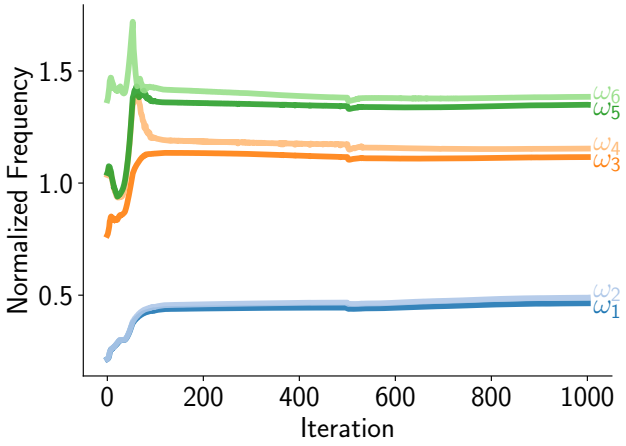

Figure 43: History of beam natural frequencies

As a first step, we solve the stress-constrained mass minimization problem resulting in a structure with a mass fraction of 37.1% and a maximum stress at 99% of the yield stress. Next, we solve the mass-constrained compliance minimization problem with the mass fraction constrained to 40% in order for the result to be comparable to the mass minimization problem. Finally, we solve the stress- and frequency-constrained mass minimization problem with a minimum normalized first natural frequency value of $\bar{\omega}_0 = 0.18$. The resulting structure has a mass fraction of 41.9%, with a maximum stress of 98% of the yield stress, and a normalized first natural frequency value of $\bar{\omega}_1 = 0.19$. In this case, the frequency constraint is active at the final design point. Table 7 summarizes the problem data for the orthogonal bracket, including problem size, values of the RAMP penalization and stress relaxation, results, and computation cost. Comparing the resulting topology of each problem, the stress-constrained case has a more open-section design, while the compliance minimization case is the most closed-off. For the case with stress and frequency constraints, there are more walled-off sections than the stress-constrained case, but fewer than the compliance mini-

Figure 44: Isometric and top views of the mass-constrained compliance minimization result for the orthogonal bracket problem

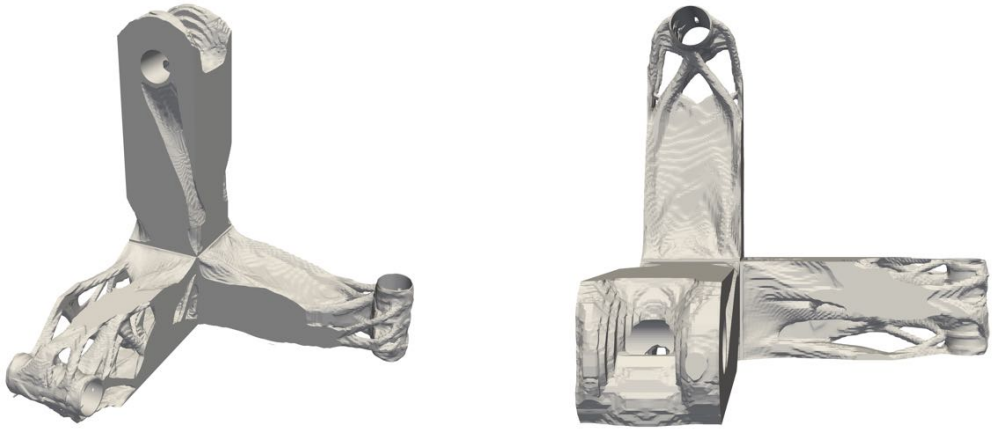

Figure 45: Isometric and top views of the stress-constrained mass minimization result for the orthogonal bracket problem

mization case. Again, here we see similarities between the stress and frequency constrained results and both the stress-based and the compliance-based results.

Figure 47 shows the material failure ratio for each result for the orthogonal bracket domain. In each case, the maximum stress ratio is achieved at both at the hole at the top, which is fully restrained, and in the reentrant corners between each member. The stress-constrained results reduces these stresses in the corners compared to the compliance minimization case. The material above the constraint does not carry very much load in any of the cases, but all the other material in the stress-constrained mass minimization case is used to effectively to carry the loads. In the stress- and frequency-constrained mass minimization case, there are some areas which have lower load-bearing utilization, particularly in the walls formed in the horizontal members, but these features contribute to increasing the fundamental frequency of the structure. The mass-constrained compliance minimization has high stress concentrations near the reentrant corners and on the boundary of the fixed hole. Much of the other material in this case shows a low load-bearing utilization.

Figure 48a shows the history of the stress and frequency constraints during the design opti-

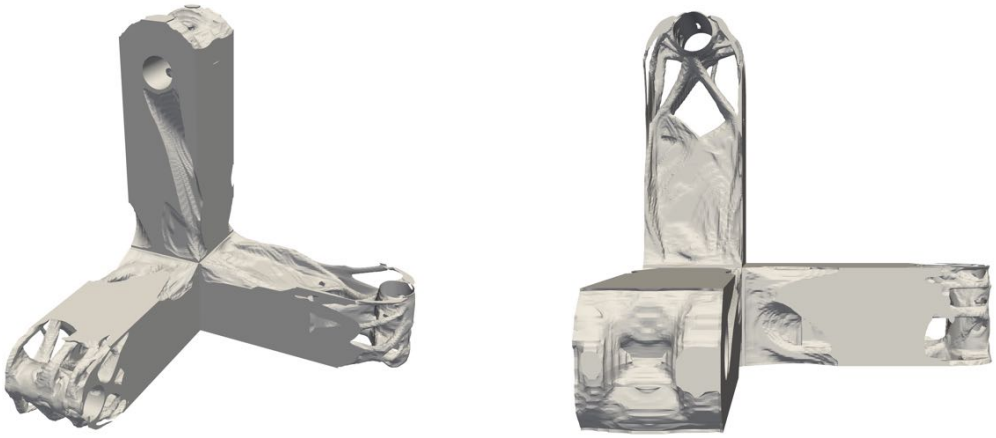

Figure 46: Isometric and top views of the stress- and frequency-constrained mass minimization result for the orthogonal bracket problem

Table 7: Problem data for the orthogonal bracket domain

	Elements	DOF	m%	q	ε	$\sigma_{\max}/\sigma_y$	$\bar{\omega}_0$	Time (h)	n_{procs}
Compliance	5,045,912	15,005,418	40%	10, 10	—	—	—	10.9	48
Stress	4,758,457	14,078,607	37.1%	8, 10	0.1	0.99	—	24.8	48
Stress & frequency	5,356,033	16,005,678	41.9%	10, 10	0.1	0.98	0.18	68.4	48

mization. The optimizer satisfies both constraints within about 100 iterations. The stress constraint violation spikes at 500 iterations due to the adaptive mesh refinement step, but quickly recovers feasibility.

Figure 48b shows the optimization history of the mass and the infeasibility for the stress- and frequency-constrained mass minimization problem, with infeasibility shown on a log scale. Designs are shown at 50, 100, 500, and 1000 iterations. Most of the mass reduction of the structure happens within the first 100 iterations, with a gradual decrease after that point. By the 50th iteration, the optimizer has removed much of the material near the holes where the loads are applied, but by iteration 100, material has started to reform in these areas. By iteration 500, the design has largely converged, but more detail emerges by the final design. Figure 49 shows the optimization history of the first six natural frequencies of the orthogonal bracket. Among these six, there are no repeated natural frequencies at any point. Each natural frequency quickly increased in the beginning of the optimization, but there are only gradual changes after the first 150 iterations. At the final design, the normalized natural frequencies are $\bar{\omega}_1 = 0.19$, $\bar{\omega}_2 = 0.22$, $\bar{\omega}_3 = 0.27$, $\bar{\omega}_4 = 0.37$, $\bar{\omega}_5 = 0.47$, and $\bar{\omega}_6 = 0.55$, respectively.

8 Conclusion

The goal of this project was to explore the potential benefits of utilizing novel through-thickness topology optimized wing structures to achieve optimal passive aeroelastic tailoring. This ambitious goal posed many technical difficulties during the course of the project, primarily due to the large

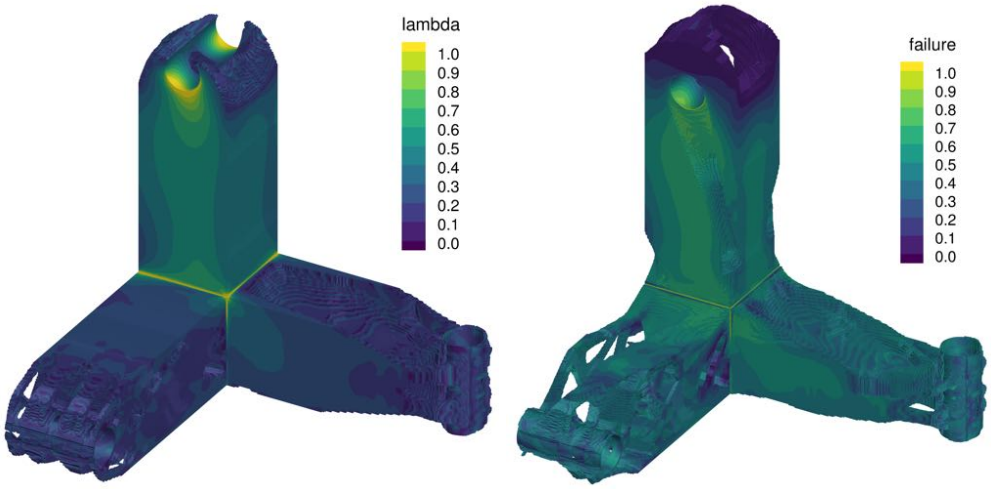

(a) Mass-constrained compliance minimization

(b) Stress-constrained mass minimization

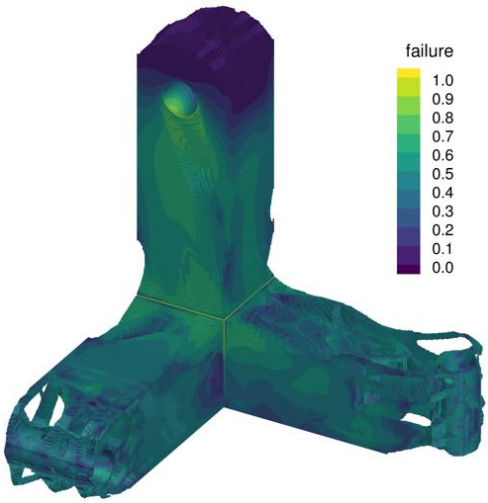

(c) Stress- and frequency-constrained mass minimization

Figure 47: Failure for the orthogonal bracket problem results

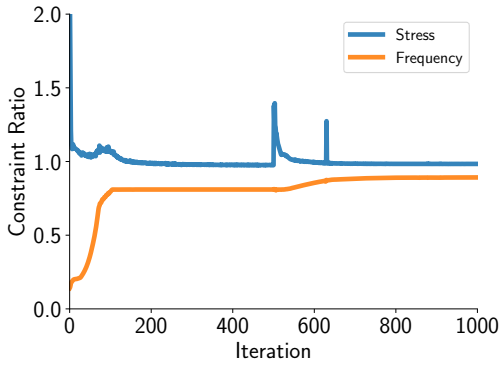

(a) Convergence of stress and frequency constraints

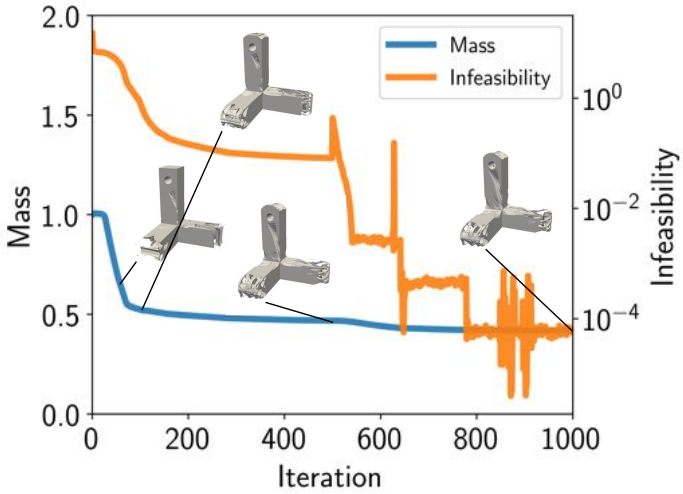

(b) History of objective and infeasibility

Figure 48: Optimization history of orthogonal bracket problem

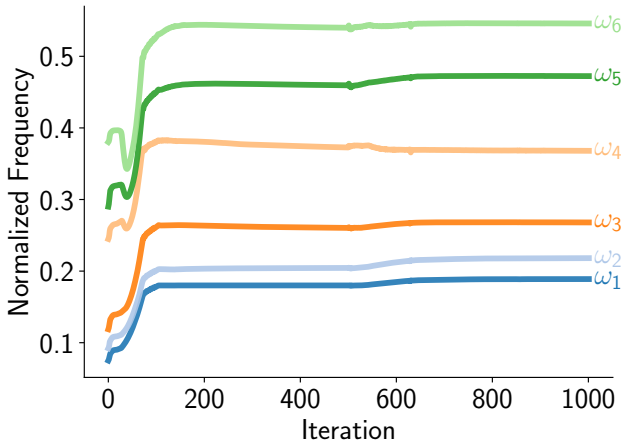

Figure 49: History of orthogonal bracket natural frequencies

design space required to parametrize arbitrary through-thickness topology through the depth of the wing. To attack this problem, we developed a suite of new state-of-the-art tools for large-scale 3D topology optimization. With these tools, we have been able to solve some of the largest stress and frequency-constrained problems that have yet been attempted, to the best of our knowledge. These problems require specialized, state-of-the-art computational methods developed specifically to leverage high-performance computing resources. The results from this project are not complete, and the ultimate goal of producing realistic through-thickness topology optimization designs has not been fully realized. However, these results are an ambitious first step and demonstrate a path forward to achieving this ultimate goal.

References

[1] M. A. Akgun, R. T. Haftka, K. C. Wu, J. L. Walsh, and J. H. Garcelon. Efficient structural optimization for multiple load cases using adjoint sensitivities. *AIAA Journal*, 39(3):511–516, 2001. doi:10.2514/2.1336.

[2] O. A. Bauchau and J. I. Craig. *Structural analysis: with applications to aerospace structures*, volume 163. Springer Science & Business Media, 2009.

[3] C. Burstedde, L. C. Wilcox, and O. Ghattas. p4est: Scalable algorithms for parallel adaptive mesh refinement on forests of octrees. *SIAM Journal on Scientific Computing*, 33(3):1103–1133, 2011. doi:10.1137/100791634.

[4] G. Cheng. Some aspects of truss topology optimization. *Structural and Multidisciplinary Optimization*, 10:173–179, 1995. ISSN 1615-147X. doi:10.1007/BF01742589.

[5] G. D. Cheng and X. Guo. ε-relaxed approach in structural topology optimization. *Structural and Multidisciplinary Optimization*, 13:258–266, 1997. ISSN 1615-147X. doi:10.1007/BF01197454.

[6] P. Duysinx and M. P. Bendsøe. Topology optimization of continuum structures with local stress constraints. *International Journal for Numerical Methods in Engineering*, 43(8):1453–1478, 1998. ISSN 1097-0207.

[7] J. Edmonds, E. Johnson, and S. Lockhart. Blossom I: a computer code for the matching problem. *IBM TJ Watson Research Center, Yorktown Heights, New York*, 1969.

[8] R. G. Grimes, J. G. Lewis, and H. D. Simon. A shifted block Lanczos algorithm for solving sparse symmetric generalized eigenproblems. *SIAM Journal on Matrix Analysis and Applications*, 15(1):228–272, 1994. doi:10.1137/S0895479888151111.

[9] T. Isaac, C. Burstedde, L. Wilcox, and O. Ghattas. Recursive algorithms for distributed forests of octrees. *SIAM Journal on Scientific Computing*, 37(5):C497–C531, 2015. doi:10.1137/140970963.

[10] G. J. Kennedy and J. E. Hicken. Improved constraint-aggregation methods. *Computer Methods in Applied Mechanics and Engineering*, 289(0):332 – 354, 2015. ISSN 0045-7825. doi:10.1016/j.cma.2015.02.017.

[11] G. J. Kennedy and J. R. R. A. Martins. A parallel finite-element framework for large-scale gradient-based design optimization of high-performance structures. *Finite Elements in Analysis and Design*, 87(0):56 – 73, 2014. ISSN 0168-874X. doi:10.1016/j.finel.2014.04.011.

[12] T. S. Kim and Y. Y. Kim. Mac-based mode-tracking in structural topology optimization. *Computers & Structures*, 74(3):375–383, 2000. doi:10.106/S0045-7949(99)00056-5.

[13] V. Kolmogorov. Blossom v: a new implementation of a minimum cost perfect matching algorithm. *Mathematical Programming Computation*, 1(1):43–67, 2009.

[14] C. Le, J. Norato, T. Bruns, C. Ha, and D. Tortorelli. Stress-based topology optimization for continua. *Structural and Multidisciplinary Optimization*, 41:605–620, 2010. ISSN 1615-147X. doi:10.1007/s00158-009-0440-y.

[15] Y. Maeda, S. Nishiwaki, K. Izui, M. Yoshimura, K. Matsui, and K. Terada. Structural topology optimization of vibrating structures with specified eigenfrequencies and eigenmode shapes. *International Journal for Numerical Methods in Engineering*, 67(5):597–628, 2006. doi:10.1002/nme.1626.

[16] S. J. Owen. A survey of unstructured mesh generation technology. In *IMR*, pages 239–267, 1998.

[17] M. Parks, E. de Sturler, G. Mackey, D. Johnson, and S. Maiti. Recycling krylov subspaces for sequences of linear systems. *SIAM Journal on Scientific Computing*, 28(5):1651–1674, 2006. doi:10.1137/040607277.

[18] R. Picelli, S. Townsend, C. Brampton, J. Norato, and H. Kim. Stress-based shape and topology optimization with the level set method. *Computer Methods in Applied Mechanics and Engineering*, 329:1–23, 2018. doi:10.1016/j.cma.2017.09.001.

[19] J.-F. Remacle, J. Lambrechts, B. Seny, E. Marchandise, A. Johnen, and C. Geuzainet. Blossom-quad: A non-uniform quadrilateral mesh generator using a minimum-cost perfect-matching algorithm. *International Journal for Numerical Methods in Engineering*, 89(9): 1102–1119, 2012. ISSN 1097-0207. doi:10.1002/nme.3279.

[20] Y. Saad. *Iterative Methods for Sparse Linear Systems*. SIAM, 2nd edition, 2003.

[21] P. Salas, L. Giraud, Y. Saad, and S. Moreau. Spectral recycling strategies for the solution of nonlinear eigenproblems in thermoacoustics. *Numerical Linear Algebra with Applications*, 22(6):1039–1058, 2015. doi:10.1002/nla.1995. URL `https://onlinelibrary.wiley.com/doi/abs/10.1002/nla.1995`.

[22] A. P. Seyranian, E. Lund, and N. Olhoff. Multiple eigenvalues in structural optimization problems. *Structural and Multidisciplinary Optimization*, 8(4):207–227, 1994.

[23] O. Sigmund and J. Petersson. Numerical instabilities in topology optimization: A survey on procedures dealing with checkerboards, mesh-dependencies and local minima. *Structural optimization*, 16(1):68–75, 1998. ISSN 0934-4373. doi:10.1007/BF01214002.

[24] G. L. Sleijpen and H. A. Van der Vorst. A Jacobi–Davidson iteration method for linear eigenvalue problems. *SIAM review*, 42(2):267–293, 2000. doi:10.1137/S0036144599363084.

[25] A. J. Torii and J. R. d. Faria. Structural optimization considering smallest magnitude eigenvalues: a smooth approximation. *Journal of the Brazilian Society of Mechanical Sciences and Engineering*, 39(5):1745–1754, May 2017. ISSN 1806-3691. doi:10.1007/s40430-016-0583-x. URL https://doi.org/10.1007/s40430-016-0583-x.

[26] S. Wang, E. d. Sturler, and G. H. Paulino. Large-scale topology optimization using preconditioned krylov subspace methods with recycling. *International journal for numerical methods in engineering*, 69(12):2441–2468, 2007. doi:10.1002/nme.1798.

[27] O. C. Zienkiewicz and J. Z. Zhu. The superconvergent patch recovery and a posteriori error estimates. part 1: The recovery technique. *International Journal for Numerical Methods in Engineering*, 33(7):1331–1364, 1992. doi:10.1002/nme.1620330702.

A Enrichment functions for reconstruction

In this work, the regular trilinear finite-element shape functions for 8-noded hexahedral elements are denoted $\mathbf{N}(\eta)$. The enrichment basis functions are constructed such that their values are zero at the nodes so that the nodal solution remains unchanged. For the trilinear case, the enrichment functions are based on the function

$$r(\eta_1) = (1+\eta_1)(1-\eta_1),$$

which is zero at $\eta_1 = -1$ and $\eta_1 = 1$. With this definition, the enrichment functions can be written as

$$\bar{\mathbf{N}}(\eta)^T = \begin{bmatrix} r(\eta_1) & \eta_2 r(\eta_1) & \eta_3 r(\eta_1) & r(\eta_2) & \eta_1 r(\eta_2) & \eta_3 r(\eta_2) & r(\eta_3) & \eta_1 r(\eta_3) & \eta_2 r(\eta_3) \end{bmatrix}.$$

The matrices $\mathbf{A}_x \in \mathbb{R}^{24\times 8}$ and $\bar{\mathbf{A}}_x \in \mathbb{R}^{24\times 9}$ are the three spatial derivatives of $\mathbf{N}(\eta)$ and $\bar{\mathbf{N}}(\eta)$ evaluated at each of the 8 node locations. Given the parametric node locations η_i, for $i = 1,\ldots,8$, these matrices can be written as

$$\mathbf{A}_x = \begin{bmatrix} \mathbf{N}_{,x}(\eta_1)^T \\ \mathbf{N}_{,y}(\eta_1)^T \\ \mathbf{N}_{,z}(\eta_1)^T \\ \vdots \\ \mathbf{N}_{,x}(\eta_8)^T \\ \mathbf{N}_{,y}(\eta_8)^T \\ \mathbf{N}_{,z}(\eta_8)^T \end{bmatrix}, \qquad \bar{\mathbf{A}}_x = \begin{bmatrix} \bar{\mathbf{N}}_{,x}(\eta_1)^T \\ \bar{\mathbf{N}}_{,y}(\eta_1)^T \\ \bar{\mathbf{N}}_{,z}(\eta_1)^T \\ \vdots \\ \bar{\mathbf{N}}_{,x}(\eta_8)^T \\ \bar{\mathbf{N}}_{,y}(\eta_8)^T \\ \bar{\mathbf{N}}_{,z}(\eta_8)^T \end{bmatrix},$$

where the comma notation here denotes differentiation with respect to a coordinate direction.

B Jacobi–Davidson method

The following algorithm details the Jacobi–Davidson solution procedure for efficient solution of large-scale generalized eigenvalue problems using iterative solution techniques.

Algorithm 1 Jacobi–Davidson method with recycling

Set $k = 0$
while $k \leq s$ **do** ▷ Orthogonalize initial set of recycled vectors
  Set $\mathbf{v}_k \leftarrow \text{ModifiedGramSchmidt}(\mathbf{M}, \mathbf{V}_{k-1}, \mathbf{R}_s\mathbf{e}_k)$ ▷ Extract column k from $\mathbf{R}_s$ and orthogonalize it
  Set $k = k+1$
end while
Compute $\mathbf{A}_s = \mathbf{V}_s^T\mathbf{K}\mathbf{V}_s$ ▷ Compute the initial reduced matrix
Set $\mathbf{E}_k = \emptyset$ ▷ Set the converged eigenvectors to the empty set
Set $k = s$
while $k \leq$ max iterations **do**
  if $k > s$ **then** ▷ Skip this orthogonalization step when $k = s$
    Set $\mathbf{v}_k \leftarrow \text{ModifiedGramSchmidt}(\mathbf{M}, \mathbf{E}_k, \mathbf{v}_k)$ ▷ Orthogonalize $\mathbf{v}_k$ against converged eigenvectors $\mathbf{E}_k$
    Set $\mathbf{v}_k \leftarrow \text{ModifiedGramSchmidt}(\mathbf{M}, \mathbf{V}_{k-1}, \mathbf{v}_k)$ ▷ Orthogonalize $\mathbf{v}_k$ against $\mathbf{V}_{k-1}$
    Compute $\mathbf{w} = \mathbf{K}\mathbf{v}_k$
    Compute new row/column of $\mathbf{A}_k$ where $[\mathbf{A}_k]_{jk} = \mathbf{w}^T\mathbf{v}_j$ and $[\mathbf{A}_k]_{kj} = \mathbf{w}^T\mathbf{v}_j$
  end if
  Solve the eigenproblem $\mathbf{A}_k\mathbf{y} = \theta\mathbf{y}$
  Compute for the lowest Ritz vector $\mathbf{u}_1 = \mathbf{V}_k\mathbf{y}_1$
  Compute the residual $\mathbf{r} = \mathbf{K}\mathbf{u}_1 - \theta_1\mathbf{M}\mathbf{u}_1$
  if $||\mathbf{r}||_2 \leq \varepsilon||\mathbf{K}\mathbf{u}_1||_2$ **then** ▷ Check for convergence of this Ritz pair
    Add $\mathbf{u}_1$ to the converged eigenvectors $\mathbf{E}_k = \mathbf{E}_{k-1} \cup \mathbf{u}_1$
    if required eigenvectors converged **then**
      break ▷ All eigenvalues and eigenvectors converged
    end if
    Compute $\mathbf{u}_2 = \mathbf{V}_k\mathbf{y}_2$, $\mathbf{r} = \mathbf{K}\mathbf{u}_2 - \theta_2\mathbf{M}\mathbf{u}_2$ vv ▷ Switch to the next Ritz pair
    Set $\mathbf{u}_1 \leftarrow \mathbf{u}_2$
  else
    Set $\mathbf{E}_k = \mathbf{E}_{k-1}$
  end if
  Set $\mathbf{Q}_k = \mathbf{E}_k \cup \mathbf{u}_1$
  Use FGMRES to approximately solve the update equation

$$(\mathbf{I} - \mathbf{M}\mathbf{Q}_k\mathbf{Q}_k^T)(\mathbf{K} - \theta\mathbf{M})(\mathbf{I} - \mathbf{Q}_k\mathbf{Q}_k^T\mathbf{M})\mathbf{t} = -\mathbf{r}$$

  Set $\mathbf{v}_{k+1} = \mathbf{t}$
  Set $k = k+1$
end while

Appendix F. Tow-Steered Hershey Bar Wing Analysis

Table of Contents

1 Introduction

This document describes the tow-steered Hershey Bar Wing Construction, Testing, and Finite Element Model (FEM). The Hershey-bar wing features tow-steered wing skins that progressively steer from 15 degrees to 70 degrees (with the spanwise direction denoting '0 degrees') across the 6' span, as shown in Figure 1. The wing is assembled with both skins steering the same direction to promote slight bend-twist coupling.

The ribs are constructed using 3-ply 0°/90°/0° laminate and attached using aluminum angle to the spars and skins. Ribs are spaced non-uniformly to improve buckling stability near the root, as shown in Figure 2.The spars are 6 plies of ±45° plies with an additional 5 ply 0°/90° padup in the root section to improve bearing strength for the fasteners reacting the load.

The Hershey-bar wing is designed to accept a point load applied at the center-chord location of the tip rib. The wing is mounted using two 6"x6" x 12" long steel angles at the root.

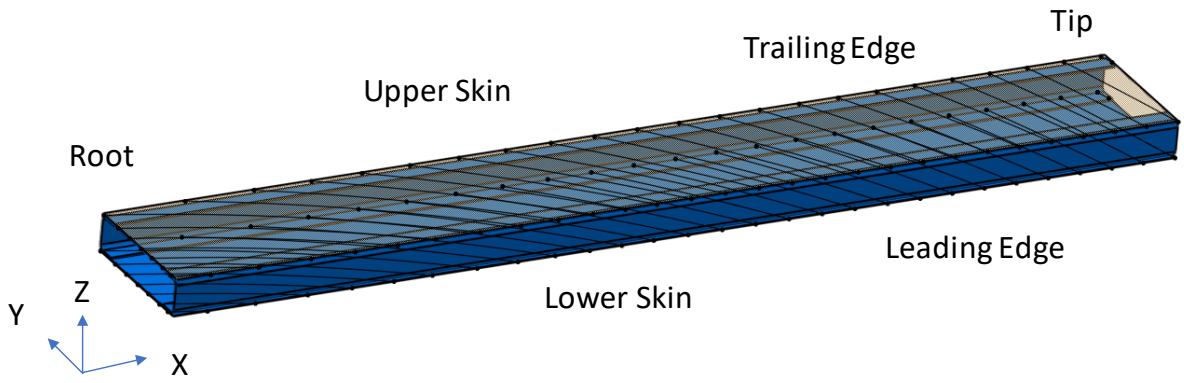

Figure 1. Hershey bar wing orientation and tow-steering paths (ribs omitted).

Figure 2. Hershey bar wing in fabrication, showing ribs and shear clips (left) and fully assembled (right).

2 FEM Material & Assumptions

In this FEM, material is represented as PCOMP material properties wherein the ply-by-ply laminate stackup is modeled within a given property. Tow-steering is enforced by assigning the appropriate material direction to each element. In-plane composite strength is assessed using the Hoffman failure criteria.

The material properties utilized for this model are provided in Tables 1 and 2. These properties are based on estimated material properties and will be updated once mechanical coupon testing is complete.

Table 1. Representative material properties for E752LT/HTS40 Unidirectional Carbon Fiber Tape (Skins).

RTA FEM Properties for Loads	
$thickness_{nom}$ (in)	0.0049
E_{11} (Msi) (average t & c)	17.1
E_{22} (Msi) (average t & c)	1.4
G_{12} (msi)	0.7
u_{12}	0.04
G_{13}, G_{23} (Msi)	0.7
Stress (80% of brochure)	
S_{11}^T – unnotched (ksi)	239
S_{22}^T– unnotched (ksi)	9.3
S_{11}^C – unnotched (ksi)	150
S_{22}^C– unnotched (ksi)	33
S_{12}–(ksi)	10.3

Table 2. Representative material properties for 8552/IM7 Plain Weave Fabric (Spars, Ribs).

RTA FEM Properties for Loads	
$thickness_{nom}$ (in)	0.0078
E_{11} (Msi) (average t & c)	9.0
E_{22} (Msi) (average t & c)	9.0
G_{12} (msi)	0.72
u_{12}	0.045
G_{13}, G_{23} (Msi)	0.7
Stress (80% of brochure)	
S_{11}^T – unnotched (ksi)	40.5
S_{22}^T– unnotched (ksi)	38.7
S_{11}^C – unnotched (ksi)	40.5
S_{22}^C– unnotched (ksi)	38.7
S_{12}–(ksi)	20.0

Each fastener is represented by a rigid spring. The structure is restrained by two pinned nodes on each spar in the first bay. A single point load is applied at the center of the closeout rib.

2.1 File Structure

The file structure is described below. All files are included in the 'Hershey Bar FEM.zip' archive file.

DATA FILES:

'HersheyBar.bdf' :
Tow-Steered Hershey-bar model

'Hershey-Bar_LinearStatic.nas' :
Initializes and runs a linear static analysis with a 75lb tip load.

'Hershey-Bar_NonlinearStatic.nas' :
Initializes and runs a nonlinear static analysis with a 75lb tip load.

'Hershey-Bar_Buckling.nas' :
Initializes and runs a linear buckling analysis with a 75lb tip load.

3 Linear Static Analysis

3.1 Deflection

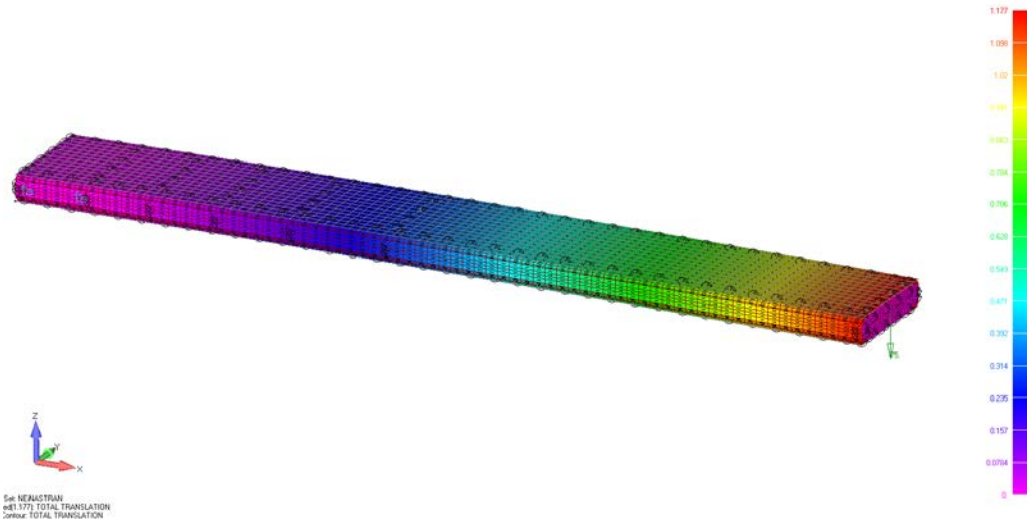

Figure 3. Deformation profile of Hershey Bar Wing subject to 75lb tip load.

The peak deflection of the Hershey bar wing under a 75lb tip load is 1.177 in.

The amount of twist induced in the wing is calculated by comparing the deflection of the trailing edge of the lower skin to the leading edge at the tip. The trailing edge corner vertical deflection is 1.174 in. The leading edge corner vertical deflection is 1.149, a difference of .025" over a chord of 10", or approximately 0.14°.

3.2 Composite Strength

The composite strength (in-plane) of the spars, ribs, and skins are computed using the Hoffman combined stress criteria. The contours are shown in Figure 4.

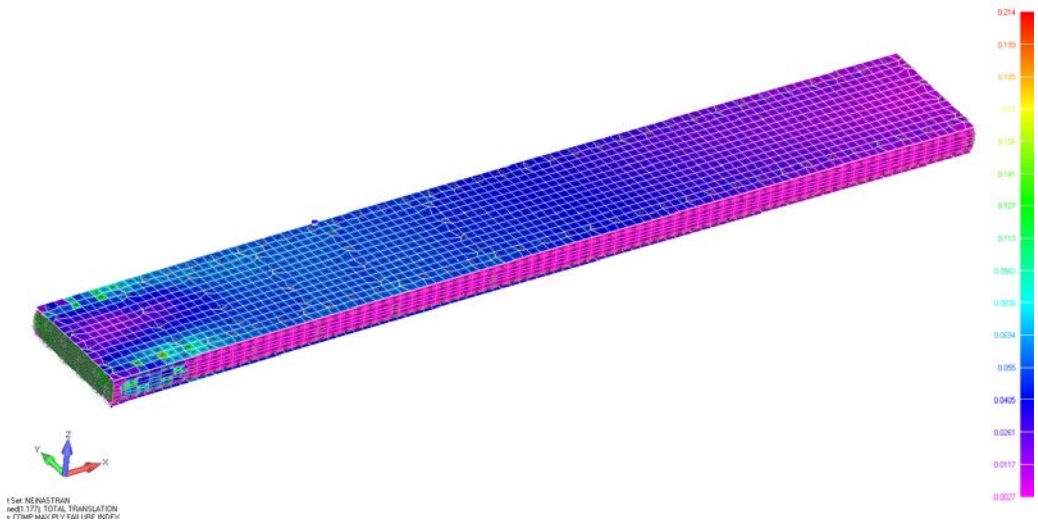

Figure 4. Deformation profile of baseline uCRM-13.5 subject to +1G load condition.

The failure index is 0.214, which provides positive margin against failure (a value of 1.0 or greater would indicate failure for the prescribed load). The Hoffman criteria is quadratic, so an estimate for margin of safety (MS) is calculated as:

$$MS = \frac{1}{FS*\sqrt{FI}} - 1 = \frac{1}{1.5*\sqrt{.214}} - 1 = +0.44.$$

Note that this calculation is conservative as it includes elements adjacent to fasteners and boundary conditions that artificially increase the local stress (these areas are typically checked for pullthrough and bearing strength independently).

3.3 Fasteners & Boundary Conditions

Boundary conditions are applied as two pinned nodes on each spar web near the root end, corresponding to nodes nearest the actual fastener locations. It is noted that while the model only specifies two boundary condition locations per spar web, the actual test article included two additional fasteners evenly spaced between the modeled fasteners. Because the two middle fasteners are neglected, the following fastener calculations are conservative.

Tensile (pull-through) loads in all fasteners are negligible.

The maximum shear load of any fastener is 391 lb. A bearing strength of 70ksi is assumed for the skins.

$$F_{bearing} = D * t * F_{bru} = .125 * (12 * .0049) * 80{,}000 = 588\ lb$$

$$MS = \frac{F_{bearing}}{FS * F_{shear}} - 1 = \frac{588}{1.5 * 391} - 1 = +0.002.$$

The fastener shear strength is 1090 lb, which is ample compared with the bearing strength.

Note: the fasteners with highest shear load occur near the root fasteners. The predicted loads are likely conservative due to additional reaction fasteners that have been omitted, which will result in a more even load distribution.

The highest shear load in a reaction fastener is 630 lb. The bearing strength of the spar is:

$$F_{bearing} = D * t * F_{bru} = .19 * (11 * .0078) * 80{,}000 = 1304\ lb$$

$$MS = \frac{F_{bearing}}{FS * F_{shear}} - 1 = \frac{1304}{1.5 * 630} - 1 = +0.38.$$

3.4 Buckling

The first linear buckling mode (Figure 5) of the Hershey bar wing occurs at an eigenvalue of 0.724 for a 75lb tip load, suggesting the onset of buckling at 54 lb. However, the wing appears to have significant post-buckling strength as suggested by the nonlinear static analysis. Figure 6 shows the deflected result of a nonlinear analysis performed with a 150 lb tip load. While the buckling mode predicted by the linear eigenvalue solver is clearly active, there remains significant useful strength beyond the onset of buckling.

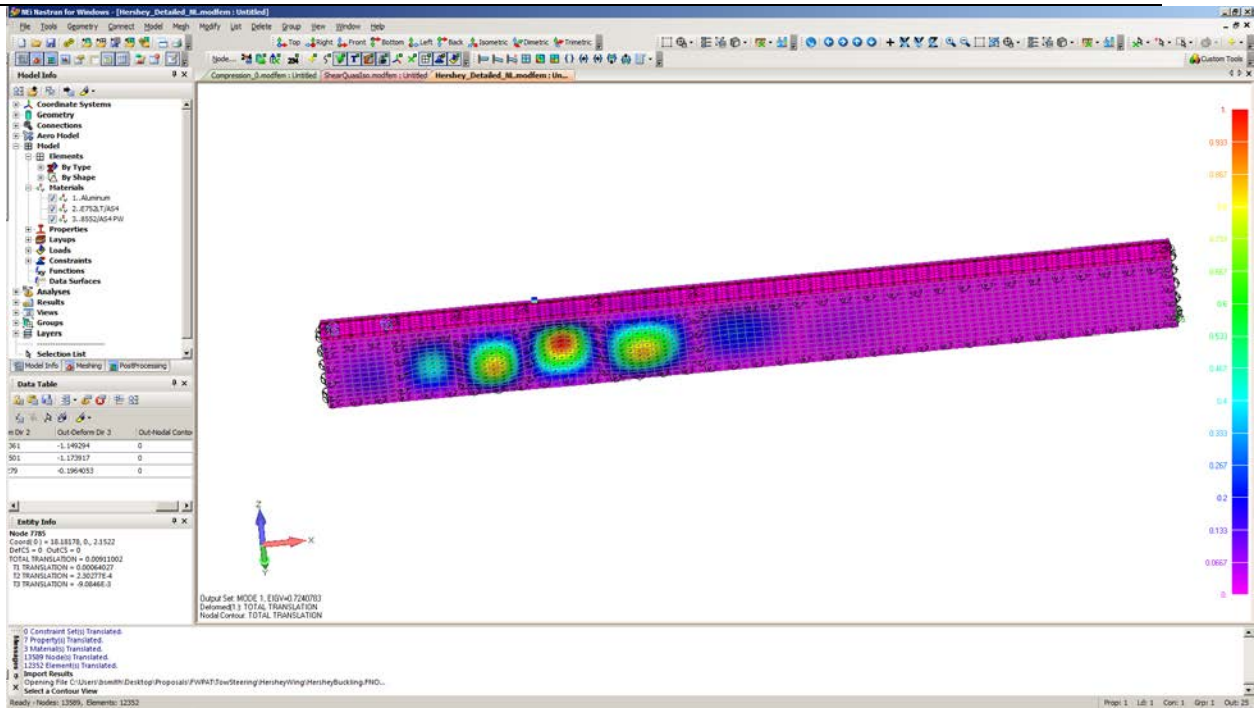

Figure 5. First buckling mode of Hershey-bar wing,

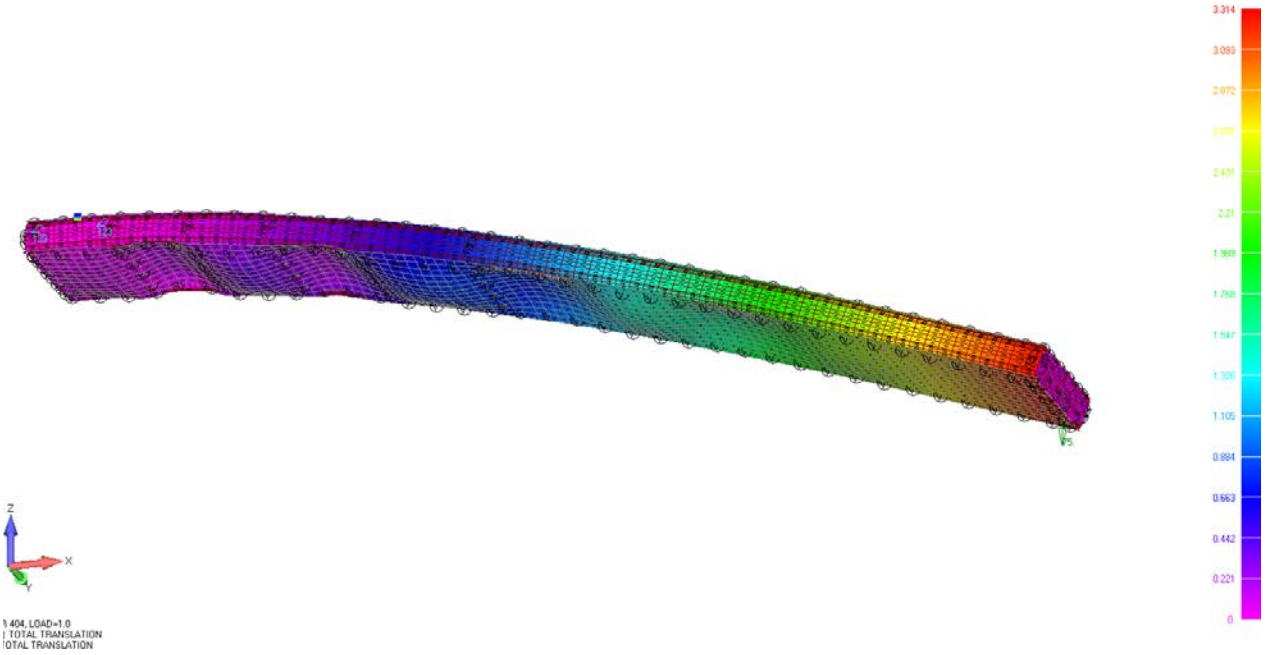

Figure 6. Nonlinear Static analysis showing significant post-buckling strength (150lb applied load).

4 Test Results

The preliminary load test performed at Aurora was intended to primarily ensure that the wingbox did not suffer from any premature failure due to manufacturing defects and secondarily, to generate an initial data set.

To perform the test, the steel mounting angles were clamped to a forklift fixture. A 67lb weight was applied to the tip by gradually lifting the weight from the floor. The forklift fixture was subsequently placed resting on a table (with additional weight from the forklift) to avoid hydraulic bleed-off, as shown in Figure 7. The 67 lb deflected shape was recorded at eight points using a laser tracker. Weight was gradually removed from the wing and the deflected shape recorded at the eight points (Figure 8).

It should be noted that because the root fixture was not perfectly rigid, the wing underwent both deflection as well as rigid-body rotation due to compliance in the forklift fixture.

Figure 7. Cantilevered Load Test. Supported by forklift resting on table. Deflection measured with laser tracker at 8 points (4 span locations x 2 chord locations).

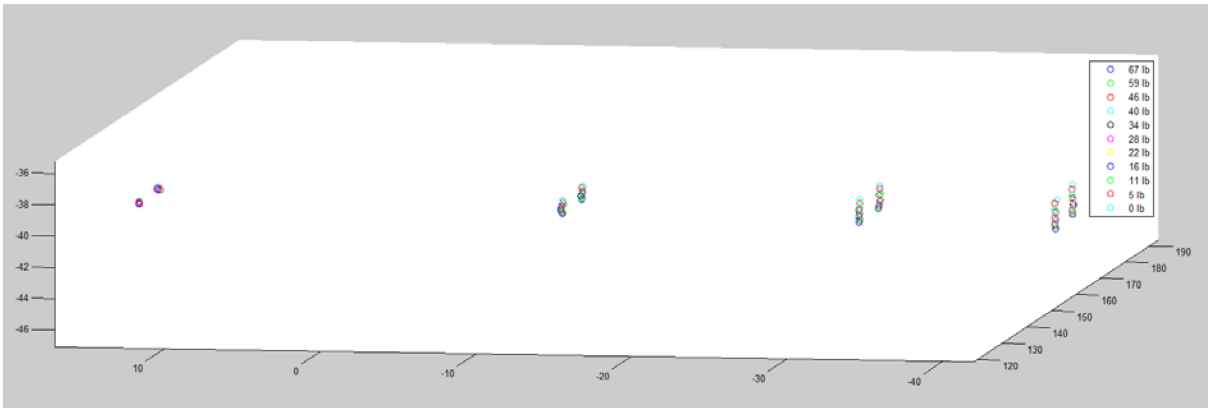

Figure 8. Laser Tracker measurements (arbitrary origin).

To correct for rigid body rotation, the cantilevered beam deflection equation with additional terms to account for rigid body rotation and translation was fitted to the data set (dotted blue line of Figure 9). The rigid body terms were then removed, which yield the corrected deflection profile (dashed blue line). A similar analysis was performed for the FEM, which also contains some rigid body motion due to a double-pinned boundary condition rather than purely cantilevered to provide a consistent basis for comparing the corrected test data. The corrected FEM deflection profile (shown in green) is also normalized to the test load of 67 lb rather than the 75lb load applied to the FEM. The equivalent EI bending stiffness of the Hershey bar wing is 29.2 x 10^6 lb-in^2 as measured by the test data compared to a prediction of 25.3 x 10^6 lb-in^2 from the FEM. Part of the 15% difference can be attributed to differences in assumed material modulus.

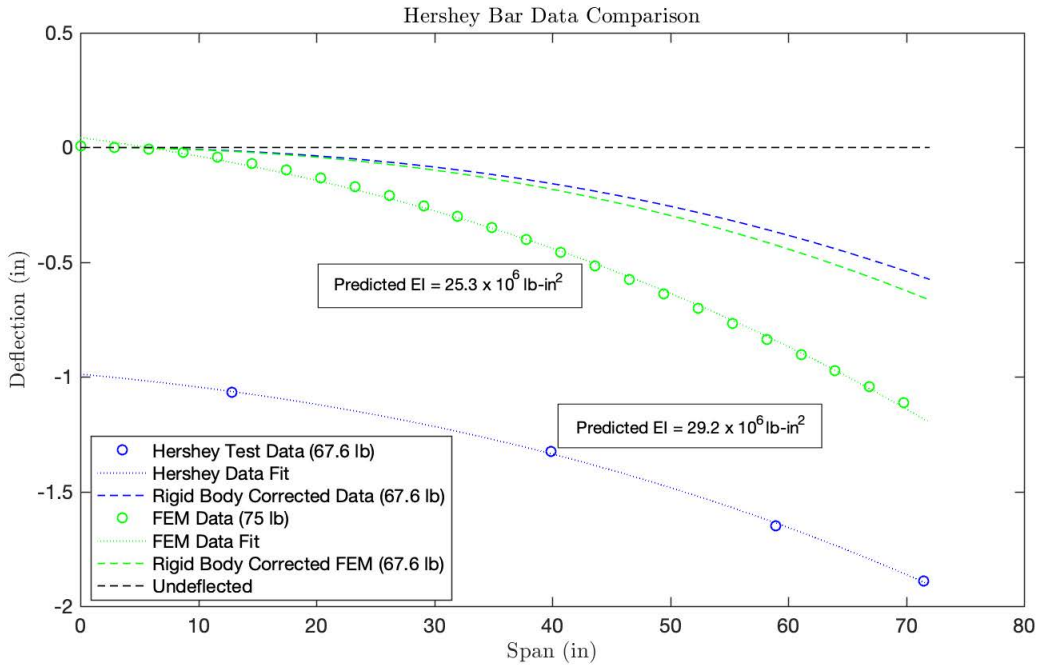

Figure 9. Hershey Bar deflection comparison corrected for rigid body motion.

The absolute deflection measured in the trailing edge tip corner is 1.909” compared to a deflection of 1.889” at the leading edge tip corner, for a total difference of 0.020” over a measurement span of 9.33”. This corresponds to a twist angle of 0.12°, compared to the FEM prediction of 0.14°.

While these values provide useful ballpark values for wing deflection and twist, the testing to be performed at AFRC is expected to yield much better data owing to more precise boundary conditions, load application, and instrumentation.

Appendix G. Test Article Scaling and Discrete Loads Analysis

Table of Contents

1 Introduction

This document describes the scaling analysis used to create the 27% scale uCRM-13.5 Test Article, loads, and generation of a discrete load plan, which approximates the continuous aerodynamic and inertial loads used to size the wing.

2 Scaling

The tow-steered uCRM-13.5 is optimized by UMICH at full scale using metric units (Newton, meters). Loads are provided as discrete tractions applied to the wing skins for aerodynamic and inertial loads. To convert these to a 27% scaled test article, the model must be scaled geometrically, and appropriate scale factors must be applied to the aerodynamic and inertial tractions. Furthermore, units are converted to English units (pound, inches) for detailed design and manufacturing.

Geometry scales linearly with the scale factor of 27%. Thickness scales linearly as well; composite thicknesses are subsequently rounded up to the nearest whole ply. No scaling is applied to material properties (modulus, density).

Loading is scaled such that the geometrically scaled structure achieves the same spanwise bending profile (curvature) as the full scale model. This is achieved by scaling all point forces quadratically with the 27% scale for a total factor of .0729. Inertial loads are scaled by first calculating the effective point-force at full scale then apply the .0729 scale factor. These scaling factors are summarized in Table 1.

Table 1. Geometric and Load Scaling Factors.

Quantity	**Multiply Full Scale Value by:**
Geometric Scaling	0.27
Meters to Inches unit conversion	39.37
Load Factor Scaling	0.0729
Newtons to Pounds unit conversion	0.2248
Modal Frequency Scaling	3.7

Because the curvature is maintained, strain, and therefore stress is also preserved. Modal frequencies scale with the inverse of scale factor (3.7). Derivation of these scaling factors is shown in Appendix A.

3 Discrete Load Plan

The load plan described in this document was developed from the full-scale uCRM-13.5 tow-steered wing provided by the University of Michigan. Seven evenly-spaced wing stations were selected to apply loads, using two load points (corresponding to the leading and trailing spars) at each wing station, for a total of 14 load points. The load vectors at each point were found such that the spanwise out-of-plane bending moment distribution, spanwise in-plane bending moment distribution, and spanwise center of lift distributions were matched as closely as possible. All force and moment calculations are scaled from the original aircraft coordinate system (x points aft, y points outboard, z points up). Units listed below are converted to English units (lbs, inches).

3.1 +2.5G Case

The +2.5G test article load point plan is summarized in Table 2 and shown as load vectors in Figure 1.

Table 2. +2.5G Test Article Load Plan.

Load #	X (in)	Y (in)	Z (in)	Fx (lb)	Fy (lb)	Fz (lb)	Resultant (lb)
1a	302.58	83.89	40.33	-314.69	484.52	3677.20	3722.31
2a	340.10	134.07	42.88	-354.96	121.22	-1525.59	1571.03
3a	377.05	183.48	43.69	-335.77	-181.38	2760.28	2786.54
4a	415.03	234.27	44.37	-265.33	-347.62	2480.60	2518.86
5a	451.96	283.66	45.36	-172.91	-302.89	1375.85	1419.37
6a	488.80	332.94	45.19	-102.14	-211.87	910.77	940.65
7a	525.35	381.70	44.87	-7.33	-132.50	190.16	231.88
1b	347.84	82.79	42.22	-314.69	-498.08	2218.17	2295.08
2b	374.30	132.68	44.19	-354.96	-489.79	6648.87	6676.33
3b	405.16	181.61	44.98	-335.77	-534.81	1882.84	1985.91
4b	436.11	230.68	44.60	-265.33	-496.66	1221.67	1345.20
5b	468.65	282.29	45.20	-172.91	-426.84	1096.41	1189.20
6b	499.94	331.90	44.94	-102.14	-205.50	686.76	724.09
7b	531.42	381.93	45.22	-7.33	59.79	-55.60	81.98

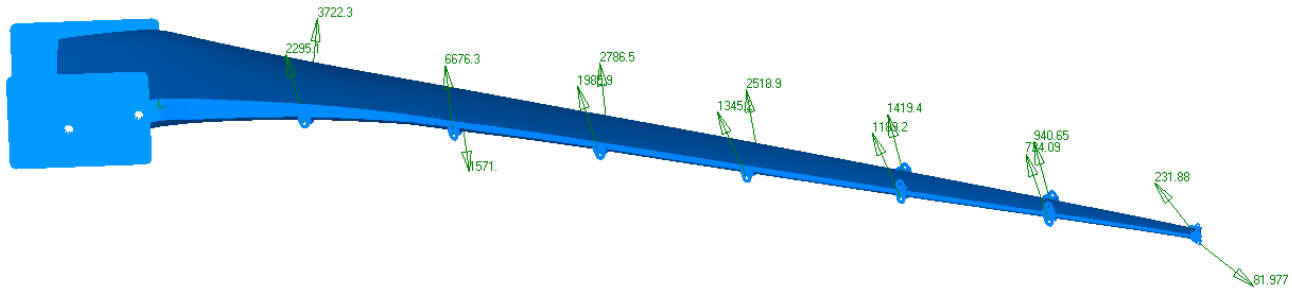

Figure 1. +2.5G Discrete Load Vectors.

Shear and moment diagrams are provided in Figures 2 – 6 for the in-plane and out of plane bending. The effect of reducing the number of spanwise load points is easily seen in the shear diagrams of Figure 2 and Figure 4, which now exhibits a step-like behavior. However, even with only seven discrete span loading locations (14 load points total), the bending moment distribution can be very well matched, as evidenced by Figure 5.

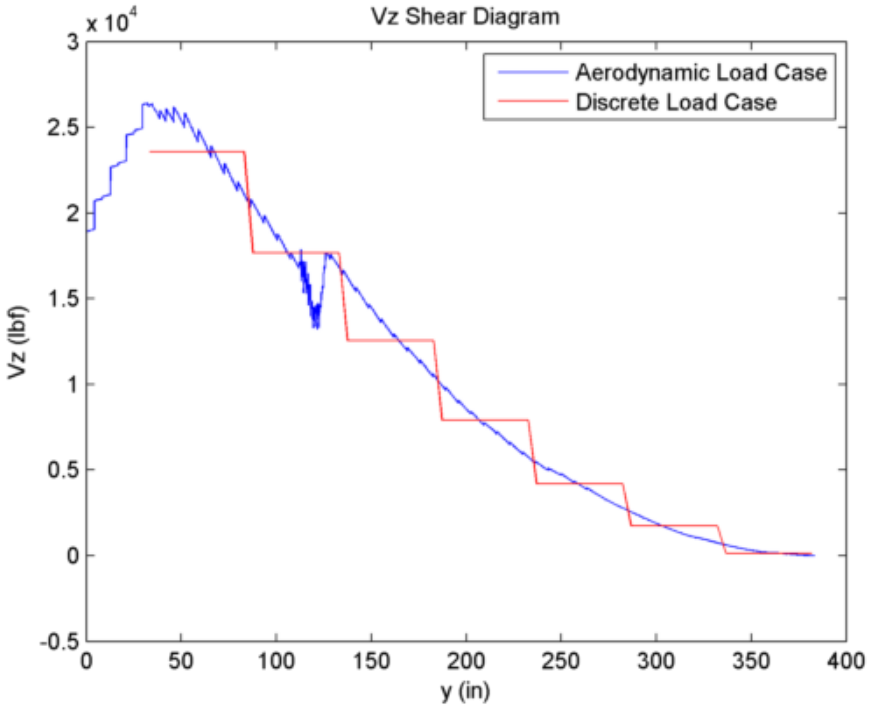

Figure 2. +2.5G Vz Shear Diagram – Discrete Load vs. Scaled Aerodynamic Load comparison.

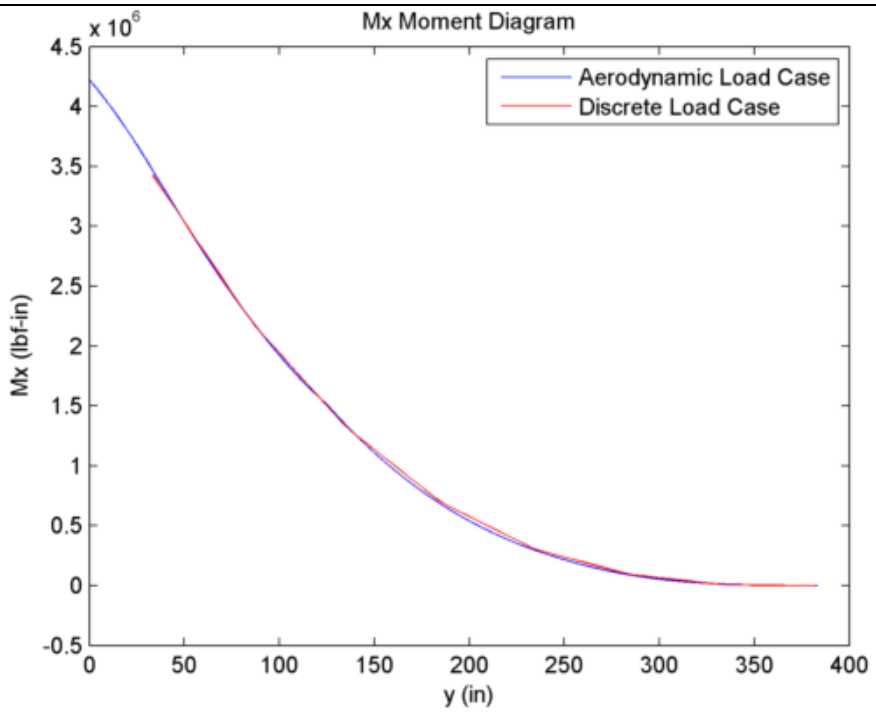

Figure 3. +2.5G Mx Moment Diagram – Discrete Load vs. Scaled Aerodynamic Load comparison.

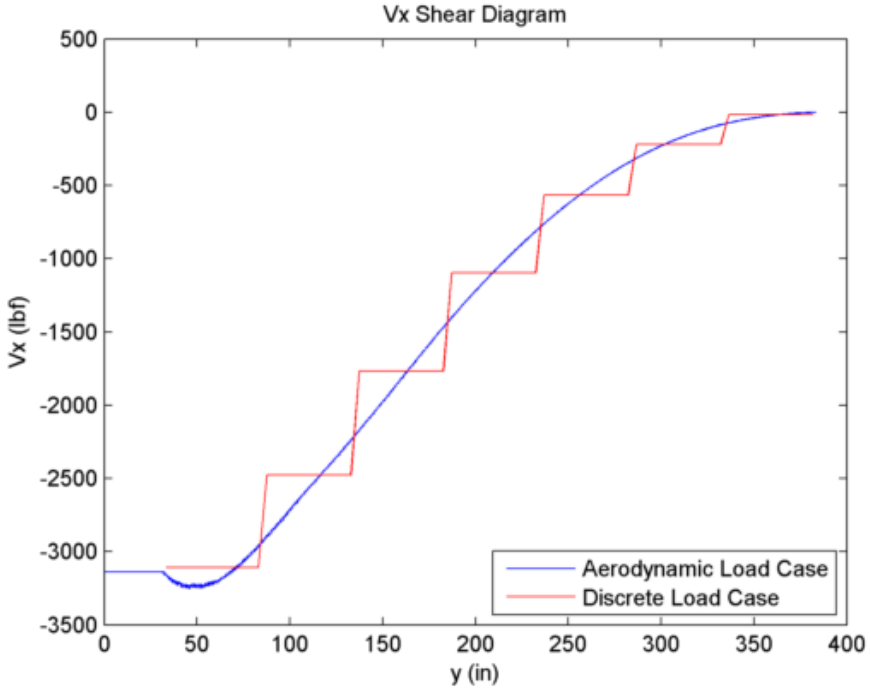

Figure 4. +2.5G Vx Shear Diagram – Discrete Load vs. Scaled Aerodynamic Load comparison.

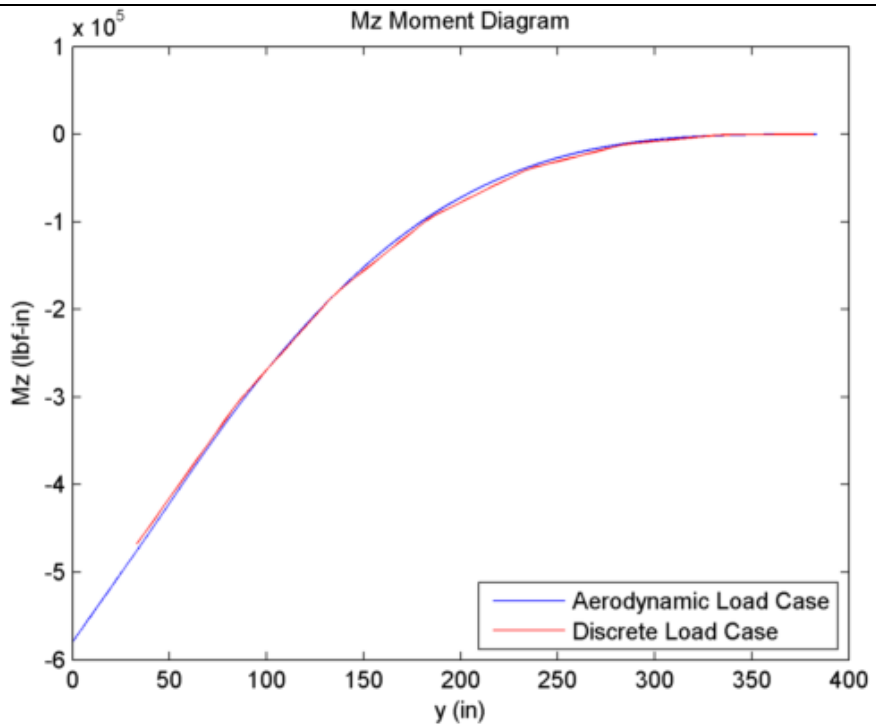

Figure 5. +2.5G Mz Moment Diagram – Discrete Load vs. Scaled Aerodynamic Load comparison.

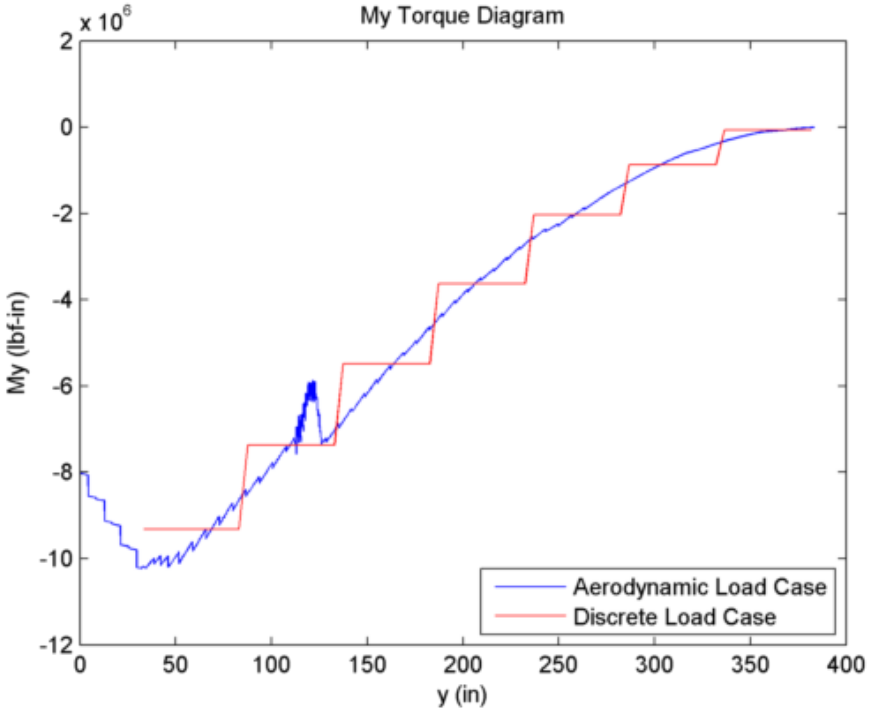

Figure 6. +2.5G My Torque Diagram – Discrete Load vs. Scaled Aerodynamic Load comparison.

3.2 -1G Case

The -1G test article load point plan is summarized in Table 3 and shown as load vectors in Figure 7.

Table 3. -1G Test Article Load Plan.

Load #	X (in)	Y (in)	Z (in)	Fx (lb)	Fy (lb)	Fz (lb)	Resultant (lb)
1a	302.58	83.89	40.33	-70.07	609.86	-1910.64	2006.84
2a	340.10	134.07	42.88	-64.79	349.23	-754.55	833.97
3a	377.05	183.48	43.69	-45.08	185.30	-1799.42	1809.50
4a	415.03	234.27	44.37	-17.29	119.01	-1466.95	1471.87
5a	451.96	283.66	45.36	6.02	64.64	-1082.50	1084.45
6a	488.80	332.94	45.19	15.46	24.18	-594.35	595.04
7a	525.35	381.70	44.87	2.19	20.63	-315.19	315.87
1b	347.84	82.79	42.22	-70.07	-56.72	230.39	247.40
2b	374.30	132.68	44.19	-64.79	-99.03	-602.13	613.65
3b	405.16	181.61	44.98	-45.08	-44.75	623.85	627.07
4b	436.11	230.68	44.60	-17.29	-37.03	695.77	696.97
5b	468.65	282.29	45.20	6.02	-38.24	727.99	729.01
6b	499.94	331.90	44.94	15.46	-22.04	402.39	403.29
7b	531.42	381.93	45.22	2.19	-3.09	234.89	234.92

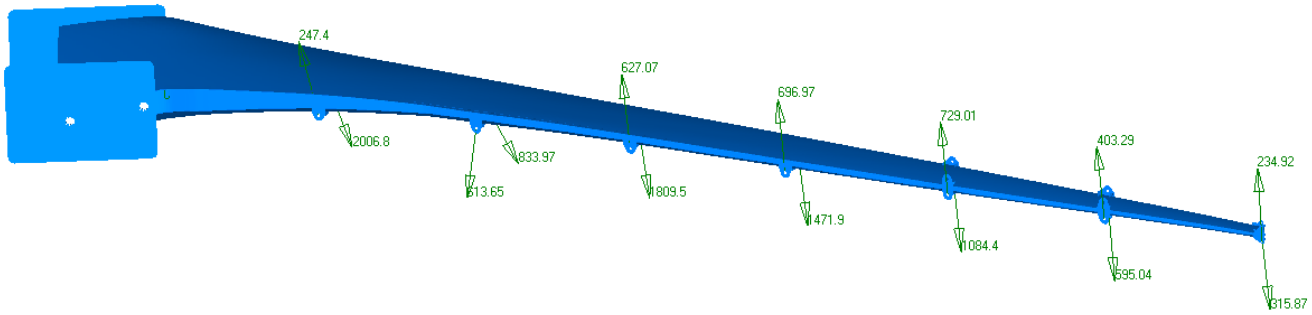

Figure 7. -1G Discrete Load Vectors.

Shear and moment diagrams are provided in Figures 8 – 12 for the in-plane and out of plane bending.

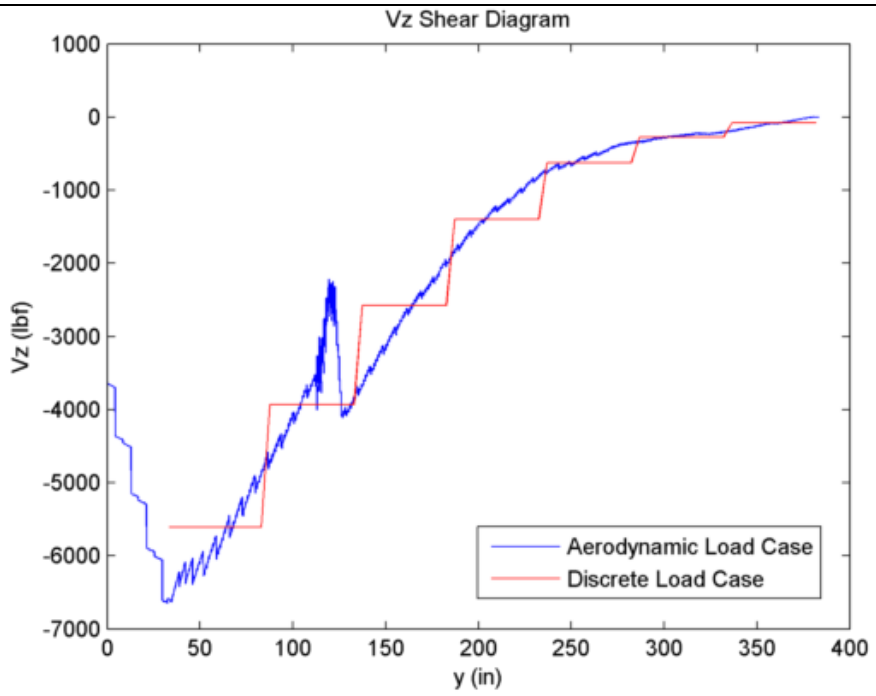

Figure 8. -1G Mz Shear Diagram – Discrete Load vs. Scaled Aerodynamic Load comparison.

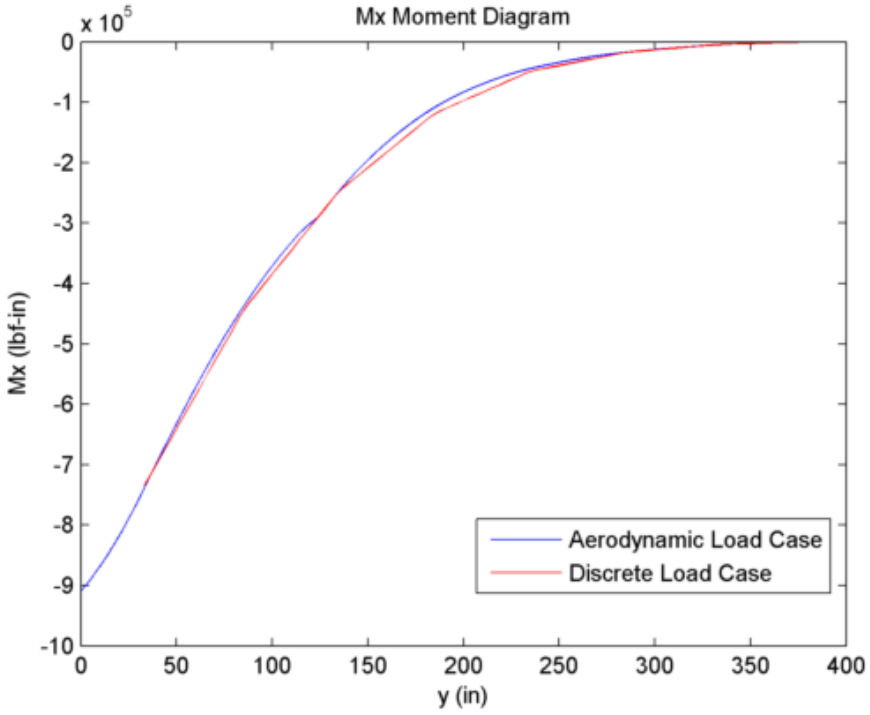

Figure 9. -1G Mx Moment Diagram – Discrete Load vs. Scaled Aerodynamic Load comparison.

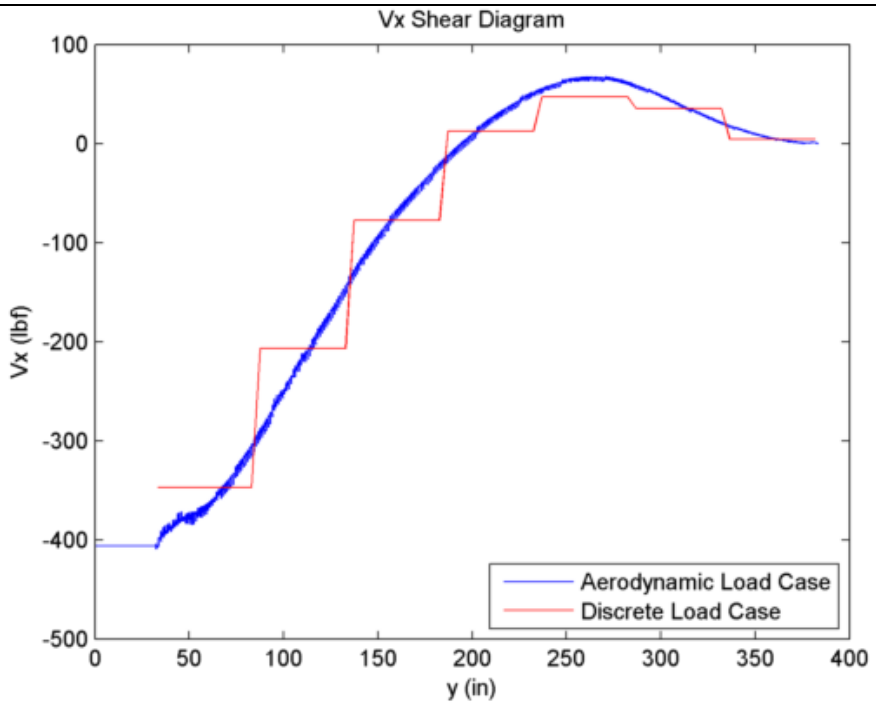

Figure 10. -1G Vx Shear Diagram – Discrete Load vs. Scaled Aerodynamic Load comparison.

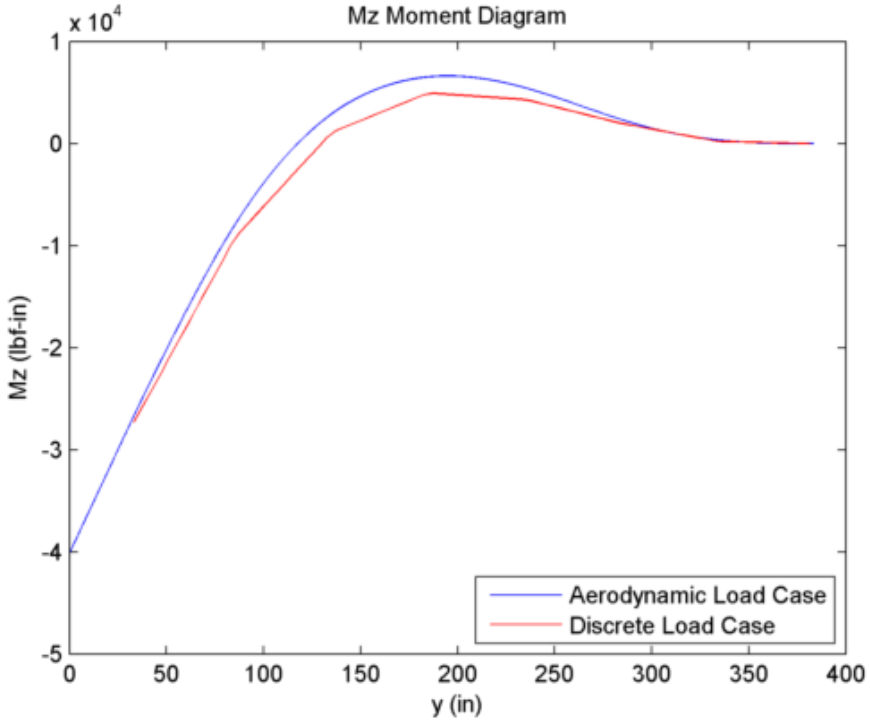

Figure 11. -1G Mz Moment Diagram – Discrete Load vs. Scaled Aerodynamic Load comparison.

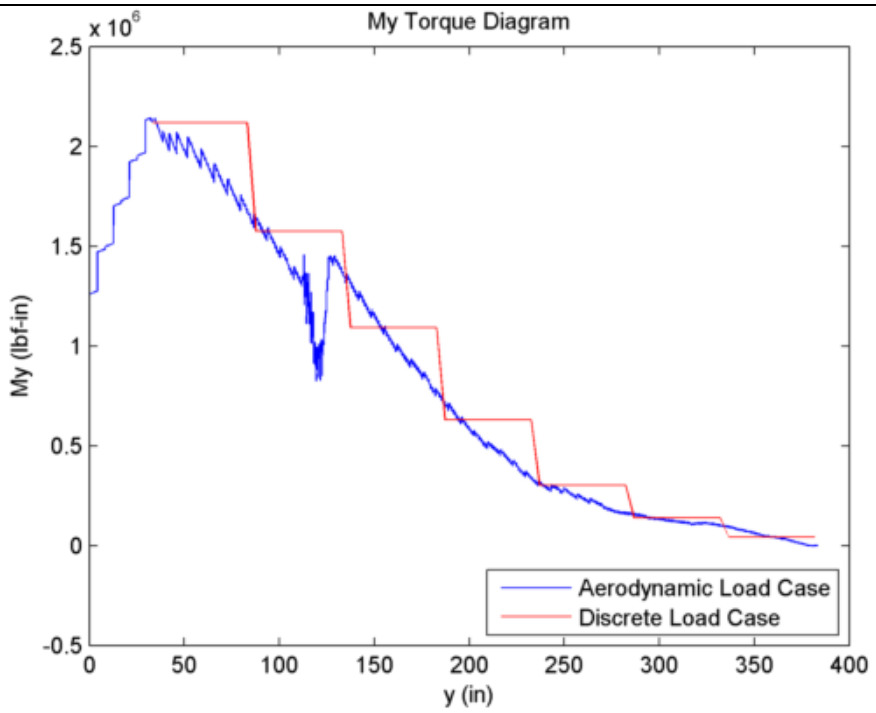

Figure 12. -1G My Torque Diagram – Discrete Load vs. Scaled Aerodynamic Load comparison.

3.3 +1G Case

The +1G test article load point plan is summarized in Table 4. +1G Test Article Load Plan and shown as load vectors in Figure 13.

Table 4. +1G Test Article Load Plan.

Load #	X (in)	Y (in)	Z (in)	Fx (lb)	Fy (lb)	Fz (lb)	Resultant (lb)
1a	302.58	83.89	40.33	26.84	157.26	1150.58	1161.59
2a	340.10	134.07	42.88	-15.94	52.12	-1091.66	1093.02
3a	377.05	183.48	43.69	-39.67	-35.71	987.30	988.74
4a	415.03	234.27	44.37	-40.52	-83.88	1031.53	1035.73
5a	451.96	283.66	45.36	-31.33	-84.96	662.37	668.53
6a	488.80	332.94	45.19	-21.41	-74.60	528.38	534.05
7a	525.35	381.70	44.87	-3.06	-56.88	204.75	212.53
1b	347.84	82.79	42.22	26.84	-229.78	1292.46	1313.00
2b	374.30	132.68	44.19	-15.94	-207.50	3416.71	3423.05
3b	405.16	181.61	44.98	-39.67	-203.02	1291.99	1308.44
4b	436.11	230.68	44.60	-40.52	-208.90	956.08	979.48
5b	468.65	282.29	45.20	-31.33	-198.43	818.21	842.51
6b	499.94	331.90	44.94	-21.41	-106.54	523.53	534.69
7b	531.42	381.93	45.22	-3.06	28.16	-78.95	83.88

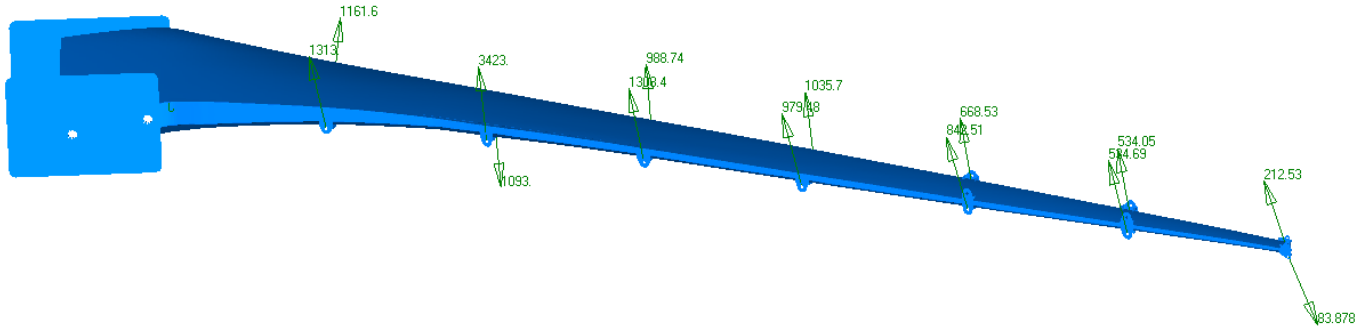

Figure 13. +1G Discrete Load Vectors.

Shear and moment diagrams are provided in Figures 14 – 18 for the in-plane and out of plane bending.

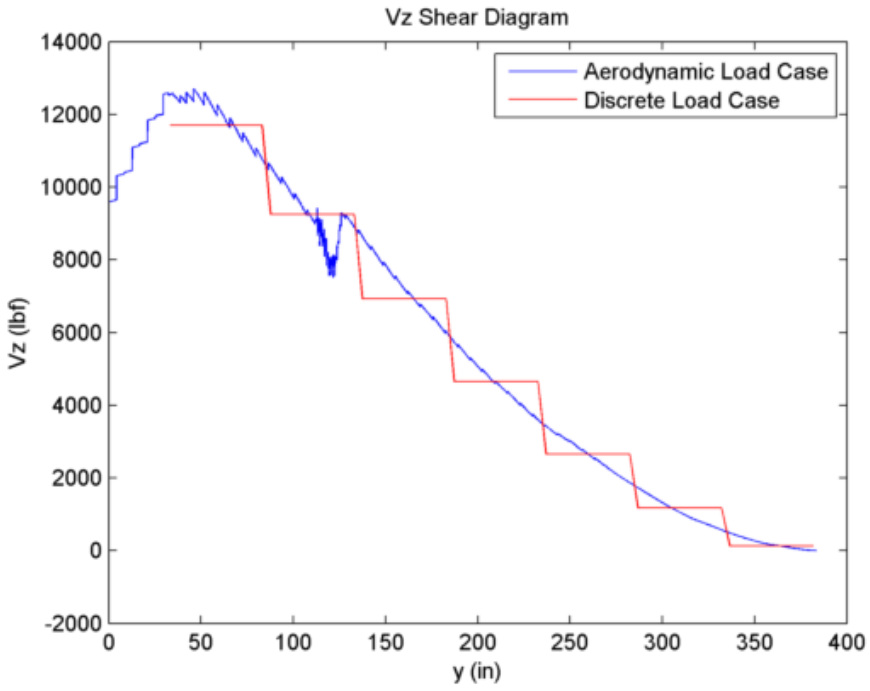

Figure 14. +1G Vz Shear Diagram – Discrete Load vs. Scaled Aerodynamic Load comparison.

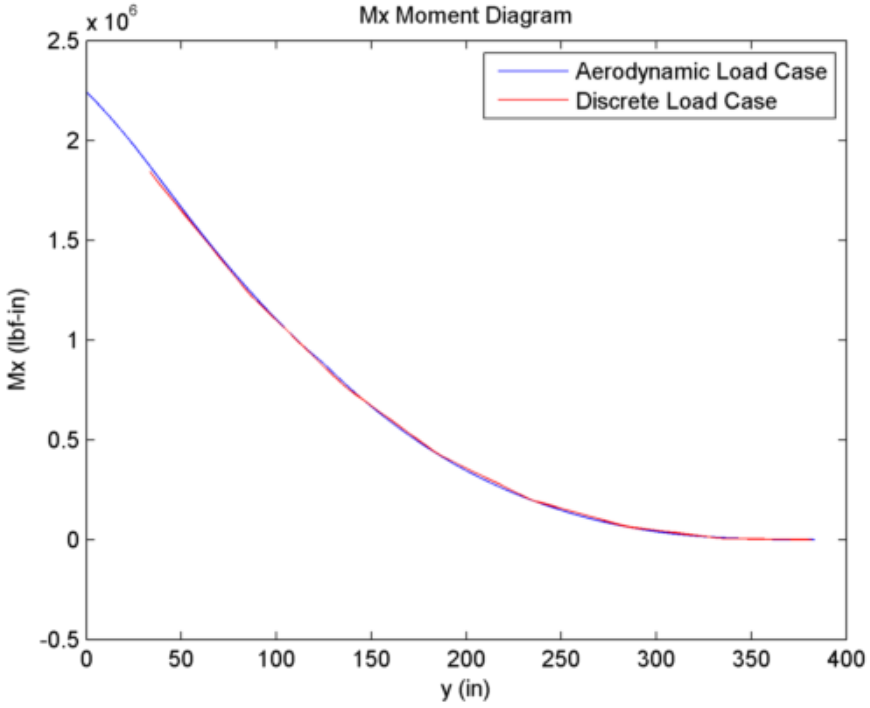

Figure 15. +1G Mx Moment Diagram – Discrete Load vs. Scaled Aerodynamic Load comparison.

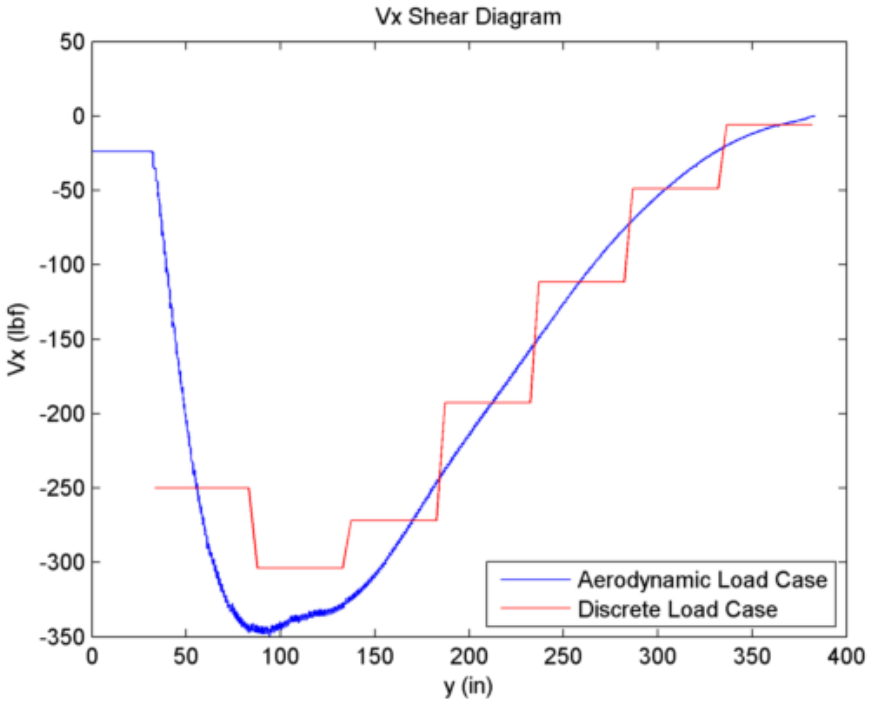

Figure 16. +1G Vx Shear Diagram – Discrete Load vs. Scaled Aerodynamic Load comparison.

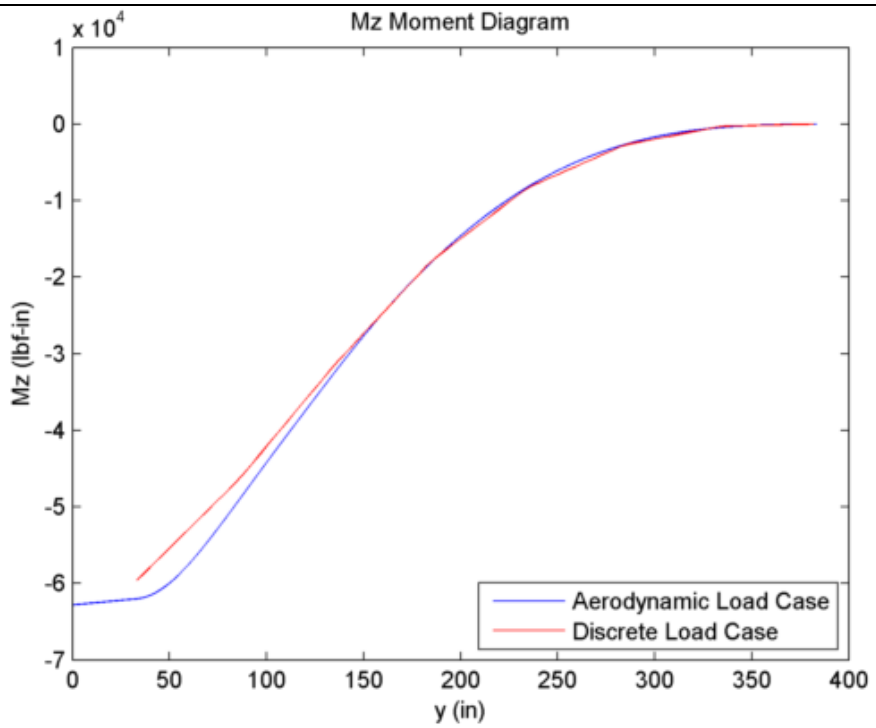

Figure 17. +1G Mz Moment Diagram – Discrete Load vs. Scaled Aerodynamic Load comparison.

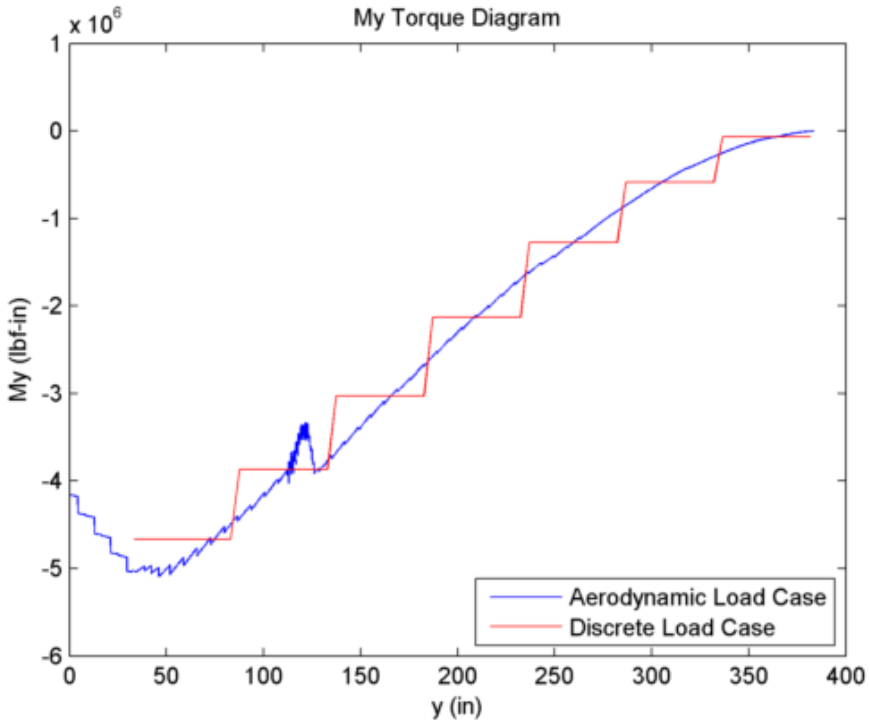

***Figure** 18. +1G My Torque Diagram – Discrete Load vs. Scaled Aerodynamic Load comparison.*

4 Conclusion

The discrete load points detailed above appear to closely approximate the moment diagrams from the continuous load case. These loads are being utilized in the CDR-level Finite Element Model. It is recommended that these loads be utilized for static load testing of the test article (load vectors may need to be modified slightly such that they remain within the test load plane – this should be done by projecting the load vector onto the test load plane).

Appendix A. Scaling Analysis

Defined:

Geometric scaling $k_b = \frac{L_{scaled}}{L_{full}}$

Material Scaling $k_E = 1$

(Material does not scale) $k_\rho = 1$

Derived:

Mass $k_M = k_\rho {k_b}^3$

Inertia $k_I = {k_b}^4$

EI $k_{EI} = k_E {k_b}^4$

Cantilevered stiffness $k_K = k_E k_b$

(from $\delta \propto \frac{FL^3}{EI}$; $K \therefore \frac{F}{\delta} = \frac{EI}{L^3}$)

Modal Frequency $k_\omega = \sqrt{\frac{k_K}{k_M}} = \frac{1}{k_b}\sqrt{\frac{k_E}{k_\rho}}$

Impose Normalized Deflection:

$$\frac{\delta}{L} \propto \frac{FL^2}{EI} \Rightarrow F \propto \frac{EI}{L^2} \therefore k_F = \frac{k_{EI}}{{k_b}^2} = k_E {k_b}^2$$

Appendix H. As-built FEM Updates

Table of Contents

List of Figures

1 Introduction

The purpose of this FEM update is to incorporate differences of the as-built uCRM-13.5 from the previously modeled wing that may have an impact on the structural response. The intent of the model is to provide a basis for GVT and static load test correlation.

The basis of the model is the NASA-provided uCRM-13.5 Test Article FEM. The FEM includes a detailed model of the test article, as well as the test interface and AFRC reaction table. The NASA-provided model also contained updates since CDR including the outboard leading aluminum spar repair and the trailing edge Rib 3 and Rib 4 angle fittings. Two updated configurations are produced: the 'with skin offset' FEM and 'no skin offset' FEM, the sole difference between the two models being the application of offsets to skin elements to account for liquid shim thickness.

The primary updates to the FEMs include:

- Adjusting the spar cap thicknesses to account for cap thickness reductions during the springback MRB process
- Implementing skin offsets to account for variations in the liquid shim thickness (*'with skin offset' FEM only*)
- Added the Rib 4 Leading Edge Doubler plate
- Adjusted the thickness of the reaction plates to match actual thickness
- Added load plate point masses
- Updated Nonstructural mass:
    - 3" pins
    - LE Reaction Plate
    - TE Reaction Plate
    - Rib 0
    - Rib 3
    - Rib 4
    - Rib 8
    - LE spar (carbon)
    - LE spar (aluminum)
    - TE spar
    - Smeared NSM on all rib and spar caps to account for remaining wing mass
- Added rotational stiffness to CBUSH elements for stability
- Deleted skipped fasteners at the leading-edge spar splice joint
- Removed element 6802 (unneeded element that was an artifact in the model?)

2 File Structure

The Finite Element Models are provided in the Zip file “uCRM Test Article Correlation FEMs.zip”, which includes a series of Nastran bulk data files, broken down by entry type and/or part, as follows:

With_Skin_Offset_Modal.dat – Nastran Header File for Modal Analysis (SOL103): Configuration with skin offsets applied to account for liquid shim thickness.

With_Skin_Offset_Static.dat - Nastran Header File for Static Analysis (SOL 101) Configuration with skin offsets applied to account for liquid shim thickness.

No_Skin_Offset_Modal.dat – Nastran Header File for Modal Analysis (SOL103) Configuration *without* skin offsets.

No_Skin_Offset_Static.dat - Nastran Header File for Static Analysis (SOL 101) Configuration *without* skin offsets.

CSYS.bdf – Includes all CSYS entries.
Materials.bdf– Includes all Material entries.
Properties.bdf – Includes all Property entries, except for Reaction Plate.
ReactionPlateProperty.bdf – Reaction Plate PSHELL entry
BCs.bdf – Includes all Boundary Condition entries (SPC)
Loads.bdf – Includes 2.5G fixed loads (applied vertically)
AFRCFixture.bdf – Includes mesh for AFRC Reaction Table and mounting hardware
GVT_constraints.bdf – Constraints for GVT analysis
Rigids.bdf – Includes all rigid elements
ReactionPlates.bdf – Includes Reaction Plate mesh
Pins.bdf – Includes 3” Pin elements
Fasteners.bdf – Includes Fastener elements (CFAST and CBUSH)
LESpar.bdf – Includes Leading Edge Spar Mesh (including LE spar splice)
TESpar.bdf – Includes Trailing Edge Spar Mesh
UpperSkin_with_offset.bdf – Includes Upper Skin Mesh with skin offsets
LowerSkin_with_offset.bdf – Includes Lower Skin Mesh with skin offsets
UpperSkin_no_offset.bdf – Includes Upper Skin Mesh without skin offsets
LowerSkin_no_offset.bdf – Includes Lower Skin Mesh without skin offsets
Rib4Doubler.bdf – Includes Rib 4 LE Doubler
Ribs.bdf – Includes all Ribs (including Rib 3 and Rib 4 TE repairs)
LoadPlateMasses.bdf – Includes Load Plate point masses
NSM.bdf – Includes all nonstructural mass entries

3 Comparison of Results

3.1 Static Deflection

For comparison purposes only, a static linear load case was evaluated using the 2.5G test loads applied in the vertical Z direction to the original NASA-provided FEM as well as the updated, “with skin offset” FEM. The tip deflection decreases by 14 inches (15%) in the “with skin offset” FEM, as shown in Figure 1.

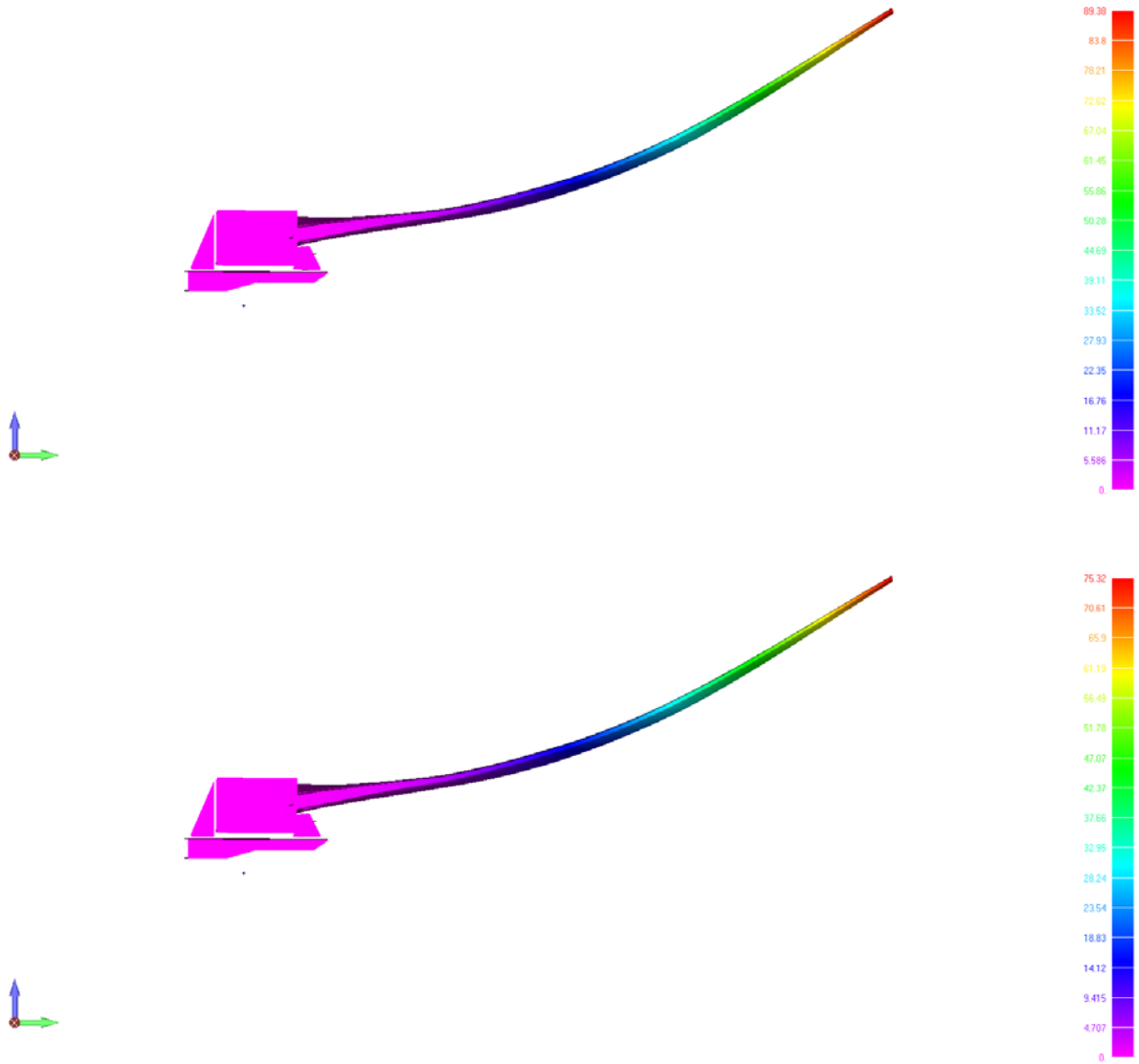

Figure 1. Comparison of static deflection from original (top) and updated (bottom) FEM. Note that the updated FEM reflects a lower tip deflection resulting from increased stiffness attributed primarily to skin offsets.

REPORT DOCUMENTATION PAGE	Form Approved OMB No. 0704–0188

1. REPORT DATE *(DD-MM-YYYY)*	2. REPORT TYPE	3. DATES COVERED *(From - To)*
01-02-2020	Contractor Report	

4. TITLE AND SUBTITLE

Passive Aeroelastic Tailoring Final Report

5a. CONTRACT NUMBER

5b. GRANT NUMBER
NNL15AA01C

5c. PROGRAM ELEMENT NUMBER

6. AUTHOR(S)
Smith, Benjamin; Brooks, Timothy; Leader, Mark; Wei Chin, Ting; Kennedy, Graeme; Martins, Joaquim; Cesnik, Carlos

5d. PROJECT NUMBER

5e. TASK NUMBER

5f. WORK UNIT NUMBER
432938.11.01.07.43.40.08

7. PERFORMING ORGANIZATION NAME(S) AND ADDRESS(ES)
NASA Langley Research Center
Hampton, Virginia 23681-2199

8. PERFORMING ORGANIZATION REPORT NUMBER

9. SPONSORING/MONITORING AGENCY NAME(S) AND ADDRESS(ES)
National Aeronautics and Space Administration
Washington, DC 20546-0001

10. SPONSOR/MONITOR'S ACRONYM(S)
NASA

11. SPONSOR/MONITOR'S REPORT NUMBER(S)
NASA/CR-2020-220425

12. DISTRIBUTION/AVAILABILITY STATEMENT
Unclassified-
Subject Category 01
Availability: NASA STI Program (757) 864-9658

13. SUPPLEMENTARY NOTES
Langley Technical Monitor: Carol D. Wieseman
Final Report

14. ABSTRACT

The Passive Aeroelastic Tailoring (PAT) project was tasked with investigating novel methods to achieve passive aeroelastic tailoring on high aspect ratio wings. The goal of the project was to identify structural designs or topologies that can improve performance and/or reduce structural weight for high-aspect ratio wings. This project considered two unique approaches which were pursued in parallel: through-thickness topology optimization and composite tow-steering.

15. SUBJECT TERMS

PAT; Passive Aeroelastic Tailoring; Static Testing

16. SECURITY CLASSIFICATION OF:			17. LIMITATION OF ABSTRACT	18. NUMBER OF PAGES	19a. NAME OF RESPONSIBLE PERSON
a. REPORT	b. ABSTRACT	c. THIS PAGE			STI Help Desk (email: help@sti.nasa.gov)
U	U	U	UU	261	19b. TELEPHONE NUMBER *(Include area code)* (757) 864-9658